UNIVERSIDADE DE SÃO PAULO
INSTITUTO DE FÍSICA DE SÃO CARLOS

Luan Bonneau Arbeletche

Simulation of extensive air showers and its detection

São Carlos

2021

Luan Bonneau Arbeletche

Simulation of extensive air showers and its detection

Thesis presented to the Graduate Program in Physics at the Instituto de Física de São Carlos of the Universidade de São Paulo, to obtain the degree of Doctor in Science.

Concentration area: Basic Physics

Advisor: Prof. Dr. Luiz Vitor de Souza Filho

Corrected version
(Original version available on the Program Unit)

São Carlos
2021

Arbeletche, Luan Bonneau

Simulation of extensive air showers and its detection / Luan Bonneau Arbeletche ; advisor Luiz Vitor de Souza Filho - Corrected version (Original version available on the Program Unit). – São Carlos, 2021.

164 p.

Thesis (Doctorate - Graduate Program in Basic Physics) – Instituto de Física de São Carlos, Universidade de São Paulo, 2021.

1. Extensive air showers. 2. Cosmic rays. 3. Very-high-energy gamma rays. I. Souza Filho, Luiz Vitor de, advisor. II. Título.

To my beloved family.

ACKNOWLEDGEMENTS

To carry out this Ph.D. course was an exceptional experience in several aspects. After moving to São Carlos, I spent four years working towards a project that culminated in what I present in this text. During this time, some individuals and groups have, maybe indirectly, contributed to this work and I would like to acknowledge them here.

First, I would like to express my gratitude to Vitor de Souza for accepting the task to supervise my PhD and for all patient and respectful advice I received during these four years. Through his example and guidance, I developed both as a scientist and as a better person.

I am also grateful to all the colleagues and friends with whom I had the lucky to work with at the Instituto de Física de São Carlos. You all certainly have affected my career and personality with your friendship and knowledge through all the conversations we had. I refrain to write every name I consider important, fearing that a simple acknowledgment can not be fair to the important contribution each of you have made to this thesis. Instead, I left to you the task of recognizing your name in these words. Specially, I thank my coworkers at Sala 5, the best at IFSC, my friends that would not miss a coffee break with an insightful conversation, the happy moments at bandejão, and everything else.

The shift at the Pierre Auger Observatory was an enriching experience I performed during the second year of my PhD. I am very grateful to Carola and Vitor for making this stay possible. I also thank Mariano, in Malargüe, for teaching me about the fluorescence detectors, for taking me to a visit at the Coihueco station, and for the excellent parrilla.

I thank my family, to whom I dedicate this thesis, and from whom I always received support, motivation, and love. I feel sorry that I have been distant during the course of my Ph.D as our proximity was always an important aspect in my life. I am certain this thesis will make you happy too.

I also dedicate this thesis to Amanda, who accepted to walk by my side during these four years in São Carlos and whose company is a never-ending source of happiness in my life. I feel very lucky and grateful for having your partnership, support, and love.

I acknowledge FAPESP Project 2015/15897-1.

This study was financed in part by the Coordenação de Aperfeiçoamento de Pessoal de Nível Superior – Brasil (CAPES) – Finance Code 001.

Think how diminished humanity would be if, under heavens constantly overclouded, as Jupiter's must be, it had forever remained ignorant of the stars. Do you think that in such a world we should be what we are?

Henri Poincarè

ABSTRACT

ARBELETCHE, L. B. **Simulation of extensive air showers and its detection**. 2021. 164p. Thesis (Doctor in Science) – Instituto de Física de São Carlos, Universidade de São Paulo, São Carlos, 2021.

Ground-based observatories allow for the detection of the most energetic forms of cosmic radiation in a multi-messenger context, including cosmic rays with energies above 10^{15} eV and gamma rays with energies above 10^{10} eV. Current experiments, such as the Pierre Auger Observatory, and forthcoming ones, such as the Cherenkov Telescope Array (CTA), have to deal with interpreting extensive air showers to reconstruct the fluxes of particles arriving at Earth. In this scenario, the general purpose of this thesis is to contribute to the improvement of the techniques used to reconstruct the properties of the primary particle in measurements of extensive air showers. In particular, four individual studies based on the simulation of air showers are presented. First, a study of the fluctuations in the atmospheric depth at which a shower reaches its maximum (X_{max}) is performed. The best functional form to describe the simulated X_{max} distributions is selected and, along with two alternative functions, parametrized. This study aims to improve the reconstruction of the relative abundances of primary masses in the ultra-high-energy regime ($E_0 > 10^{17}$ eV) and to provide a practical tool for any other studies depending on X_{max} distributions. Second, the angular distribution of Cherenkov light emitted from extensive air showers is parametrized using simulations performed in a broad energy range: from 100 GeV to 1 EeV. For this, a functional form to describe the angular distribution of Cherenkov photons is built using analytical arguments, and its parameters are constrained to describe the simulated showers. The resulting parametrization can be used to reconstruct the properties of air showers both through fluorescence detectors and Imaging Atmospheric Cherenkov Telescopes (IACT). Third, a technique to measure X_{max} through IACTs is developed. The proposed technique is shown to provide a resolution comparable to that of fluorescence detectors, allowing for mass composition studies around the knee in the cosmic-ray spectrum. Fourth, the problem of modeling hadronic interactions is visited in the context of the CTA observatory. An analysis based on simulations is performed to determine the extent to which image parameters reconstructed by IACTs are influenced by uncertainties in hadronic interaction models. Then, a computation of the uncertainty on the estimated CTA sensitivity curve due to hadronic interaction models is performed.

Keywords: Extensive air showers. Cosmic rays. Very-high-energy gamma rays.

RESUMO

ARBELETCHE, L. B. **Simulação de chuveiros atmosféricos extensos e sua detecção**. 2021. 164p. Tese (Doutor em Ciências) – Instituto de Física de São Carlos, Universidade de São Paulo, São Carlos, 2021.

Observatórios terrestres permitem a detecção da radiação cósmica em altas energias em um contexto de multi-mensageiros, incluindo raios cósmicos com energias acima de 10^{15} eV e raios gama com energias acima de 10^{10} eV. Experimentos atuais, tais como o Observatório Pierre Auger, e em fase de construção, como o Cherenkov Telescope Array (CTA), devem lidar com a interpretação de chuveiros atmosféricos extensos para reconstruir os fluxos de partículas que chegam na Terra. Neste cenário, o objetivo geral desta tese é contribuir para a melhoria das técnicas usadas na reconstrução das propriedades da partícula primária em medidas de chuveiros atmosféricos extensos. Em particular, três estudos individuais baseados em simulações de chuveiros são apresentados. Primeiro, faz-se um estudo da profundidade atmosférica na qual um chuveiro atinge seu máximo ($X_{\max}$). Determina-se a melhor forma funcional para descrever as distribuições de $X_{\max}$ simuladas e, junto com duas funções alternativas, apresenta-se uma parametrização desta. Tem-se por objetivo neste estudo aperfeiçoar a reconstrução das abundâncias relativas de massas no fluxo primário de raios cósmicos ultraenergéticos ($E_0 > 10^{17}$ eV), bem como fornecer uma ferramenta prática para outros estudos que dependam das distribuições de $X_{\max}$. Em um segundo estudo, a distribuição angular de luz Cherenkov emitida por chuveiros atmosféricos extensos é parametrizada utilizando chuveiros simulados em uma ampla gama de energias: de 100 GeV a 1 EeV. Para tal, uma forma funcional descrevendo a distribuição angular de fótons Cherenkov é construída usando argumentos analíticos e seus parâmetros são obtidos de forma a descrever os chuveiros simulados. A parametrização resultante pode ser utilizada na reconstrução de chuveiros tanto por detectores de fluorescência como por telescópios de imagem por Cherenkov atmosférico (IACT). No terceiro estudo, o conceito de uma técnica para medir $X_{\max}$ usando IACTs é elaborado. Mostra-se que a técnica é capaz de fornecer uma resolução comparável àquela de detectores de fluorescência, permitindo estudos de composição primária em energias ao redor do joelho do espectro de raios cósmicos. Por último, o problema da descrição de interações hadrônicas é visitado no contexto do Observatório CTA. Faz-se uma análise baseada em simulações para determinar em que medida os parâmetros de imagem reconstruídos em IACs são influenciados por incertezas presentes em modelos de interações hadrônicas. Em seguida, calcula-se a incerteza sobre a curva estimada de sensibilidade do CTA devido a incertezas em modelos hadrônicos.

Palavras-chave: Chuveiros atmosféricos extensos. Raios cósmicos. Raios gamma de altas energias.

LIST OF FIGURES

LIST OF TABLES

CONTENTS

1 INTRODUCTION

A central goal in astroparticle physics is to understand the nature of the cosmic radiation, including the environments in which astroparticles acquire energy or are emitted and the fields through which they propagate and interact. From the experimental perspective, a major concern is to characterize the fluxes of cosmic particles with precision and high statistics so that the measured data can help to constrain and select astrophysical models. As the astroparticles arrive at Earth in different types and in a vast energy range, several regimes of detection with different techniques are used to measure these particles. In particular, the ultra-high-energy cosmic rays ($E > 10^{17}\,\mathrm{eV}$) and very-high-energy gamma rays ($E > 10^{11}\,\mathrm{eV}$) can only be detected indirectly through the observation of extensive air showers.

The extensive air showers are cascades of particles and radiation triggered by the entrance of a cosmic particle in the atmosphere. Observable footprints of these cascades carry information about the primary particle and allow ground-based detectors to explore an energy window that would be inaccessible otherwise due to limited statistics. Although reconstruction of the properties of the primary particle is viable, difficulties exist in this process because a precise knowledge about the relations between shower observables and the properties of the primary particle is mandatory. The current paradigm is to use Monte Carlo simulations to connect shower observables with the characteristics of the primary particle. Considering this scenario, this thesis uses simulations of extensive air showers to build knowledge essential for experiments based on shower detection. In particular, this work is strongly motivated by the study of ultra-high-energy cosmic rays at the Pierre Auger Observatory and the astronomy made with very-high-energy gamma rays, mainly in view of the forthcoming Cherenkov Telescope Array. Four independent contributions are presented.

The first contribution is a study about the fluctuations of the depth at which an extensive air shower reaches its maximum number of charged particles (X_{max}). This variable is subject to large fluctuations, reflecting the stochastic nature of particle interactions in a shower. The X_{max} has been extensively used as an estimator of the mass composition of cosmic rays in the ultra-high-energy regime. At the Pierre Auger Observatory, this parameter is being measured with unprecedented precision through fluorescence detectors, allowing for X_{max} analyses using its entire distribution, rather than only its first and second moments. The description of the distribution of X_{max} in correlation with the primary particle is necessary to derive the relative abundances of primary masses from measurements. In this thesis, a search for the best functional form to describe the distributions of X_{max} is performed and a parametrization as a function of the primary energy and mass

is presented.

A second contribution from this thesis is related to the radiation of Cherenkov light from extensive air showers. The Cherenkov radiation is important for experiments relying on detection of light from air showers as it contributes to the signal in both cosmic ray and gamma-ray detectors. The precise description of the emission of Cherenkov light from air showers allows for the development of improved reconstruction techniques. In this thesis, a parametrization of the angular distribution of the Cherenkov light in air showers is presented. This study comprises a single parametrization that works in a broad energy interval and covers the entire angular range relevant for the detection of air showers.

In the third contribution, the ability of imaging telescopes to measure X_{max} is investigated. This study, fruit of a collaboration, has as motivation to push the capabilites of imaging telescopes as detectors of cosmic rays. A technique to measure X_{max} is proposed and its performance is investigated. In particular, the simulation procedure is detailed and the obtained resolution, comparable to that of fluorescence detectors, is presented.

The fourth and final contribution is a search to better understand the interplay between uncertainties in hadronic interactions and uncertainties associated with measurements in ground-based gamma-ray observatories. In the first part of this study, imaging telescopes are simulated using various combinations of hadronic interaction models and the distributions of basic image parameters are derived. Discrepancies between results from different models are quantified. This first study motivates the second part, in which the estimated sensitivity of the Cherenkov Telescope Array is shown to be significantly dependent on the model chosen to describe the hadronic interactions during the simulation of extensive air showers.

This document is organized in two parts: Chapters 2, 3, and 4 review concepts that motivate and permeate the results of this thesis; Chapters 5, 6, 7, and 8 are embodied by the principal results. In particular, Chapter 2 outlines the field of ultra-high-energy cosmic rays and puts the problem of determining the mass composition into perspective. The Pierre Auger Observatory is detailed in this chapter. Following, Chapter 3 reviews the field of astronomy with very-high-energy gamma rays and presents the concept of the Cherenkov Telescope Array. Chapter 4, the last of the first part, discusses the physics of extensive air showers and introduces the methods available to simulate them. The second part starts in Chapter 5, in which the parametrization of X_{max} distributions is presented. Chapter 6 is dedicated to the studies on the emission of Cherenkov light from extensive air showers. Next, Chapter 7 covers the measurement of X_{max} using imaging telescopes. In Chapter 8, hadronic interactions are investigated in the context of imaging telescopes. Finally, some closing remarks are given in Chapter 9.

2 ULTRA-HIGH-ENERGY COSMIC RAYS

Cosmic rays, in a comprehensive definition, are particles of any type carrying enough energy to propagate from distant cosmic sources to Earth, where they can be detected. These particles are observed in a broad energy range, including extreme values of $\sim 10^{20}\,\mathrm{eV}$, much beyond the highest achievable energy in human-made accelerators. Regarding the composition, fully ionized nuclei are preponderant ($> 99\%$) in the observed flux. In the ultra-high-energy end of the spectrum ($E > 10^{17}\,\mathrm{eV}$), the cosmic rays are believed to be a product of the most energetic extragalactic environments. Thereby, the motivation to detect and study the Ultra-High-Energy Cosmic Rays (UHECR) is related to the quest to understand the Universe from a microscopic scale, in which the dynamics of particle interactions are defined, to a macroscopic one, as particles propagate through astronomical distances.

The fundamental problem in UHECR research is to find the origin of this radiation, which requires describing both the acceleration of particles to extreme energies and the propagation through galactic and extragalactic fields. From an experimental perspective, three are the basic measurable quantities that can help to answer this question: the energy spectrum, the arrival directions, and the mass composition of the primary radiation. It is of interest in this thesis to understand the methods used to detect the UHECR, as it motivates the contributions presented in Chapters 5 and 6, and to build knowledge about the progress in the cosmic-ray physics. To this purpose, this chapter reviews the cosmic-ray science and discusses the experimental methods of the Pierre Auger Observatory. The discussion is organized as follows. In Section 2.1, an overview of the cosmic-ray science is presented, first from a historical perspective describing the evolution of the experimental techniques, and then the energy spectrum and the importance of measuring the mass composition of UHECR are discussed. Later, in Section 2.2, the techniques employed at the Pierre Auger Observatory are described, and a selection of important measurements from this experiment are presented. Finally, some concluding remarks are given in Section 2.3.

2.1 Overview of Cosmic-Ray Science

2.1.1 Historical perspective

The discovery of a radiation of cosmic origin did not happen until 1912, when the Austrian physicist Victor Hess performed a series of balloon ascents carrying electroscopes that led him to observe that the ionization of air at 5 km of altitude is more than twice that at sea level. In his own words, Hess concluded that these observations “seem to be readily explained by the assumption that a radiation of very high penetrating power enters

our atmosphere from above, and still produces in the lowest layers a part of the ionization observed". (1–2) The discovery was immediately followed the problem of determining the nature and the origin of this radiation. One of Hess' flights, performed during a partial solar eclipse, lead him to infer that the Sun was not a major source of this radiation, showing the signal came from sources further in space. (3)

At first skeptical about Hess' findings, between 1922 and 1923, Millikan reported on a series of measurements of the ionization of air in which he found no evidence for the cosmic radiation. (4) As pointed out by Hillas, this counterpoint to Hess' results is important, as it shows "that wrong conclusions can be readily drawn from cosmic-ray experiments unchecked by different techniques or different physicists". (2) Later on, in 1926, Millikan described measurements of the ionization in snow-fed lakes through which he found unambiguous proof of a radiation traveling downwards, coming from outside the Earth. (5) He deduced this radiation comprised very penetrating gamma rays with an energy of about $\sim 30\,\mathrm{MeV}$, to which he referred as the *cosmic rays*, and also mistakenly suggested as their origin the synthesis of elements from hydrogen in space. It is interesting to see that the picture accepted was that of a very penetrating gamma ray entering the atmosphere from above and losing part of its energy after successive elastic collisions in air before reaching ground. The ionization observed was thought to be a consequence of recoiling electrons after these collisions. (2)

In the 1930s, as the experimental techniques developed, the picture of a very penetrating gamma ray able to reach the ground was steadily being replaced by that of a cascade of *secondary* electrically charged particles started by a very energetic *primary* cosmic ray interacting in the upper atmosphere. In particular, the use of Geiger-Müller counters arranged in coincidence allowed Bothe and Kolhörster to infer that the radiation observed was of corpuscular nature. (2,6) The use of cloud chambers combined with electromagnets, on the other hand, allowed the discovery of the positron by Anderson (7) and the observation of electron-positron pair creation by Blackett and Occhialini in 1933. (8) Moreover, *showers* of particles emerging from metal plates were frequently observed in the cloud chambers, for which a very plausible explanation had been elaborated: fast electrons emit gamma rays, which induce electron-positron pair creation in the field of atomic nuclei, and so on, with all particles moving in approximately the same direction. (2) The scale of the cosmic-ray-induced showers, however, was not completely understood.

A very important contribution to the understanding of cosmic-ray-induced showers was made by Pierre Auger and his group. Rolland Maze, working in Auger's group, improved the resolving time of coincidence circuits to $5\,\mu\mathrm{s}$. (9) This technique allowed Auger to observe coincidence events with detectors separated by distances up to $300\,\mathrm{m}$. By noting that the rate of these events exceeded the chance rate expected from the resolving time of their circuit, they correctly concluded the observations should be due

to extensive air showers induced by primary cosmic rays in the upper atmosphere. An important conclusion presented by Auger in his report of 1939 was that these showers would require a primary particle of at least 10^{15} eV to reach the particle content observed at the ground. (10) This result extended the highest energy of the then known cosmic-ray spectrum by several orders of magnitude as earlier estimates predicted energies of ~ 10 GeV. (3)

During the 1940s and the 1950s, a race to measure the energy spectra, the mass composition, the arrival directions of the cosmic radiation, and the properties of cosmic-ray particles led physicists to devise several detection techniques, some of which are still used in current observatories. A breakthrough was the pioneering work of John Linsley, who started the operation of the first km^2-scale array at the Volcano Ranch experiment in 1959 (11) and, in 1963, published the first measurement of the cosmic-ray spectrum at energies above 10^{18} eV. (12) These measurements included an event of energy slightly above 10^{20} eV, pushing again the limits of the known energy spectrum of cosmic rays. Other km^2-scale ground arrays whose operation started in the 1960s include the Haverah Park experiment (13), the SUGAR (14), the AGASA (15), and, finally, the Yakutsk array (16), which is still in operation.

The discovery of the Cosmic Microwave Background (CMB) radiation in 1965 brought an important implication to the astrophysics of UHECR. Soon after the first observation of the CMB, Greisen (17) and independently Zatsepin and Kuz'min (18) noted that protons of energy higher than 4×10^{19} eV would interact with the 2.7 K background photons and produce secondary pions, therefore losing energy and suppressing the observed spectrum at energies higher than this threshold. It was also noted in these two works that the process of photo-disintegration would suppress the incoming particle flux at Earth even in scenarios in which the primary flux is dominated by nuclei heavier than hydrogen. What is now known as the GZK effect, at the time of its proposal, became a further motivation for the operation of large ground arrays. Before being confirmed by the HiRes experiment (19) and the Pierre Auger Observatory (20), the existence of the GZK suppression was a matter of tension between the results of the AGASA and the Fly's Eye observatories. (21–23) The Fly's Eye observatory, later updated to become the HiRes experiment, was the pioneer of the fluorescence-detection technique.

During the 1990s, James Cronin and Alan Watson formed a collaboration to plan the construction of a major observatory with an area larger than 1000 km^2 that would help to answer the long-standing questions in UHECR astrophysics. The tension between the AGASA and the Fly's Eye experiments acted as further motivation for the development of a larger observatory, as a larger collection area would result in enough statistics to unveil the spectrum at ultra-high energies. After a design study in 1995, a project was developed for an observatory comprising two sites of 3000 km^2 collection areas, one in each

hemisphere. Because of funding limitations, only the Pierre Auger Observatory (24), at the southern hemisphere, was accomplished and is taking data since 2004. (3) Fortunately, the AGASA and the HiRes collaborations joined efforts to construct an observatory with an area of 700 km^2, the Telescope Array (25), in the northern hemisphere. Both Pierre Auger and Telescope Array observatories take advantage of technical developments and expertise gained in the many previous experiments. The synergy between these two observatories allow for a full-sky coverage in the ultra-high-energy range and for important crosschecks between their measurements.

As of today, regarding the UHECR, many advances in understanding their nature have been made after several experiments and, in particular, the construction and operation of the Pierre Auger Observatory. Indeed, the energy spectrum has been precisely measured (26) and important studies on the mass composition have been performed. (27–33) Still, the origin of these particles remains an unsolved problem. Below, the energy spectrum of cosmic rays and the measurements of the primary mass composition at ultra-high energies are discussed.

2.1.2 The energy spectrum

The energy spectrum of cosmic rays – the flux of particles arriving at Earth as a function of its energy E – encompasses about eleven orders of magnitude, ranging from few 10^9 eV up to 10^{20} eV. Its shape can be roughly described by a power law: $J(E) \propto E^{-\alpha}$. The spectral index α is in the range $\alpha \approx 2.7$–3.0 throughout the spectrum and changes in α mark regions of different physical interpretation and carry information about the acceleration, the propagation, and the sources of the cosmic radiation. A compilation of measurements of the all-particle spectrum of cosmic rays, scaled by a factor of $E^{2.5}$, is shown in Figure 1.

Direct measurements of cosmic rays are possible at energies below 10^{14} eV. In this energy range, the incoming particle flux is high enough for particle detectors (either levitated to the upper atmosphere on board of balloons or placed in space satellites) to collect enough statistics for the reconstruction of the spectrum of individual components. It is accepted that most of these low-energy cosmic rays are of galactic origin, accelerated at supernova remnants (SNR), and the approximately constant spectral index of the observed spectrum is due to a combination of the spectrum of particles accelerated at their sources and the effects of diffusion in the magnetic field of the galaxy. (35–36) High-accuracy measurements, however, have recently shown that the spectrum of individual elements cannot be described by a plain power law, but present some subtle spectral features. (35, 37–38)

A well-established feature of the cosmic-ray spectrum is the so-called *knee*: a steepening of the all-particle flux at about 4×10^{15} eV, which is clear in Figure 1. Although an

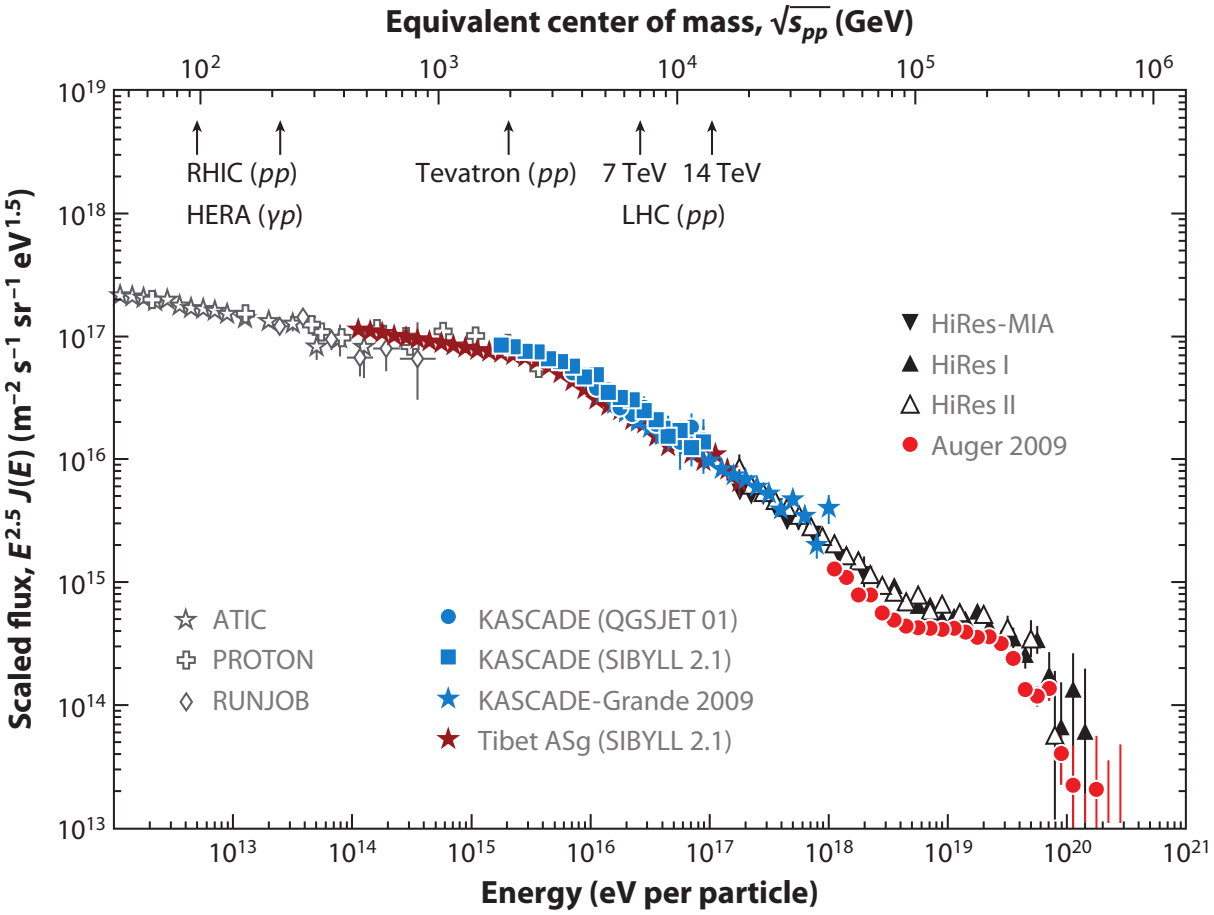

Figure 1 – The all-particle cosmic ray spectrum as measured from several experiments.

Source: ENGEL; HECK; PIEROG (34)

explanation of the knee is still a matter of debate, its cause is probably connected to a limitation of the maximum energy to which cosmic rays are accelerated in our galaxy. This hypothesis predicts that the maximum energy of the accelerated protons causes a softening in the observed all-particle spectrum, and the rigidity dependence of the acceleration processes leads to the existence of subsequent, less pronounced knees. (38) The positions of the cutoffs are expected to be proportional to the nuclear charge $E_{\mathrm{cut}}(Z) \approx Z \cdot 4.5\,\mathrm{PeV}$. (39) It is also possible to explain the knee in terms of propagation effects, in which protons above the knee can escape from the galaxy, thus leading to a steepening in the observed flux. The leakage of heavier primaries, at energies above the knee, would also cause the existence of secondary softenings. Both these complementary scenarios require the all-particle flux to be dominated by protons at the knee with a trend towards heavier elements above it and are supported by KASCADE data (40) and by observations of a second knee near 10^{17} eV. (41–44) The most notable experimental challenges to study the knee arise because at these energies, and above, the decreasing flux makes direct measurements hardly attainable.

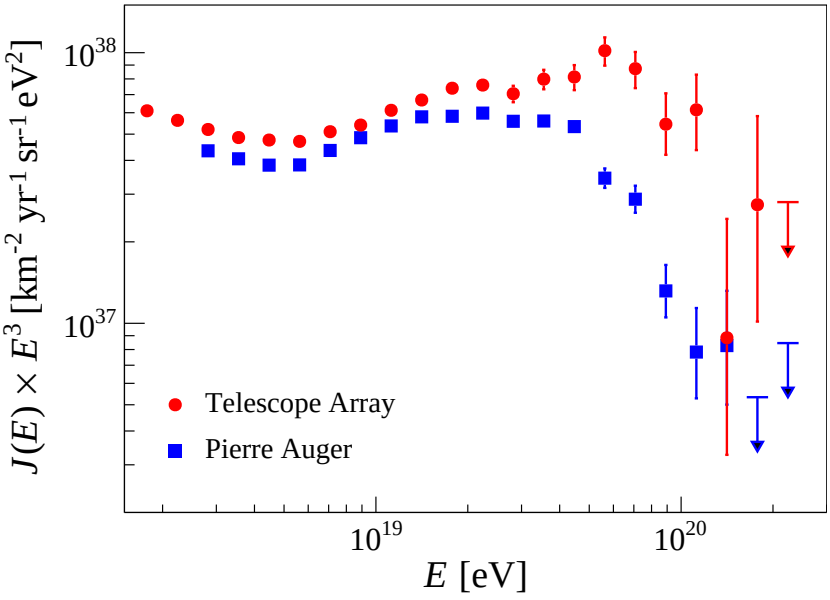

Figure 2 – Comparison of the ultra-high energy cosmic-ray spectrum as measured by the Pierre Auger (Auger) and the Telescope Array (TA) observatories.

Source: Adapted from AAB *et al.* (26)

At about 5×10^{18} eV, the observed flux suffers a hardening, a feature known as the *ankle* of the spectrum. Despite the existence of the ankle being well established, its physical origin is still not well explained. (45) The ankle has been first observed at the Volcano Ranch experiment and, since then, a simple explanation is usually cast: it may be caused by a transition from a galactic-dominant to an extragalactic-dominant origin of the cosmic rays observed at Earth, in which the hardening corresponds to the onset of a proton flux of extragalactic origin. (12,46) The extragalactic origin of the most energetic particles has been recently supported by anisotropy studies at the Pierre Auger Observatory. (47–48) However, the turning point from a galactic to an extragalactic dominated flux is still undetermined and strongly correlated to the mass composition at ultra-high energies.

The flux above the ankle is so small that only giant arrays, such as the Pierre Auger Observatory, can collect enough data to disentangle its spectral features. A comparison of the flux of ultra-high energy cosmic rays as measured by the Pierre Auger Observatory and the Telescope Array is detailed in Figure 2. Data from both observatories agree within systematics in the energy range below 10^{19} eV (49), confirming the existence of the second knee around 10^{17} eV and of the ankle at 5.0×10^{19} eV (4.9×10^{19} eV) in Auger (Telescope Array). At energies above the ankle, data from the Telescope Array is compatible with a single power law up to 6.5×10^{19} eV, after which a suppression takes place. (50) This is in contrast with the spectrum measured at the Pierre Auger Observatory, that exhibits a softening at about 1.3×10^{19} eV and a suppression at 5×10^{19} eV. (26, 51) It is important to note that the discrepancies between the spectra above $\sim 10^{19}$ eV persist even after

a rescaling of the measured energies to account for known systematic effects. (49) The suppression of the cosmic-ray flux is, though, a well-established feature of the spectrum.

2.1.3 Astrophysical models and the importance of the mass composition

On general grounds, phenomenological models for UHECR have to deal with two elements: i) the sources, including their distribution in space and time and the acceleration mechanisms, and ii) the propagation, including energy losses and interactions. The level to which parameters can be constrained and, importantly, to which models can be rejected, strongly depends on the quality and the precision of the data they are confronted to. Prior to the data from the Pierre Auger Observatory, there was a running paradigm that provided a simple, however effective, explanation to UHECR based on a pure proton composition. (45, 52–53)

In the so-called *dip* model (52–53), the flux of UHECR is assumed to be of only protons, which are accelerated at sources with a generic power-law injection $\propto E^{\gamma_g}$, where the spectral index γ_g and a flux normalization are the only two free parameters. In this case, the only relevant astrophysical background are the CMB photons, with which protons can undergo the process of pair production

$$p + \gamma_{\rm CMB} \rightarrow p + e^+ + e^- \tag{2.1}$$

and of photo-pion production

$$p + \gamma_{\rm CMB} \rightarrow p + \pi^0. \tag{2.2}$$

Along with these two processes, adiabatic energy losses (red shift) due to the expansion of the Universe are also important. Each of the two aforementioned interactions affects the measured spectra in several ways. The photo-pion production process is responsible for a suppression of the flux at $E_{\rm GZK} \approx 4\times10^{19}$ eV, corresponding the *GZK cutoff*. Furthermore, this process causes a *bump* in the flux towards smaller energies because of the pileup of protons that had lost part of their energy. The signature from the pair-production process is a dip in the measured spectrum between 1×10^{18} eV and 4×10^{19} eV, and two flattenings: one at $E \sim 1\times10^{19}$ eV, reproducing the ankle, and a second at $E \sim 1\times10^{18}$ eV, related to a transition from galactic to extragalactic cosmic rays. A fit to data predicts a value of $\gamma_g = 2.7$ for the acceleration at sources. (52)

A useful quantity to verify the effects of the dip model on the observed spectrum is the so-called modification factor $J(E) = J_p(E)/J_{\rm unm}(E)$, where $J_p(E)$ is the proton spectrum considering all interactions and energy losses and $J_{\rm unm}(E)$ is the unmodified spectrum considering only the adiabatic energy losses. The theoretical predictions for $J(E)$ as computed in reference (38) compared to data from four experiments claiming a pure proton composition are shown in Figure 3. It is seen from this figure that the dip

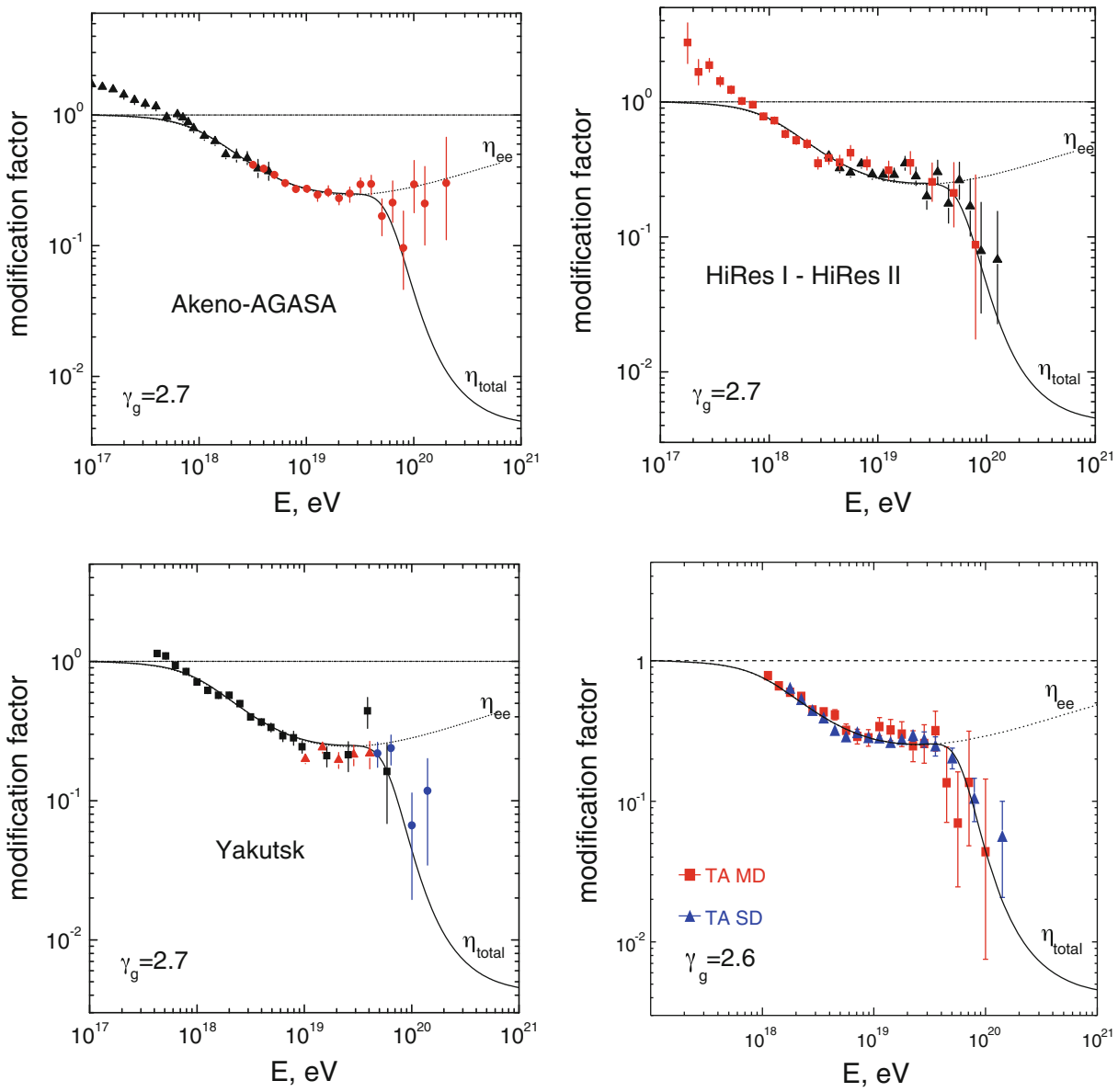

Figure 3 – Modification factor η_{total} in the dip model compared to measurements from four experiments (indicated inside the plots) whose data are compatible with a pure proton composition. η_{ee} is the modification factor disregarding the photo-pion production process. References for the data sets can be found in. (38)

Source: ALOISIO *et al.* (38)

model provides a very attractive explanation for the observed spectral features. This model was supported by mass-composition data available in the early 2000s, in particular from the HiRes (54–55) and the Yakutsk experiments (56), all in favor of a proton-dominated composition at the highest energies.

Nevertheless, in view of the mass-composition measurements at the Pierre Auger Observatory, the scenario of a pure-proton composition is strongly disfavored and the previously running paradigm breaks down. (45, 57) As discussed in Section 2.2.4, results from the Pierre Auger Observatory are compatible with an increasingly heavier composition above the ankle. (27–33) Moreover, evidence has been found for a mixed composition already at the ankle. (30)

In this new scenario, astrophysical models have to deal with additional degrees of freedom describing the relative abundances of primary masses in the observed spectrum, which still cannot be unambiguously resolved from data. Besides the processes of pair production and photo-pion production, to which bound nucleons are also subject, nuclei can interact with background photons in the intergalactic medium via photo-disintegration

$$A + \gamma_{\mathrm{CMB,EBL}} \rightarrow (A - B) + B\,. \tag{2.3}$$

Regarding the background photons, the Extragalactic Background Light (EBL) also comes into play in the case of propagating nuclei. As a result, these interactions not only interfere in the observed energy spectrum but also change the underlying mass composition of the accelerated spectra.

In this sense, some models (57–60) have been proposed to accommodate the results from the Pierre Auger Observatory. A common finding in these models, and here is a turning point in the understanding about the sources, is that the increasingly heavier composition towards the highest energies may be a sign of rigidity-dependent acceleration mechanisms. This observation has two important consequences: the first is that protons do not have to be accelerated up to $\sim 10^{20}\,\mathrm{eV}$, but to some $\sim 10^{18}\,\mathrm{eV}$, and the second is that the suppression is not only a GZK effect but also relates to a limitation at the sources. Moreover, it is argued that either a very hard spectrum at sources ($\gamma_{\mathrm{g}} \approx 1$) (57) or an enhanced proximity to ultra-high energy cosmic ray sources (60) is necessary to fit the observed data.

Of particular interest is a study of the Pierre Auger Collaboration (61), recently updated and discussed in reference (51), in which a combined fit of the energy spectrum and of the depth of shower maximum X_{max} (see Section 4.1.3 for a description of X_{max}) of UHECR as measured at the Pierre Auger Observatory is performed. An illustration of this combined fit is found in Figure 4. These studies reassure that the spectral features at ultra-high energies are reproduced by the envelope of individual elemental groups accelerated with hard spectra by a mechanism with a single rigidity cutoff. The suppression

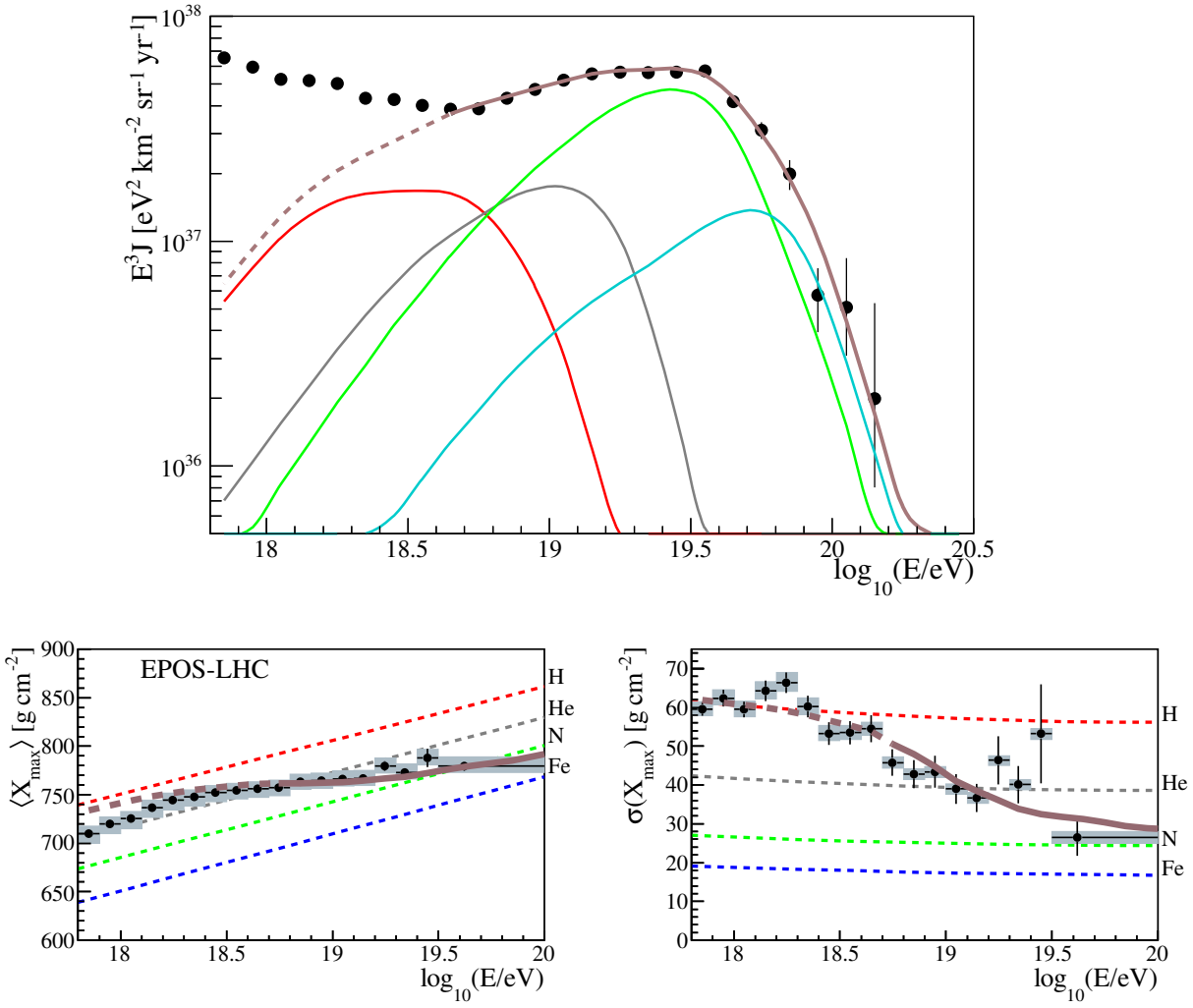

Figure 4 – Combined fit of spectrum (upper plot) and mass composition (lower plots) to the data from the Pierre Auger Observatory. The lower plots show the resulting average and standard deviation of $X_{\max}$ against the measured values. Line colors represent the primary masses, indicated in the lower plots.

Source: AAB *et al.* (61)

at extreme energies is because of a combination of photo-disintegration of nuclei and a source limitation. An important finding of reference (61) is that the theoretical uncertainties related to the development of extensive air showers are, in general, much larger than the statistical uncertainties on fit parameters.

In summary, the mass composition of the flux of UHECR observed at Earth is a fundamental piece of information to understand the origin of these particles. The Pierre Auger Observatory has already provided important results in this direction, with strong implications for astrophysical models. Unfortunately, unambiguous data on the relative abundances of primary masses are still not available, and their existence would provide a strong constraint to astrophysical models by reducing the number of free parameters.

2.2 The Pierre Auger Observatory

The Pierre Auger Observatory (24) is the largest cosmic-ray experiment developed to measure the properties and map the sources of the most energetic cosmic radiation. It operates thanks to the efforts of over 400 scientists from 17 countries in a world-wide collaboration. The observatory has been designed as a hybrid experiment, combining surface detectors to measure shower particles at the ground and fluorescence detectors to observe the longitudinal development of the air showers. The experiment is in the city of Malargüe, Argentina, and has been taking data since 2004, before completing its construction in 2008. Since then, the Pierre Auger Collaboration has published the most precise data on the spectrum, the anisotropies, and the mass composition of the UHECR.

Bearing in mind the impossibility of describing such a complex facility and all its achievements in the present thesis, below only the surface array and the fluorescence detectors are presented and the reconstruction algorithms are discussed. These are the principal instruments of the Pierre Auger Observatory. A brief discussion on the measurements of the energy spectrum and the mass composition is elaborated. Emphasis will be given towards aspects relevant to the subsequent chapters of this thesis.

2.2.1 The surface array

The surface array of the Pierre Auger Observatory is formed by 1660 surface-detector stations spread over an area of $\sim 3000\,\mathrm{km}^2$ in a triangular grid of 1.5 km separation, with 60 of those forming a smaller *infill* array with half the separation, covering an area of $23.5\,\mathrm{km}^2$. Each surface detector is a coated polyethylene tank of 3.6 m diameter and 1.2 m height filled with ultra-pure water. Three photomultiplier tubes are symmetrically placed on the upper surface of the tank to collect the Cherenkov-light signal from passaging shower particles. Additional components include solar panels and batteries to provide energy to the electronics. A GPS receiver and its antenna are installed to allow for event timing and communication with the central data-acquisition system. A schematic

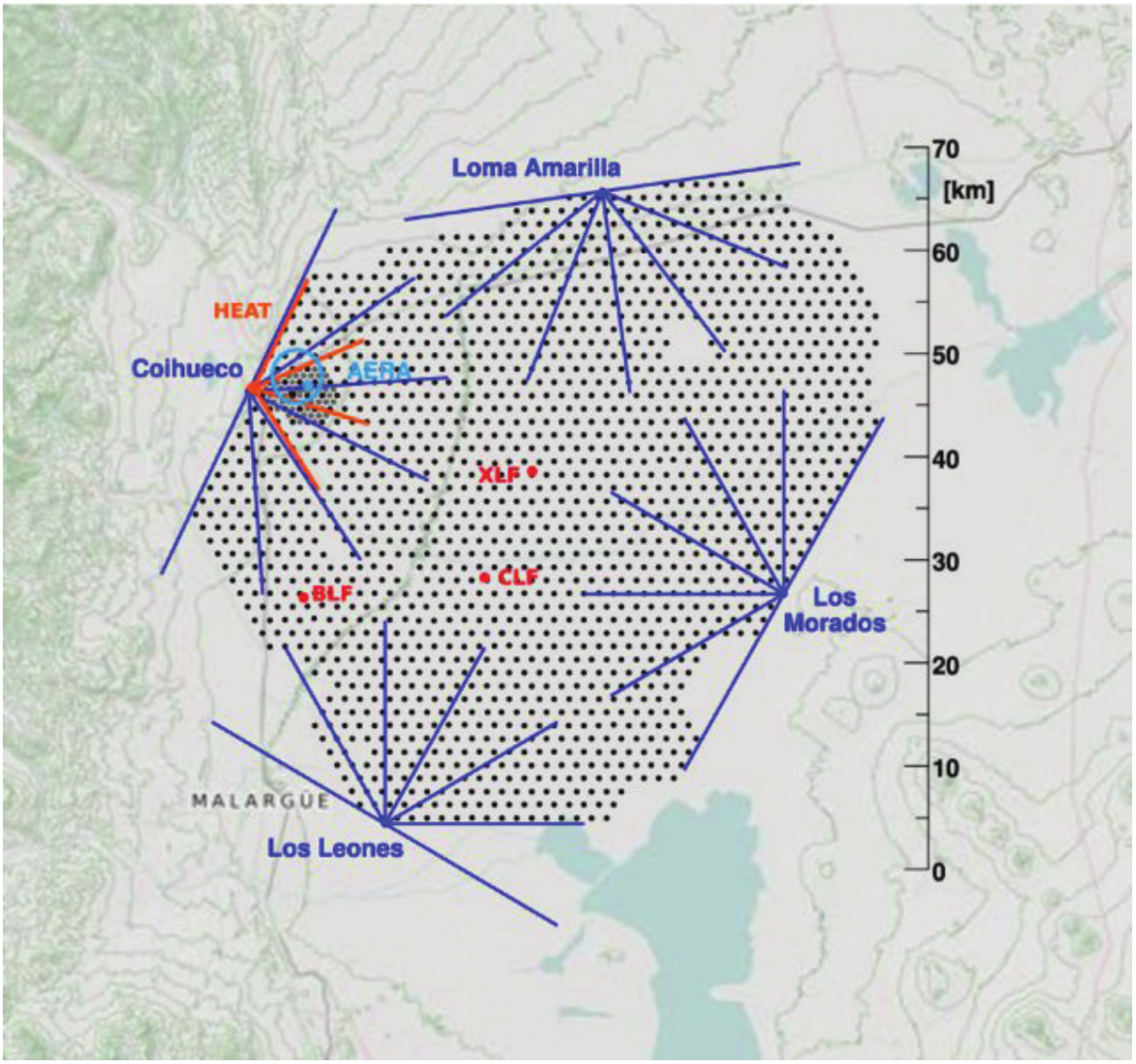

Figure 5 – Representation of the detectors of the Pierre Auger Observatory. Water-Cherenkov surface detectors are shown as black dots. The blue lines delimit the field of view of the six fluorescence detectors at each of the four baseline stations: Morados, Leones, Coihueco, and Loma Amarilla. The field of view of each HEAT telescope is shown in orange. The AERA system of radio detectors is located in the light-blue area. Also shown are the positions of the laser facilities (XLF, CLF, and BLF) for atmospheric monitoring as the red dots.

Source: AAB *et al.* (62)

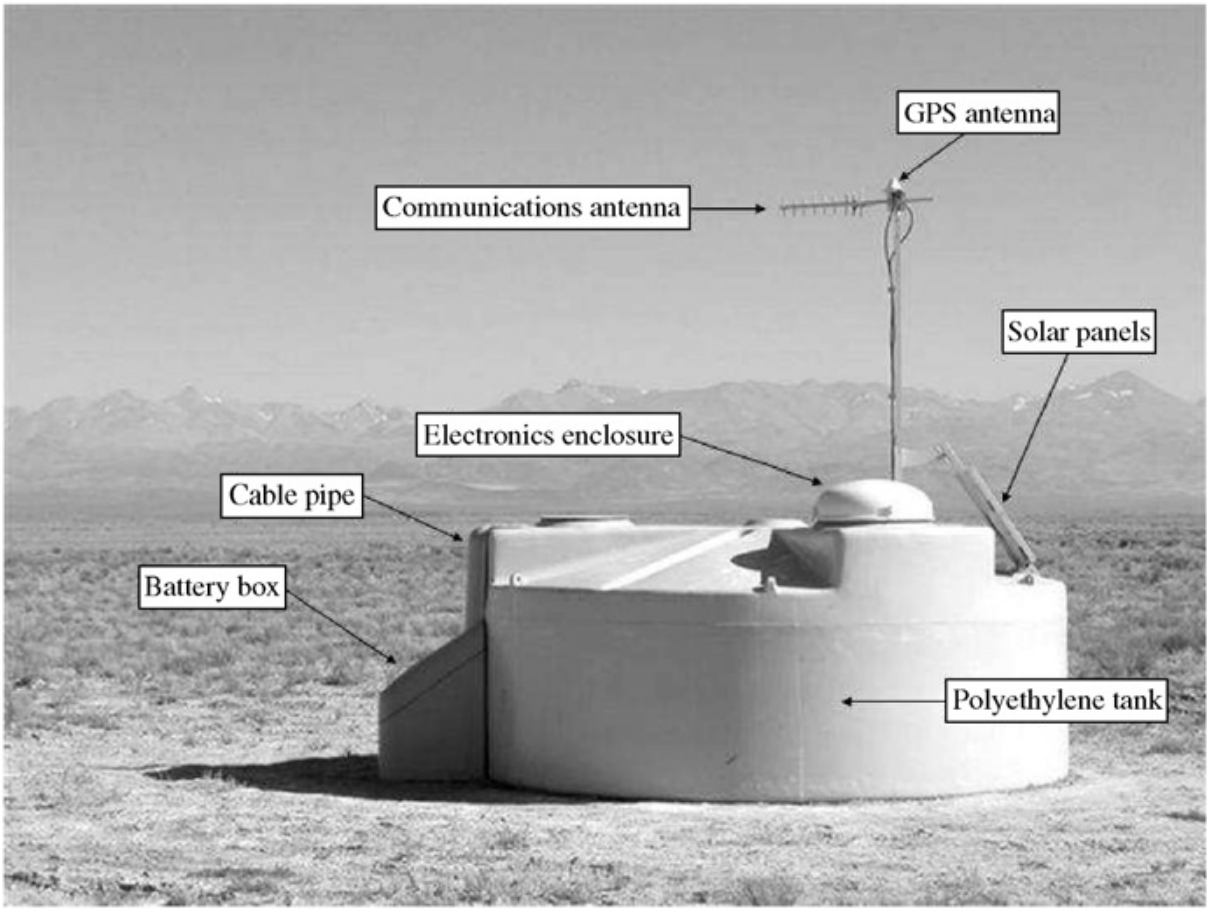

Figure 6 – Surface station at the Pierre Auger Observatory and indication of its main components.

Source: ALLEKOTTE *et al.* (63)

view of a surface station is shown in Figure 6. As the operation of a surface station is independent of weather or other external conditions, it can operate with a duty-cycle of almost 100%. (63) The trigger chain of the surface array is such that showers with energy above 3×10^{18} eV are selected with 99% efficiency, with a rate of about 3×10^{-5} Hz. (64)

A shower can be effectively reconstructed from the surface array using timing and signal information from stations triggered in coincidence. The geometry reconstruction uses the start times of the signals at each triggered station t_i to fit the expected values $t_{\mathrm{sh}}(\vec{x}_i)$ from a shower front moving at the speed of light

$$\chi^2 = \sum_i \frac{\left[t_i - t_{\mathrm{sh}}(\vec{x}_i)\right]^2}{\sigma_{t_i}^2}\,, \tag{2.4}$$

where σ_{t_i} are the estimated uncertainties in t_i and $\vec{x}_i$ are the detector positions. The shape of the shower front is addressed in two different frameworks: it can be a front with constant curvature (in the *Herald* reconstruction) or correspond to an inflating sphere

with a fixed starting point (in the *Observer* reconstruction). The existence of two independent reconstruction frameworks, Herald and Observer, is important as it allows for cross-checking, validation, and the study of systematics. Both frameworks result in an angular resolution better than 1.4° that improves with the increase of zenith angle and energy. (65)

As for the shower size, a lateral distribution function $S(r)$ is used to fit the total signal on the triggered stations. In the general form, the lateral distribution function is

$$S(r) = S_{1000} \cdot f_{\mathrm{LDF}}(r)\,, \tag{2.5}$$

where S_{1000} is the shower-size estimator, corresponding to the expected signal at 1 km from the shower core, so that the normalization $f_{\mathrm{LDF}}(1\,\mathrm{km}) = 1$ applies. This method of using a shower-size estimator at a fixed distance to the shower core aims to minimize shower-to-shower fluctuations of this quantity. Two functional forms are used for the function $f_{\mathrm{LDF}}(r)$ in the different *Herald* and *Observer* reconstruction frameworks. In both, the slopes of $f_{\mathrm{LDF}}(r)$ are parametrized in terms of S_{1000} and the zenith angle θ of the shower axis. A maximum-likelihood procedure is then adopted to get the position of the shower core $\vec{x}_{\mathrm{c}}$ and S_{1000}:

$$\ln \mathcal{L} = \sum_i \ln P\left(S_{1000}, \vec{x}_{\mathrm{c}} | S_i, \vec{x}_i\right)\,, \tag{2.6}$$

where S_i and $\vec{x}_i$ are the observed signal and the position of the i-th station. The function $P\left(S_{1000}, \vec{x}_{\mathrm{c}} | S_i, \vec{x}_i\right)$ is such that it considers both the triggered stations and the non-triggered stations where a signal would be expected. (65)

To estimate the primary energy, the dependence of S_{1000} with the shower zenith angle θ is taken into account in terms of the Constant Intensity Cut (CIC) method. The CIC method is an empirical procedure that considers the attenuation of the electromagnetic part of the shower with atmospheric depth, which is proportional to $\sec\theta$. Effectively, the shower-size estimator S_{1000} is converted to a zenith-independent estimator S_{38} through $S_{1000}(\theta) = S_{38} \cdot f_{\mathrm{CIC}}(\theta)$, where the attenuation factor $f_{\mathrm{CIC}}(\theta)$, derived from observations, is a polynomial in $\cos\theta$ and $f_{\mathrm{CIC}}(38°) = 1$. Finally, a set of high-quality hybrid events, reconstructed by both the fluorescence detectors and the surface array, is used to correlate S_{38} with the energy reconstructed by the fluorescence detectors E_{FD}. This correlation, shown in Figure 7, is well described by a power law: $E_{\mathrm{FD}} = A \cdot (S_{38})^B$. This method results in a systematical uncertainty of about 14% in the energy reconstruction from the surface array above 10^{18} eV. (26) A similar method was also developed for the estimation of the primary energy in inclined showers ($60° \leq \theta \leq 80°$) based on the size estimator N_{19}, which is sensible to the muonic component. (66) Since the energy reconstructed by the ground array is calibrated by the fluorescence detectors, uncertainties of the reconstruction with the latter are automatically propagated to the energy estimated from the former.

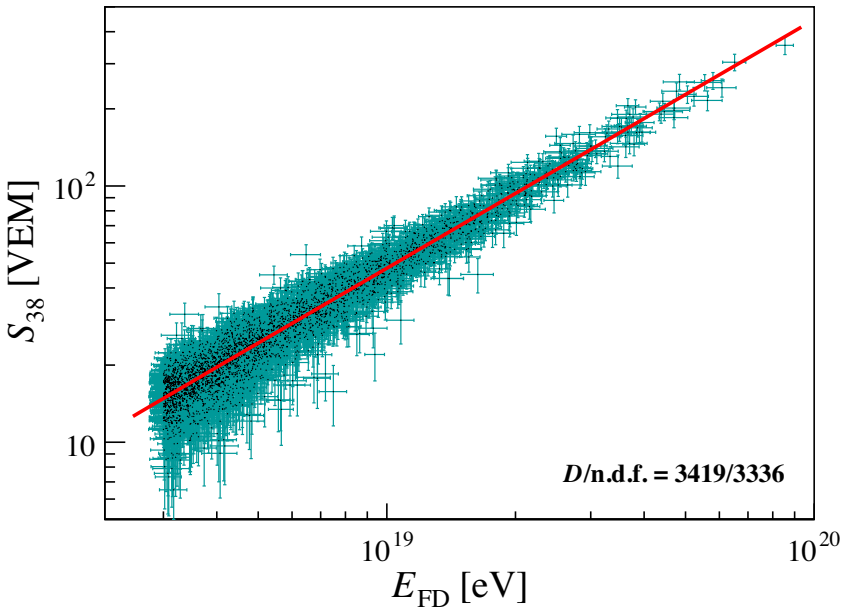

Figure 7 – Correlation between the shower-size estimator S_{38} and the energy reconstructed by the fluorescence detectors E_{FD} in a set of selected hybrid events. The red line is a power-law fit described in text.

Source: AAB *et al.* (26)

2.2.2 The fluorescence detectors

The Pierre Auger Observatory comprises four stations of fluorescence detectors: Coihueco, Loma Amarilla, Los Morados, and Los Leones, whose positions are depicted in Figure 5. Each station includes six independent telescopes with a field of view of $30° \times 30°$ in azimuth and elevation, so that every station covers 180° in azimuth and the region from 0° to 30° in elevation. The combined field of view of the four stations overlooks the entire surface array. An additional fifth station, the High Elevation Auger Telescopes (HEAT), at the Coihueco site, has three telescopes observing elevation angles from 30° to 58°. The HEAT, along with the infill array below its field of view, observe showers with energies around and below 10^{18} eV. (24)

The optical system of the telescopes combines a shutter, that is opened only when conditions are appropriate for data taking, the aperture system, containing a filter and a corrector lens, a large mirror, and a fast-timing camera. A schematic view of a fluorescence telescope is shown in Figure 8. The filter at the aperture is aimed to absorb visible light and transmit photons in the range from ~ 290 nm up to ~ 410 nm, within which most of nitrogen-fluorescence light is emitted. (68) The mirror, built in segments, has a total area of $\sim 13\,\mathrm{m}^2$ and reflects light towards the camera, whose position lies in the focal surface of the telescope. (67) The camera, aided by a sophisticated electronic- and software-based trigger system, register shower candidates based on the time evolution on tracks of

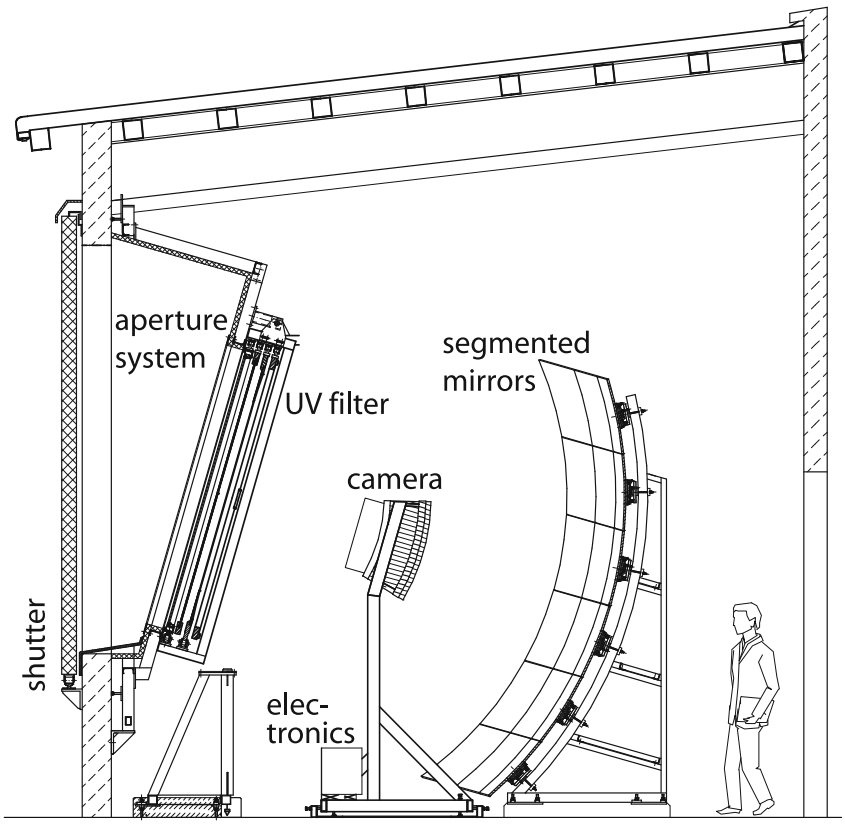

Figure 8 – Illustration of a fluorescence telescope at the Pierre Auger Observatory indicating its main components.

Source: ABRAHAM *et al.* (67)

triggered pixels. Operation of the fluorescence detectors is done remotely, either at the central data-acquisition room in Malargüe or from distant offices, and requires a group of scientists to monitor atmospheric conditions, to calibrate the system, and to control the data taking. Limitations imposed by external conditions, such as the moonlight and the weather, impose a duty-cycle of about 14% to the fluorescence detectors.

An example of a shower track registered by the fluorescence detectors is shown in the left plot of Figure 9. From the registered tracks, the longitudinal profile of a shower is reconstructed in a two-step procedure. First, the time evolution of the signal is used to perform a geometrical reconstruction and compute the direction of the shower axis. Second, the signal amplitudes along the shower track are used to reconstruct the calorimetric energy-deposit profile.

For the geometrical reconstruction, detailed in reference (69), a Shower-Detector Plane (SDP) is defined as in Figure 10 according to the signal-weighted viewing directions of the triggered pixels and the telescope position. Subsequently, the shower is assumed to be a point-like source of isotropic light moving at the speed of light, for which the arrival

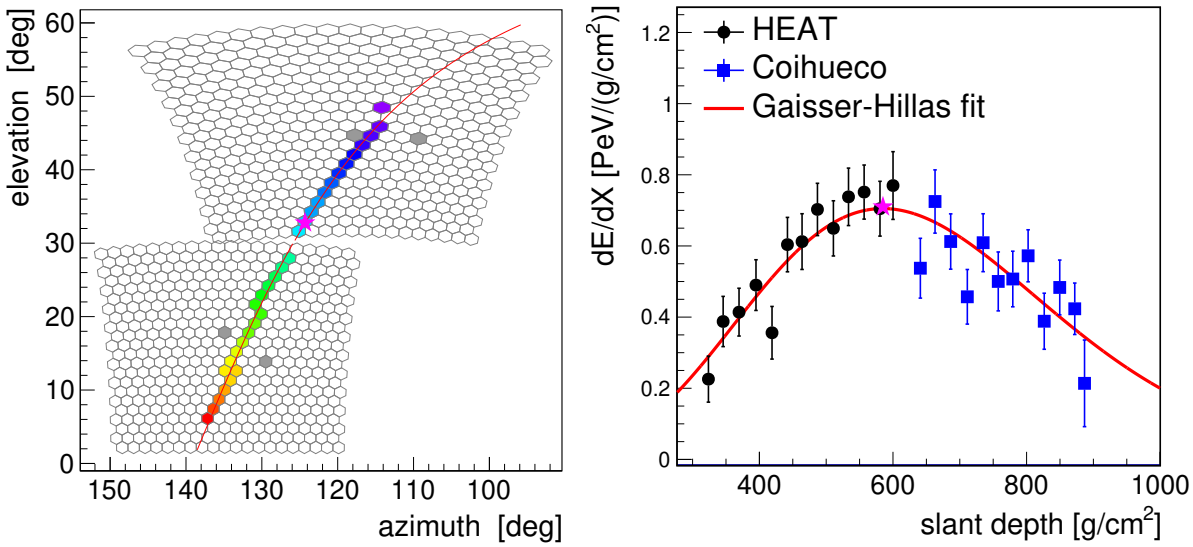

Figure 9 – Example of a longitudinal profile reconstructed by the fluorescence detectors at the Pierre Auger Observatory. Left: shower track observed in coincidence at HEAT (upper) and Coihueco (lower) cameras. Colors represent the time dependency of the signal, evolving from blue to red. Right: Reconstructed longitudinal profile combining the signal from the two cameras. Also shown is the fit to a Gaisser-Hillas function (red line) and the reconstructed depth of shower maximum $X_{\max}$ (pink dot).

Source: BELLIDO (31)

time of photons at the i-th triggered pixel is found to be

$$t_i = t_0 + \frac{R_{\mathrm{P}}}{c} \tan\left(\frac{\chi_0 - \chi_i}{2}\right) , \tag{2.7}$$

where R_{P} is the smallest distance between the shower axis and the detector, t_0 is the time at which the shower front passes through R_{P}, χ_0 is the angle between the horizontal and the shower axis measured along the SDP, and χ_i is the viewing angle of the i-th pixel. The parameters t_0, R_{P}, and χ_0 completely specify the shower axis and are obtained by fitting the data, possibly including additional timing information from the surface array. (67) With this method, the shower axis can be reconstructed with an angular resolution of 0.6°. (67, 70)

The reconstruction of longitudinal profiles is a more complicated procedure, as it involves further insights about light emission from air showers and its transport in the atmosphere. As an output, this procedure aims at obtaining the calorimetric energy-deposit profile $\mathrm{d}E_{\mathrm{cal}}/\mathrm{d}X$, illustrated in the right plot of Figure 9. The approach employed at the Pierre Auger Observatory follows from the algorithm prescribed in reference (71), in which the light produced at depth X_i and reaching the aperture at time t_i is the sum of three contributions:

$$y_i = y_i^{(\mathrm{Fl})} + y_i^{(\mathrm{CD})} + y_i^{(\mathrm{CS})} . \tag{2.8}$$

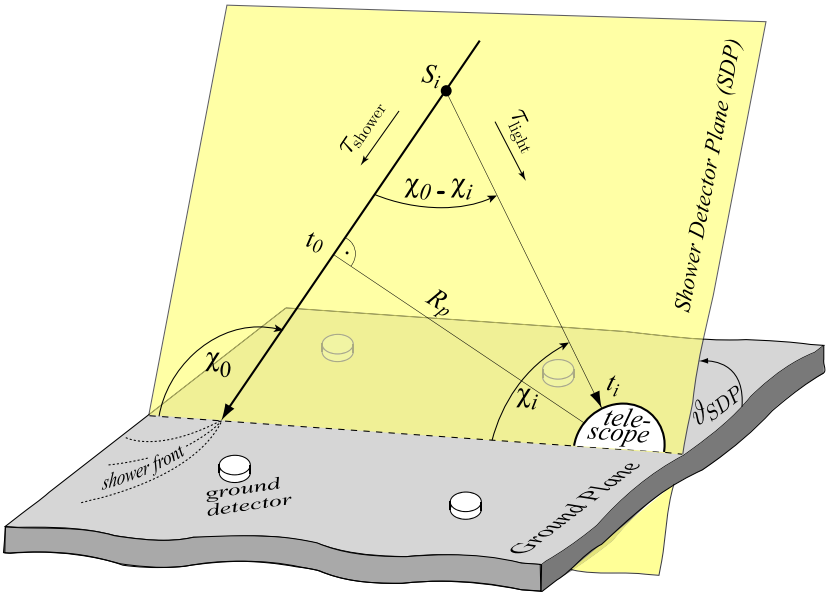

Figure 10 – Illustration of the shower-detector plane and the geometrical shower reconstruction of an extensive air shower in a fluorescence telescope.

Source: KUEMPEL; KAMPERT; RISSE (69)

Namely, the contributions are from the direct (unscattered) fluorescence light $y_i^{(\mathrm{Fl})}$, the direct Cherenkov light $y_i^{(\mathrm{CD})}$, and the scattered Cherenkov light $y_i^{(\mathrm{CS})}$. Whereas the angular distribution of fluorescence light at emission is isotropic, the production of Cherenkov light follows an intricate angular distribution that depends on the energy and angular distributions of electrons in the air shower. In this sense, under the assumption that the number of electrons in the air shower at depth X_i is proportional to the energy deposit per unit slant depth at this position w_i, a parametrization of the angular distribution of the emitted Cherenkov photons is used to compute $y_i^{(\mathrm{CD})}$. In Chapter 6, a detailed discussion on the emission of Cherenkov light from air showers is performed, and a novel parametrization is presented.

Having reconstructed the longitudinal profile $\mathrm{d}E_{\mathrm{cal}}/\mathrm{d}X$ of a shower (shown as black dots in Figure 9), the next step is to perform a fit to a Gaisser-Hillas function (72)

$$\frac{\mathrm{d}E_{\mathrm{cal}}}{\mathrm{d}X} = w_{\max} \left(\frac{X - X_0}{X_{\max} - X_0} \right)^{\frac{X_{\max} - X_0}{\lambda}} \exp\left(\frac{X_{\max} - X}{\lambda} \right) , \tag{2.9}$$

where $X_{\max}$ is the depth of shower maximum, $w_{\max}$ is the energy deposit per unit slant depth at $X_{\max}$, λ describes the shower width and X_0 is the virtual starting point of the shower development. The calorimetric energy E_{cal}, corresponding to the energy deposited by the shower in the atmosphere, is given by the track-length integral of the fitted longitudinal profile for which a simple closed form expression exists. (71) Finally, to get the energy of the primary particle E_0, it is necessary to consider that a substantial fraction ϵ_{inv} of the primary energy is converted into the weakly interacting muons and neutrinos,

and therefore is unnoticed by the fluorescence detectors. Accordingly, the primary energy E_0 relates to E_{cal} via

$$(1 - \epsilon_{\mathrm{inv}}) \cdot E_0 = E_{\mathrm{cal}} \,. \tag{2.10}$$

In the Pierre Auger Observatory, a data-driven method is adopted to derive the value of ϵ_{inv}. (73)

Typically, events registered by the fluorescence detectors at the Pierre Auger Observatory are dominated by the fluorescence yield, with a secondary contribution from Cherenkov light, for which the reconstruction process just described applies. This is the case for the most energetic events in which the shower core hits the array at several kilometers from the fluorescence detectors and the angle between the shower axis and the telescope viewing direction is large. In these showers, only the Cherenkov light emitted at large angles ($> 5°$) from the shower direction is important and the scattered Cherenkov light plays an important role. Recently, however, there has been a growing interest in less-energetic events developing closer to the telescope cameras, whose signal is dominated by direct Cherenkov light and the two reconstruction steps are reconciled in a single profile-constrained geometry fit. (74–76) These analyses reaffirm the importance of the study carried in Chapter 6 in the context of the Pierre Auger Observatory. Furthermore, the reconstruction of Cherenkov-dominated events approaches fluorescence detectors to the methods used in imaging Cherenkov detectors, such as those discussed in Chapter 3. Results published in reference (77), and discussed in Chapter 7, are also important in this context as they show the longitudinal profiles observed via Cherenkov light do not follow a Gaisser-Hillas function.

2.2.3 Measurements of the energy spectrum

Since its inception, the Pierre Auger Collaboration has published several measurements of the energy spectrum in the range from $10^{18}\,\mathrm{eV}$ up to $10^{20}\,\mathrm{eV}$ using the surface array and the fluorescence detectors. (20, 26, 66, 79–80) The most recent measurement and the newly discovered features of the ultra-high-energy spectrum were already discussed in Section 2.1.2.

Recently, the observation of Cherenkov-dominated events has allowed for the observation of the spectrum down to energies of $3 \times 10^{16}\,\mathrm{eV}$. (75) Along with measurements from the infill array (81), it was possible to characterize the second knee in the spectrum from the complementary, cross-calibrated measurements at the Pierre Auger Observatory. A compilation of the most recent measurements from the different techniques is shown in Figure 11.

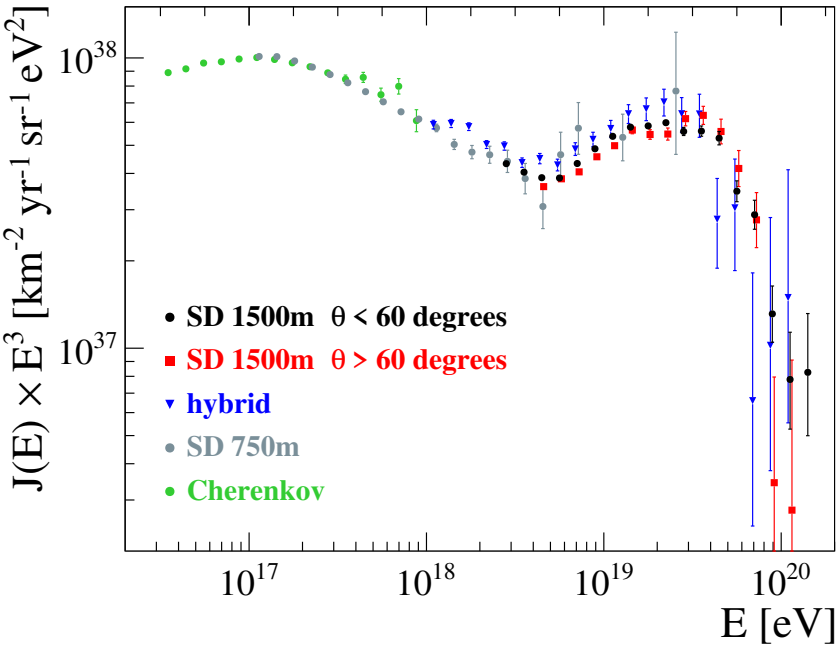

Figure 11 – Energy spectrum of cosmic rays measured at the Pierre Auger Observatory using different techniques.

Source: VERZI (78)

2.2.4 Measurements of the mass composition

Extremely important to understand the nature of the UHECR, the primary composition has been studied in several analyses at the Pierre Auger Observatory. Typically, the primary mass is inferred by comparing shower observables to Monte Carlo simulations. This procedure carries large uncertainties, since models for hadronic interactions have to be extrapolated to energies higher than those reached by particle colliders, at which their parameters are constrained. Besides, the stochastic nature of air showers makes impossible to infer the mass composition on a shower-by-shower basis. For the analysis of the primary composition, the less model-dependent the theoretical prescription of an observable is and the higher the quality of a data sample, the more accurate the analysis.

The most frequently used variable in mass-composition studies is the depth of shower maximum X_{max}, whose average $\langle X_{\mathrm{max}} \rangle$ and variance $\sigma^2(X_{\mathrm{max}})$ are sensible to the distribution of primary masses (28,82) (see Chapter 4). Besides, as X_{max} is mostly affected by the electromagnetic component of the shower, uncertainties on X_{max}-based analyses are reduced compared to other analyses because of the small dependency on hadronic interaction models. At the Pierre Auger Observatory, a set of fiducial volume cuts are applied in the event selection to ensure the measured values of $\langle X_{\mathrm{max}} \rangle$ and $\sigma(X_{\mathrm{max}})$ correspond to those of the real distribution (83–84), thus allowing for a direct comparison to theoretical predictions.

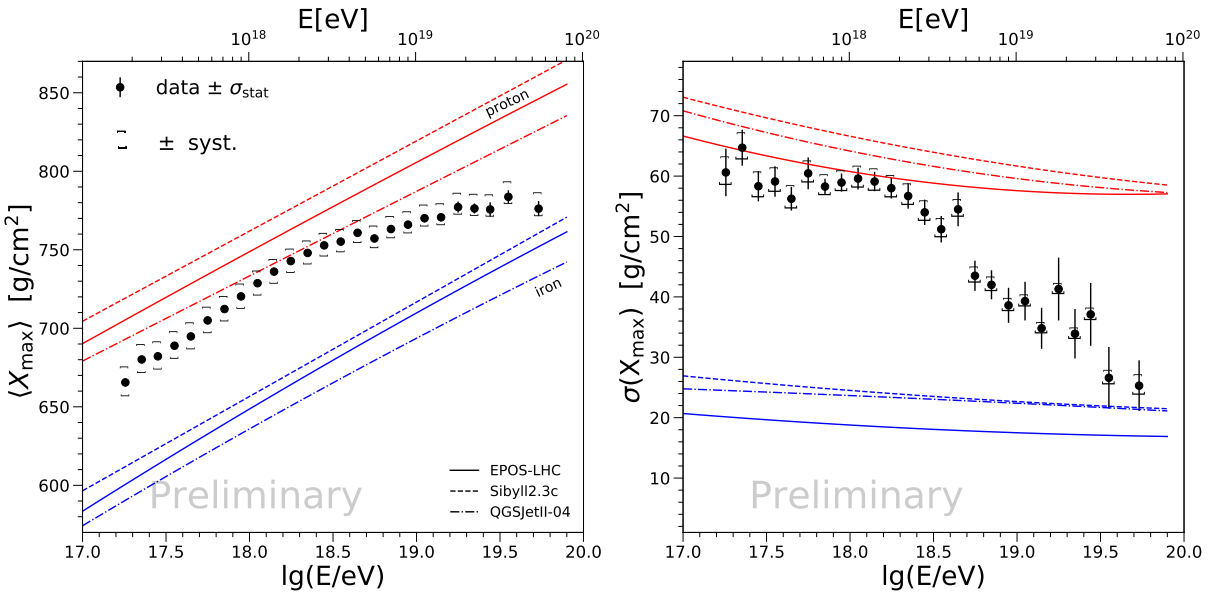

Figure 12 – Average and standard deviation of the $X_{\max}$ distributions as measured by the fluorescence detectors at the Pierre Auger Observatory.

Source: YUSHKOV (33)

In Figure 12, a comparison between recent measurements of $\langle X_{\max} \rangle$ and $\sigma(X_{\max})$ to Monte Carlo predictions for energies above $10^{17.2}$ eV is presented. From the analysis of $\langle X_{\max} \rangle$ alone (left plot), it is seen that there is a trend towards lighter elements as the energy increases below the ankle ($\sim 10^{18.3}$ eV), and an increasingly heavier composition from the ankle to the highest energies. The trend of $\sigma(X_{\max})$ (right plot) also shows the composition becomes heavier as the energy increases. (27,33,84) Excellent agreement was found with a method to estimate $\langle X_{\max} \rangle$ based on the rise time of the signals at the surface detectors, which allowed for an estimation of $\langle X_{\max} \rangle$ up to 10^{20} eV with larger samples than those available from the fluorescence detectors. (32,85)

Inferences on the primary mass composition based on $X_{\max}$ were further performed directly based on the measured $X_{\max}$ distributions in references. (29,31) Such analyses, in contrast to those based on mean and variance, allow for a quantitative estimate of the relative abundances of primary masses. Indeed, in reference (31), the measured $X_{\max}$ distributions are used to fit the fractions of individual components based on parametrizations of simulated $X_{\max}$ distributions. The illustrative cases of the fractions of proton, helium, nitrogen, and iron obtained in reference (31) are shown in Figure 13. Regarding the theoretical predictions for $X_{\max}$ distributions, this type of analysis carries uncertainties related to the hadronic interactions models and also to the functional form used to parametrize the $X_{\max}$ distributions. Studies on the description of $X_{\max}$ distributions and a novel set of parametrizations are discussed in Chapter 5.

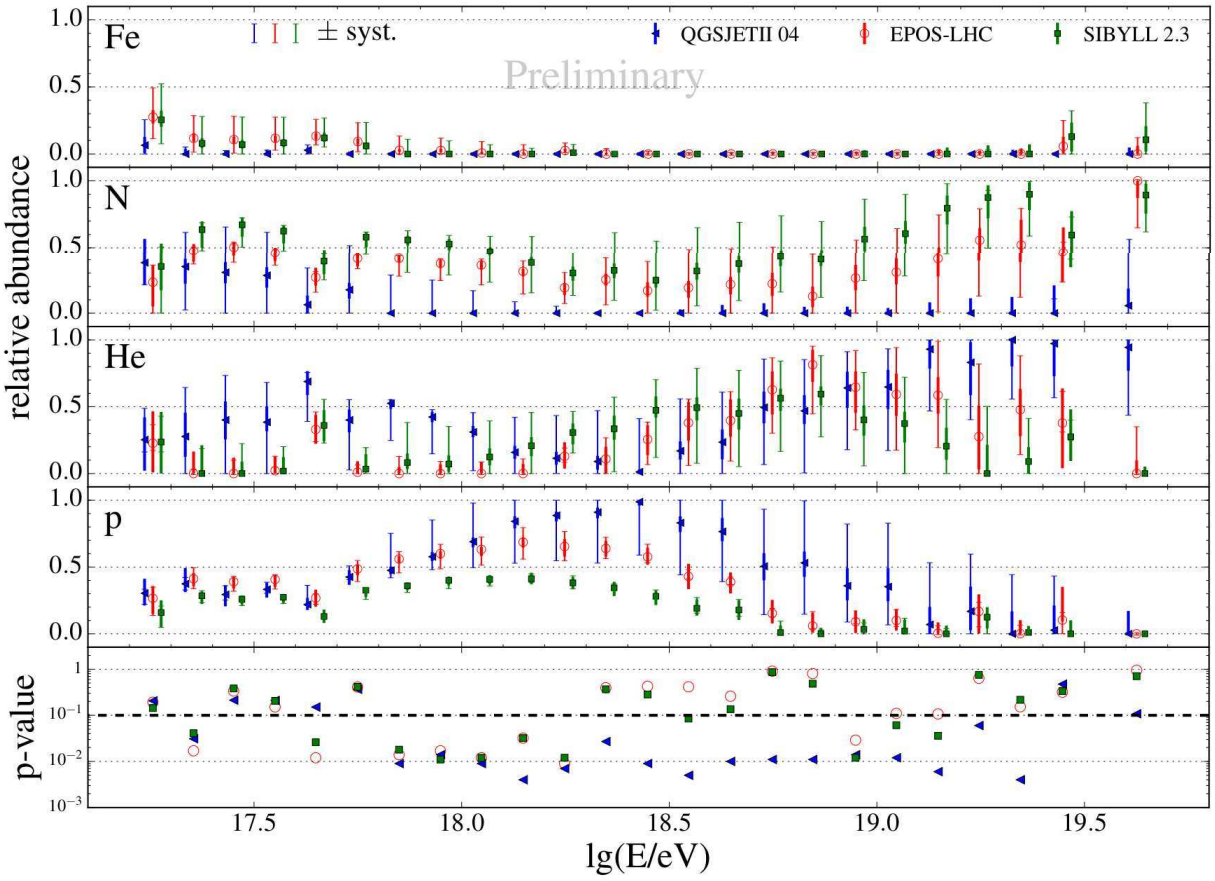

Figure 13 – Fitted fractions of primary masses from measured $X_{\max}$ distributions at the Pierre Auger Observatory.

Source: BELLIDO (31)

2.3 Conclusion

In this chapter, some aspects of cosmic-ray research have been outlined and the Pierre Auger Observatory, an instrument built to detect UHECR, has been presented. From a historical perspective, it has been seen that the science of cosmic rays developed around the fundamental question of determining the origin and nature of these particles. Although measurements have revealed the energy spectrum of these particles to high precision, an unambiguous determination of their mass composition is lacking. This information would strongly constrain theoretical models of cosmic-ray acceleration and propagation. By looking at measurements from the Pierre Auger Observatory, it becomes clear that the problem of determining the mass composition of UHECR is not only a technical limitation, but is also limited by the capability of interpreting the observables from extensive air showers.

In this sense, this thesis presents contributions in Chapters 5 and 6 that might allow for an improved interpretation of the measurements of $X_{\max}$ and an improved re-

construction of this quantity. In view of the importance of $X_{\max}$ to determining the mass composition, results of this thesis ultimately contribute to solving the problem of determining the mass composition of UHECR.

3 VERY-HIGH-ENERGY GAMMA-RAY ASTRONOMY

Photons of non-thermal origin are emitted within a broad wavelength range from cosmic sources and travel through straight lines before they can be observed at Earth. They act, therefore, as direct messengers from the physical processes within the radiating celestial object. Astronomy made with very-high-energy gamma rays, in particular, is aimed at characterizing the morphology, the spectral energy distribution, and time variability of sources of photons with energies exceeding some tens of GeV up to some hundreds of TeV. It is a relatively new science, whose maturity has been reached with the current generation of ground-based observatories, all in operation for less than two decades. Prospects for this science are many. They range from the search for cosmic-ray accelerators, a now century-long-standing problem, to the observation of dark matter, or even tests of the validity of fundamental theories in extreme scenarios. These prospects become even more interesting in face of the forthcoming Cherenkov Telescope Array (CTA), a major observatory for very-high-energy gamma-ray astronomy. This observatory will comprise the two largest arrays of imaging atmospheric Cherenkov telescopes (IACT) ever built, one in the northern and one in the southern hemisphere. In order to explore its full potential, the CTA will certainly require an improvement in the methods used to reconstruct the primary fluxes through the observation of extensive air showers.

The operation of IACTs, both in current observatories and in the CTA, motivates the studies of Chapters 6 and 7 of this thesis. Therefore, the present chapter is devoted to review aspects of very-high-energy gamma-ray astronomy with emphasis on experimental techniques, rather than focusing on the astrophysical aspects of the gamma-ray science. The organization is as follows. Section 3.1 summarizes gamma-ray astronomy. It includes a brief account for the historical development of gamma-ray astronomy, a discussion on the imaging technique, and an outline of the known sources of very-high-energy gamma rays. Following, Section 3.2 discusses what will be the CTA observatory once its construction is finished. A selection of key science plans of the CTA project are also outlined in this section. Some last words are given in Section 3.3 so to have a wider outlook of gamma-ray astronomy in the context of this thesis.

3.1 Overview of gamma-ray astronomy

3.1.1 Historical perspective

Historically, the field of gamma-ray astronomy is closely tied to the physics of cosmic rays. (86–88) In the late 1940s and early 1950s, experiments in the upper atmosphere established to no doubts that the primary flux of cosmic rays is mostly composed of protons, with a smaller contribution from heavier nuclei. (2) The discovery that most of the

primary radiation is electrically charged turned out to be, in some sense, disappointing as the direction of the incoming rays can not be traced back to their sources due to deflections in cosmic magnetic fields. At that time, it was also established that the abundant radio signal from some astrophysical objects could not be associated to thermal emission, but fit to the synchrotron radiation from cosmic-ray electrons in the surrounding magnetic field (89), thereby connecting radio emission with possible cosmic-ray sources. The list of known radio sources included the Crab Nebula, a supernova remnant. This gave support to the previous thought (90) that supernovae are effective cosmic-ray accelerators within the Galaxy. However, there were no clues on how to connect the acceleration of protons and nuclei with signals from supernovae or other candidate sources. This changed in the late 1950s, when ideas emerged suggesting that sources accelerating the bulk of cosmic rays could be associated with the radiation of gamma rays. (91–92) These ideas have set a powerful impetus to develop methods to observe very-high-energy gamma rays from cosmic sources.

From the experimental side, developments were made already in the 1950s. Blackett estimated in 1948 that a fraction of about 10^{-4} of the night-sky brightness should be due to Cherenkov radiation from the general flux of cosmic rays. After getting in touch with this idea in 1952, Galbraith and Jelley conjectured about the possibility of observing Cherenkov-light flashes from extensive air showers and have set a rudimentary detector (a single mirror to reflect light into a lone photomultiplier tube mounted on the interior of a garbage can) to catch the Cherenkov-light pulses from air showers. (93) They could observe the light pulses in coincidence with an array of Geiger-Müller counters, thus directly correlating the signal at the telescope with the cosmic radiation. (94) To use a telescope with small angular acceptance to detect gamma-ray showers was ideal since most Cherenkov light is emitted within a small angular region ($< 1.5°$) around the shower axis, thus allowing for the search of point-like sources. With a technique set and the motivation to search for cosmic-ray sources through gamma rays, many were the attempts in these early days to correlate shower counts in excess of the background with the direction of source candidates. Unfortunately, prior to the 1980s, even with somewhat more elaborated telescopes, no convincing detection of gamma-ray sources through ground-based observations was made. (95)

In view of the difficulties faced by ground-based observatories, satellite-based detectors appeared as a viable alternative for gamma-ray astronomy already in the 1970s as they offer easier separation between gamma-rays and the overwhelming hadronic background. In 1972, a report on the results from instruments flew aboard the OSO-3 satellite was published. (96) This report claimed the discovery of cosmic gamma rays with energies above $\sim 50\,\mathrm{MeV}$, with the distribution of arrival directions revealing a clear enhancement of emission in the Galactic plane region and the existence of a diffuse, isotropic component of softer spectrum. Other three space missions, the SAS-2 (97–98), the COS-B (99),

and the CGRO (100), were launched respectively in 1972, 1975, and 1991. The latter, carrying the EGRET detector (101), operated through 1996. The EGRET could detect gamma rays from 20 MeV up to 30 GeV and presented the first complete sky survey (102) and an extensive catalogue (103) listing 271 distinct sources – some of these have been found to be artifacts of the analysis. (102) These three missions were the predecessors of the two gamma-ray missions currently in operation aboard spacecrafts: the AGILE (104), launched in 2007, and the Fermi (105), launched in 2008. The AGILE is covering the gamma-ray band between 30 MeV and 50 GeV. The Fermi mission, with its Large Area Telescope (Fermi-LAT), is detecting gamma-rays in the range from 30 MeV to 300 GeV. Significant advances were made in the high-energy gamma-ray regime (from some MeV to some hundreds of GeV) with these two missions, with a wealth of sources being detected. (106) Nevertheless, observations in the very-high-energy regime (above hundreds of GeV) would only become possible through ground-based observatories with their large effective collection areas.

Back in the 1960s, a project was set that resulted in a major achievement for ground-based gamma-ray astronomy: the Whipple Observatory at Mt. Hopkins, led by T. Weekes. This project comprised the deployment of a telescope with a 10-m multi-faceted mirror and a science program with observations concentrated on the Crab Nebula. (107) The Whipple telescope started operations in 1968 with a single 12.5 cm photomultiplier tube on the mirror focus, which was later updated to two, offset by an angle of 2.4° to allow for simultaneous observation of the on-source and off-source regions of the sky (108) (known as the *wobble mode* (109), still used today). By 1972, after many nights of observation, no detection of point sources were made except an unconvincing (87) 3σ excess from the Crab nebula. (110) It was soon realized that an improvement in instrumental sensitivity to gamma-ray fluxes was necessary to achieve ground-based gamma-ray astronomy. To circumvent this problem, K. Turver and T. Weekes proposed in 1978 a method to record images from air showers using matrices of photomultiplier tubes, whereby a separation between proton and gamma-ray events would be possible. (111) They also pointed out that an array with four such telescopes would improve sensitivity even further. (112)

The imaging technique, pioneered by the Whipple collaboration in the 1980s, made ground-based gamma-ray astronomy possible. For that, the 10-m Whipple telescope was updated in 1983 with a pixelated camera comprising 37 photomultiplier tubes spaced by 0.5° in a hexagonal grid. (113) The camera was able to register images from the Cherenkov light emitted by the air showers. Along with this instrumental improvement, came the need for improved analysis techniques. To separate gamma-ray showers from the hadronic background based on the shower images was necessary. First, a simple gamma-ray selection relying on the intensity of the signal in the two hottest pixels allowed for a 5.6σ observation of the Crab Nebula, published in 1985. (114) Then, Hillas contributed importantly in this direction. After performing detailed Monte Carlo simulations for the

updated Whipple telescope, Hillas showed that each image could be parametrized according to its position, orientation, and spread on the camera. Using simple cuts defining the signal and background domains of the parameter distributions, the method would lead to a reduction of $\sim 98\%$ on the protonic background while keeping about two-thirds of the gamma-ray showers. (115) By 1989, the Whipple collaboration reported on a 9σ detection of TeV gamma rays from the Crab Nebula by relying on the imaging technique and the *Hillas parameters*. (113) This was the first statistically significant detection of a gamma-ray source using a ground-based detector. After that, the Whipple telescope was equipped with a high-resolution camera of 109 pixels (116) which, along with a new data-based method for gamma-hadron discrimination using Hillas parameters (117), allowed for a 45.5σ observation of the Crab Nebula in 1991 (118), which highlighted the power of the imaging technique. At this point, ground-based gamma-ray astronomy at very-high energies was already a reality.

More sources would become known in the following years. After the success with the Crab Nebula, the Whipple Observatory performed campaigns in the 1990s to search for extragalactic objects. (119–120) Started in 1992, a campaign looking for blazars with small redshifts listed by the EGRET satellite resulted in the first detection of an extragalactic very-high-energy gamma-ray source: the nearby galaxy Markarian 421. (121) As sources farther away were not detected in this campaign, Punch et al. noted when reporting the discovery of the Markarian 421 that it has provided experimental evidence that TeV photons are strongly absorbed due to the interaction with the extragalactic background light. (121) Moreover, very-high-energy gamma-ray astronomy with extragalactic objects has been proven to be possible after this detection. As of 1995, a search for nearby blazars was started in which the second extragalactic TeV gamma-ray emitter was found: the Markarian 501. (122) According to Catanese *et al.* (119), as the Markarian 501 "was not identified in EGRET catalogs as a significant source, it highlighted the ability of ground-based gamma-ray telescopes to complement not only the results of the space-based gamma-ray telescopes, but also to augment them." From this point on, several observatories had studied and developed even further the experimental techniques. Among those, the successful application of the stereoscopic technique at the HEGRA observatory was a major achievement.

The Cherenkov-telescope array at the HEGRA site, on La Palma, Canary Islands, operated with five telescopes composing a single stereoscopic detector through 1998. Four of the telescopes were deployed at the corners of a 100 m square, with the fifth at its center. Each telescope comprised a multi-mirror reflector with an area of $8.5\,\mathrm{m}^2$ (corresponding to an aperture of 3.3 m) and a 271-pixel camera. (123–124) Despite previous attempts from other observatories to implement the observation with multiple Cherenkov telescopes (125–128), the HEGRA array was the first to find the optimal configuration (through Monte Carlo simulations) and reach improved sensitivity. (129–130) An array-

based trigger ensured that events at HEGRA were registered simultaneously by multiple telescopes and the combination of images allowed not only for an improved gamma-hadron separation but also improved angular resolution compared to single-telescope observations. (131) The HEGRA array confirmed and improved measurements of sources already detected, as well as discovered new sources of very high-energy gamma rays. Namely, the HEGRA discovered the supernova remnant Cassiopeia A (132), the radio galaxy M87 (133), and an unidentified source near Cygnus. (134) Beyond these important results, the HEGRA served as a prototype to prove the capabilities of the stereoscopic technique and paved the way for the technique used in the current generation of imaging telescopes.

In 2002, the operation of the Cherenkov-telescope system at HEGRA was ended in favor of the execution of two major projects: the H.E.S.S.* (135–137), fully operational since 2003, and the MAGIC† (138–139), operating since 2004. Likewise, the Whipple collaboration started the VERITAS‡ (140–141) project, whose operation started in 2007. These three stereoscopic systems, comprising two (MAGIC), four (VERITAS), and five (H.E.S.S.) imaging telescopes, as shown in Figures 14, 15, and 16, are the main gamma-ray observatories in the GeV to TeV range operating today. Apart from those, a totally different technique based on the observation of air showers through high-altitude arrays of particle detectors has been successfully implemented at the HAWC§ observatory. (142) As opposed to the imaging telescopes, which require clear, dark nights to operate, a ground-based particle array allows for a duty cycle of about 100% with a wide angular acceptance. (143) Observing the sky since 2015, the HAWC has already published a large catalog with new sources (144) and its operation is in synergy with the imaging systems, from which combined analyses can be derived. (145–146)

With the operation of the current generation of observatories, about one new source was detected every month (129) and the TeVCat (151) lists 229 TeV gamma-ray sources in its catalog¶ as of Jan. 2021. An illustrative representation of the development of gamma-ray astronomy in the past 30 years is shown as a *kifune plot* (152) in Figure 17. This plot shows the evolution on the number of gamma-ray sources detected by ground-based instruments (red) compared to the number of gamma-ray sources detected by experiments in satellites (blue), and to the number of sources detected in X-ray (green). The number of sources seen by ground-based detectors has jumped from 1 to 229 in only 30 years. A sky map with known TeV gamma-ray sources is shown in Figure 18, in which the galactic plane is seen to be densely populated. Beyond discovering numerous sources,

* High Energy Stereoscopic System
† Major Atmospheric Gamma Imaging Cherenkov telescopes
‡ Very Energetic Radiation Imaging Telescope Array System
§ High-Altitute Water Cherenkov
¶ Accounting for the "default" and "newly announced" catalogs of TeVCat.

Figure 14 – The MAGIC gamma-ray observatory.

Source: THE MAGIC TELESCOPES (147)

Figure 15 – The VERITAS gamma-ray observatory.

Source: VERITAS: Very Energetic Radiation Imaging Telescope Array System (148)

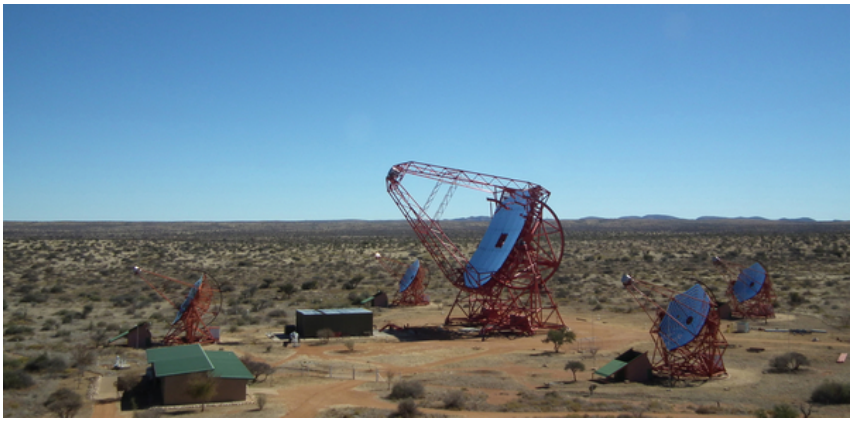

Figure 16 – The H.E.S.S. gamma-ray observatory.

Source: THE HIGH ENERGY STEREOSCOPIC SYSTEM (149)

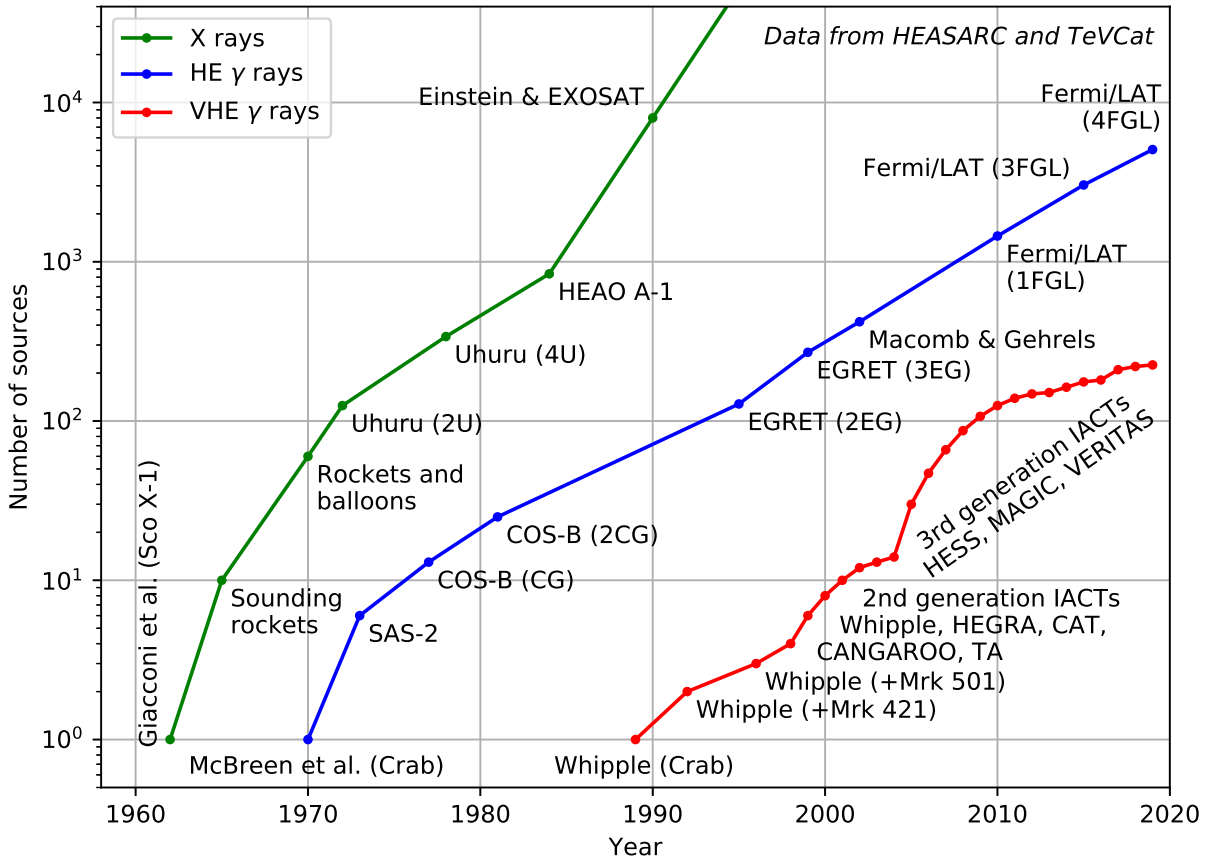

Figure 17 – Evolution of the number of known sources in different wavelength bands.

Source: FEGAN (150)

measurements from the current generation of observatories allowed for precise studies of the morphology of extended gamma-ray emitters and precise characterization of their energy spectrum.

As a now well-founded science (153–154), the very-high-energy gamma-ray astronomy still pursues its initial aim of finding cosmic-ray accelerators and signals from their interactions with background photon fields during propagation. (155–156) Nevertheless, this science has grown to include a much more broad range of topics such as tests of fundamental physics (157), the search for dark-matter signals (158), indirect measurements of extragalactic photon backgrounds (159), and the understanding of high-energy astrophysical phenomena. (160) Moreover, the evolution of this science entailed the development of complex apparatus which allow for other studies such as the measurement of cosmic-ray fluxes and its mass composition. (161–162) In view of these objectives, the deployment of a new generation of observatories with even higher sensitivity is in the short-term time horizon. (163–164) A world-wide collaboration has been formed to design and construct the Cherenkov Telescope Array (CTA) which, by inheriting the expertise from previous

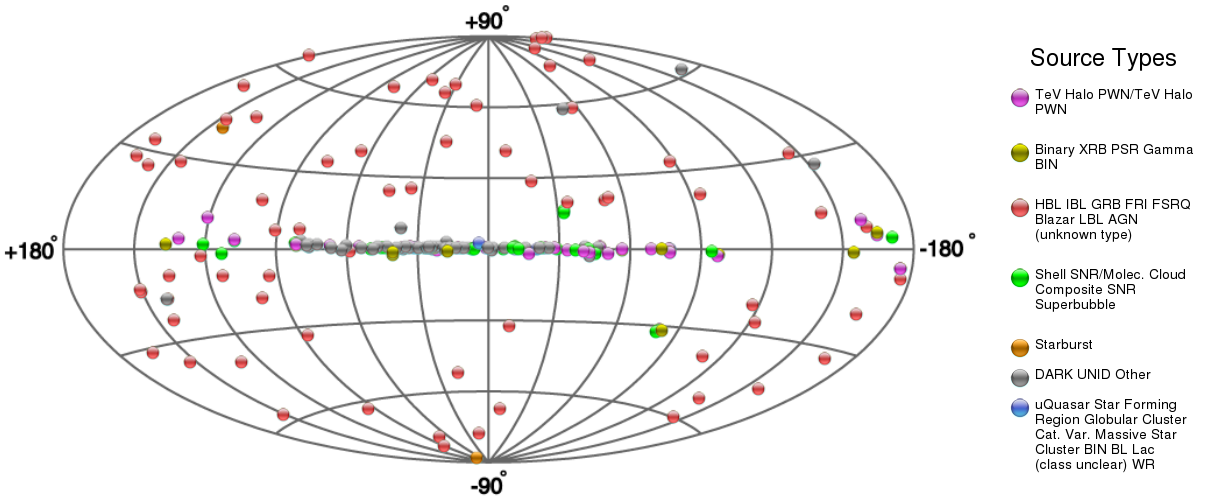

Figure 18 – Sky map with gamma-ray sources detected by ground-based instruments.

Source: WAKELY; HORAN (151)

experiments, will lead gamma-ray observations in the range from 30 GeV up to 300 TeV by combining different sizes of imaging telescopes. The CTA project and its status are described in more details in Section 3.2.

3.1.2 The imaging technique

The imaging technique is a central aspect of ground-based gamma-ray astronomy as historically, and presently, it is at the foundation of ground-based gamma-ray astronomy. The method, for which a detailed description can be found in references (165–166), is outlined in this section.

An imaging telescope for ground-based gamma-ray astronomy has two main components: a large reflector and a fast-timing camera (165), as illustrated in Figure 19. The reflector is typically a multi-faceted mirror of area A_{m} mounted in a dish in either a parabolic (139) or Davies-Cotton (135, 140) optical design, although prototypes with two reflectors are currently being tested. (168) On the mirror focus lies the telescope camera comprising either a hexagonal or square matrix of juxtaposed pixels. Each pixel has a light-collecting cone that drives photons coming from a small angular region Ω_{pix} in the sky to a light-sensible element in which photons are converted into an electronic signal. The whole system efficiency for photon conversion ϵ results from the product of the mirror reflectivity and the quantum efficiency of the camera. When triggered by a shower, the signal on the camera is integrated over a time window τ of some nanoseconds. In such an instrument, the signal-to-noise ratio S is roughly

$$S \propto \sqrt{\frac{\epsilon A_{\mathrm{m}}}{\tau \Omega_{\mathrm{pix}}}} \,, \tag{3.1}$$

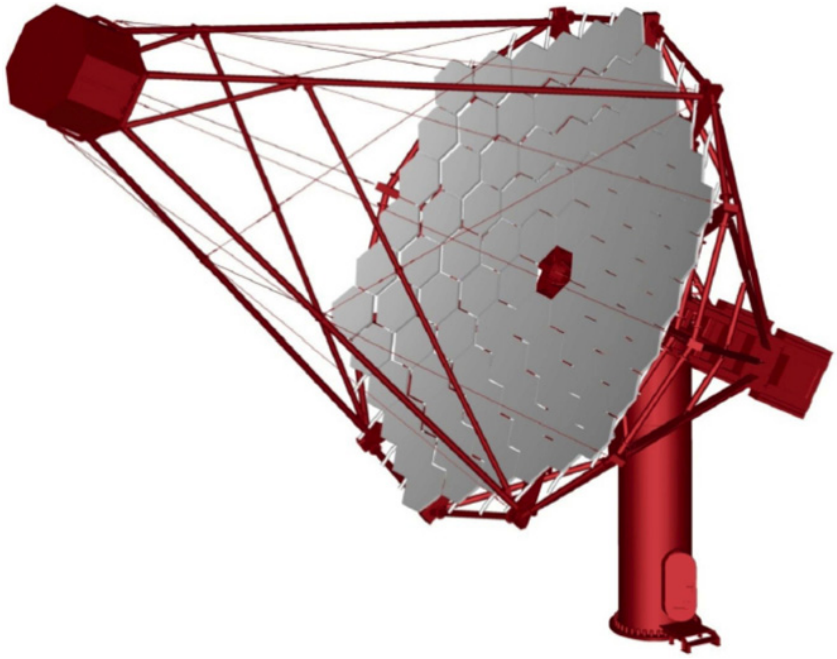

Figure 19 – Depiction of a generic IACT, illustrating its mirror (in gray) and its camera.

Source: ACHARYA *et al.* (167)

which is inversely proportional to the lower energy detection threshold. (165) Therefore, imaging telescopes for gamma-ray astronomy rely on large reflective surfaces and rather small pixel sizes ($\lesssim 0.1°$) to resolve shower images. Typically combining hundreds to thousands of pixels, an imaging telescope has a field of view of about some degrees ($\approx 5°$). The integration time τ has to be minimized, but considering it has to be enough to collect all light from a shower. (140, 169)

A sketch of the process of imaging a shower is shown in Figure 20. The figure shows that initially a shower grows in size as it penetrates into the atmosphere, then reaches a maximum and decreases before finally being absorbed. The lateral spread of particles also increases as a shower develops. As the charged particles continuously radiate Cherenkov light, photons emitted at different altitudes and distances to the shower axis reach the camera at unique positions to compose an image. The topology of the image is, therefore, a consequence of the distribution of charged particles, which varies from shower to shower and depends on the properties of the primary particle. Notably, images from gamma-ray showers are typically distinct from those resulting from hadronic showers, as illustrated in Figure 21. Indeed, gamma-ray showers produce images of approximately elliptical shapes, while hadronic showers typically result in erratic patterns in the camera. Apart from the properties of the primary particle (type, incoming direction, and energy), the image of a shower varies according to the impact parameter (distance between the telescope and the shower core) and the observation angle (between the shower axis and the pointing direction of the telescope).

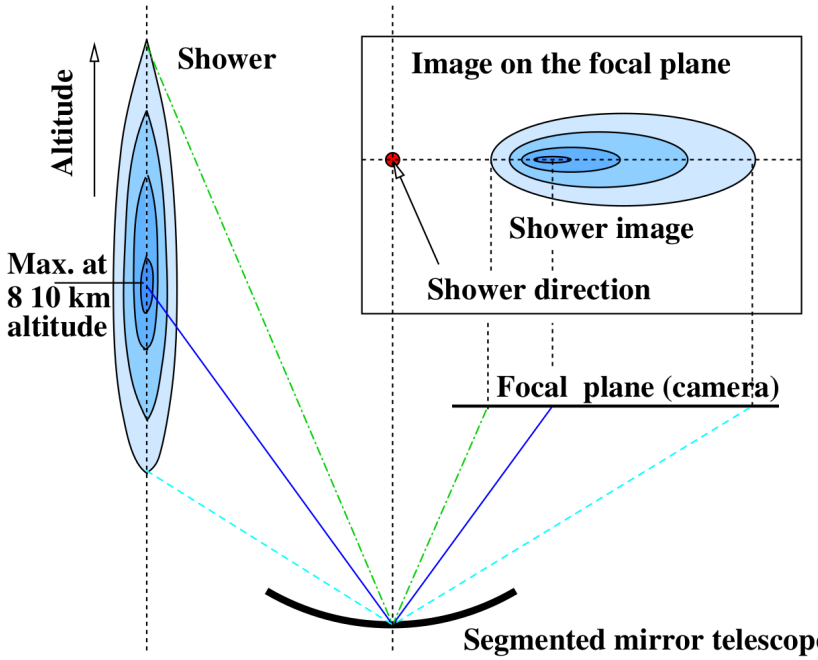

Figure 20 – Illustration of the imaging technique for ground-based gamma-ray astronomy. The spacial distribution of Cherenkov-light emission is shown in blue, in the left part of the figure. The image reflected by the mirror (in black) is shwon in the top-right corner.

Source: VÖLK; BERNLÖHR (166)

Stereoscopic systems rely on the observation of showers simultaneously by different telescopes, thus allowing for the reconstruction of the primary particle from a combination of multiple images. For instance, the intersection of the major axes from elliptical images of gamma-ray showers at different telescopes reconstruct the incoming direction of the primary particle, as illustrated in Figure 22. The image analysis is used to classify events as hadronic or gamma-ray showers, allowing to decimate the number of background events. For spectral analysis of sources, shower images are also used to reconstruct the primary gamma-ray energies. Generically, images are processed in two steps: first, an image-cleaning procedure is performed by selecting a set of adjacent pixels whose signal is dominated by Cherenkov light rather than the night-sky background light; then, the cleaned images are subject to some reconstruction algorithm used to determine the primary particle type, direction, and energy. Several algorithms are available for the image analysis process, some of which are described below. These methods, although independent, can be combined in multi-variate analyses which allow for an improved characterization of the primary particle. (170)

Hillas parameters

This approach, introduced by Hillas (115) and discussed in references (113, 165, 172), build on the fact that gamma-ray showers produce images on the camera that are

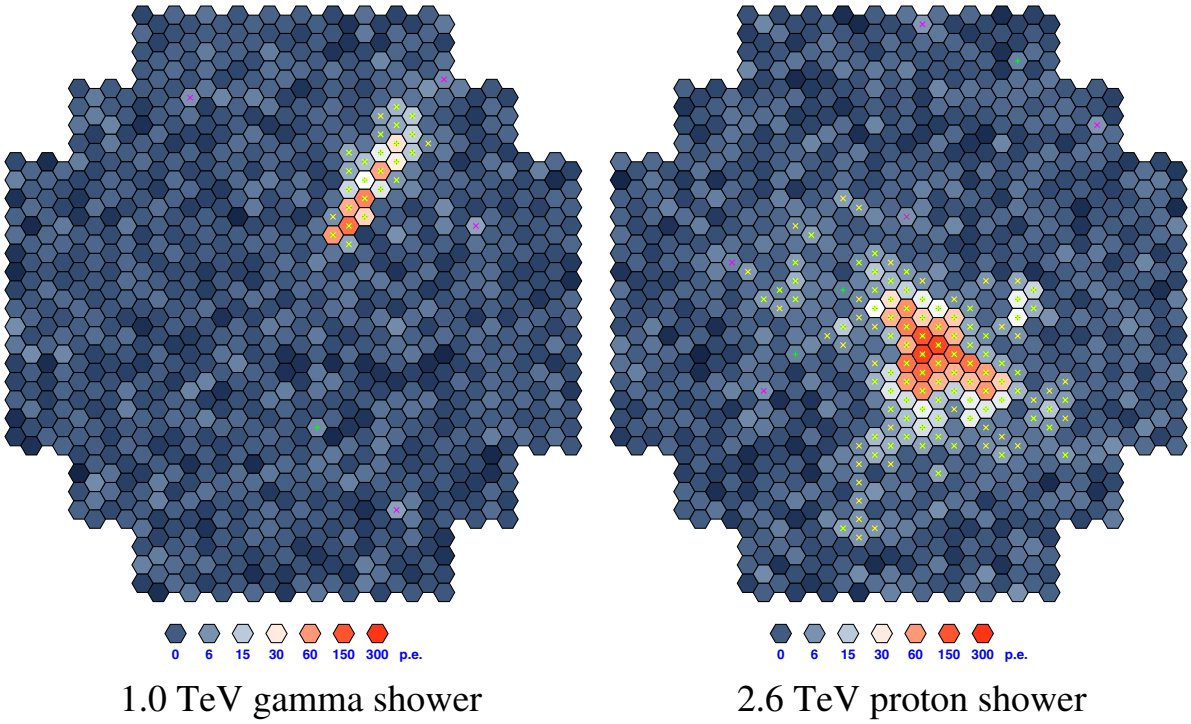

Figure 21 – Illustration of the differences between images of gamma-ray and hadronic showers. Left: 1.0 TeV gamma-ray shower. Right: 2.6 TeV proton shower.

Source: VÖLK; BERNLÖHR (166)

close to an ellipse, in contrast to images from hadronic showers. Therefore, an image can be parametrized in terms of its length, width, orientation, and position on the camera. This parametrization is illustrated in Figure 23. In stereoscopic analysis, different images are combined according to the number of triggered telescopes to get the mean-scaled parameters. (171)

Typically, analyses based on Hillas parameters perform the geometrical reconstruction of a shower according to the intersection of the major axes from each image, as illustrated in Figure 22. A first step for background reduction comprises the comparison of the mean-scaled image parameters with distributions known a priori, either entirely derived from Monte Carlo simulations or using off-source observations from which the distribution of parameters from the background can be obtained. (171) Statistical methods, typically based on machine learning algorithms (173), are used to classify showers as gamma-ray-induced or hadronic-induced on a shower-by-shower basis. This selection results in an efficiency ϵ_γ for selecting gamma-ray showers and a fraction ϵ_p of surviving background events, for which a quality factor $Q = \epsilon_\gamma/\sqrt{\epsilon_p}$ of about $Q \sim 400$ is obtained. (165) However, electron-induced showers can not be distinguished from gamma-ray showers solely based on the Hillas parameters. (174) To further improve the selection efficiency, a reduc-

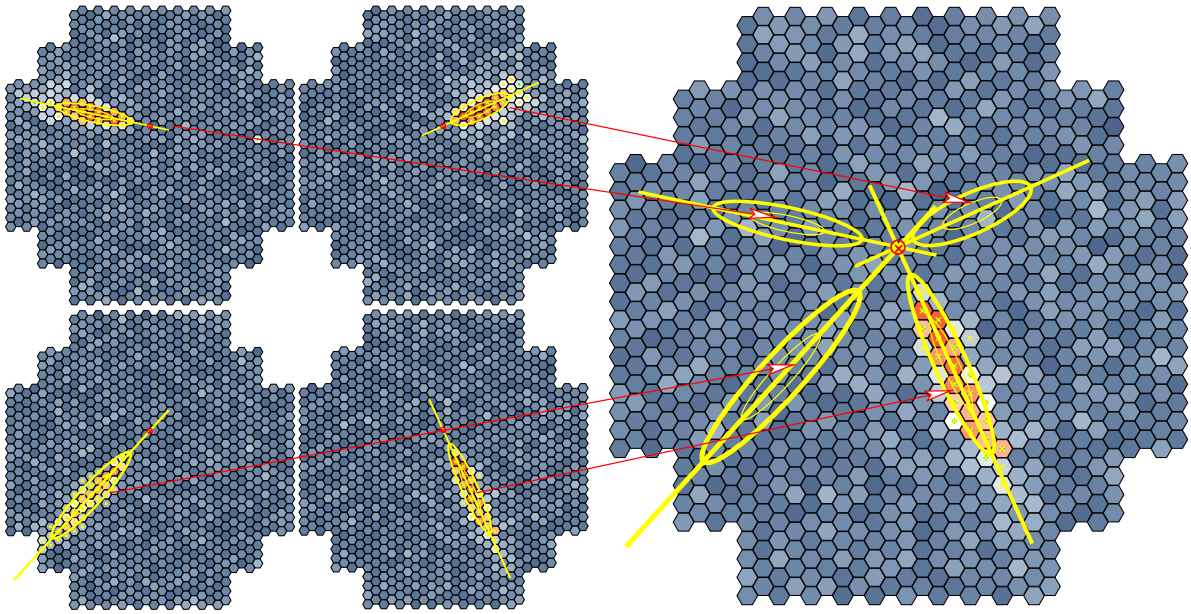

Figure 22 – Depiction of the stereoscopic method in the reconstruction of the shower arrival direction. Left: four telescopes detect independent images. Right: the arrival direction can be determined by the intersection of the major axes of individual images.

Source: VÖLK; BERNLÖHR (166)

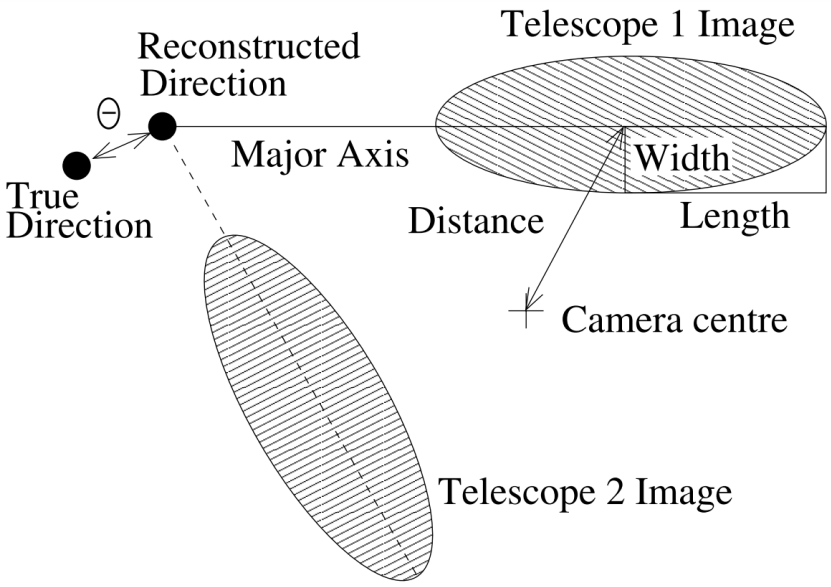

Figure 23 – Illustration of the paramerization of shower images according to shape, position, and orientation.

Source: AHARONIAN *et al.* (171)

tion of the background is achieved based on the distributions of the offset angle between the reconstructed shower direction and the source location (angle Θ in Figure 23). (171)

As for the primary energy reconstruction, this method requires further analysis of the image size on the different telescopes in correlation with the impact parameter and the arrival direction of the shower. Simulations of air showers based on Monte Carlo methods are required for this purpose. (87)

Template-based analysis

The method based on shower-image templates was developed by the CAT[‖] collaboration as an alternative to the Hillas-parameters-based reconstruction. (175) It relies on the modeling of the average Cherenkov-light emission profiles from air showers and the computation of the expected images as a function of the primary gamma-ray energy E_γ, the impact parameter D, and the two angles defining the shower direction (θ, ϕ). A likelihood function is built to compare actual measured images to those expected from the model. The maximization of this likelihood function allows to reconstruct the shower parameters E_γ, D, θ, and ϕ. Moreover, the classification of gamma-ray events and rejection of the background can be performed according to the maximized value of the likelihood function. The original method has been updated in reference (176) and, more recently, a method entirely based on the simulation of the average images (rather than parametrizing the shower behavior) was developed. (177)

3D reconstruction

A method similar to the template-based analysis was proposed in references. (178–179) This model assumes that a gamma-ray shower can be modelled by a three-dimensional gaussian photosphere, whose transverse width is characterized by a parameter σ_T and the longitudinal development by σ_L, termed the 3D-width and 3D-length, respectively. Additional parameters of this model are the shower barycentre B, corresponding to the depth of shower maximum, the position of the impact point given by the coordinates x_0 and y_0, the polar angles of the shower direction θ_0 and ϕ_0, and the total number N_c of Cherenkov photons emitted by the shower.

To reconstruct the shower parameters, a function $I(\theta)$ describing the angular distribution of Cherenkov photons emitted by the shower is proposed. In the original work (178), the following simple parametrization is used

$$I(\theta) = \begin{cases} K & , \text{if } \theta \leq \eta \,, \\ K(\eta/\theta)\exp\left(-\frac{\theta-\eta}{4\eta}\right) & , \text{if } \theta > \eta \,, \end{cases} \tag{3.2}$$

where $K = 1/(9\pi\eta^2)$ and $\eta = 15\,\mathrm{mrad}\,\sqrt{\cos\xi}$ depends on the zenith angle ξ of the shower direction. An integral over the line of sight of each pixel in each telescope allows to com-

[‖] Cherenkov Array at Themis

pute the expected signal in terms of the model parameters. To get the best parameters describing a measured shower, a likelihood function is built and maximized by varying the free parameters from which the shower geometry and the primary energy are reconstructed. The fitted parameters allow for a gamma-hadron discrimination analogous to the Hillas-parameters-based analysis.

In view of the simulations of the function $I(\theta)$ presented in Chapter 6, Equation 3.2 is seen to be oversimplified. Indeed, the alternative description of $I(\theta)$ presented in Chapter 6 largely improves the description of the angular distribution of Cherenkov light in air showers and can be employed in such class of reconstruction algorithms.

Machine learning algorithms

The idea to use artificial neural networks for pattern recognition in Cherenkov-imaging telescopes was already present in the early 1990s, soon after the development of the imaging technique. (116) However, only recently enough computational power became available for the application of such complex algorithms. Still premature, these methods (180–182) can perform a pixel-wise analysis of the images, after being trained by a controlled data set, and promise an improvement in the extraction of relevant features from the detected showers.

3.1.3 Known gamma-ray sources

Many types of very-high-energy gamma-ray sources have already been detected by the current generation of Cherenkov-telescope arrays, including galactic and extragalactic ones. A well-organized catalog of these sources is maintained by S. Wakely and D. Horan in the TeVCat. (151) A summary of the 229 sources listed by the TeVCat is shown in Table 1. Below, the most abundant types of known sources are briefly discussed.

Supernova remnants

Once the elements that release energy through nuclear-fusion processes within the core of a massive star become unavailable, the star collapses under its own gravitational pressure and gives rise to a supernova explosion. (129) The explosion ejects material from the outer shells of the star, forming an expanding supernova remnant (SNR); the collapsed star itself becomes a dense object such as a neutron star or possibly a black hole. As the expanding ejecta interacts with the interstellar medium, diffusive acceleration processes (183–184) take place and result in a population of particles with relativistic energies. These particles, in their turn, interact with the ambient magnetic fields, the ambient photon fields, and matter to produce non-thermal radiation, including gamma rays. (153)

The importance of SNRs to cosmic-ray physics is central as the standard model of galactic cosmic rays predicts the bulk of particles at least up to $\sim 10^{15}$ eV are accelerated

Table 1 – Summary of TeV gamma ray sources listed by the TeVCat (151) as of Jan. 2021.

Location	Classification			Number
Galactic	Supernova remnants	Pulsars		4
		Pulsar-wind nebulae		34
		Shell-like		14
		Molecular clouds		10
		Composite		2
	Binary systems			11
	TeV halo			3
	Massive star clusters			3
	Super bubble			2
	Globular clusters			1
Extragalactic	Active galatic nuclei	Blazar	Bl Lac	63
			FR-I	4
			FSRQ	8
			Unknown type	3
		Unknown type		2
	Gamma-ray bursts			4
	Starburst galaxy			2
Unidentified				59
Total				229

Source: By the author

in this type of object. An important question, therefore, is whether the signal of TeV gamma-rays from SNRs can be correlated to hadronic processes in its ambient. So far, no definitive solution has been given. (153)

Typically, SNRs are observed as extended objects, and their morphology in gamma-rays can be reconstructed from observations in ground-based detectors. A sub-classification of SNRs is commonly given according to their morphology (shell-like structure) and the ambient in which they expand (possibly within dense molecular clouds).

Pulsars and pulsar-wind nebulae

Pulsars are rapidly rotating and highly magnetized neutron stars created after a supernova explosion. Being so, they can accelerate electrons to very-high energies which, submerged in the intense magnetic field, emit non-thermal radiation at all wavelengths carrying the periodic signature from the rotating star. Sometimes, pulsars are accompanied by an extended wind of energetic electrons carrying most of its rotational energy, in which very-high-energy radiation is also emitted. Such extended objects are known

as the pulsar-wind nebulae (PWNe). (185) Only four pulsars have been observed by ground-based observatories to date: the Crab pulsar (186–187), the Vela pulsar (188), the Geminga pulsar (189), and PSR B1706-44. (190) PWNe, on the other hand, are the most abundant class of known TeV gamma-ray emitters in the Galaxy, with 34 being listed in the TeVCat, including the Crab, the Vela, and the Geminga nebulae. A large fraction of PWNe became known after the 10-year sky survey performed by H.E.S.S. (191), in which 14 sources were firmly identified as PWNe. (192)

Binary systems

A binary system is typically composed of a massive star rotating around a denser object, such as a pulsar or a black hole. The accretion of matter in one companion of such systems is a source of high-energy particles that can radiate gamma rays by interacting with the ambient in which they are accelerated. (129) Indeed, the radiation of gamma-rays is expected to occur either in microquasars, in which a jet is formed due to the accretion of matter in a black hole, or in a scenario of shock between a pulsar wind and a stellar wind. (153) As an example, the η-Carinae system has been recently observed by H.E.S.S.. (193) Another interesting example is the binary system SR J2032+4127, whose orbit has a period of $\sim$ 50 years and has been detected in the TeV range during its periastron in 2017 by MAGIC and VERITAS. (194) Apart from these two, other nine binary systems have been observed in the very-high-energy range.

Galactic centre

The whole galactic plane contains many sources of TeV gamma rays. (191) In particular, a diffuse gamma-ray emission has been observed within a region of 200 pc in the Galactic Centre (GC) and seen to be compatible with the signal expected from propagation of cosmic-ray protons and nuclei. (195) More recently, the H.E.S.S. collaboration has published a very precise measurement of the TeV gamma-ray flux from the GC in which evidence for an accelerator of PeV cosmic rays within the central 10 pc of the Galaxy has been found. (196) This is an interesting discovery as a suspected supermassive black hole lies at the dynamical center of the Galaxy and can be responsible for the acceleration of cosmic rays up to PeV energies. (153, 196–197)

Extragalactic sources: active galactic nuclei

Active Galactic Nuclei (AGN) is the most common type of extragalactic TeV gamma-ray sources detected so far. AGNs are characterized by jets of highly collimated relativistic outflows powered by the accretion of matter in a supermassive black hole. (129) Different types of AGN exist and are classified according to the spectra of radio emission, optical emission, and the orientation of the jet. (185) Among all classes, blazars (AGNs with a jet toward the observer) are the most common type seen in very-high-energy gamma rays. (151) Examples of blazars detected in very-high-energy gamma rays include

the Markarian 421 (121) and the Markarian 501. (122) The radiation from blazars is characterized by strong variability and flaring activity, which has been observed in very-high-energy gamma radiation. (198–199)

Starburst galaxies

Two galaxies without activity in the center have been observed in the very-high-energy gamma-ray band. (200–201) This type of galaxy is believed to have a very-high rate of star formation, which results in a high rate of supernova explosions. Therefore, starburst galaxies probably are efficient cosmic-ray accelerators. Interaction of those with the interstellar gas densities may lead to pionic emission of gamma-rays. (153)

Transient emission: the gamma-ray bursts

Gamma-ray bursts (GRBs) are unpredictable extragalactic events in which a flare of gamma-rays is emitted for a short period. Although GRBs were copiously detected in space-based detectors (202) in the high-energy range, the observation of such transient phenomena in ground-based detectors is difficult because of their limited field of view (typically $\lesssim 5^{\circ}$) and the time required (of few seconds) to point the telescopes in follow-up observations. The origin of this phenomenon is not known and all current observatories have programs to detect this type of source. (203–206) A total four GRBs have been detected so far by ground-based observatories.

3.2 The Cherenkov Telescope Array

The Cherenkov Telescope Array (CTA) is a world-wide effort to design, construct, and operate the next generation of IACT observatories. The concept (167) permeating the CTA project aims at a) providing an instrument that technically outperforms current observatories and b) realizing an open observatory for very-high-energy gamma-ray astronomy. CTA, from its design to construction and operation, builds upon the expertise gained by different collaborations in current and previous IACT observatories, and its complexity is such that a wide-world collaboration with over 1500 scientists are working towards its implementation. Below, some conceptual aspects of the CTA are presented. Then, an overview of its scientific program is discussed.

3.2.1 Description of the experiment

As an open observatory, CTA will gather data from observation time dedicated to its key science projects (206), but will also receive proposals for observations from the external community, which will be selected competitively. The open-observatory concept foresees that all data from the CTA will be made publicly available. This concept will allow a larger community to benefit from the CTA with the potential of resulting in a large scientific output. (207)

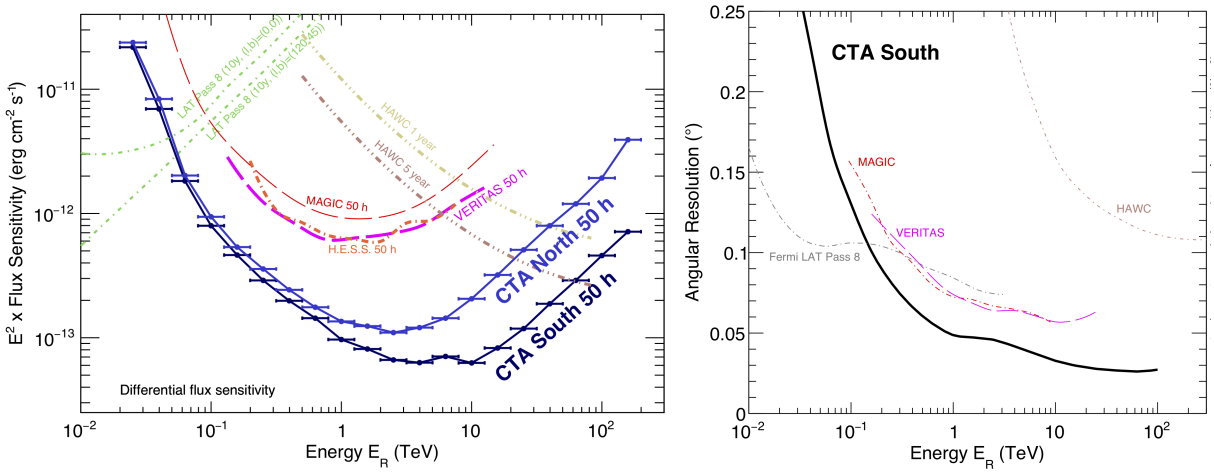

Figure 24 – Performance of the CTA in comparison to current observatories. Differential flux sensitivity (left) and angular resolution (right) are shown as a function of the reconstructed gamma-ray energy.

Source: CHERENKOV TELESCOPE ARRAY OBSERVATORY (208)

From the technical side, the performance goals of the CTA require a major improvement when compared to previous observatories. Mainly, it is expected to broaden the energy range covered by current IACT systems, to improve the differential sensitivity, and to improve the angular resolution. To achieve these goals, two observatories will be constructed: CTA-South, in Paranal, Chile, and CTA-North, in La Palma, Canary Islands. The expected overall performance of the CTA is summarized in Figure 24, in which the differential sensitivity and angular resolution are plotted compared to the current ground-based gamma-ray observatories. The broad energy range covered by CTA will cause a desired overlap with other types of instruments: satellite-based, on the low-energy range, and particle-detector ground arrays at TeV energies.

To cover the energy range from 30 GeV to 300 TeV, three types of telescopes will be deployed in the CTA. Low-energy showers ($E \leq 100$ GeV) will be detected by Large-Sized Telescopes (LST), comprising large photon-collection areas to detect the faint Cherenkov-light from the least energetic showers efficiently. In this energy range, only a few telescopes are required to reach the expected sensitivity of the CTA. As the energy increases, telescope sizes can be made smaller, as showers become brighter, while the effective area covered by the telescopes must increase to counterbalance the effect of a decreasing flux. Indeed, in the core energy range (0.1 TeV$< E \leq 10$ TeV), arrays with some Middle-Sized Telescopes (MST), similar to those of current systems, will operate. At the highest energies, many Small-Sized Telescopes (SST) will be deployed.

The two arrays, CTA-South and CTA-North, will differ in layout. CTA-South will be the largest array of the two. It will comprise all three of the aforementioned telescope

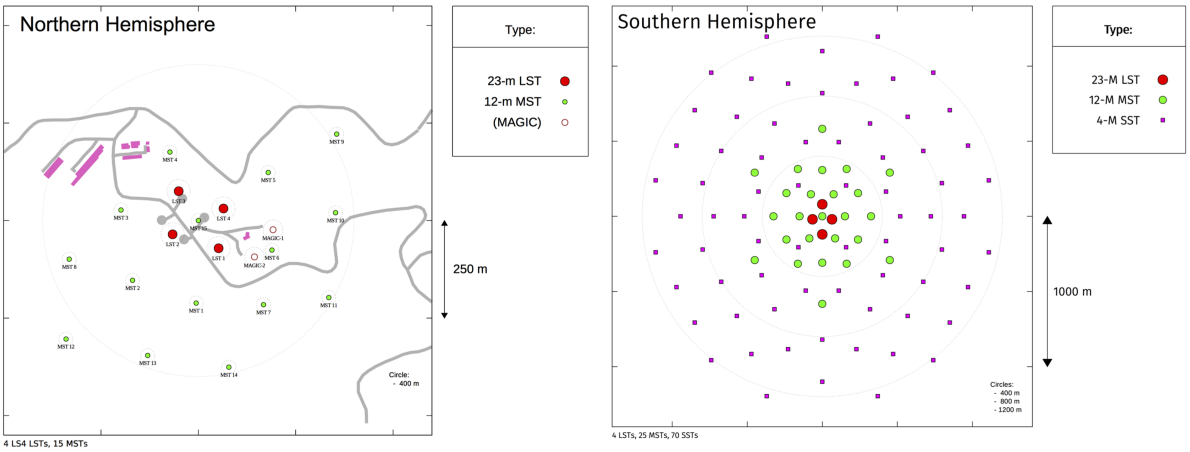

Figure 25 – Baseline design for the CTA north (left) and south (right) arrays.

Source: CHERENKOV TELESCOPE ARRAY OBSERVATORY (208)

types: four LSTs, 25 MSTs, and 70 SSTs, in a total of 99 telescopes. CTA-North, on the other hand, will have four LSTs and 15 MSTs, but no SSTs. The baseline layouts of the two arrays are illustrated in Figure 25. By combining observations from the two arrays, the CTA will have full-sky coverage and will be able to perform the first extragalactic survey and improve the understanding of the galactic centre through a precise galactic-plane survey. (209)

Technology for the three types of telescope is already being prototyped by distinct groups. The prototypes are illustrated in Figure 26. Construction of the first LST prototype was completed in 2018 on-site, in La Palma. This telescope has a large parabolic mirror of 23 m diameter, a camera with 1855 pixels, and a field of view of 4.5°. (210) Two prototypes exist for the MSTs: one with a single Davies-Cotton-design (DC) mirror, and the alternative Schwarzschild-Couder Telescope (SCT). The DC prototype has a 11.5 m diameter mirror, a camera with $\sim$ 1800 pixels and a wide field of view of 7.5°. The SCT prototype, on the other hand, combines two mirrors in its optical system, a very-pixelated camera with 11328 silicon-photomultipler pixels, and a field of view of 7.6°. (168, 211) Finally, regarding the SSTs, three prototypes were tested (212–214) and a final design has been proposed taking into account the experience from all projects. This final design will comprise a dual-mirror telescope with a primary reflector of 4.3 m diameter, a camera with 2368 pixels, and a total field of view of 10.5°.

With its construction currently under way, the CTA works as a very active collaboration producing technologies, studying scientific prospects, and developing analysis techniques. Moreover, the CTA has an outreach program to reach people outside the scientific community. (208) Regarding the analysis techniques for the CTA, the Analysis and Simu-

Figure 26 – Prototypes of CTA telescopes. Top: the large-size telescope. Middle left: the Davies-Cotton designed mid-sized telescope. Middle right: the dual mirror Schwarzschild-Couder mid-sized telescope. Bottom: the dual mirror Schwarzschild-Couder small sized telescope.

Source: CHERENKOV TELESCOPE ARRAY OBSERVATORY (208)

lation Working Group (ASWG) is actively developing a framework, the CTAPIPE (215), to incorporate all parts of the low-level data processing, from the processing of raw shower images to the shower reconstruction. Working together with the ASWG, the present author has contributed to a study on the influence of hadronic interaction models on the estimated sensitivity of the CTA, summarized in Chapter 8.

3.2.2 Scientific prospects

Owing to its outstanding capabilities, the list of science prospects for the CTA is very extensive. A document (206) has been elaborated by the CTA collaboration describing the key science projects that will take a large part of the observation time. According to this document, the questions that will be addressed by the CTA can be classified into three broad themes:

- **Search for the origin and the role of relativistic cosmic particles**. This theme includes the search for astrophysical objects that can accelerate cosmic rays and to understand through which process they are accelerated. To understand the importance of cosmic rays to star and galaxy formation also fits into this category. These questions will be addressed by the CTA, for instance, through its precise survey on the galactic centre, the Large Magelanic Cloud survey, and also through the extragalactic survey. These three surveys have the potential to unveil new sources of very-high-energy gamma-rays and the measurement of their spectra can be used to better understand the associated particle acceleration mechanisms. Measurements of AGNs, star-forming systems, and galaxy clusters will also contribute in this direction.

- **Probes of extreme cosmic environments**. Some extreme astrophysical objects lack an understanding from a theoretical perspective. These sources include, for instance, black holes, neutron stars, and relativistic jets. The physical processes at work in such environments are poorly known. As an example, CTA will have the potential to discover and measure the flux of gamma rays from AGN jets and transients such as gamma-ray bursts. Observations of both will serve as vital information on extreme environments.

- **Exploration of possible physics scenarios beyond the standard models.** The long-distance propagation of gamma rays from cosmic sources to Earth makes these particles ideal probes of the limits of the standard model of particle physics. In particular, the detailed measurement of fluxes from different astrophysical objects can be used to investigate, for instance, effects of Lorentz invariance violation and the coupling of gamma-rays to axion-like particles. Beyond that, some models for dark matter predict it could annihilate to produce observable gamma rays. If this

is the case, the CTA will have the potential to search for signatures of dark matter with a sensitivity much larger than any other instrument of its type.

3.3 Conclusion

Some aspects of very-high-energy gamma-ray astronomy have been presented in this chapter. It has been seen that this science has been a flourishing research field since the first detection of a gamma-ray source made by ground detectors in 1989. Since then, this science has developed just as many as the instrumental techniques did. Maturity has been reached with the current generation of IACTs, from which it has been gathered that multiple, complex analysis techniques are in order to explore the potential of these telescopes. Indeed, facing the advent of the CTA, with its complex structure, studies on the detection and reconstruction of extensive air showers using Cherenkov light are timely.

Results from the current thesis are motivated by the detection of Cherenkov light from air showers in IACT systems. In particular, the use of parametrized angular distributions of Cherenkov light to reconstruct air showers motivates the study of Chapter 6. The capabilities of IACTs to measure the mass composition of cosmic rays are visited in Chapter 7. Uncertainties on IACT measurements related to the simulation of extensive air showers ate the principal topic of Chapter 8.

4 EXTENSIVE AIR SHOWERS

Cosmic rays of undetermined origin are accelerated throughout the Universe and propagate across astronomical distances before they can reach the proximity of Earth. Whenever one of these particles penetrates into the atmosphere, it finds in air an opaque propagation medium mostly composed of nitrogen, oxygen, and argon. These gas molecules act as targets for the incoming cosmic particle. Indeed, a first microscopical interaction of quantum-mechanical nature is responsible to convert the primary cosmic ray into a bunch of secondary particles in the upper atmosphere. The secondaries delve deeper in air, most times leaving behind some sort of radiation, and interact again or decay, producing more secondaries. This process takes place copiously, causing the number and diversity of particles to increase in a cascade-like process whilst the energy per particle continuously decreases. At some point, the average energy of the cascade particles is not enough to maintain the particle production processes in a rate larger than absorption, and the cascade fades. Some products of this cascade, finally, are able to reach the ground both as radiation and as particles from decays and high-energy interactions. This is a simplified outline of the phenomenon known as extensive air showers, whose physical interest stems mainly from the possibility of observing primary cosmic rays at energies not reachable by direct detectors.

In this chapter, concepts of air-shower physics fundamental for this thesis are revisited and discussed in view of the results presented in the succeeding chapters. In particular, Section 4.1 introduces some characteristics from extensive air showers and their basic observables. Section 4.2 focuses on the computational approaches available to simulate extensive air showers, giving particular emphasis to the methods employed in the next chapters. In Section 4.3, an overview of the Cherenkov-light phenomenon and its generation in air showers is given. Finally, Section 4.4 draws some concluding remarks.

4.1 Heuristic models and the basic observables

To some extent, the properties of an extensive air shower are determined by the properties of the particle whose interaction with air initially triggered the cascade. Distinction is made between pure electromagnetic cascades – those induced by a photon or by an electron* – and the hadronic cascades – those induced by a single nucleon, nuclei, or possibly any other type of hadron. In either case, the observable quantities of an extensive air shower are expected to be related to the properties of the primary particle, such as its type, its energy E_0, and, in case of nuclei, its mass A. A well-reasoned mapping between

* The term electron is used here to refer indistinguishably to the negative electron or its positive counterpart, the positron.

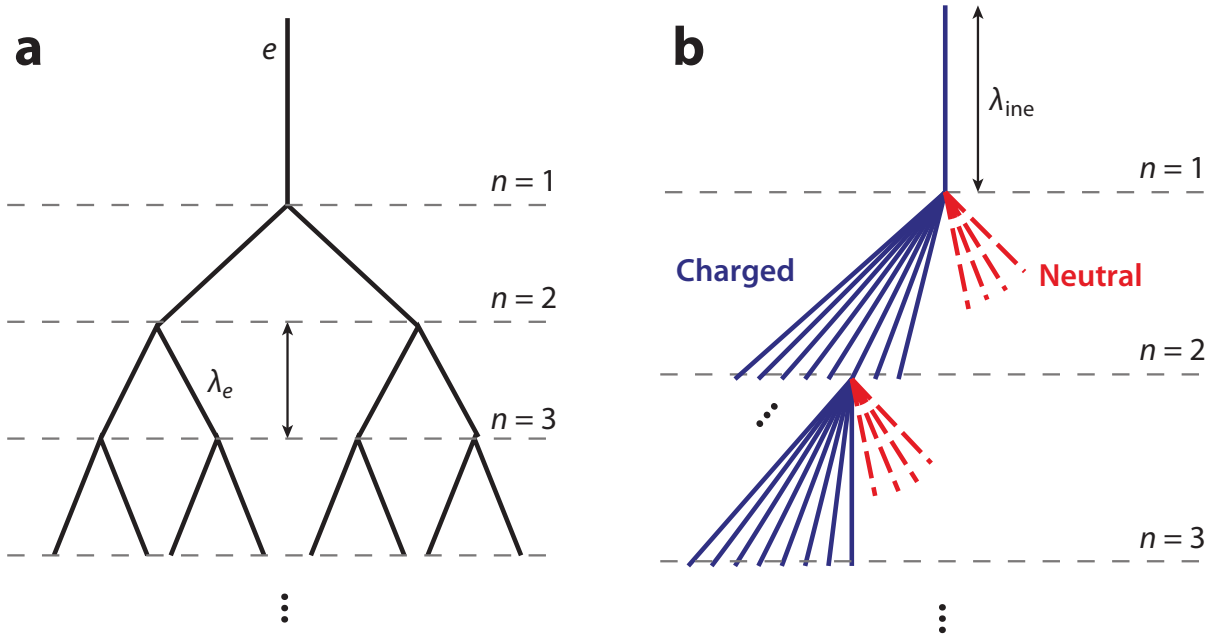

Figure 27 – Depiction of the Heitler (left) and of the Heitler-Matthews (right) models for electromagnetic and hadronic cascades.

Source: ENGEL; HECK; PIEROG (34)

the properties of the primary particle and the values of measured quantities allows for the indirect reconstruction of the properties of the primary particle. Unfortunately, to understand the exact functional form in which these relations are established is no simple task because of the complex nature of particle interactions that occur during shower development and to the large particle numbers involved. In this sense, it is instructive to make an appeal to simplified analytic models that allow for a heuristic interpretation of the relation between air-shower observables and the characteristics of the primary particle. Of course, a more realistic description of extensive air showers is possible through computer-based simulations, discussed in Section 4.2, although in this case some fundamental physical insights are left unclear. In this section, basic shower observables and their properties are discussed in terms of simple analytic models to build an essential level of understanding about the extensive air showers. Whenever appropriate, comparisons to results from simulations will be presented to support and set right the conclusions drawn from the simplified models.

4.1.1 Electromagnetic cascades

The physics of electromagnetic cascades, in a first approximation, can be addressed in terms of the so-called Heitler model, idealized by Carlson and Oppenheimer (216) and discussed by Heitler in reference. (217) This model builds on the fact that an electron

loses, on average, half its energy to bremsstrahlung radiation ($e^{\pm} \to e^{\pm}\gamma$) after traversing a thickness $\lambda_e = X_0 \ln 2$, where X_0 is the radiation length in the propagation medium. In a rather simplified approximation, the energy lost is assumed to be carried by a single photon, emitted exactly when the electron reaches λ_e. After this two-body splitting, the electron and the photon, each, carry half the initial energy. As for the propagation of a photon, on the other hand, most of its energy is dissipated through pair production ($\gamma \to e^+e^-$) and the mean free path is of the same order of λ_e. Therefore, every photon is assumed to propagate exactly a thickness λ_e before splitting into an electron-positron pair sharing the photon energy in equal amounts. In this branching scheme, depicted in Figure 27 left, the average number of particles (electrons + photons) increases as $N(X) \sim 2^{X/d} = \mathrm{e}^{X/X_0}$, where, for not too small X, two-thirds are electrons and one-third are hard photons. Reversely, the energy per particle is inversely proportional to the number of particles and therefore amounts to $E(X) \sim E_0 \cdot \mathrm{e}^{-X/X_0}$ for a cascade started by a primary of energy E_0. After reaching a depth $X^{\gamma}_{\max}$, the energy per particle drops below some value ξ_{crit}, after which most energy is lost through ionization and emission of soft photons, no longer producing pairs, and therefore the cascade ceases. By inverting the expression for $E(X)$, this depth is easily found to be

$$X^{\gamma}_{\max}(E_0) \approx X_0 \ln\left(\frac{E_0}{\xi_{\mathrm{crit}}}\right) , \tag{4.1}$$

at which the number of electrons is

$$N^{\gamma}_{e,\max}(E_0) \approx \frac{2}{3}\frac{E_0}{\xi_{\mathrm{crit}}} , \tag{4.2}$$

where the super-index γ is used to unambiguously indicate the results are for an electromagnetic cascade. The quantity ξ_{crit} is known as the critical energy; it depends on the propagation medium and in air amounts to $\xi_{\mathrm{crit}} \approx 87$ MeV. (218)

Albeit the Heitler model oversimplifies the description of electromagnetic cascades, it is rich in the sense that it introduces two important observables and relates them to the energy of the primary particle: a logarithmic dependence in the case of $X^{\gamma}_{\max}$ and a linear relation for $N^{\gamma}_{e,\max}$. The estimate of $X^{\gamma}_{\max}$ in Equation 4.1 remarkably agrees with the more realistic treatment in terms of diffusion equations (219–220) and also with predictions of the average $\langle X^{\gamma}_{\max}\rangle$ from full Monte Carlo simulations up to 1 EeV, as shown in the left plot of Figure 28. Above 1 EeV, the departure of $\langle X^{\gamma}_{\max}\rangle$ from the naïve prediction of the Heitler model results from a combination of the Landau-Pomeranchuk-Migdal effect (221), which causes showers to be more penetrating (222), and the probable early interaction of a primary photon with the geomagnetic field before its entrance into the atmosphere (223), causing $X^{\gamma}_{\max}$ to be significantly shallower. (224–225) Regarding the average number of electrons at the shower maximum $\langle N^{\gamma}_{e,\max}\rangle$, the Heitler model overestimates the real value by a factor of about 10, as shown in the right plot of Figure 28, but correctly approximates $\langle N^{\gamma}_{e,\max}\rangle \propto E_0$.

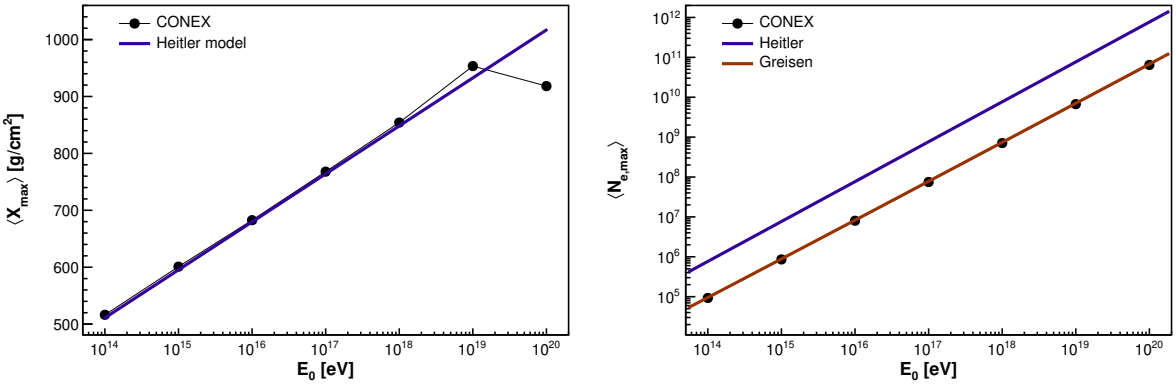

Figure 28 – Average depth of shower maximum (left) and average number of electrons at maximum (right) in electromagnetic cascades. Simulations with CONEX (black dots) are compared to predictions from analytical calculations.

Source: By the author

Both $X^{\gamma}_{\max}$ and $N^{\gamma}_{e,\max}$ relate to the *longitudinal profiles* of extensive air showers, to be understood as the number of particles versus the atmospheric depth $X(h) = \int_h^{\infty} \rho(l)\mathrm{d}l$ to which a shower has penetrated, where $\rho(h)$ is the atmospheric density and h is altitude. The *lateral distribution*, that is, the spread of shower particles perpendicular to the shower axis direction, is not accounted for in the Heitler model.

A more precise account for the description of longitudinal profiles of electromagnetic cascades has been computed soon after the discovery of extensive air showers in terms of diffusion equations. (219) In particular, the approximate solution given by Greisen to the average number of electrons with energies above ξ_{crit} in an electromagnetic cascade of primary energy E_0 reads

$$N_e(E_0, t) = \frac{0.31}{\sqrt{\ln(E_0/\xi_{\mathrm{crit}})}} \exp\left[\frac{X}{X_0}\left(1 - \frac{3}{2}\ln s\right)\right] , \tag{4.3}$$

where s is a parameter called shower age, discussed in Section 4.1.5, and $X^{\gamma}_{\max}$ is given by Equation 4.1. (220) The number of electrons at maximum can be obtained from the Greisen profile in Equation 4.3 by taking $X = X^{\gamma}_{\max}$ and $s = 1$. In accordance with Equation 4.1, this results in

$$N^{\gamma}_{e,\max}(E_0) = \frac{0.31}{\sqrt{\ln(E_0/\xi_{\mathrm{crit}})}} \left(\frac{E_0}{\xi_{\mathrm{crit}}}\right) , \tag{4.4}$$

whose comparison with simulations, shown in Figure 28 reveals excellent agreement. Average longitudinal profiles of gamma-ray induced showers of different primary energies are well described by the Greisen profile, as shown in Figure 29. The longitudinal profiles shown in this figure more accurately represent the development of an electromagnetic cascade than the Heitler model: the growth and then decay of the cascade are due to particle

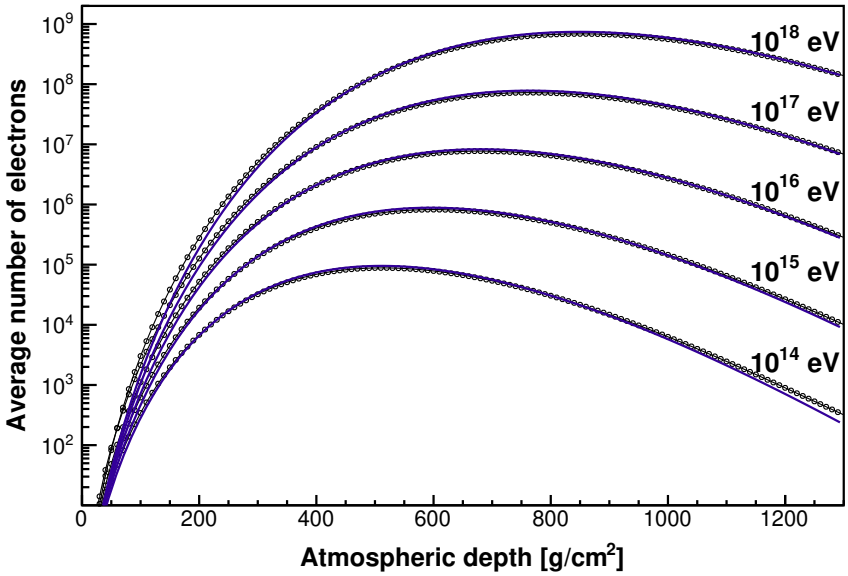

Figure 29 – Average longitudinal profiles of electromagnetic showers at different primary energies. Simulations with CONEX (black dots) are compared with the Greisen profile function (blue).

Source: By the author

multiplication and to a progressive softening of the energy spectrum of shower particles. Meanwhile, ionization, Cherenkov radiation, and other radiation processes steadily dissipate the primary energy in the atmosphere and can be used to reconstruct the longitudinal profiles. (71)

4.1.2 Hadronic cascades

Showers initiated by protons or nuclei are more complex than the pure electromagnetic cascades, as the strong nuclear force dominates over the electromagnetic interactions at cosmic-ray energies. When, say, a high-energy proton enters the atmosphere, it will interact in the field of atomic nuclei and produce a series of secondary particles in a process like

$$p + A \rightarrow p + Y + \pi^{\pm,0} + K^{\pm,0} + \ldots , \tag{4.5}$$

where Y are the remnants of the interacting nucleus of mass A and p, at the right side of the expression, is the probably surviving initial proton, arising as the leading particle among the secondaries. The products of the first interaction will propagate further, increasing the cascade size through successive interaction or decay processes, until the energy is dissipated in the atmosphere. Notably, the number of pions largely overcomes that of other types of particles in hadron-hadron processes (226–227) and to a large extent determine how a cascade develops. (228) Of particular importance is the production of neutral pions (π^0) in the hadronic interactions. These short-lived mesons ($c\tau = 25\,\mathrm{nm}$) quickly decay through the channel $\pi^0 \rightarrow 2\gamma$ (branching ratio $\sim 98.8\%$) and feed a preponderant

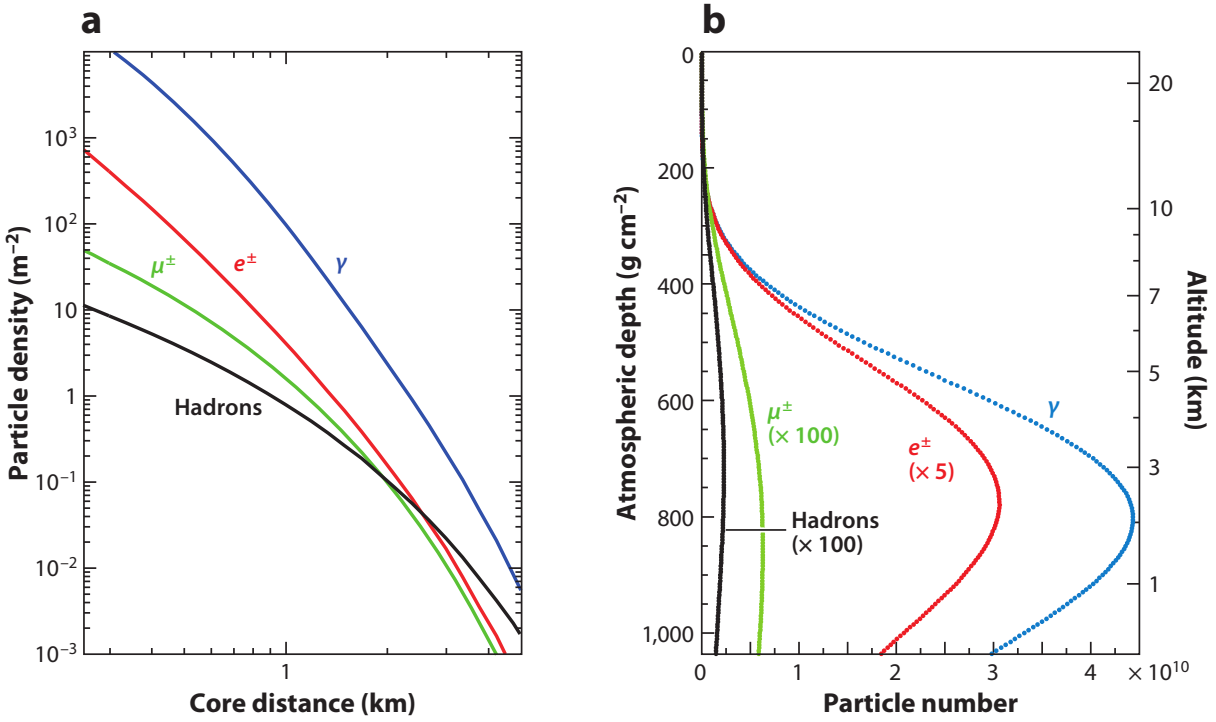

Figure 30 – Average simulated lateral distributions at 870 g/cm^2 (left) and longitudinal profiles (right) of vertical 10^{19} eV proton showers.

Source: ENGEL; HECK; PIEROG (34)

electromagnetic component in hadronic showers. Charged pions ($\pi^{\pm}$), on the other hand, typically propagate and interact with air nuclei, unless their energy is below some critical value ξ^{π}_{crit}, when the decay length becomes smaller than the interaction length for these particles. Being $\pi^{\pm} \rightarrow \mu^{\pm} + \nu_{\mu}(\bar{\nu}_{\mu})$ the preferred decay channel of charged pions (with a branching ratio $\sim 99.99\%$), the decay of low energy $\pi^{\pm}$ gives rise to a muonic component in air showers that is able to reach the ground almost unattenuated. The role of charged kaons $K^{\pm}$, whose number produced in hadronic interactions is also relevant, is similar to that of $\pi^{\pm}$ as the lifetime of these particles is $c\tau = 3.7\,\text{m}$ and they typically decay into muons. The average lateral distributions and longitudinal profiles of the multiple components of a 10^{19} eV proton shower are shown in Figure 30.

To accommodate for protons as primary particles in a simple calculation of the depth of maximum, the following reasoning is in order. A proton of energy E_0 traverses a mean free path $\lambda_p(E_0)$ in air, corresponding to its interaction length, after which it interacts with an air nucleus and produces, on average, $\eta(E_0)$ secondary particles. In an approximation analogous to the Heitler model, E_0 is assumed to be equally shared among the secondary products. After this first interaction, a dominant electromagnetic subshower is produced by the decay of the secondary π^0s into a pair of photons, whose energy is $E_0/2\eta(E_0)$. This proton-induced cascade will reach a maximum number of electrons at an

atmospheric depth corresponding to the sum of the depth of the primary interaction λ_p and the depth of maximum $X^{\gamma}_{\max}$ of the dominant electromagnetic subshower. In this scheme, it is useful to approximate the average multiplicity and the mean free path, respectively, as $\eta(E_0) \approx a_\eta E_0^{b_\eta}$ and $\lambda_p(E_0) \approx X_0(a_\lambda - b_\lambda \ln E_0)$ (229–231), so that, in accordance with Equation 4.1,

$$X^p_{\max}(E_0) \approx X_0\Big[a_\lambda - \ln(2\xi_{\text{crit}} a_\eta) + (1 - b_\lambda - b_\eta)\ln E_0\Big] \,, \tag{4.6}$$

where the index p indicates the expression is for a proton-induced shower. Using realistic values for the coefficients a_λ, b_λ, a_η, and b_η in the expression above does not yield a correct estimation for the absolute value of $X^p_{\max}$ when compared to Monte Carlo simulations, as noted in reference. (229) This inconsistency was expected, as the model oversimplifies the description of extensive air showers. Nevertheless, Equation 4.6 captures the insight that $X^p_{\max} \sim \lambda_p + \Delta X_{\max}$, which is important to investigate fluctuations of this variable, as well as it introduces a correct functional form for the elongation rate Λ, defined as $\Lambda \equiv {}^{\mathrm{d}\langle X_{\max}\rangle}/_{\mathrm{d}\ln E_0}$.

Regarding the elongation rate, if Equation 4.6 is interpreted as the average value for proton-induced showers, a constant value is implied, which is

$$\Lambda^p = X_0(1 - b_\lambda - b_\eta) \,. \tag{4.7}$$

For $b_\lambda, b_\eta > 0$, as expected from particle physics, Equation 4.7 puts an upper bound to Λ^p which is equivalent to the radiation length X_0. This upper bound would coincide with the unphysical case in which $b_\lambda = b_\eta = 0$, corresponding to a proton-nucleus cross section and a secondary multiplicity not evolving with energy. Such result (a constant Λ^p and $\Lambda^p < X_0$) is known as the elongation rate theorem, introduced by Linsley in reference (232) and discussed in references. (82, 84, 218, 233) The elongation rate theorem is fundamental on experimental analyses of $X_{\max}$, as discussed below in the context of nuclei-induced showers. Furthermore, introducing a constant free parameter c not dependent on the primary energy E_0, the elontagation rate theorem suggests the modelling of $\langle X^p_{\max}\rangle$ as

$$\langle X^p_{\max}\rangle(E_0) = c + \Lambda^p \ln E_0 \,. \tag{4.8}$$

A further development of a simple branching model for proton-induced showers allowing for a description of the muonic component was introduced by Matthews (229,234) in what is now known as the Heitler-Matthews model. In his approach, Matthews assumes all particles produced in hadronic interactions are pions, of which two-thirds are $\pi^\pm$ and one-third are π^0. Every hadronic particle traverses a depth λ_{ine} before interacting again, except π^0s, which are assumed to decay immediately after being created. A constant number η_{ch} of charged pions is assumed to be produced in a hadronic interaction either started by a primary proton or by a secondary charged pion, regardless of the particle

energy. Having set the main parameters, the overall picture of the model is analogous to the Heitler model: a primary proton enters atmosphere and traverses a depth λ_{ine} before interacting and producing η_{ch} charged pions and $\eta_{\text{ch}}/2$ neutral pions; neutral pions decay and feed the electromagnetic cascade; charged pions further traverse a depth λ_{ine} and interact, producing η_{ch} charged pions each and the corresponding number of neutral pions; and so on. In this scheme, illustrated in Figure 27, each n-th layer of atmosphere of thickness λ_{ine} will contain $N_\pi = (\eta_{\text{ch}})^n$ hadrons of energy $E_\pi = (2/3\eta_{\text{ch}})^n E_0$. When the energy E_π drops below the critical value ξ^π_{crit}, all charged pions decay into muons, whose number is found to be

$$N^p_\mu(E_0) = \left(\frac{E_0}{\xi^\pi_{\text{crit}}}\right)^\beta \,, \tag{4.9}$$

with $\beta = \ln(\eta_{\text{ch}})/\ln(\frac{3}{2}\eta_{\text{ch}})$. Conceptually, the Heitler-Matthews model is again an over-simplification of the air shower physics aiming to get qualitative results, just as in the original Heitler model. However, Equation 4.9 correctly predicts the evolution of $\ln N_\mu$ as linear in $\ln E_0$.

4.1.3 Nuclear primaries

The preceding discussion of proton-induced showers can be generalized to the case of nuclear primaries in view of the superposition model, in which a nucleus of mass A and energy E_0 is assumed to be equivalent to A free nucleons of energy E_0/A. This is justified by the observation that the binding energy of the bound nucleons is much smaller than the typical kinetic energy of a cosmic ray. In this case, a shower initiated by a cosmic-ray nucleus of mass A is to be interpreted as the superposition of the A showers generated by each nucleon. Consequently, some observables will have the additive property, such as those related to the shower size. The number of muons, for instance, can be obtained from Equation 4.9 by replacing $E_0 \to E_0/A$ and adding a factor of A (229–230, 235), resulting in

$$N_\mu(E_0, A) = A^{1-\beta}\left(\frac{E_0}{\xi^\pi_{\text{crit}}}\right)^\beta \,, \tag{4.10}$$

that is, the number of muons in an air shower is expected to increase with the primary mass proportional to $A^{1-\beta}$. An obvious implication from this result is that the number of muons measured at the ground is an estimator of A (236) as well as of E_0. (66)

The depth of maximum X_{max}, on the other hand, is not an additive property as each subshower is expected to reach a maximum number of particles at the same average value. From this, assuming the primary flux to have an average logarithmic mass $\langle \ln A \rangle$ at an energy E_0, the replacement $E_0 \to E_0/A$ in Equation 4.8 prescribes an average depth of maximum given by

$$\langle X_{\text{max}} \rangle(E_0) = c + \Lambda^p\Big(\ln E_0 - \langle \ln A \rangle\Big) \,, \tag{4.11}$$

from which it is gathered that the heavier the primary mass, the less penetrating is a shower. Apart from the absolute value, Equation 4.11 prescribes a constant elongation rate $\Lambda = \Lambda^p$ independent of the primary mass if $\langle \ln A \rangle$ does not change with energy. In contrast, if $\langle \ln A \rangle$ is assumed to explicitly depend on E_0, the elongation rate becomes

$$\Lambda(E_0) = \Lambda^p \left(1 - \frac{\mathrm{d}\langle \ln A \rangle}{\mathrm{d} \ln E_0} \right) , \tag{4.12}$$

suggesting that if Λ changes with E_0, the primary mass composition is also changing. Thus the importance of the elongation rate in experimental analysis: the evolution of $\langle X_{\max} \rangle$ with E_0 is an accessible observable and provides vital information on the primary mass composition. (33, 82) The result of Equation 4.12 is to be considered valid under the condition that assumptions from particle physics, encoded in Λ^p, as well as the superposition model are, at least in approximate form, also valid.

4.1.4 Fluctuations

All the reasoning above relied on interpreting the average behavior of extensive air showers. Such discussion resulted in a qualitative description of the relation between the average values of some shower observables and the average characteristics of the primary cosmic-ray flux. Were the extensive air showers free from intrinsic fluctuations, relations such as those in Equations 4.11 and 4.10 could provide an unambiguous determination of the primary mass and energy of every shower in an experimental analysis, provided the free parameters of the model are given and the observables are measured. However, this is not the case. In reality, observables of an extensive air shower are of stochastic nature, and each cascade is more precisely understood as the realization of a stochastic process. As a consequence, the distributions of observables from showers of different primary types overlap and an unambiguous characterization of the primary particle is not possible on a shower-by-shower basis. From a statistical perspective, the measurement of fluctuations on observables also characterizes the primary flux. The role of fluctuations in the longitudinal profiles in gamma-ray-, proton-, and iron-induced showers of 100 PeV is illustrated in the left plot of Figure 31. It can be drawn from this figure that the fluctuations are an intrinsic property of extensive air showers and, from comparison of profiles from different primaries, that the extent to which showers fluctuate depends on the primary particle type.

The measurement of fluctuations on $X_{\max}$ is a typical source of information about the primary particle type, along with its average. (82) Following the reasoning that resulted in Equation 4.11, the variance of $X_{\max}$ distributions, $\sigma^2(X_{\max})$, can be approximated by

$$\sigma^2(X_{\max})(E_0) = \sigma^2_{\mathrm{sh}}(X_{\max}) + \Lambda^p \sigma^2(\ln A) , \tag{4.13}$$

where $\sigma^2(\ln A)$ is the variance of logarithmic masses on the primary flux at energy E_0 and $\sigma^2_{\mathrm{sh}}(X_{\max})$ accounts for intrinsic shower-to-shower fluctuations, which depends both

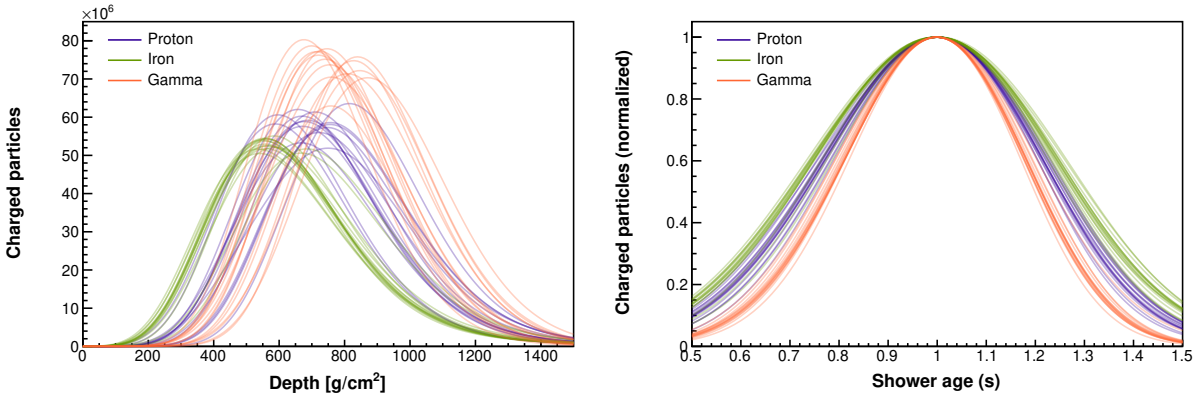

Figure 31 – Longitudinal profiles of extensive air showers as a function of atmospheric depth (left) and shower age (right).

Source: By the author

on E_0 and the relative abundances of primary masses. This result, in somewhat more elaborated form, has been used in experimental analyses to derive the evolution of $\langle \ln A \rangle$ with the primary energy from measurements of $\langle X_{\max} \rangle$ and $\sigma(X_{\max})$. (28) Such method however has the limitation of not providing the exact fractions of different mass groups, as different combinations of primary mass abundances can result in a same value of $\langle \ln A \rangle$. This limitation can be overcome by relying on the analysis of $X_{\max}$ fluctuations not based only on the first two moments but on its entire distribution. Methods to derive the relative primary mass abundances from measured $X_{\max}$ distributions are discussed in references. (29,31,237–238) As a common factor, these methods need to know a priori the shape of $X_{\max}$ distributions in terms of the primary energy and mass. The description and the parametrization of the $X_{\max}$ distributions in the regime of ultra-high-energy cosmic rays are covered in Chapter 5.

To get a heuristic insight about shower-to-shower fluctuations, in particular of $X_{\max}$, consider again the Heitler model, in which $X^{\gamma}_{\max}$ is written as the sum of interaction lengths of different generations of particles. Considering the interaction length of each generation to fluctuate according to an exponential law of scale parameter $\lambda_e = X_0 \ln 2$, as expected for a single particle, then the Heitler model predicts $X^{\gamma}_{\max}$ follows a gamma distribution,

$$\frac{\mathrm{d}N_{X^{\gamma}_{\max}}}{\mathrm{d}X^{\gamma}_{\max}} = \frac{1}{\lambda_e \Gamma(n_c)} \left(\frac{X^{\gamma}_{\max}}{\lambda_e} \right)^{n_c - 1} \mathrm{e}^{-X^{\gamma}_{\max}/\lambda_e} , \tag{4.14}$$

where $n_c = \log_2(E_0/\xi_{\mathrm{crit}})$ is the number of generations required for particle energies to drop below ξ_{crit}. In Figure 32, the prediction from Equation 4.14 (red, dashed line) is compared to the simulation (black solid) of the $X^{\gamma}_{\max}$ distribution from 100 TeV gamma-ray showers. As expected, being too simplified, this crude model fails to describe the fluctuations by overestimating the width of the distribution. If, on the other hand, only

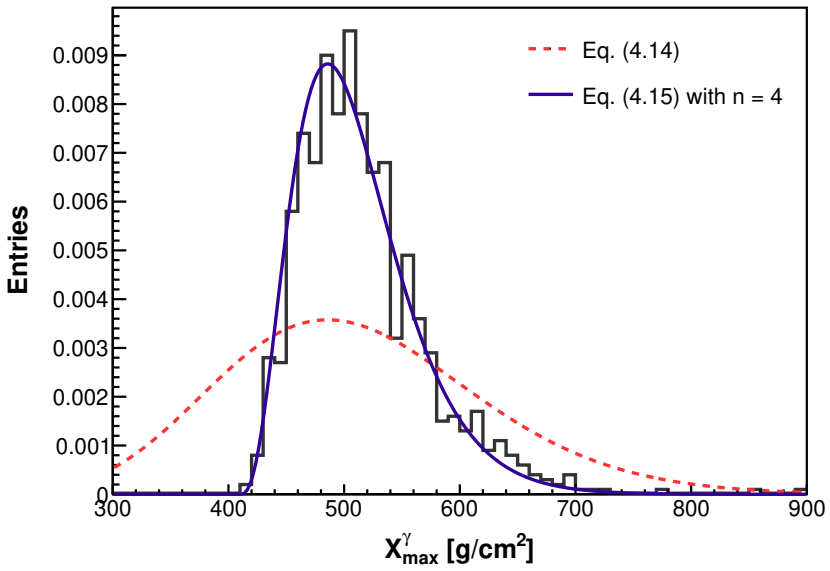

Figure 32 – $X^{\gamma}_{\max}$ distribution from 1000 100 TeV gamma-ray showers simulated with CONEX (black) in comparison to analytical models.

Source: By the author

the tracks of the first few n generations are considered to fluctuate, then the substitutions $n_{\mathrm{c}} \to n$ and $X^{\gamma}_{\max} \to X^{\gamma}_{\max} - \lambda_e(n_{\mathrm{c}} - n)$ apply and Equation 4.14 can be restated as

$$\frac{\mathrm{d}N_{X^{\gamma}_{\max}}}{\mathrm{d}X^{\gamma}_{\max}} = \frac{\mathrm{e}^{n_{\mathrm{c}}-n}}{\lambda_e \Gamma(n)} \left(\frac{X^{\gamma}_{\max}}{\lambda_e} + n - n_{\mathrm{c}} \right)^{n-1} \mathrm{e}^{-X^{\gamma}_{\max}/\lambda_e} , \tag{4.15}$$

with n being a free parameter of this simple model. Suppose, say, $n = 4$, meaning fluctuations of only the first four generations are considered, then Equation 4.15 provides a reasonable approximation to the simulated distributions, as can be seen in Figure 32 (blue, solid line).

Formally, the result from the previous paragraph is not correct. However, from a heuristic perspective, it provides an interpretation of air showers that is essentially plausible: most fluctuations in air shower observables arise from fluctuations from few interactions at the shower start, when particle numbers are still small and the output from interactions affect the entire shower development. A discussion in this direction is given by Greisen, who states that once a shower "is well under way, further fluctuations in the development are small because of the great number of particles that interact independently of each other. The place where the fluctuations are most serious is near the origin, where chance variations in the behavior of one or a few particles may retard or accelerate the entire subsequent development." (220)

4.1.5 Shower universality and the age parameter

That shower-to-shower fluctuations are reduced when cascades reach close to the point of maximum development, $X_{\max}$, is a fundamental result. This means that if showers are expressed as a function of some parameter describing its stage of evolution with respect to $X_{\max}$, instead of the penetrated thickness X, then shower-to-shower fluctuations can be minimized. A common choice for such parameter is the shower age s, which arises from cascade theory (219–220) and has the form

$$s = \frac{3X}{X + 2X_{\max}} \, . \tag{4.16}$$

A comparison of the longitudinal profiles of multiple showers normalized by their size at maximum and expressed as a function of s is shown in the right plot of Figure 31. The comparison of the two plots in this figure reveals the interesting fact that, at least for a common primary particle, profiles approximate a universal behavior when expressed in terms of s.

The concept that different showers at a same age present a common behavior is known as shower universality. (218, 239) This concept has been explored in Monte Carlo simulation of extensive air showers (240–244), and has been established that not only the total number of electrons is universal but also their energy spectrum and angular distribution, as illustrated in Figure 33. Since the seminal work of Hillas in 1982 (245), the age parameter has been used to parametrize characteristics of extensive air showers such as the energy spectrum and the angular distribution of electrons from Monte Carlo simulations. The concepts of shower age and universality are very important in Chapter 6, in which a parametrization of the angular distribution of Cherenkov photons in air showers is presented.

4.2 Computational techniques

In what concerns the reconstruction of the primary cosmic-ray flux from measurements of extensive air showers, the current paradigm is to rely on simulations to correlate observables with the characteristics of the primary particle. This is because computer simulations currently provide the only way to describe the complete development of an extensive air shower for any type of primary particle, including the intrinsic shower-to-shower fluctuations. Accordingly, values of observables and their fluctuations can be parametrized in terms of the primary particle so to be used in experimental analyses. This concept of parametrizing observables using simulations is at the core of the results presented in Chapters 5, 6, and 7 of this thesis. In light of this, the current section is dedicated to review the different strategies available for simulating extensive air showers.

It has been seen in the previous section that an extensive air shower develops according to the propagation of particles in the cascade, including their interactions with

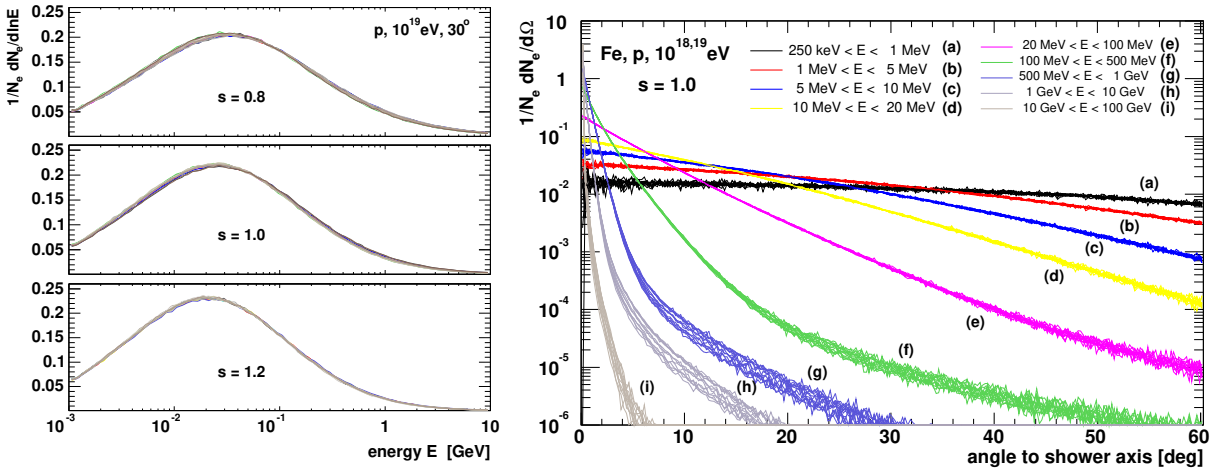

Figure 33 – Shower universality in Monte Carlo simulated cascades. Left: energy spectrum of shower electrons at three different shower ages from an ensemble of 15 individual 10^{19} eV proton showers. Right: angular distribution of electrons at the shower maximum from a group of proton- and iron-induced showers.

Source: NERLING *et al.* (240)

air nuclei, decays, and radiation processes. From a computational perspective, thus, a method to store particles in memory and simulate their interactions and decay chances is mandatory. Two are the main algorithms used in the astroparticle physics community for that purpose: the full Monte Carlo approach, available in the CORSIKA package (246), and a hybrid approach, combining a full Monte Carlo for the early shower development with the numerical solution of cascade equations, available in the CONEX (247–249) package.

4.2.1 Full Monte Carlo approach

In CORSIKA, the simulation process relies on the concept of a first-in-last-out particle stack (250), which at the start of the computational process contains a single primary particle. At the beginning, this primary is removed from the stack and its propagation in the atmosphere is simulated, in which a first interaction point is chosen at random according to its inelastic cross section in air and the atmospheric density profile. The target of the interaction is chosen by chance between nitrogen, oxygen, and argon, respecting realistic values for the relative densities in air. From this first interaction, a final state comprising a set of secondary particles is determined at random by employing a Monte Carlo event generator suited for the particle type, which could be electromagnetic or hadronic. Each secondary particle, then, is sent back to the particle stack if its energy exceeds a pre-defined cutoff value. Next, the program enters a loop, in which the last particle sent to the stack is separated from it and its propagation, radiation, energy

deposit, and interaction or decay are simulated, sending particles back to the stack when appropriate. The simulation of a shower will be complete under two conditions: either the stack becomes empty because every particle is below the cutoff energy for its type or all particles have crossed the last observation level, whose altitude is set prior to the simulation. Along the computational process, two main pieces of information are stored to be available at the end of the simulation: the total number of particles of each type as a function of atmospheric depth – the longitudinal profiles – and the characteristics (type, position, arrival time, energy, and momentum) of each particle crossing the observation level – the lateral distributions.

Electromagnetic subshowers are simulated in CORSIKA using the EGS4 (251) package, which describes the standard quantum-electrodynamic interaction of electrons, muons, and photons with the air nuclei, as well as the multiple Coulomb scattering of electrons. Hadronic interactions and cross sections are treated via phenomenological models available in Monte Carlo event generators. Two physical regimes of hadronic interactions, of low and high energy, are defined in the framework of CORSIKA and a threshold energy E_{thr}, typically of 80 GeV, is a configurable parameter. In both regimes, a set of models is available and has to be chosen a priori during program compilation. In the low energy regime ($E_{\mathrm{lab}} < E_{\mathrm{thr}}$), the most used models are UrQMD (252) and FLUKA. (253) These low-energy hadronic interaction models are known to be a source of uncertainties in the description of extensive air showers, as well as the choice of the threshold energy E_{thr} (254), although not as important as the high-energy interaction models. (255) Uncertainties related to high-energy hadronic interaction models are the most important in the simulation of hadronic air showers. (34, 256) The hadronic interaction models available in CORSIKA include QGSJetII-04 (257), EPOS-LHC (258), and Sibyll 2.3. (259)

Stated as above, disregarding uncertainties in describing interaction processes, the full Monte Carlo approach appears, conceptually, as the simplest possible: it relies on the simulation of every shower particle with as many details as possible. However, shortcomings emerge due to the large particle number in very energetic showers. Suppose, for instance, a cascade started by a proton of 10^{20} eV that can have at its maximum $\sim 10^{11}$ particles. In this case, a memory of hundreds of GB would be necessary to store the four-momentum and four-position of all particles in double precision, making the simulation prohibitive for a normal computer. Besides, as the shower size grows approximately linearly with energy, so does the time requirement for a complete simulation, which can easily turn into a requirement of months for a single shower. This is even more problematic in case Cherenkov-light emission and propagation are simulated (260), as the number of photons is much larger than the number of electrons. Therefore, algorithms to reduce the number of simulated particles are necessary to make full Monte Carlo simulations viable at very high energies.

The strategies for shower reduction, in CORSIKA, include the employment of particle cutoffs, set by the user to avoid the simulation of particles not relevant for a particular analysis. These cutoffs are set separately for hadrons, muons, electrons, and photons. For the elaboration of the results of Chapters 6 and 7 using Cherenkov light from air showers, for instance, a cutoff of 20 MeV is used for electrons, because electrons with energies below this value do not radiate Cherenkov photons. Using this cutoff, no other reduction mechanism is necessary for showers with energies up to $\sim 1\,\mathrm{PeV}$.

Showers with energies above 1 PeV, as those used in Chapter 6, become very time-demanding in a full Monte Carlo simulation, even when the appropriate particle cutoffs are set. Therefore, another shower-reduction algorithm called the statistical thinning (246) is employed. This method, available CORSIKA, discards all particles with energies below a fraction ϵ_{th} of the primary energy emerging from an interaction, except one, randomly selected. To the surviving particle, a statistical weight is added corresponding to the sum of weights of the discarded particles. The smaller the value chosen for ϵ_{th}, the more detailed the simulation, but also the more computational resources it will require. As a side effect, this algorithm introduces artificial fluctuations (of unphysical origin) in the simulated particle distributions. To reduce this effect a maximum weight ω_{max} is defined, and can be set by the user, after reaching which particles are not subject to the thinning process.

4.2.2 Hybrid method

For some analyses based on shower simulations, the lateral distribution of shower particles is of no interest. This is the case of the X_{max}-based study presented in Chapter 5, for which only the longitudinal energy-deposit profile of the simulated showers is necessary to extract the value of X_{max}. In such cases, some approximations can be employed in the computational algorithms to simplify and speed up the simulation process. In particular, the CONEX package builds on a one-dimensional hybrid scheme for the computation of longitudinal profiles of extensive air showers. To solve the development of air showers in one-dimension means that particle displacements perpendicular to the shower axis are not considered at all, but only their movement along the shower axis. Apart from that, the Monte Carlo method used in CONEX is very similar to that employed in CORSIKA, described above, except no thinning algorithm is used. In place of that, particles whose energies are below 0.5% of the primary particle energy are used as the boundary conditions for the numerical solution of a system of one-dimensional integro-differential cascade equations. As particle energies in a shower typically fall below this fraction after only a few interactions, the use of cascade equations results in a speedup of the simulations of several orders of magnitude.

From the cascade equation side, CONEX aims to solve a set of functions $N_i(E, X)$,

describing the average number of particles of type i with energies in the interval between E and $E + \mathrm{d}E$ found in the atmospheric depth interval between X and $X + \mathrm{d}X$. The differential-to-total cross section ratios describing the average transition rate between different particle types are tabulated from the same interaction models as used in CORSIKA in discretized energy intervals. Particle decays and the energy deposit from charged particles are also considered in the cascade equations. As for the fluctuations, it has been established in references (247, 261) that the approach used in CONEX is enough to correctly treat the distribution of observables, including the $X_{\max}$.

4.3 Cherenkov light from air showers

Detection of light from extensive air showers is an important aspect in many cosmic-ray observatories. In the most abundant form, light is emitted isotropically due to the excitation of nitrogen molecules in air. Also abundant is the radiation of Cherenkov photons by ultra-relativistic electrons in the cascades. It is a notable fact that the emission of Cherenkov light is almost collimated with the shower axis. Thus, most times, it overcomes the fluorescence-light signal in showers observed close to their core. (76, 166) Even at great distances from the shower core, the Cherenkov photons scattered in air contribute significantly to the observed signal. (71) To understand the characteristics of this peculiar form of radiation therefore is key to the observation of air showers. As the characterization of the angular distribution of Cherenkov light is the topic of Chapter 6, in this section some general characteristics of this phenomenon are discussed. This section also comes in support of Chapter 7, in which Cherenkov light from air showers is proposed as a way to access $X_{\max}$.

4.3.1 Cherenkov radiation

When a charged particle moves fast through a dielectric medium, it will produce a transient, local polarization, after which a spherical electromagnetic pulse follows. In case the particle velocity $v = \beta c$ exceeds the phase velocity of light in the medium $v_{\mathrm{l}} = c/n$, where n is the refractive index, pulses from successive points of the particle track will interfere constructively in a particular angle θ and result in a plane wave that can be observed at large distances. The resulting radiation expands around the particle track in a conical shape with semi-opening angle θ and the apex accompanying the particle movement. (262–263) This phenomenon is analogous to the mechanical shock-wave generated by an object at supersonic speed and is illustrated in Figure 34.

Neglecting the small recoil of the charged particle due to the emission of photons, simple geometrical inspection of the rightmost sketch in Figure 34 through Huygens' principle is enough to reveal the angle θ is given by

$$\cos\theta = \frac{1}{\beta n} \,. \tag{4.17}$$

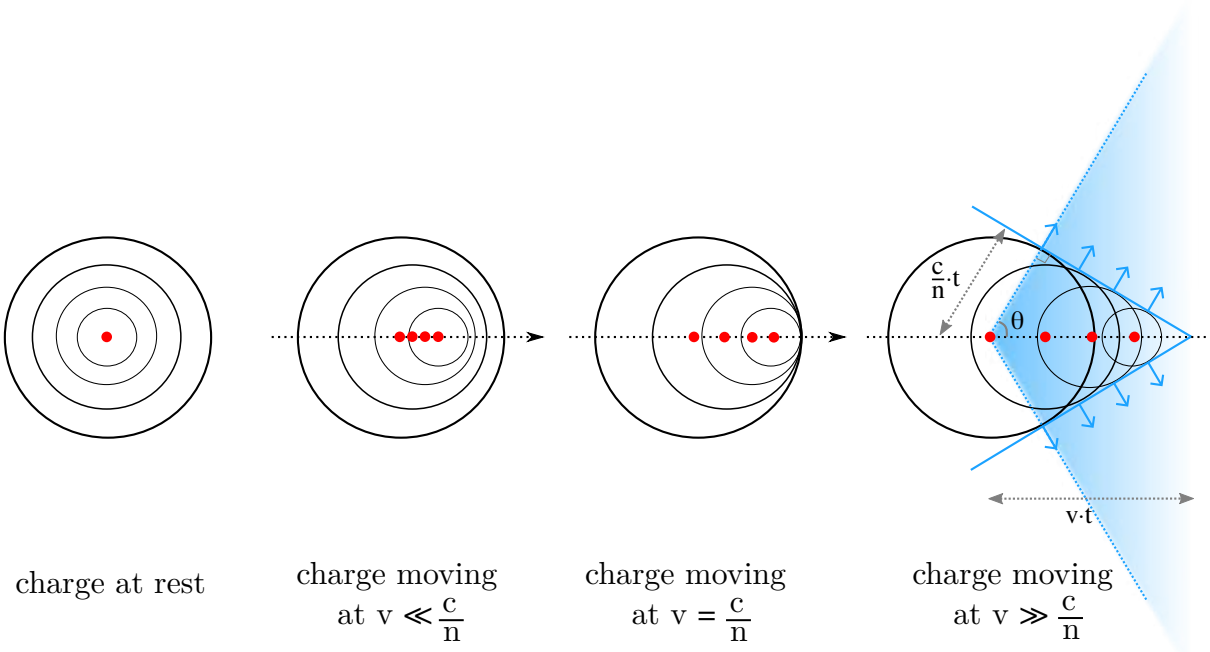

Figure 34 – Illustration of the process of Cherenkov radiation.

Source: JARDIN-BLICQ (264)

The simple relation posed in Equation 4.17 has some noteworthy physical implications. First, the Cherenkov-light emission angle increases with the particle velocity β and has a maximum for $\beta = 1$, equivalent to $\theta_{\max} = \operatorname{acos}(1/n)$, determined by the refractive index alone. Second, the condition $|\cos\theta| \leq 1$ reflects there is a threshold velocity $\beta_{\text{thr}} = 1/n$, below which no Cherenkov radiation occurs. In terms of the energy of the moving particle, assumed to be of rest mass m, the threshold for radiation is

$$E_{\text{thr}} = \frac{mc^2}{\sqrt{1 - n^{-2}}} \,. \tag{4.18}$$

Third, if the refractive index varies along the particle track, so does the emission angle θ. The latter observation has an important consequence for the emission of Cherenkov light in atmospheric showers because the refractive index decreases with altitude h.

As the moving charged particle emits light quanta through Cherenkov radiation, part of its energy is lost. Indeed, the average energy lost through the emission of Cherenkov light per unit track length interval $\mathrm{d}\ell$ can be computed by (262)

$$\frac{\mathrm{d}E}{\mathrm{d}\ell} = \frac{\hbar\alpha}{c} Z^2 \int_{\beta n > 1} \left(1 - \frac{1}{\beta^2 n^2(\omega)}\right) \omega \mathrm{d}\omega \,, \tag{4.19}$$

in which the refractive index depends on the frequency of the emitted light ω and the integral covers values of ω for which $\beta n(\omega) > 1$. The quantity Z represents the particle charge in units of the elementary electric charge e.

Typical air-shower detectors have quantum efficiencies in a bounded wavelength range, say, between λ_1 and λ_2. In such case, the integral in Equation 4.19 is performed in a limited interval among which the refractive index can be regarded as approximately constant $n(\omega) \approx n$. To estimate the signal in a detector, it is useful to express the energy loss in terms of a photon count $N_{\rm ph}$ through $\hbar\omega \mathrm{d}N_{\rm ph} = \mathrm{d}E$. With this, Equation 4.19 is seen to be equivalent to

$$\frac{\mathrm{d}N_{\rm ph}}{\mathrm{d}\ell} = 2\pi\alpha Z^2 \left(\frac{1}{\lambda_1} - \frac{1}{\lambda_2}\right)\left(1 - \frac{1}{\beta^2 n^2}\right) . \tag{4.20}$$

Bearing in mind that the refractive index in air is $n = 1 + \delta \approx 1$, the approximation

$$1 - \frac{1}{\beta^2 n^2} = 1 - \left(1 - \frac{m^2c^4}{E^2}\right)^{-1} (1+\delta)^{-2} \approx 2\delta \left(1 - \frac{E_{\rm thr}^2}{E^2}\right) \tag{4.21}$$

applies in the previous expression, which results in

$$\frac{\mathrm{d}N_{\rm ph}}{\mathrm{d}\ell} \approx 4\pi\alpha\delta Z^2 \left(\frac{1}{\lambda_1} - \frac{1}{\lambda_2}\right)\left(1 - \frac{E_{\rm thr}^2}{E^2}\right) . \tag{4.22}$$

Dividing the equation above by the local air density ρ and assuming an explicit dependence on the altitude for ρ and n result in the Cherenkov-photon yield per unit thickness $Y_\gamma(E, h)$, used in Chapter 6.

4.3.2 Light from air showers

In extensive air showers, therefore, the bulk of radiated Cherenkov photons will be characterized by three aspects:

- characteristics of the atmosphere that, through changes in the refractive index, modify the Cherenkov emission angle (Equation 4.17), the threshold energy for emission (Equation 4.18), and the yield per particle (Equation 4.22);
- the energy spectrum of shower electrons, related to the yield of Equation 4.22 and to the Cherenkov emission angle (Equation 4.17);
- the angular and lateral spread of electron tracks, around which individual Cherenkov cones are emitted.

Therefore, the characterization of the bulk of Cherenkov photons can be described in terms of two parameters in a shower: the shower age, describing how electrons evolve in the atmosphere, and the altitude, describing the evolution of the refractive index. A more deep insight on how to take these elements in consideration to obtain the resulting distribution of Cherenkov photons from a shower is given in Chapter 6.

Some general characteristics of Cherenkov-light emission from extensive air showers are summarized in Figure 35. In the sketch at the left of this figure, it is shown that the

variation of the Cherenkov-light emission angle with altitude [from $\sim 0.2^\circ$ at $h = 30\,\mathrm{km}$ to $\sim 1.5^\circ$ at sea level (130)] has as a consequence the superposition of Cherenkov photons in a ring (light annulus) with a radius of about $\sim 150\,\mathrm{m}$, concentric with the shower core. Charged particles reaching closer to the ground will fill the area inside this annulus and give rise to a pool of Cherenkov photons. The resulting density of Cherenkov photons versus the distance to the shower core is shown in the upper-right plot of Figure 35 for different primary gamma-ray energies. In this plot, the peak due to the ring and the Cherenkov pool are clear. The time structure of the arrival times of photons emitted at different altitudes is sketched in the lower-right plot of the same figure. This plot shows that close to the shower core, inside the Cherenkov pool, photons from smaller altitudes arrive first, followed by the photons emitted from higher altitudes in a time range of few nanoseconds ($\sim 5\,\mathrm{ns}$ at the shower core). Right at the Cherenkov ring, photons from different altitudes reach ground almost simultaneously, in a time interval of about $\sim 2\,\mathrm{ns}$. For increasingly larger impact distances, Cherenkov photons from high altitudes arrive first, and the signal can be spread in an interval of several nanoseconds.

As a last consideration, it is interesting to look at the relation between the angular distribution of shower particles and the distribution of Cherenkov photons at ground. Due to the production of particles with high transverse momenta in hadronic interactions, electrons of showers induced by hadrons typically have a broader angular distribution compared to pure electromagnetic cascades. Moreover, the distribution of particle tracks has a more erratic pattern in low-energy hadronic showers, because of the relatively small particle numbers. This is illustrated in Figure 36. Accordingly, as Cherenkov cones have narrow opening angles, the resulting distributions of Cherenkov photons at the ground from hadronic and electromagnetic showers differ, as shown in Figure 36.

4.4 Conclusion

In this chapter, a review on some topics of extensive air showers has been presented. Some of the visited concepts pervade the studies developed in this thesis, which are presented in the following chapters. These basic concepts include, for instance, the correlation between X_{max} and the primary composition. Also, an insight about X_{max} has been obtained by writing it as a sum of the first interaction point with the later shower development, which is used in Chapter 5 to get a possible functional form to describe the X_{max} distributions. Two other concepts that result very useful in the context of this thesis are the shower age and universality. It is by relying on the concept of universality that results of Section 6 are derived.

The methods used to simulate extensive air showers in the following chapters have been presented and their limitations have been discussed. Attention was also given to the fundamentals of Cherenkov light emission in extensive air showers in view of its

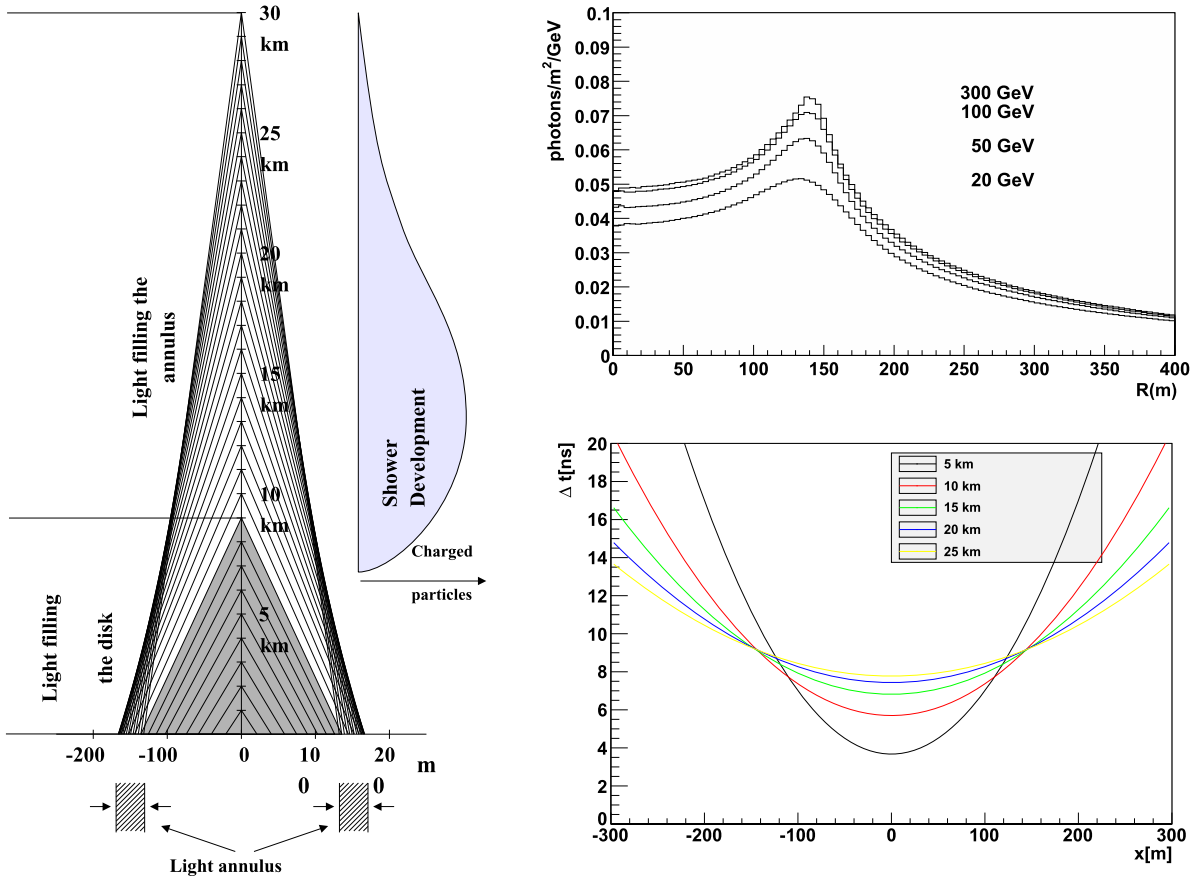

Figure 35 – Characteristics of Cherenkov-light emission in air showers. Left: sketch of Cherenkov light emission from extensive air showers, highlighting the formation of a Cherenkov ring. Top right: density of Cherenkov photons versus distance to shower core. Bottom right: time delay of Cherenkov photons arriving at the ground as a function of the distance to the core and the emission height.

Source: NAUROIS; MAZIN (130)

importance for the results derived in Chapters 6 and 7.

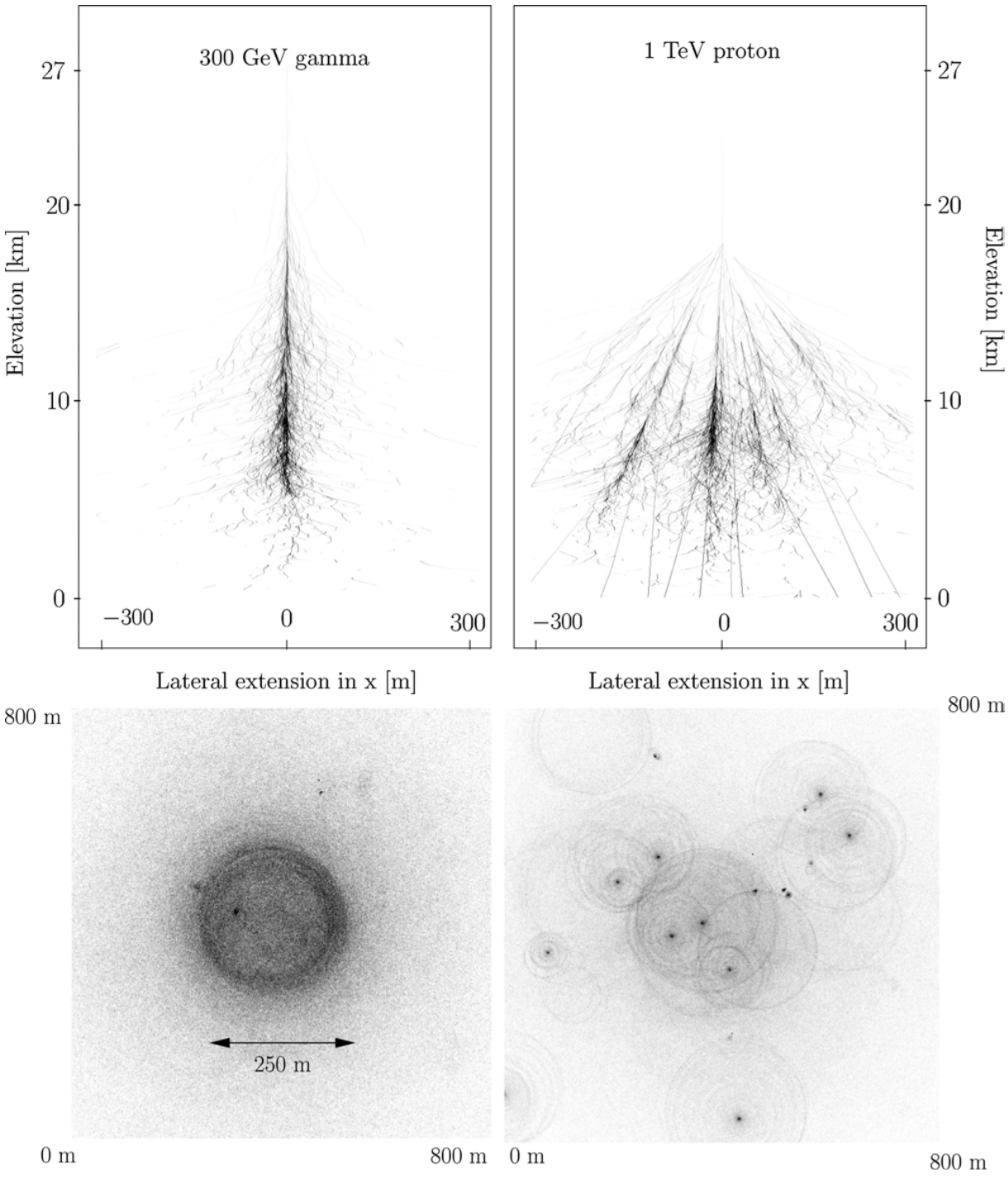

Figure 36 – Top: projection of particle tracks of an extensive air shower in a plane, showing the spread of shower particles. Bottom: resulting distributions of Cherenkov photons at the ground. Left: 300 GeV vertical gamma-ray shower. Right: 1 TeV vertical proton shower.

Source: AHARONIAN *et al.* (165)

5 ON THE PARAMETRIZATION OF THE DISTRIBUTIONS OF DEPTH OF SHOWER MAXIMUM OF ULTRA-HIGH ENERGY EXTENSIVE AIR SHOWERS

Astroparticle Physics 116 (2020) 102389

Contents lists available at ScienceDirect

Astroparticle Physics

journal homepage: www.elsevier.com/locate/astropartphys

On the parametrization of the distributions of depth of shower maximum of ultra-high energy extensive air showers

Luan B. Arbeletche*, Vitor de Souza

Instituto de Física de São Carlos, Universidade de São Paulo, Av. Trabalhador São-carlense 400, São Carlos, Brazil

ARTICLE INFO

Article history:
Received 7 March 2019
Revised 19 July 2019
Accepted 6 September 2019
Available online 11 September 2019

ABSTRACT

The distribution of depth in which a cosmic ray air shower reaches its maximum number of particles (X_{max}) is studied and parametrized. Three functions are studied for proton, carbon, silicon, and iron primary particles with energies ranging from 10^{17} eV to 10^{20} eV for three hadronic interaction models: EPOS-LHC, QGSJETII.04, and SIBYLL2.3c. The function which best describes the X_{max} distribution of a mixed composition is also studied. A very large number of simulated showers and a detailed analysis procedure are used to guarantee negligible effects of undersampling and of fitting in the final results. For the first time, a comparison of several functions is presented under the same assumption with the intention of selecting within them the best functional form to describe the X_{max} distribution. The Generalized Gumbel distribution is shown to be the best option among the options for a general description of all cases. The Log-normal distribution is also a good choice for some cases while the Exponentially Modified Gaussian distribution has shown to be the worst choice in almost all cases studied. All three functions are parametrized as a function of energy and primary mass.

1. Introduction

The relative abundance of particle compositions in ultra-high energy cosmic rays (UHECR) is of key importance in the understanding of their acceleration mechanisms and interactions with extra-galactic radiation fields. The maximum particle energy of each source, the probability of escape from the acceleration region, the luminosity of the sources classes, the mean free path of the interaction on the way to Earth and the deviation angle in the magnetic fields are examples of fundamental astrophysics phenomena which depend on the particle type (mass and/or charge). A major improvement in our understanding of UHECR physics will not be possible without a precise determination of the abundance of each particle type. With this in mind, the two most important UHECR observatories (The Pierre Auger and the Telescope Array Observatories) are implementing upgrades to enhance their capabilities to determine the relative abundances of particle types arriving on Earth.

At these energies, the particles hitting Earth, called primary particles, are not directly observed. Their interaction with the atmosphere generates a cascade of particles which is measured by telescopes and ground detectors. The properties of the primary particle can be reconstructed from the detected signal of the shower. The most used and reliable parameter to determine the primary particle type is the depth at which the cascade reaches its maximum number of particles (X_{max}). These extensive air showers are very complex branching processes whose stochastic behavior, although well understood in terms of particle interaction processes, cannot be solved analytically. Thus, fluctuations of important global quantities such as X_{max} have no known functional form. In this sense, one always has to rely on Monte Carlo simulations to understand the intrinsic fluctuations of extensive air showers. Moreover, an approximation to the functional form of global variables can only be determined by the parametrization of simulated quantities.

Constant improvements in the fluorescence technique have allowed the Pierre Auger Observatory to measure X_{max} with a systematic uncertainties of about $\pm 8\,g/cm^2$ [1] and the TA Collaboration quotes systematic uncertainties of $\pm 17.4\,g/cm^2$ [2]. The resolution in $\langle X_{max} \rangle$ are quoted to be smaller than $25\,g/cm^2$ for the Pierre Auger Observatory measurements. The precision in measuring X_{max} is such that new studies are based on the full distribution instead of only its moments [1–5].

In this context, a good understanding of the X_{max} distribution shape is mandatory since many steps in the analysis procedures depend on knowing *a priori* its expected shape. The adoption of a particular parametrization may cause a wrong interpretation of X_{max} distributions when studying the primary fractions and their

* Corresponding author.
E-mail address: luan.arbeletche@ifsc.usp.br (L.B. Arbeletche).

https://doi.org/10.1016/j.astropartphys.2019.102389
0927-6505/

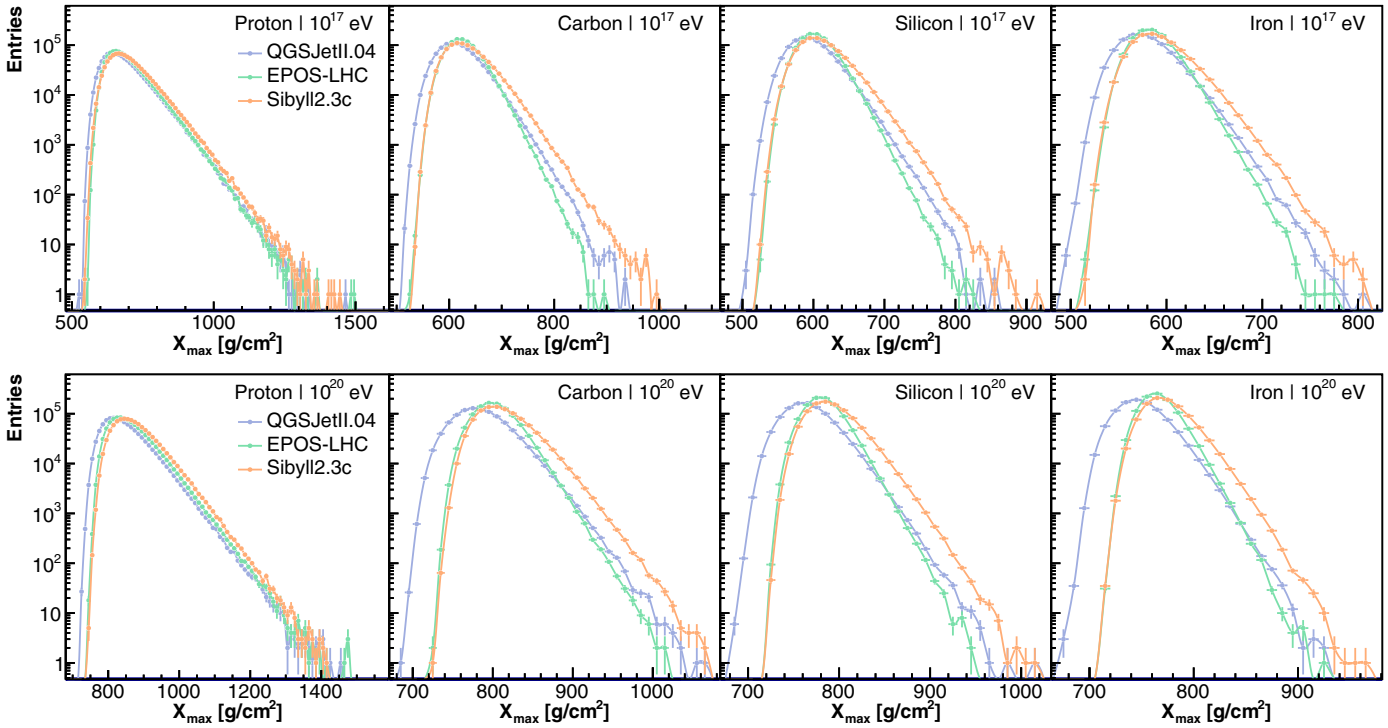

Fig. 1. Examples of simulated $X_{\max}$ distributions for four different primary masses (proton, carbon, silicon, iron) and three hadronic interaction models (QGSJetII.04, EPOS-LHC and Sibyll2.3c) at the energies 10^{17} eV (upper panel) and 10^{20} eV (lower panel).

evolution with energy. Some functions have been proposed to describe the $X_{\max}$ distribution [6,7] but no comparison between them is available. In this paper, three functions are used to describe the $X_{\max}$ distribution and a detailed statistical comparison between them is presented. The purpose of this paper is to select the best description of the $X_{\max}$ distribution and parametrize its dependencies with energy and mass.

This study is based on Monte Carlo simulations of air shower which are discussed in Section 2. In Section 3, the functions used to describe the $X_{\max}$ distribution are presented and discussed. Section 4 presents the results of the fits and Section 6 presents the conclusions.

2. Simulation of $X_{\max}$ distributions

Large samples of extensive air showers are simulated using the software CONEX [8]. This software is an implementation of a one-dimensional hybrid model of the longitudinal development of particle cascades which has been extensively tested [6]. Four atomic nuclei are considered: proton, carbon, silicon and iron (A = 1, 12, 28 and 56, respectively) with energies ranging from 10^{17} eV to 10^{20} eV in steps of 1 in $\log_{10}(E_0/\text{eV})$. The incident zenith angle of the primary cosmic rays is set to 75 °. The longitudinal development is sampled in steps of 10 g/cm^2 until particles reach sea level, corresponding to a slant depth of 3860 g/cm^2. The energy cutoff for hadrons, muons, electrons, and photons is 1 GeV, 1 GeV, 1 MeV and 1 MeV, respectively. Given the known dependence on hadronic interaction models [9–11], three post-LHC hadronic interaction models are considered: EPOS-LHC [12], QGSJetII.04 [13] and Sibyll2.3c [14]. For each combination of primary mass, energy and hadronic interaction model, 10^6 showers are simulated.

CONEX provides the depth at which a shower reaches its maximum number of particles (Xmx variable in CONEX output) and the depth at which the energy deposit profile reaches its maximum (XmxdEdX in CONEX output). Xmx and XmxdEdX are calculated by fitting a quadratic function around the maximum of the longitudinal particle and energy deposit profile, respectively. Details of the fitting procedure can be found in the CONEX manual [8]. These variables are compared and a maximum difference of 0.8 ± 3.4 g/cm^2 between them is found in all simulated cases. Given that the difference between these variables is very small, much smaller than the uncertainties of the measurements, the depth at which the shower reaches the maximum number of particles (Xmx=$X_{\max}$) is used in the following calculations. The small difference and statistical uncertainty between Xmx and XmxdEdX also illustrate the quality of the fit done in CONEX.

Showers with two maxima in the longitudinal profile, the so-called double bump showers [15], for which the depth of shower maximum is not an unambiguously defined quantity, are removed from our analysis. The double bump showers are identified by searching the longitudinal profiles with more than two inflection points by computing the second derivative of profiles at each point in terms of finite differences. This approach effectively removes showers with two pronounced peaks. The fraction of removed profiles is below 0.4% for all combinations of primary, energy and hadronic model.

Examples of simulated $X_{\max}$ distributions for some primary masses with energies of 10^{17} eV (upper panel) and 10^{20} eV (lower panel) are shown in Fig. 1. Primary types are indicated in the top-right corner of each plot. Each colored line corresponds to simulations done with a particular hadronic interaction model, indicated in the legend of the left plots. These distributions, as already known, have an accentuated positive skew that results from the exponential nature of particle interaction length distributions. Note, in Fig. 1, the logarithm scale in the y-axis and the very small fluctuations of each point. In this illustration, $X_{\max}$ was binned in intervals of 10 g/cm^2. As a result from the large simulated samples,

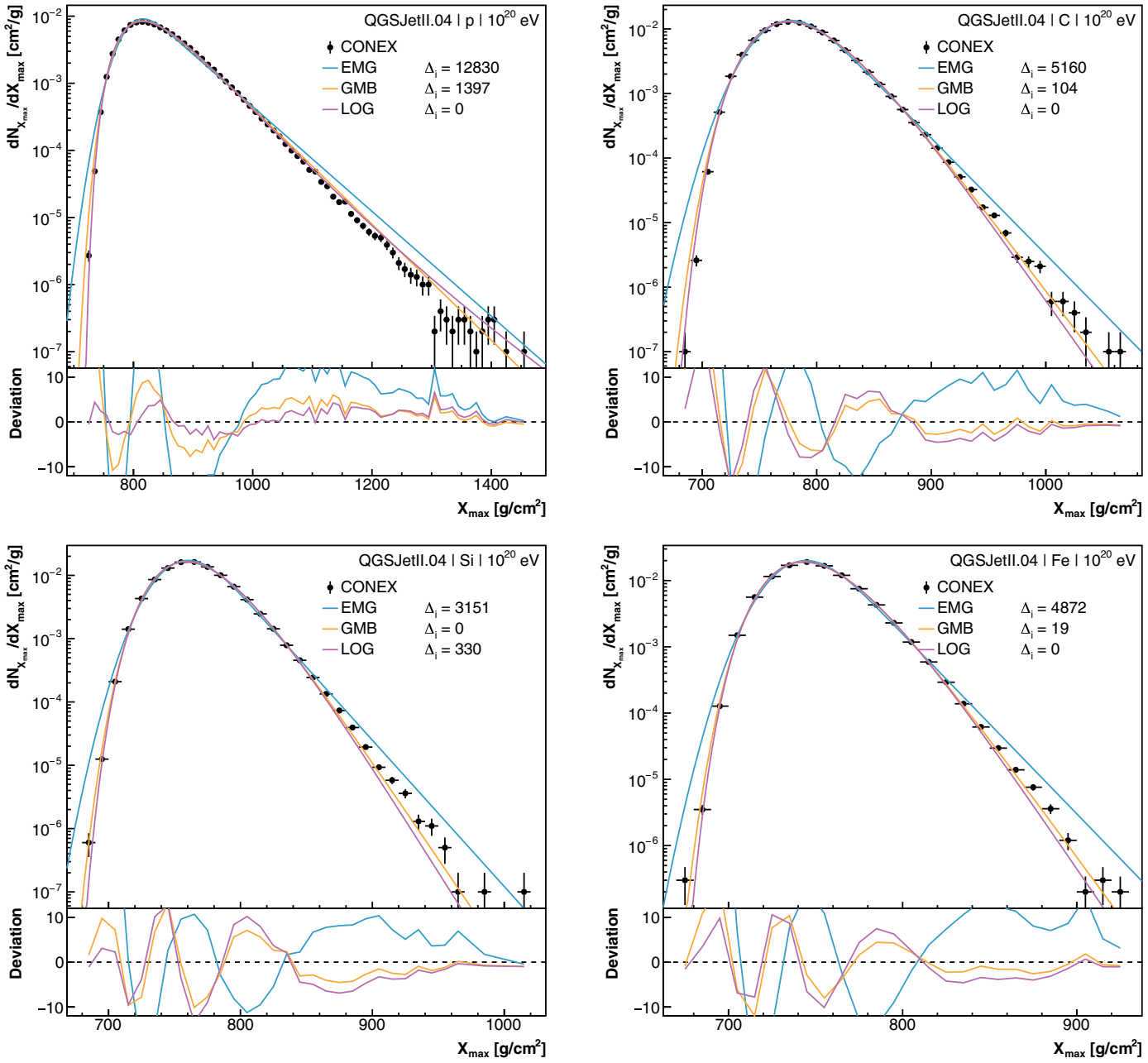

Fig. 2. Examples of fits of $X_{\max}$ distributions. The primary particle is indicated at the top-right corner of each plot. Fit functions are shown as colored solid lines, while the simulated $X_{\max}$ distribution is shown as circular dots. The bottom panels show the deviation of each fitted function to the simulated point, defined as the difference between the function and the point divided by the statistical uncertainty of the point. Only results for QGSJetII.04 are shown in this example.

fluctuations in the obtained distributions become larger only for very deep showers.

3. Proposed functions to describe the $X_{\max}$ distributions

In this section, three functions are studied to parametrize the $X_{\max}$ distributions: Exponentially Modified Gaussian, Generalized Gumbel, and Log-normal. They are going to be explained below and, whenever possible, an interpretation of their parameters is going to be given. Other functions have also been tested: Amoroso, Lévy α-stable, Fréchet, Exponentiated Fréchet, Exponentiated Exponential, Landau and Gamma, but either they do not showed a good description of the $X_{\max}$ distributions or they unreasonably increased the number of fitting parameters without providing a better description of data. The motivation for each function is also going to be briefly explored.

3.1. Exponentially Modified Gaussian distribution

The Exponentially Modified Gaussian (EMG) distribution was proposed in [6] to describe $X_{\max}$ distributions. It is motivated by the assumption that $X_{\max}$ can be decomposed as $X_{\max} = X_{\text{first}} + \Delta X_{\max}$, where X_{first} is the depth of the first interaction and $\Delta X_{\max}$ represents the shower development after the first interaction. While X_{first} is known to have an exponential distribution with the mean free path λ, the distribution of $\Delta X_{\max}$ is unknown. The simplest approach is to assume that $\Delta X_{\max}$ is normally distributed with an average μ and variance σ^2, so that

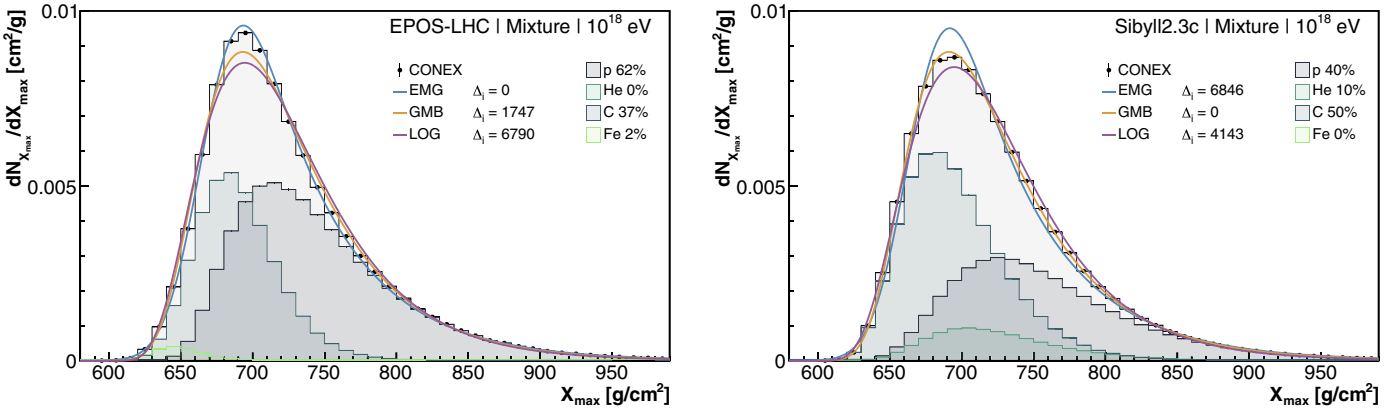

Fig. 3. Example of $X_{\max}$ distributions at an energy of 10^{18} eV following the fractions shown in Table 2. Filled histograms with color lines represent the distribution of each primary particle. Black dots shows the sum of all particles. Color lines shows the result of the fit of proposed functions to the distribution of all particles (black dots). Left panel for EPOS-LHC and right panel for Sibyll2.3c.

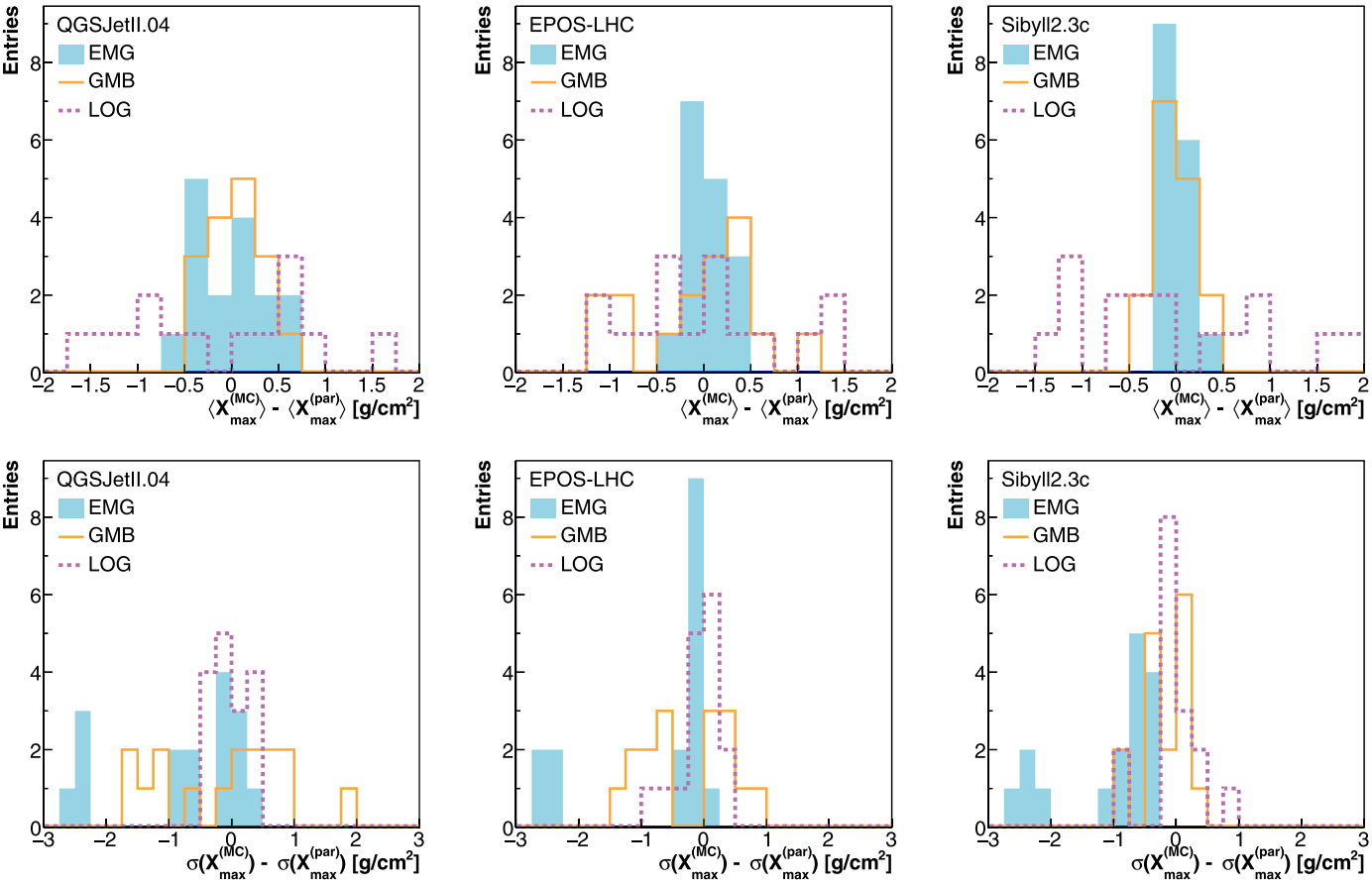

Fig. 4. Error on the first moment (upper plots) and second moment (lower plots) between the parametrized distributions (par) and the simulated (MC) $X_{\max}$ distributions.

$X_{\max}$ is distributed according to the convolution of an exponential and a Gaussian. The resulting function is:

$$f(x) = \frac{1}{2\lambda} \exp\left(-\frac{x-\mu}{\lambda} + \frac{\sigma^2}{2\lambda^2}\right) \operatorname{erfc}\left(\frac{\mu - x + \sigma^2/\lambda}{\sqrt{2}\sigma}\right), \qquad (1)$$

where $\operatorname{erfc}(x)$ is the complementary error function.

The EMG has three parameters that can be interpreted in terms of extensive air showers physics. λ, μ and σ are related to the decay factor of the exponential, the depth of maximum of the distribution and the width of the distribution, respectively. σ and λ influence both the width and the mean of the $X_{\max}$ distribution in different ways, mathematically $\langle X_{max} \rangle = \mu + \lambda$ and $\mathrm{RMS}(X_{\max}) = \sqrt{\sigma^2 + \lambda^2}$. The EMG function has already been employed in studies such as the determination of $X_{\max}$ moments from Pierre Auger Observatory [1], the comparison between Pierre Auger Observatory and Telescope Array $X_{\max}$ data [3] and the proposal of new methods to study the mass composition from real $X_{\max}$ data [4].

3.2. Generalized Gumbel distribution

The Gumbel distribution arises in the field of extreme value statistics to describe the frequency of extreme events (either minimum or maximum) in series of independent and identi-

Table 1
Relative AIC values (Δ_i) of the fit of the unbinned X_{max} distributions for the three hadronic interaction models and primary particle energy ranging from 10^{17} eV to 10^{20} eV. Note that a value of zero for a model means that this is the best model for the respective energy, mass and hadronic model combination.

Primary	Proton				Carbon				Silicon				Iron			
$\log_{10}(E_0/\text{eV})$	17	18	19	20	17	18	19	20	17	18	19	20	17	18	19	20
QGSJetII.04																
EMG	10113	11209	12226	12830	6636	6099	5181	5160	4213	3743	3447	3151	4920	5251	4875	4872
GMB	675	1044	1285	1397	131	105	32	104	0	0	0	0	0	0	0	19
LOG	0	0	0	0	0	0	0	0	402	381	384	330	202	79	81	0
EPOS-LHC																
EMG	8932	10507	13115	14264	4325	3884	3728	3027	2156	1236	1315	0	1742	1066	1571	1563
GMB	28	573	1425	1865	0	0	0	0	0	0	0	475	0	0	0	0
LOG	0	0	0	0	232	293	262	272	526	629	643	1222	681	754	781	802
Sibyll2.3c																
EMG	9319	10117	11619	12648	11851	11493	11277	10987	6492	6637	6559	6269	6542	6282	5655	4954
GMB	420	666	1103	1362	914	805	760	713	0	0	0	0	0	0	0	0
LOG	0	0	0	0	0	0	0	0	247	182	123	139	326	379	495	538

Table 2
Primary fractions which best describes the X_{max} distributions measured by the Pierre Auger Observatory [5] at the energies used in this paper.

Model	EPOS-LHC		QGSJetII.04		Sibyll2.3c	
$\log(E_0/\text{eV})$	18	19	18	19	18	19
p	61.5%	9.5%	63.2%	35.6%	40.4%	2.8%
He	0.0%	62.0%	36.8%	64.4%	9.7%	38.7%
C	36.7%	28.5%	0.0%	0.0%	49.9%	58.5%
Fe	1.8%	0.0%	0.0%	0.0%	0.0%	0.0%

Table 3
Relative AIC values (Δ_i) of the fit of the unbinned X_{max} distributions for the three hadronic interaction models and mix of primary particle. Note that a value of zero for a model means that this is the best model for the respective energy, mass and hadronic model combination.

Model	EPOS-LHC		QGSJetII.04		Sibyll2.3c	
$\log(E_0/\text{eV})$	18	19	18	19	18	19
EMG	0	5557	6093	5415	6846	9378
GMB	1747	0	0	0	0	200
LOG	6790	991	4813	1457	4143	0

cally distributed random variables [16]. The Generalized Gumbel distribution (GMB) [17] is written as

$$f(x) = \frac{1}{\sigma}\frac{\lambda^\lambda}{\Gamma(\lambda)}\exp\left\{-\lambda\left[\frac{x-\mu}{\sigma} + \exp\left(-\frac{x-\mu}{\sigma}\right)\right]\right\}. \quad (2)$$

Note that for $\lambda = 1$ one recovers the standard Gumbel distribution. Eq. (2) was proposed by Ref. [7] to describe X_{max} distributions.

The importance of the GMB distribution in extreme value statistics and its relation with the statistics of sums [18] can give some insight on its use to describe the X_{max} distribution. Suppose a series of random variables X_k is exponentially distributed according to

$$g_k(x) = \frac{\lambda + k}{\sigma}e^{-(\lambda+k)x/\sigma}. \quad (3)$$

It has been shown in Ref. [19] that the distribution of the sum $\sum_{k=0}^{\infty} X_k$ converges exactly to Eq. (2) after a convenient shift and re-scaling of X_k. That is, the asymptotic sum of exponentially distributed random variables with increasing amplitudes converges to a GMB distribution. Based on it, it is possible to interpret X_{max} as a sum of interaction depths of multiple generations of particles, similar to the model proposed in Ref. [20], but with variable interaction lengths, and to write

$$X_{max} = \sum_{k=0}^{\eta-1} X_k, \quad (4)$$

where η is the number of generations of particles. If $\eta \to \infty$ the distribution of the sum converges to Eq. (2). In this scenario, the mean free path of the first interaction is given by σ/λ. The scale parameter σ describes how fast the average interaction lengths change between generations of particles. The location parameter (μ) of Eq. (2) is introduced to shift the mean of the distribution.

For finite η, the sum above follows a beta-exponential distribution [21]:

$$f(x) = \frac{1}{\sigma B(\eta,\lambda)}e^{-\lambda x/\sigma}\left(1 - e^{-x/\sigma}\right)^{\eta-1}, \quad (5)$$

where $B(x, y)$ is the beta function, defined for $x, y \geq 0$. If a location parameter (μ) is added to the beta-exponential distribution, it could as well be considered a candidate to describe X_{max} distributions. The beta-exponential distribution was also tested following the method explained below, however, it did not show any improvement in the description of X_{max} distribution in comparison to the GMB. Since the beta-exponential function has one parameter more than the GMB, it was decided to keep only the GMB for further studies which in total has also three parameters.

3.3. Log-normal distribution

The log-normal distribution is characteristic of stochastic processes where the variable of interest can be written as a product of independent and identically distributed random variables so that its logarithm is normally distributed according to the central limit theorem. The log-normal distribution (LOG) proves to be difficult to interpret in terms of extensive air showers. However, as it will be shown later, it provides a good description of X_{max} distributions. The probability density function is given by

$$f(x) = \begin{cases} 0, & \text{if } x \leq m \\ \dfrac{1}{\sqrt{2\pi}\sigma}\dfrac{1}{x-m}\exp\left\{-\dfrac{[\ln(x-m)-\mu]^2}{2\sigma^2}\right\}, & \text{if } x > m. \end{cases} \quad (6)$$

It has three parameters m, μ and σ related to the position of the peak, the width of the distribution and the length of the tail, respectively.

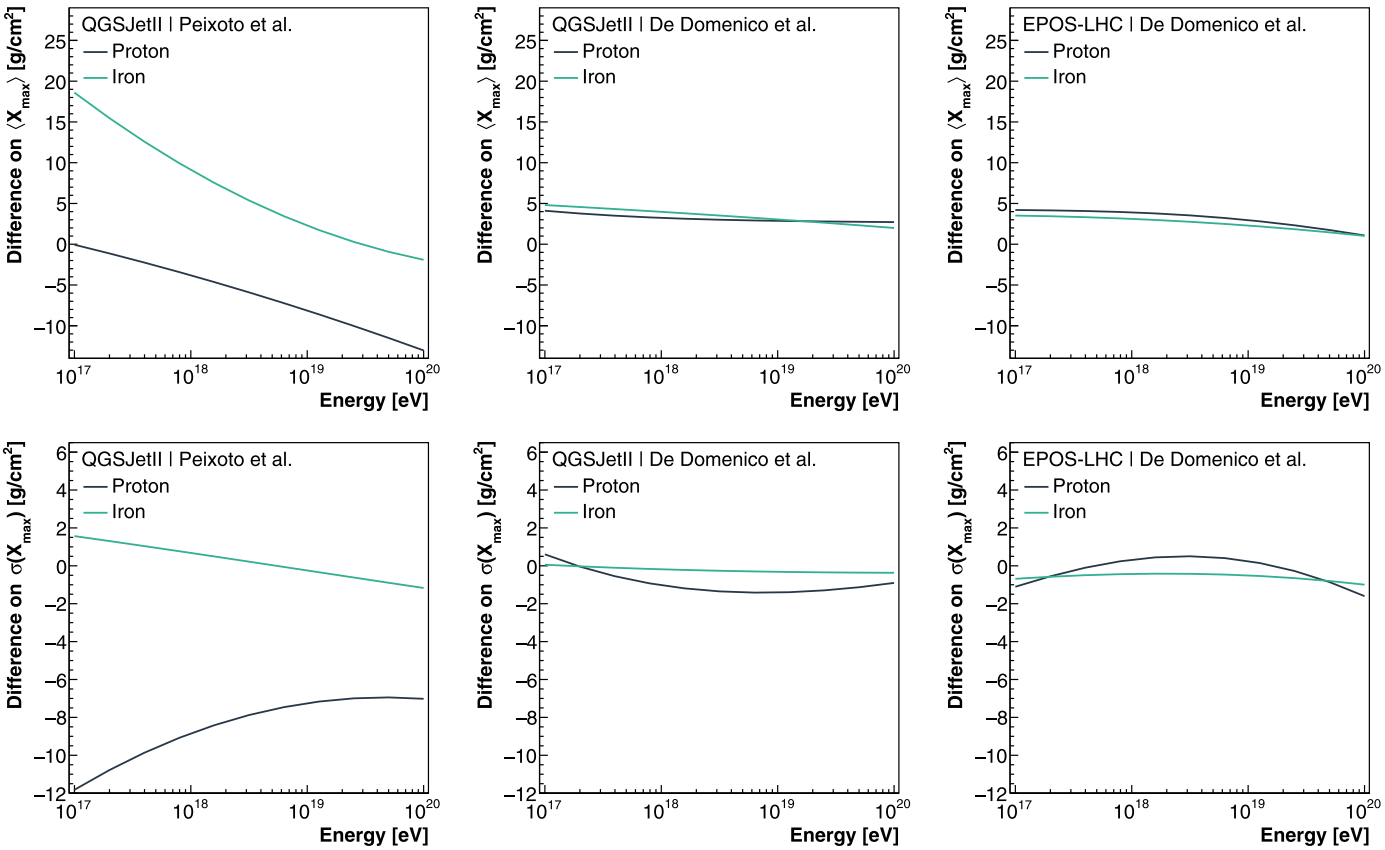

Fig. 5. Comparison between first (upper plots) and second (lower plots) moments of parametrized X_{max} distributions with parametrizations from [6] (left) and [7] (middle and right). Results are shown only for parametrizations based on simulations with the same hadronic model, which is indicated in the top-left corner of each plot.

4. Fitting the X_{max} distributions

The X_{max} distributions of each combination of primary mass, energy and hadronic interaction model are fitted using the three functions presented in the previous sections. The best description of the X_{max} distributions is achieved by searching for the three parameters in each function which resulted in the maximum likelihood. The X_{max} distributions are not binned (unbinned fit). The Minuit [22] library available within the ROOT analysis framework [23] is used in the fitting procedure.

Examples of fitting results are presented in Fig. 2 for simulations obtained with QGSJetII.04 at an energy of 10^{20} eV. Only for illustration purposes, the distributions are binned in intervals of $10\,g/cm^2$. Note the logarithmic scale in the y-axis. The primary particle is indicated at the top-right corner of each plot. Fit functions are shown as colored solid lines, while the simulated X_{max} distribution is shown as circular dots. The bottom panels show the deviation (pull values) of each fitted function to the simulated point, defined as the difference between the function and the point divided by the statistical uncertainty of the point.

Fig. 2 shows that the EMG distribution is not able to describe the simulated distributions for small and large X_{max} values. No clear preference between the GMB and the LOG distributions is seen.

Values of the Akaike Information Criterion (AIC) for each case are shown in Table 1. Since the absolute value of the AIC has no meaning in this unbinned fit, the values shown are relative (Δ_i) to the smallest AIC in each case. Reader is referred to Appendix A for the definition of AIC.

The first notable fact in Table 1 is that the EMG distribution has the worst AIC value for every primary, energy and hadronic interaction model except one: silicon - 10^{20} eV - EPOS-LHC for which the AIC value is slightly better than the GMB fit. This makes the EMG distribution the worst selection among the three functions described here to describe X_{max} distributions of single primary particles.

The GMB and LOG distributions represent similar good description of the X_{max} distributions. The LOG distribution performs better for low mass primaries (proton and carbon) and the GMB distribution performs better for heavier primaries (silicon and iron). But the differences between the quality of the fit of GMB and LOG are only marginal.

4.1. Mixed composition

The X_{max} distributions of events with energy between 10^{18} eV and 10^{19} eV measured by the Pierre Auger Observatory can be better described by a combination of primary particles rather than a pure element [5,24]. Therefore in the analysis of these distributions it is important that the used function is able to describe also mixes compositions instead of only pure samples. In this section, the proposed functions are going to be tested against a mix of primary particles. The simulated X_{max} distributions are mixed following the fraction which best describes the data of the Pierre Auger Observatory as shown in Ref. [5] and Table 2. Fig. 3 shows two examples of mixtures at 10^{18} eV for EPOS-LHC and Sibyll2.3c models. Distributions are binned in intervals of $10\,g/cm^2$ for illustration purposes. The resulting mixture is fitted by the three proposed functions.

The Δ_i values for the fits are shown in Table 3. The GMB shows an overall better description of the distributions, losing only marginally to the EMG for EPOS-LHC at 10^{18} eV and LOG for Sibyll2.3c at 10^{19} eV.

5. Parametrization of X_{max} distributions as a function of energy and mass

The three proposed functions are used to fit the simulated X_{max} distributions for proton, carbon, silicon and iron with energies ranging from 10^{17} eV to 10^{20} eV in steps of 1 in $\log_{10}(E_0/\text{eV})$. Each function has three parameters as shown in Section 3. These parameters are modeled as a function of primary energy and mass. The proposed functional form is:

$$\theta(E_0, A) = a(A) + b(A)\log_{10}E_0 + c(A)(\log_{10}E_0)^2\,, \tag{7}$$

where

$$\begin{aligned} a(A) &= a_0 + a_1\log_{10}A + a_2(\log_{10}A)^2\,,\\ b(A) &= b_0 + b_1\log_{10}A + b_2(\log_{10}A)^2\,,\\ c(A) &= c_0 + c_1\log_{10}A + c_2(\log_{10}A)^2\,. \end{aligned} \tag{8}$$

Values obtained for the parameters a_i, b_i and c_i and their corresponding statistical uncertainties are found in Appendix B. Note that a value of zero in Table 4 means the inclusion of that parameters leads to a worse fit of the simulated distribution.

The error caused by the use of Eqs. (7) and (8) to calculate the parameters as a function of mass and energy was determined by evaluating the differences between the first and second moments of the parametrized distributions and the simulated distributions for each mass and energy. Results are shown as histograms in Fig. 4. The upper plots show the deviations on the first moment of the X_{max} distributions for each hadronic interaction model indicated in the top left corner of each box. The lower plots show the differences for the second moment of the X_{max} distributions. The largest difference between the proposed parametrization and the simulations is 2 g/cm^2 for the first moment and 3 g/cm^2 for the second moment.

Ref. [6] (Peixoto et al.) and [7] (de Domenico et al.) also proposed parametrizations of the X_{max} distributions. The comparison of these parametrizations with the ones presented here is meaningful only when the same hadronic interaction models was used. Fig. 5 compares first and second moments of the previously proposed parametrizations with the ones presented in this paper for simulations performed with QGSJetII.04 and EPOS-LHC hadronic interaction models. Previous parametrizations differs on the $\langle X_{max}\rangle$ by as much as 20 g/cm^2 and on RMS(X_{max}) by as much as 12 g/cm^2.

6. Conclusion

The X_{max} distribution is of great importance in UHECR studies and some functional forms have been proposed to describe it. In this paper, for the first time, three functions have been selected, explained, and compared to simulated X_{max} distributions. A large sample of showers (10^6) has been generated for each point in a wide range of parameters space: four atomic nuclei have been considered: proton, carbon, silicon and iron with energies ranging from 10^{17} eV to 10^{20} eV and three hadronic interaction models: EPOS-LHC, QGSJetII.04, and Sibyll2.3c. The primaries have also been mixed with fractions given by the best description of the Pierre Auger Observatory data.

In total three functions have been tested. Two were taken from the literature: Generalized Gumbel distribution [7] and Exponentially Modified Gaussian distribution [6], and, in addition, the Log-normal distribution has been used as well. All functions have three parameters. The parameters have been fitted to the simulated X_{max} distributions and the result is shown in table 4. The excellent quality of the fits allows the prediction of the first and second moments of the X_{max} distribution with a maximum error of 2 and 3 g/cm^2, respectively.

The function that shows an overall best description of the X_{max} distributions is the Generalized Gumbel distribution, followed by the Log-normal distribution. In some specific cases, the Log-normal distribution has a slightly better fit to the simulated distributions. However, in many other cases, the Generalized Gumbel distribution is much better than the Log-normal distribution. In studies of measured X_{max} distribution, it is not possible to know beforehand which is the primary particle. Moreover, the hadronic interaction model dependence of the analysis must be minimized. For those reasons, the Generalized Gumbel distribution is proposed here as the best choice because it shows the best description for most of the cases. The Exponentially Modified Gaussian distribution is the one which most poorly describes the simulated showers among the three functions studied for almost all cases.

Acknowledgments

Authors acknowledge FAPESP Project 2015/15897-1. VdS acknowledge CNPq. This study was financed in part by the Coordenação de Aperfeiçoamento de Pessoal de Nível Superior - Brasil (CAPES) - Finance Code 001. Authors acknowledge the National Laboratory for Scientific Computing (LNCC/MCTI, Brazil) for providing HPC resources of the SDumont supercomputer (http://sdumont.lncc.br). Thanks to Roger Clay and Michael Unger for reading and commenting the manuscript.

Appendix A. Akaike information criterion

The Akaike Information Criterion (AIC) [25,26] is defined as

$$\text{AIC} = 2k - 2\log\left(\mathcal{L}(\vec{\theta})\right), \tag{9}$$

where k is the number of fitted parameters and $\mathcal{L}$ is the maximized value of the likelihood function for the fitted parameter set $\vec{\theta}$. Given a set of models, the AIC criterion calculates the relative quality of each model in describing the data. From its definition, it is expected that the model with the smaller AIC value in a set is the one that has the smallest statistical distance to the data set used to fit model parameters.

Given that the absolute values of AIC carry no meaning and depend on the sample size, in this paper, model selection is based on the computation of the so-called Akaike differences (Δ_i), or relative AIC. These are defined as the AIC values of each model with respect to the model with the smaller AIC, that is,

$$\Delta_i = \text{AIC}_i - \text{AIC}_{\text{min}}\,. \tag{10}$$

The relative AIC values provide a strong support for model selection in terms of information theory. A value of $\Delta_i = 0$ means that a model is preferred among the set to describe fitted data. Small values of Δ_i indicate that this model is not the best for the particular data set, but is competitive and should not be discarded. Large values of Δ_i, on the other hand provide a strong argument against the ith model.

Appendix B. Parameter values

In Section 5 a method to describe the evolution of X_{max} distributions energy and mass is proposed in terms of Eqs. (7) and (8). This appendix compiles fitted parameters a_i, b_i and c_i of Eq. (8). Table 4 shows the values of fitted parameters whereas Table 5 shows their statistical uncertainties.

Table 4
Fitted parameters of Eq. (8) describing the evolution of X_{max} distributions as a function of primary energy and mass. Details in Section 5.

Exponentially modified gaussian									
QGSJetII.04	a_1	a_2	a_3	b_1	b_2	b_3	c_1	c_2	c_3
λ	391.6	−354.39	97.21	−31.848	31.654	−9.193	0.7526	−0.7955	0.2407
μ	−544.3	−152.02	−33.81	76.067	17.644	1.251	−0.4692	−0.5436	0
σ	44.9	−2.7	−4.35	−1.03	0.25	0	0	0	0
EPOS-LHC	a_1	a_2	a_3	b_1	b_2	b_3	c_1	c_2	c_3
λ	478.15	−576.14	204.98	−41.845	55.499	−20.799	1.0336	−1.4561	0.5626
μ	−757.99	−133.86	−32.58	99.306	15.373	0.914	−1.053	−0.4468	0
σ	239.07	−50.64	−18.25	−23.27	7.411	0.778	0.624	−0.2493	0
Sibyll2.3c	a_1	a_2	a_3	b_1	b_2	b_3	c_1	c_2	c_3
λ	389.8	−199.83	3.46	−31.021	16.28	0.168	0.7148	−0.3993	0
μ	−784.86	−3.33	−15.91	100.993	−0.983	0.433	−1.0377	0	0
σ	80.76	8.01	−10.2	−4.684	−0.815	0.526	0.0988	0	0
Generalized Gumbel									
QGSJetII.04	a_1	a_2	a_3	b_1	b_2	b_3	c_1	c_2	c_3
λ	1.24	11.74	−6.85	−0.088	−1.393	0.855	0.00302	0.04702	−0.02778
μ	−368.79	−238.75	−32.14	61.443	25.159	1.255	−0.1138	−0.7326	0
σ	55.9	20.9	−15.9	−1.08	0.32	0	0	0	0
EPOS-LHC	a_1	a_2	a_3	b_1	b_2	b_3	c_1	c_2	c_3
λ	4.34	−4.84	4.83	−0.4489	0.427	−0.314	0.01325	0	0
μ	−565.11	−211.43	−36.32	82.199	22.453	1.288	−0.6189	−0.6475	0
σ	377.3	324	−228.1	−37.67	−29.63	22.436	1.0216	0.7366	−0.5955
Sibyll2.3c	a_1	a_2	a_3	b_1	b_2	b_3	c_1	c_2	c_3
λ	0.02	0.16	0.11	0.038	0.014	0	0	0	0
μ	−537.61	−131.99	−19.68	78.952	11.515	0.731	−0.4886	−0.3366	0
σ	60	24	−17	−1.06	−1.5	0.78	0	0	0
Log-normal									
QGSJetII.04	a_1	a_2	a_3	b_1	b_2	b_3	c_1	c_2	c_3
μ	8.974	−0.84	0.317	−0.3978	0.0684	−0.0344	0.0096	0	0
σ	0.532	−0.08	−0.04	−0.0065	−0.01	0.0066	0	0	0
m	−1152.4	64.9	−50	129.78	−8.74	4.65	−1.846	0	0
EPOS-LHC	a_1	a_2	a_3	b_1	b_2	b_3	c_1	c_2	c_3
μ	14.745	−2.04	0.043	−1.058	0.2761	−0.023	0.02806	−0.00752	0
σ	0.034	−0.31	0.0043	0.0544	−0.00104	0.00582	−0.001768	0	0
m	−1745.1	−168.6	23.9	198.41	4.04	0.64	−3.738	0	0
Sibyll2.3c	a_1	a_2	a_3	b_1	b_2	b_3	c_1	c_2	c_3
μ	5.78	−0.03	−0.059	−0.0422	−0.0094	0	0	0	0
σ	0.551	−0.151	0.014	−0.0086	0.0026	0	0	0	0
m	−1085.3	−66.4	24.2	120.33	2.68	−1.38	−1.493	0	0

Table 5
Statistical uncertainty on fitted parameters of Eq. (8) describing the evolution of X_{max} distributions as a function of primary energy and mass. Details in Section 5.

Exponentially modified gaussian									
QGSJetII.04	a_1	a_2	a_3	b_1	b_2	b_3	c_1	c_2	c_3
λ	0.1	0.08	0.05	0.006	0.004	0.003	0.0003	0.0002	0.0001
μ	0.1	0.08	0.05	0.006	0.005	0.003	0.0003	0.0002	0
σ	0.4	0.3	0.03	0.02	0.02	0	0	0	0
EPOS-LHC	a_1	a_2	a_3	b_1	b_2	b_3	c_1	c_2	c_3
λ	0.08	0.06	0.04	0.005	0.003	0.002	0.0002	0.0002	0.0001
μ	0.08	0.06	0.04	0.005	0.004	0.002	0.0002	0.0002	0
σ	0.05	0.04	0.02	0.003	0.002	0.001	0.0002	0.0001	0
Sibyll2.3c	a_1	a_2	a_3	b_1	b_2	b_3	c_1	c_2	c_3
λ	0.1	0.08	0.04	0.006	0.004	0.002	0.0003	0.0002	0
μ	0.1	0.07	0.04	0.006	0.004	0.002	0.0003	0	0
σ	0.07	0.05	0.03	0.004	0.003	0.002	0.0002	0	0

(*continued on next page*)

Table 5 (*continued*)

Generalized Gumbel									
QGSJetII.04	a_1	a_2	a_3	b_1	b_2	b_3	c_1	c_2	c_3
λ	0.01	0.03	0.02	0.0008	0.002	0.001	0.00003	0.00009	0.00006
μ	0.09	0.06	0.04	0.005	0.004	0.002	0.0003	0.0002	0
σ	0.9	0.8	0.1	0.05	0.04	0	0	0	0
EPOS-LHC	a_1	a_2	a_3	b_1	b_2	b_3	c_1	c_2	c_3
λ	0.01	0.04	0.03	0.0009	0.002	0.001	0.00003	0	0
μ	0.07	0.05	0.03	0.004	0.003	0.002	0.0002	0.0001	0
σ	0.2	0.2	0.1	0.02	0.01	0.008	0.0007	0.0006	0.0004
Sibyll2.3c	a_1	a_2	a_3	b_1	b_2	b_3	c_1	c_2	c_3
λ	0.03	0.04	0.007	0.001	0.002	0	0	0	0
μ	0.08	0.06	0.04	0.005	0.004	0.002	0.0002	0.0002	0
σ	1	3	2	0.06	0.1	0.08	0	0	0
Log-normal									
QGSJetII.04	a_1	a_2	a_3	b_1	b_2	b_3	c_1	c_2	c_3
μ	0.006	0.007	0.004	0.0004	0.0004	0.0002	0.00002	0	0
σ	0.007	0.02	0.01	0.0004	0.001	0.0006	0	0	0
m	0.7	0.8	0.5	0.05	0.04	0.03	0.002	0	0
EPOS-LHC	a_1	a_2	a_3	b_1	b_2	b_3	c_1	c_2	c_3
μ	0.006	0.007	0.004	0.0004	0.0004	0.0002	0.00002	0.00002	0
σ	0.002	0.001	0.0009	0.0001	0.00007	0.00005	0.000005	0	0
m	0.6	0.7	0.4	0.04	0.04	0.02	0.002	0	0
Sibyll2.3c	a_1	a_2	a_3	b_1	b_2	b_3	c_1	c_2	c_3
μ	0.02	0.02	0.002	0.0009	0.0008	0	0	0	0
σ	0.007	0.005	0.0007	0.0004	0.0003	0	0	0	0
m	0.6	0.5	0.3	0.04	0.03	0.02	0.002	0	0

References

[1] A. Aab, et al., Pierre Auger Collaboration, Phys. Rev. D 90 (12) (2014) 122005.
[2] R.U. Abbasi, et al., Telescope array collaboration, Astrophys. J. 858 (2) (2018) 76.
[3] V. de Souza, Pierre Auger and telescope array collaborations, PoS ICRC 2017 (522) (2018).
[4] S. Blaess, J.A. Bellido, B.R. Dawson, arXiv:1803.02520.
[5] J. Bellido, Pierre Auger Collaboration, PoS ICRC 2017 (506) (2018).
[6] C.J.T. Peixoto, V. de Souza, J.A. Bellido, Comparison of the moments of the X_{max} distribution predicted by different cosmic ray shower simulation models, Astropart. Phys. 47 (18) (2013).
[7] M. De Domenico, M. Settimo, S. Riggi, E. Bertin, Reinterpreting the development of extensive air showers initiated by nuclei and photons, JCAP 1307 (050) (2013).
[8] T. Bergmann, R. Engel, D. Heck, N.N. Kalmykov, S. Ostapchenko, T. Pierog, T. Thouw, K. Werner, One-dimensional hybrid approach to extensive air shower simulation, Astropart. Phys. 26 (2007) 420–432.
[9] R. Engel, D. Heck, T. Pierog, Extensive air showers and hadronic interactions at high energy, Annu. Rev. Nucl. Part. Sci. 61 (2011) 467–489.
[10] R.D. Parsons, C. Bleve, S.S. Ostapchenko, J. Knapp, Systematic uncertainties in air shower measurements from high-energy hadronic interaction models, Astropart. Phys. 34 (2011) 832–839.
[11] L.B. Arbeletche, V.P. Gonçalves, M.A. Muller, Investigating the influence of diffractive interactions on ultra - high energy extensive air showers, Int. J. Mod. Phys. A 33 (26) (2018) 1850153.
[12] T. Pierog, I. Karpenko, J.M. Katzy, E. Yatsenko, K. Werner, EPOS LHC: test of collective hadronization with data measured at the CERN large Hadron Collider, Phys. Rev. C. 92 (2015) 034906.
[13] S. Ostapchenko, Monte Carlo treatment of hadronic interactions in enhanced Pomeron scheme: QGSJET-II model, Phys. Rev. D. 83 (2011) 014018.
[14] A. Fedynitch, F. Riehn, R. Engel, T.K. Gaisser, T. Stanev, arXiv:1806.04140.
[15] C. Baus, R. Engel, T. Pierog, R. Ulrich, M. Unger, Proceedings of the 32nd ICRC.
[16] E.J. Gumbel, Statistics of Extremes, Dover Pub., 2004.
[17] E. Bertin, Phys. Rev. Lett. 95 (17) (2005) 170601.
[18] M. Clusel, E. Bertin, Global fluctations in physical systems: a subtle interplay between sum and extreme value statistics, Int. J. Mod. Phys. B 22 (20) (2008) 3313–3368.
[19] T. Antal, M. Droz, G. Györgyi, Z. Rácz, 1/f noise and extreme value statistics, Phys. Rev. Lett. 87 (24) (2001) 240601.
[20] J. Matthews, A Heitler model of extensive air showers, Astropart. Phys. 22 (2005) 387.
[21] S. Nadajarah, S. Kotz, The beta exponential distribution, Reliab. Eng. Syst. Safe 91 (6) (2006) 689–697.
[22] F. James, M. Roos, Minuit - a system for function minimization and analysis of the parameter errors and correlations, Comput. Phys. Commun. 10 (1975) 343.
[23] R. Brun, F. Rademakers, ROOT: an object oriented data analysis framework, Nucl. Instrum. Meth. A 389 (81) (1997).
[24] A. Aab, et al., Pierre Auger Collaboration, Phys. Rev. D 90 (12) (2014) 122006.
[25] H. Akaike, B.N. Petrov, F. Csaki, Information theory as an extension of the maximum likelihood principle, in: Proceedings of the International Symposium on Information Theory, second ed., Akademiai Kiado, Budapest, 1973.
[26] K.P. Burnham, D.R. Anderson, Model Selection and Inference: A Practical Information-Theoretical Approach, second ed., Springel-Verlag, New York, 1998.

6 PARAMETRIZATION OF THE ANGULAR DISTRIBUTION OF CHERENKOV LIGHT IN AIR SHOWERS

Parametrization of the angular distribution of Cherenkov light in air showers

Luan B. Arbeletche* and Vitor de Souza†

Instituto de Física de São Carlos, Universidade de São Paulo,

Av. Trabalhador São-carlense 400, São Carlos, Brasil.

Abstract

The Cherenkov light produced in air showers largely contributes to the signal observed in ground-based gamma-ray and cosmic-ray observatories. Yet, no description of this phenomenon is available covering both regions of small and large angles to the shower axis. To fill this gap, a parametrization of the angular distribution of Cherenkov photons is performed in terms of a physically-motivated parametric function. Model parameters are constrained using simulated gamma-ray and proton showers with energies in the TeV to EeV region. As a result, a new parametrization is obtained that improves the precision of previous works. Results presented here can be used in the reconstruction of showers with imaging Cherenkov telescopes as well as in the reconstruction of shower profiles with fluorescence detectors.

* luan.arbeletche@ifsc.usp.br

† vitor@ifsc.usp.br

I. INTRODUCTION

A large amount of Cherenkov light is produced in extensive air showers [1] and several experimental techniques have been proposed to explore this signal to study astroparticle physics. The generation of light in the cascade is highly dominated by electrons. The emission of Cherenkov light by relativistic electrons including geometry, intensity, and wavelength is explained by classical electrodynamics [2], which has been used as an inspiration for the development of robust detection techniques.

The total signal produced by all particles in the air shower evolves as the cascade deepens in the atmosphere. The correct description of this evolution is mandatory to extract physical results from measurements. This problem is common to all collaborations running ground-based detectors, including Imaging Atmospheric Cherenkov Telescopes (IACT) and Fluorescence Detectors (FD), and also to proposed space experiments. In particular, to reconstruct the properties of the primary particle, it is necessary to understand the properties of Cherenkov-light production in air showers, including the longitudinal distribution, the lateral distribution, and the angular distribution. In this paper, special attention is given to the description of the angular distribution of Cherenkov photons in air showers.

IACTs are of fundamental importance for the Very High Energy (VHE) gamma-ray astronomy ($E_0 > 100\,\mathrm{GeV}$). The identification and the reconstruction of the primary gamma-ray are done by interpreting the Cherenkov light detected by telescopes at ground. Current observatories [4–6] are equipped with some (≤ 5) telescopes with few degrees ($< 5^\circ$) of field of view installed hundred meters apart from each other. The Cherenkov Telescope Array (CTA) [7] is the next-generation IACT system presently under development. The CTA baseline design calls for 118 telescopes to be installed at two sites covering areas of $0.6\,\mathrm{km}^2$ in La Palma, Spain and $4\,\mathrm{km}^2$ in Paranal, Chile. The angular distribution of Cherenkov photons in an air shower determines the image shape detected by IACTs and is therefore a key aspect in many reconstruction techniques [8–10].

FDs have been long used to study Ultra-High Energy Cosmic Rays (UHERC) [11]. These telescopes have been optimized to measure the isotropic fluorescence light emitted by nitrogen molecules due to the passage of charged particles in the atmosphere. The telescopes in operation [12, 13] have large aperture ($\approx 30^\circ$) and cover a detection area of thousands km^2. The fluorescence and Cherenkov emission produce signals in the telescopes in the overlapping

wavelength band of 300-450 nm, making it impossible to separate their signals. Traditionally, Cherenkov light was considered as an unwanted noise in the FD measurements [13], but recently the Cherenkov light seen by FDs has been used as signal to detect showers with energies down to 2 PeV [14–16]. Direct Cherenkov light is also used to study UHECR with ground detectors [17, 18] and is proposed to be used as an important signal source in future space experiments [19]. The angular distribution of Cherenkov photons in an air shower is an important feature for all UHECR experiments because it determines the lateral spread of light and the balance between fluorescence and Cherenkov-light signals measured by the FDs, including large angles ($> 10°$) and great distances (several km) from the shower axis.

The number of Cherenkov photons produced in an air shower reaching a detector at a given distance from the shower axis can be calculated only if the angular distribution of photons is known. Reversely, the reconstruction of the primary particle properties is only possible if the measured amount of light in each detector is converted into the amount of light emitted by the particles in the shower. The angular distribution of Cherenkov photons is determined by the convolution of the longitudinal development of electrons[1], the energy distribution of electrons, the angular distribution of electrons, the scattering of electrons, the refractive index, the geomagnetic field effects, and the scattering of photons [20–24].

Influenced by the main techniques detecting Cherenkov light (IACT and FD), the study of the angular distribution of Cherenkov photons has been divided respectively in two regimes: (a) gamma-ray primaries, small angles $< 10°$, and TeV energies and (b) cosmic ray primaries, large angles $> 10°$, and highest energies (10^{17} eV). Experiments have measured the angular distribution of Cherenkov photons [25] in regime (b). Since the pioneering work [21], the angular distribution was simulated for regime (a) [8] and (b) [24, 26].

In this paper, the angular distribution of Cherenkov photons is simulated using the most updated simulation software and a new parametrization based on shower physics is proposed. The parametrization presented here improves the precision in the description of the angular distribution of Cherenkov light in comparison to models found in previous publications [8, 24, 26]. Beside the needed update of the parametrizations concerning the new shower models made available after the previous works, this paper aims at the improvement of the precision requested by the new generation of experiments [7, 19] and at the refinement demanded by the new uses of Cherenkov light as the main signal source in FD analyses [15, 16]. Moreover,

[1] The term *electrons* here refer to both electrons and positrons.

a unified view of the two regimes is presented for the first time.

This paper is organized as follows. In section II, an exact model to compute the angular distribution of Cherenkov photons is derived. This model is simplified in section III to obtain a simple form in terms of free parameters. The parameters of the model are constrained by Monte Carlo simulations in section IV. A discussion of the results and a comparison to previous works are presented in section V and some final remarks are given in section VI.

II. EXACT MODEL FOR THE CHERENKOV LIGHT ANGULAR DISTRIBUTION

A mathematical description of the number of Cherenkov photons emitted in a given angular interval as a function of the shower development in the atmosphere, $\mathrm{d}^2N_\gamma/\mathrm{d}\theta\,\mathrm{d}X$, is presented in this section. Each physical quantity relevant to this description is identified and explained below.

Electrons are responsible for over 98% of the Cherenkov-photon content in a shower [24]. Therefore it is assumed in this study that all photons are emitted by electrons. Figure 1 depicts the composition of angles determining the final angular distribution of Cherenkov photons. Shown is that an electron emitted during the shower development is subject to scattering in the atmosphere and its trajectory forms an angle θ_p with the shower axis. Such an electron will emit Cherenkov photons in a cone of half-aperture angle θ_em around its propagation path. The two angles θ_em and ϕ_em (measured in a plane perpendicular to the moving electron track) determine the direction of the emitted photon. Finally, the emitted photon forms an angle θ with the shower axis.

It is the interplay between the Cherenkov emission angle θ_em and the scattering angle of electrons θ_p that determines the distribution of the resulting Cherenkov-photon angle θ. In the beginning of the shower, most electrons move parallel to the shower axis, therefore $\theta_\mathrm{p} \approx 0 \Rightarrow \theta \approx \theta_\mathrm{em}$. The angle θ_em, in its turn, is an increasing function of the atmospheric depth and reaches a maximum value of about 1.5° at sea level. As the cascade develops further, electrons scatter multiple times, increasing the fraction of particles with large θ_p values. Indeed, the effect of multiple scattering generates electrons with $\theta_\mathrm{p} > \theta_\mathrm{em}$ and therefore $\theta > \theta_\mathrm{em}$. As a consequence, for $\theta_\mathrm{p} \gg \theta_\mathrm{em} \Rightarrow \theta \approx \theta_\mathrm{p}$, so that the angular distribution of Cherenkov photons approximately reproduces the angular distribution of electrons in the

shower.

The number of Cherenkov photons emitted by electrons with energy E and angle $\theta_{\rm p}$ in a shower per interval of depth $\mathrm{d}X$ is given by[2]

$$\mathrm{d}N_\gamma = N_e(s)\,\frac{\mathrm{d}N_e}{\mathrm{d}E}(E,s)\,\mathrm{d}E\,\frac{\mathrm{d}N_e}{\mathrm{d}\theta_{\rm p}}(\theta_{\rm p},E)\,\mathrm{d}\theta_{\rm p}\,Y_\gamma(E,h)\,\sec\theta_{\rm p}\,\mathrm{d}X\,\frac{\mathrm{d}\phi_{\rm em}}{2\pi}\,, \tag{1}$$

where s is the shower age[3] and h is the emission height above sea level. $N_e(s)$ is the total number of electrons, $\mathrm{d}N_e/\mathrm{d}E$ is the energy distribution of electrons, and $\mathrm{d}N_e/\mathrm{d}\theta_{\rm p}$ is the angular distribution of electrons. The function $Y_\gamma(E,h)$ represents the number of photons emitted by one electron per depth interval (yield) and the factor of $\sec\theta_{\rm p}$ takes into account the correction in the length of the electron track due to its inclined trajectory. Photons are uniformly distributed in $\phi_{\rm em}$ (factor of $1/2\pi$). According to reference [24], $Y_\gamma(E,h)$ is given by

$$Y_\gamma(E,h) \approx 4\pi\,\alpha\,\frac{n(h)-1}{\rho(h)}\left(\frac{1}{\lambda_1}-\frac{1}{\lambda_2}\right)\left(1-\frac{E_{\rm thr}^2(h)}{E^2}\right)\,, \tag{2}$$

in which $\alpha \approx 1/137$ is the fine-structure constant, $n(h)$ is the refractive index of the medium, $\rho(h)$ is the atmospheric density, and λ_i the wavelength interval of the emitted photons. The threshold energy $E_{\rm thr}$ for an electron to produce Cherenkov light is $E_{\rm thr}(h) = m_e c^2/\sqrt{1-n^{-2}(h)}$, where m_e is the electron rest mass.

The dependency of $\mathrm{d}N_\gamma$ on the angle between the Cherenkov photon and the shower axis directions, θ, is found after a change of variable from $\phi_{\rm em}$ to θ (see Figure 1)

$$\cos\theta = \cos\theta_{\rm p}\cos\theta_{\rm em} - \sin\theta_{\rm p}\sin\theta_{\rm em}\cos\phi_{\rm em}\,, \tag{3}$$

which leads to

$$\begin{aligned}\mathrm{d}\phi_{\rm em} &= 2\left|\frac{\mathrm{d}\phi_{\rm em}}{\mathrm{d}\theta}\right|\mathrm{d}\theta \\ &= \frac{2\,\sin\theta\,\mathrm{d}\theta}{\sqrt{\sin^2\theta_{\rm p}\sin^2\theta_{\rm em}-(\cos\theta_{\rm p}\cos\theta_{\rm em}-\cos\theta)^2}}\,,\end{aligned} \tag{4}$$

[2] The dependency on the primary particle energy (E_0) is omitted here for brevity and discussed in terms of simulated showers in the following sections. For the purpose of this section, E_0 may be regarded as fixed.

[3] $s = 3X/(X+2X_{\rm max})$ where $X_{\rm max}$ is the depth in which the shower reaches the maximum number of particles.

in which a factor of 2 was added to account for the fact that there are always two values of $\phi_{\rm em}$ resulting in the same value of θ (see Figure 2). The half-aperture angle of the Cherenkov radiation cone, $\theta_{\rm em}$, relates to the particle velocity β by the usual expression

$$\cos\theta_{\rm em} = \frac{1}{\beta\, n}\ . \tag{5}$$

Substitution of Equation (4) into Equation (1) gives

$$\begin{aligned} {\rm d}N_\gamma = & N_e(s)\,\frac{{\rm d}N_e}{{\rm d}E}(E,s)\,{\rm d}E\,\frac{{\rm d}N_e}{{\rm d}\theta_{\rm p}}(\theta_{\rm p},E)\,{\rm d}\theta_{\rm p}\,Y_\gamma(E,h)\,\sec\theta_{\rm p}\,{\rm d}X \\ & \times\ \frac{1}{\pi}\frac{\sin\theta\,{\rm d}\theta}{\sqrt{\sin^2\theta_{\rm p}\sin^2\theta_{\rm em}-(\cos\theta_{\rm p}\cos\theta_{\rm em}-\cos\theta)^2}}\ . \end{aligned} \tag{6}$$

Finally, to obtain the desired angular distribution of Cherenkov photons, ${\rm d}^2N_\gamma/{\rm d}\theta\,{\rm d}X$, it is necessary to integrate Equation (6) over all possible values of electron energies E and angles $\theta_{\rm p}$. Integration over E must assert that relation (5) is satisfied, therefore E takes values for which $E > E_{\rm thr}(h)$. Limits of the integral over electron angles $\theta_{\rm p}$ should take only values that contribute to θ. From Figure 2 and Equation (3), it is found that this interval is $|\theta-\theta_{\rm em}| < \theta_{\rm p} < \theta+\theta_{\rm em}$. Thus, the exact angular distribution of Cherenkov photons is given by

$$\begin{aligned} \frac{{\rm d}^2N_\gamma}{{\rm d}\theta\,{\rm d}X}(\theta,s,h) = & \frac{1}{\pi}\,N_{\rm e}(s)\,\sin\theta\int_{E_{\rm thr}(h)}^{\infty}{\rm d}E\,Y_\gamma(E,h)\,\frac{{\rm d}N_{\rm e}}{{\rm d}E}(E,s) \\ & \times\int_{|\theta-\theta_{\rm em}|}^{\theta+\theta_{\rm em}}\frac{{\rm d}N_e}{{\rm d}\theta_{\rm p}}(\theta_{\rm p},E)\,\frac{{\rm d}\theta_{\rm p}}{\cos\theta_{\rm p}\sqrt{\sin^2\theta_{\rm p}\sin^2\theta_{\rm em}-(\cos\theta_{\rm p}\cos\theta_{\rm em}-\cos\theta)^2}}\ . \end{aligned} \tag{7}$$

III. APPROXIMATED MODEL FOR THE CHERENKOV LIGHT ANGULAR DISTRIBUTION

In this section, an approximation of the above equation is proposed to obtain a simpler yet meaningful description of the angular distributions of Cherenkov light. The idea is to summarize the angular distribution to a minimum set of parameters, allowing its parametrization.

First, note that the integration in $\theta_{\rm p}$ is done in a very narrow interval given that $\theta_{\rm em} <$

1.5°. Therefore it is possible to consider that $\sec\theta_{\rm p}\,{\rm d}N_e/{\rm d}\theta_{\rm p}$ varies little within integration limits and, in a first approximation, can be taken as constant and calculated in the mean angle $\langle\theta_{\rm p}\rangle$ of the range in between the integration limits

$$\begin{aligned}\frac{{\rm d}^2N_\gamma}{{\rm d}\theta\,{\rm d}X}(\theta,s,h) \approx \frac{1}{\pi}\,N_{\rm e}(s)\,\sin\theta \int_{E_{\rm thr}(h)}^{\infty}{\rm d}E\;Y_\gamma(E,h)\,\frac{{\rm d}N_{\rm e}}{{\rm d}E}(E,s) \\ \times\,\frac{1}{\cos\langle\theta_{\rm p}\rangle}\frac{{\rm d}N_e}{{\rm d}\theta_{\rm p}}(\langle\theta_{\rm p}\rangle,E) \\ \times\int_{|\theta-\theta_{\rm em}|}^{\theta+\theta_{\rm em}}\frac{{\rm d}\theta_{\rm p}}{\sqrt{\sin^2\theta_{\rm p}\sin^2\theta_{\rm em}-(\cos\theta_{\rm p}\cos\theta_{\rm em}-\cos\theta)^2}}\,,\end{aligned} \tag{8}$$

where

$$\langle\theta_{\rm p}\rangle = \begin{cases}\theta_{\rm em}\,, & \text{if}\quad \theta\le\theta_{\rm em}\\ \theta\,, & \text{if}\quad \theta>\theta_{\rm em}\end{cases}\,. \tag{9}$$

The remaining integral over $\theta_{\rm p}$ is a complete elliptic integral of the first kind and can be approximated by a logarithmic function

$$\begin{aligned}\int_{|\theta-\theta_{\rm em}|}^{\theta+\theta_{\rm em}}\frac{{\rm d}\theta_{\rm p}}{\sqrt{\sin^2\theta_{\rm p}\sin^2\theta_{\rm em}-(\cos\theta_{\rm p}\cos\theta_{\rm em}-\cos\theta)^2}} \approx \\ \frac{1}{\sin\langle\theta_{\rm p}\rangle}\begin{cases}\pi-\log\left(1-\frac{\theta}{\theta_{\rm em}}\right)\,, & \text{if}\quad \theta\le\theta_{\rm em}\\ \pi-\log\left(1-\frac{\theta_{\rm em}}{\theta}\right)\,, & \text{if}\quad \theta>\theta_{\rm em}\end{cases}\,.\end{aligned} \tag{10}$$

The abbreviation below is introduced

$$I(\theta,\theta_{\rm em},E) = \frac{1}{\sin\langle\theta_{\rm p}\rangle}\begin{cases}\pi-\log\left(1-\frac{\theta}{\theta_{\rm em}}\right)\,, & \text{if}\quad \theta\le\theta_{\rm em}\\ \pi-\log\left(1-\frac{\theta_{\rm em}}{\theta}\right)\,, & \text{if}\quad \theta>\theta_{\rm em}\end{cases}\,, \tag{11}$$

and by noting that $\cos\theta_{\rm em} = 1/\beta n$ rapidly converges to $1/n$ as the electron energy increases, it is reasonable to assume that $\cos\theta_{\rm em} = 1/n$ for all electrons. With this assumption the function $I(\theta,\theta_{\rm em},E)\sim I(\theta,\theta_{\rm em}) = I(\theta,h)$ becomes independent of the electron energy[4]

$$\begin{aligned}\frac{{\rm d}^2N_\gamma}{{\rm d}\theta\,{\rm d}X}(\theta,s,h) \approx \frac{1}{\pi}\,N_{\rm e}(s)\,\sin\theta\,I(\theta,h) \\ \times\int_{E_{\rm thr}(h)}^{\infty}{\rm d}E\;Y_\gamma(E,h)\;\frac{{\rm d}N_{\rm e}}{{\rm d}E}(E,s)\;\frac{1}{\cos\langle\theta_{\rm p}\rangle}\frac{{\rm d}N_e}{{\rm d}\theta_{\rm p}}(\langle\theta_{\rm p}\rangle,E)\,.\end{aligned} \tag{12}$$

[4] From now on $\theta_{\rm em} = \arccos(1/n)$.

The validity of the approximations done until here were tested using Monte Carlo simulations of air showers and the results shown in Appendix A.

The remaining integral over electron energies,

$$\int_{E_{\rm thr}(h)}^{\infty} {\rm d}E\; Y_\gamma(E,h)\; \frac{{\rm d}N_{\rm e}}{{\rm d}E}(E,s) \frac{1}{\cos\langle\theta_{\rm p}\rangle} \frac{{\rm d}N_e}{{\rm d}\theta_{\rm p}}(\langle\theta_{\rm p}\rangle, E)\;, \tag{13}$$

has been studied before in references [24, 26]. A parametric form to describe this quantity is proposed here

$$K(\theta,s,h) = C\,\langle\theta_{\rm p}\rangle^{\nu-1} {\rm e}^{-\langle\theta_{\rm p}\rangle/\theta_1} \left(1+\epsilon\,{\rm e}^{\langle\theta_{\rm p}\rangle/\theta_2}\right)\;, \tag{14}$$

where ν, θ_1, θ_2, and ϵ are parameters varying with shower age, height (or refractive index), and, possibly, the primary energy. The constant C is intended to normalize Equation (14) according to Equation (13). In the next section the parameters of this function are going to be studied and the quality of the description is going to be tested. The approximated model is summarized as

$$\frac{{\rm d}^2 N_\gamma}{{\rm d}\theta\;{\rm d}X}(\theta,s,h) = \frac{1}{\pi}\, N_{\rm e}(s)\;\sin\theta\, I(\theta,h)\, K(\theta,s,h). \tag{15}$$

IV. PARAMETRIZATION OF THE CHERENKOV LIGHT ANGULAR DISTRIBUTION

Monte Carlo simulations of air showers are done using the CORSIKA 7.6900 package [27]. Gamma-ray and proton showers are simulated with energies between 100 GeV and 1 EeV in intervals of 1 in $\log_{10}(E_0/{\rm eV})$. For each combination of primary type and energy, at least 120 showers are simulated. Simulations are performed for vertical showers and showers inclined at 20°. QGSJETII.04 [28] and URQMD [29] are used as high- and low-energy hadronic interaction models, respectively. The U.S. standard atmosphere model is used in the simulations and the refractive index is considered to be independent of the wavelength ($180\,{\rm nm} \leq \lambda \leq 700\,{\rm nm}$) of the emitted photons. Cherenkov photons are produced in bunches of maximum five. The COAST option is used to store the angle between the Cherenkov photons and the shower axis directions, θ. $X_{\rm max}$, which is used to compute the shower age, is extracted from the longitudinal development of charged particles by fitting a Gaisser-Hillas function [30].

The approximated model summarized in Equation (15) suggests that the angular distri-

bution of Cherenkov photons should vary with shower age and atmospheric height. Both dependencies are made clear in the upper plots of Figure 3, where the angular distribution of Cherenkov photons of five randomly chosen gamma-ray-induced air showers at different values of s and h are compared. From the cascade theory [31–33], the angular distributions of Cherenkov light in gamma-ray showers are expected to be independent of the primary particle energy and this is confirmed in the bottom-left plot of Figure 3. In the case of proton showers, some dependency on the primary energy is observed in the bottom-right plot of the same figure. These plots also reiterate the fact that distributions with common age, height, primary type, and primary energy are similar.

Taking this dependency into account, the angular distribution of Cherenkov photons in a given interval with mean age $\bar{s}$ and height $\bar{h}$ in a shower of energy E_0 can be described by

$$\frac{\mathrm{d}N_\gamma}{\mathrm{d}\theta}(\theta, \bar{s}, \bar{h}, E_0) = N \, \sin\theta \, I(\theta, \bar{h}) \, K(\theta, \bar{s}, \bar{h}, E_0) \,, \tag{16}$$

in which N (different from $N_e(s)$) is a normalization constant which depends on the parameters of $K(\theta, \bar{s}, \bar{h}, E_0)$.

The parameters of $K(\theta, \bar{s}, \bar{h}, E_0)$ are considered to be

$$\begin{aligned}
\nu(s, n) &= p_{0,\nu} \, (n-1)^{p_{1,\nu}} + p_{2,\nu} \log(s) \,, \\
\theta_1(s, n, E_0) &= p_{0,\theta_1} \, (n-1)^{p_{1,\theta_1}} \, (E_0/\mathrm{TeV})^{p_{2,\theta_1}} + p_{3,\theta_1} \log(s) \,, \\
\theta_2(s, n) &= \theta_1(s, n) \, (p_{0,\theta_2} + p_{1,\theta_2} s) \,, \\
\epsilon(E_0) &= p_{0,\epsilon} + p_{1,\epsilon} \, (E_0/\mathrm{TeV})^{p_{2,\epsilon}} \,.
\end{aligned} \tag{17}$$

The coefficients $p_{i,\mu}$ are the parameters of the model to be fitted. In these equations, the dependence in height, h, was changed by the dependence in the refractive index, n, to make the parametrization independent of the atmospheric model used in the simulations.

The simulated angular distributions of Cherenkov photons are fitted with this model. For that, a multinomial likelihood function (L_{MLE}) is built taking into account every simulated distribution from shower ages in the interval $0.8 \leq s \leq 1.2$. A single value of refractive index n is associated with each distribution according to the emission height. Histograms are weighted by the inverse of the primary energy in TeV, so the contribution from showers of distinct energies to L_{MLE} are of the same order of magnitude. Gamma-ray and proton

showers are fit separately, as distributions strongly depend on the primary particle type in lower energies. All coefficients $p_{i,\mu}$ are allowed to vary in the fit procedure. In the case of gamma showers, however, the energy dependency is dropped (p_{2,θ_1}, $p_{1,\epsilon}$, $p_{2,\epsilon} = 0$). Fitted values of $p_{i,\mu}$ and their associated confidence intervals are found in Tables I and II.

V. RESULTS

In this section, the parametrization proposed in the previous section is compared to the Monte Carlo distributions and to previous works. Figure 4 shows the simulated angular distribution of Cherenkov photons in comparison to four models for one single gamma-ray (upper panel) and one single proton shower (lower panel). The ability of the presented parametrization to describe the simulated data both around the peak of the distributions and at the small and large θ regions is evident in this figure. Predictions from the models presented in Refs. [24, 26] are shown in the region $\theta > 5^\circ$ only, for which they are defined.

Figure 5 shows the overall quality of the models by comparing their average relative deviation to the simulated distributions for four combinations of primary type and energy. Three shower ages ($s = 0.8$, 1.0, and 1.2) are shown. It is clear that the model proposed here has many advantages. The model presents the smaller deviation from the simulations for a large angular range. For gamma-ray showers, the deviation is very small ($< 5\%$) for angles smaller than 25°. For proton showers, the deviation of the model developed here improves with energy.

Results presented in this work are optimized with simulated showers having energies from 100 GeV (1 TeV, in case of proton) to 1 EeV. The quality of the model measured with respect to shower energy can be assessed in Figure 6, where the average relative deviation is shown at $s = 1.0$ for all studied energies. For both primaries, this deviation is smaller than 10% in a wide angular and energy interval. In the case of gamma-ray showers (left box), the big deviation seen for 100 GeV gamma-ray showers above $\theta = 30^\circ$ is related to the small number of photons in this region. On average, 99.8% of the Cherenkov photon content of 100 GeV gamma-ray fall in the region $\theta < 30^\circ$. This figure confirms again the quality of the proposed model and ensures its adequacy to be employed in both the aforementioned regimes (a) and (b).

VI. CONCLUSION

To understand the nature and to describe the angular distribution of Cherenkov photons in air showers is of great importance in current experimental astrophysics. An exact model has been derived in Section II to describe the angular distribution photons in terms of the unknown energy and angular distributions of electrons. In Section III, successive approximations to this exact model have lead to a factorized form for the angular distributions of Cherenkov photons: a first term, I, depending on the maximum Cherenkov emission angle and a second term, K, depending on the energy and angular distributions of electrons. A simple parametric form has been proposed to describe this second term, overcoming the necessity of describing the two-dimensional energy and angular distribution of electrons. Parameters of this model have been obtained by fitting Monte Carlo simulations in Section IV.

The direct comparison of the parametrization and Monte Carlo simulations in Section V has shown the excellent capability of the model to describe the angular distributions of Cherenkov photons. The use of this model has many advantages as it is able to: 1) cover both small and large angular regions, including the peak around $\theta_{\rm em}$ and 2) cover a large energy interval, from hundreds of GeV to EeV energies. The parametrization presented here is therefore adequate to be employed in both the reconstruction of gamma-rays and cosmic-rays in IACT systems and also in the study of extensive air showers with fluorescence detectors.

ACKNOWLEDGMENTS

LBA and VdS acknowledge FAPESP Project 2015/15897-1. This study was financed in part by the Coordenação de Aperfeiçoamento de Pessoal de Nível Superior - Brasil (CAPES) - Finance Code 001. Authors acknowledge the National Laboratory for Scientific Computing (LNCC/MCTI, Brazil) for providing HPC resources of the SDumont supercomputer (http://sdumont.lncc.br). VdS acknowledges CNPq.

Appendix A: Validation of approximations

In this Appendix the models presented in Section II (exact) and Section III (approximated) are compared to a direct simulation of the angular distribution of Cherenkov pho-

tons. This comparison is shown in Figure 7 for the case of a vertical 1 PeV gamma-ray air shower at three different shower ages. The inset plot shows the region of large angles ($\theta > 5°$). The angular distributions of Cherenkov photons directly extracted from the simulation (reference) are represented by the filled curves. The dashed blue (exact model) and solid orange (approximated model) lines show the computation of the angular distributions of Cherenkov photons using Equations (7) and (15), respectively. For these computations, the energy and angular distributions of electrons ($\mathrm{d}N_e/\mathrm{d}E$ and $\mathrm{d}N_e/\mathrm{d}\theta_\mathrm{p}$) were extracted from the same simulation.

From Figure 7 it is seen that in the region of $\theta > 5°$ (inset plot) the curves of both models appear superimposed with the reference distributions for the three ages being shown. Further insight about the quality of these models in the region of smaller angles can be obtained by inspection of Figure 8, where the relative deviations between both models and the reference distribution are studied.

The exact model presents no deviation with respect to the reference distribution, except in the region around the peak of this distribution where a deviation of $< 10\%$ is found, as can be seen in Figure 8. However, this may be attributed to a side effect of binning the electron distributions ($\mathrm{d}N_e/\mathrm{d}E$ and $\mathrm{d}N_e/\mathrm{d}\theta_\mathrm{p}$) used as input in Equation (7).

The approximated model of Section III, on the other hand, deviates less than 10% from the reference distribution at $s = 1.0$ (center plot). At the ages of $s = 0.8$ (upper plot) and $s = 1.2$ (lower plot), on the other hand, this deviation is typically smaller than 20%, except at the peak. While this approximation is not as good as the exact model, it validates the idea that it is possible to approximately reproduce the shape of the angular distribution of Cherenkov photons as a product of two functions, as claimed in Section III.

---

[1] W. Galbraith, J.V. Jelley, Nature **171**(4347), 349 (1953). doi:10.1038/171349a0

[2] P.A. Čerenkov, Phys. Rev. **52**, 378 (1937). doi:10.1103/PhysRev.52.378

[3] V. Zatsepin, J. Exp. Theor. Phys. **20**(2) (1965)

[4] https://www.mpi-hd.mpg.de/hfm/HESS/

[5] http://www.magic.iac.es/

[6] http://veritas.sao.arizona.edu/

[7] B.S. Acharya et al. (CTA Consortium), Astropart. Phys. **43**, 3 (2013). doi: 10.1016/j.astropartphys.2013.01.007

[8] M. Lemoine-Goumard, B. Degrange, M. Tluczykont, Astropart. Phys. **25**, 195 (2006). doi: 10.1016/j.astropartphys.2006.01.005

[9] C.-C. Lu for the H.E.S.S. Collaboration, in *33rd International Cosmic Ray Conference (ICRC 2013): The Astroparticle Physics Conference* , ed. by A. Saa (Sociedade Brasileira de Fisica, São Paulo, Brazil, 2014), p. 3147

[10] J. Aleksić et al. (MAGIC Collaboration), Astropart. Phys. **72**, 76 (2016). doi: 10.1016/j.astropartphys.2015.02.005

[11] G.L. Cassiday et al. (HiRes Collaboration), Astrophys. J. **356**, 669 (1990). doi: 10.1086/168873

[12] J. Abraham et al. (Pierre Auger Collaboration), Nucl. Instrum. Meth. A **620**, 227 (2010). doi: 10.1016/j.nima.2010.04.023

[13] R.U. Abbasi et al. (Telescope Array Collaboration), Astrophys. J. **858**(2), 76 (2018). doi: 10.3847/1538-4357/aabad7

[14] M. Unger, B.R. Dawson, R. Engel, F. Schüssler, R. Ulrich, Nucl. Instrum. Meth. A **588**, 433 (2008). doi:doi.org/10.1016/j.nima.2008.01.100

[15] V. Novotny for the Pierre Auger Collaboration, in *Proceedings of 36th International Cosmic Ray Conference — PoS(ICRC2019)*, Madison, 2019, vol. 358, p. 374

[16] R. U. Abbasi et al. (Telescope Array Collaboration), Astrophys. J. **865**(1), 74 (2018). doi: 10.3847/1538-4357/aada05

[17] N. Budnev et al., Astropart. Phys. **50-52**, 18 (2013). doi:10.1016/j.astropartphys.2013.09.006

[18] A.A. Ivanov, S.P. Knurenko, I.Y. Sleptsov, New J. Phys. **11**(6), 065008 (2009). doi: 10.1088/1367-2630/11/6/065008

[19] L.A. Anchordoqui et al., Phys. Rev. D **101**, 023012 (2020). doi:10.1103/PhysRevD.101.023012

[20] T. Stanev, K. Vankov, S. Petrov, J.W. Elbert, in *17th International Cosmic Ray Conference*, vol. 6 (Commissariat a L'Energie Atomique, 1981, Paris, France, 1981), vol. 6, p. 256

[21] A.M. Hillas, J. Phys. G: Nucl. Part. Phys. **8**(10), 1461 (1982). doi:10.1088/0305-4616/8/10/016

[22] J.W. Elbert, T. Stanev, S. Torii, in *Proceedings 18th International Cosmic Ray Conference*, vol. 6 (Tata Institute of Fundamental Research, Bangalore, India, 1983), vol. 6, p. 227

[23] M. Giller, G. Wieczorek, A. Kacperczyk, H. Stojek, W. Tkaczyk, J. Phys. G: Nucl. Part. Phys.

30(2), 97 (2004). doi:10.1088/0954-3899/30/2/009

[24] F. Nerling, J. Blümer, R. Engel, M. Risse, Astropart. Phys. **24**(6), 421 (2006). doi: 10.1016/j.astropartphys.2005.09.002

[25] R. M. Baltrusaitis et al. (HiRes Collaboration), J. Phys. G **13**, 115 (1987). doi:10.1088/0305-4616/13/1/013

[26] M. Giller, G. Wieczorek, Astropart. Phys. **31**, 212 (2009). doi: 10.1016/j.astropartphys.2009.01.003

[27] D. Heck, J. Knapp, J. Capdevielle, G. Schatz, T. Thouw, CORSIKA: A Monte Carlo code to simulate extensive air showers. Tech. Rep. FZKA-6019, Forschungszentrum Karlsruhe, Karlsruhe (1998)

[28] S. Ostapchenko, Phys. Rev. D **83**, 014018 (2011). doi:10.1103/PhysRevD.83.014018

[29] M. Bleicher, et al., J. Phys. G **25**, 1859 (1999). doi:10.1088/0954-3899/25/9/308

[30] T.K. Gaisser, A.M. Hillas, in *15th International Cosmic Ray Conference*, vol. 8 (Bulgarian Academy of Sciences, 1977), vol. 8, p. 353

[31] B. Rossi, K. Greisen, Rev. Mod. Phys. **13**, 240 (1941). doi:10.1103/RevModPhys.13.240

[32] K. Kamata, J. Nishimura, Prog. Theor. Phys. Suppl. **6**, 93 (1958). doi:10.1143/PTPS.6.93

[33] K. Greisen, Annu. Rev. Nucle. Sci. **10**(1), 63 (1960). doi:10.1146/annurev.ns.10.120160.000431

TABLE I. Coefficients describing the angular distribution of Cherenkov photons in gamma-ray air showers.

μ	$p_{0,\mu}$ ($\pm$err)	$p_{1,\mu}$ ($\pm$err)	$p_{2,\mu}$ ($\pm$err)	$p_{3,\mu}$ ($\pm$err)
ν	0.34329 (0.00006)	−0.10683 (0.00002)	1.46852 (0.00004)	–
θ_1	1.4053 (0.0002)	0.32382 (0.00002)	0	−0.048841 (0.000003)
θ_2	0.95734 (0.00008)	0.26472 (0.00005)	–	–
ϵ	0.0031206 (0.0000006)	0	0	–

TABLE II. Coefficients describing the angular distribution of Cherenkov photons in proton air showers.

μ	$p_{0,\mu}$ ($\pm$err)	$p_{1,\mu}$ ($\pm$err)	$p_{2,\mu}$ ($\pm$err)	$p_{3,\mu}$ ($\pm$err)
ν	0.21155 (0.00006)	−0.16639 (0.00003)	1.21803 (0.00006)	–
θ_1	4.513 (0.001)	0.45092 (0.00003)	−0.008843 (0.000002)	−0.058687(0.000006)
θ_2	0.90725 (0.00008)	0.41722 (0.00005)	–	–
ϵ	0.009528 (0.000002)	0.022552 (0.000007)	−0.4207 (0.0002)	–

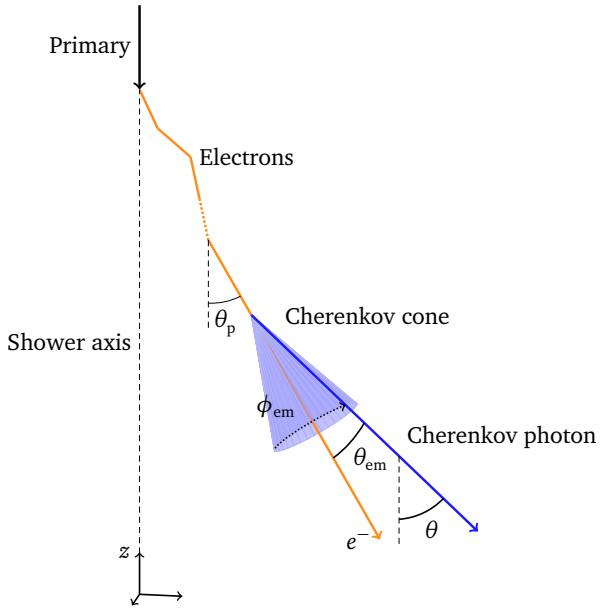

FIG. 1. Definition of the relevant angles for Cherenkov light emission in air showers. The blue cone represents the emission of Cherenkov photons around the emitting electron trajectory, in orange. The final angle between each Cherenkov photon (blue trajectory) and the shower axis is denoted by θ.

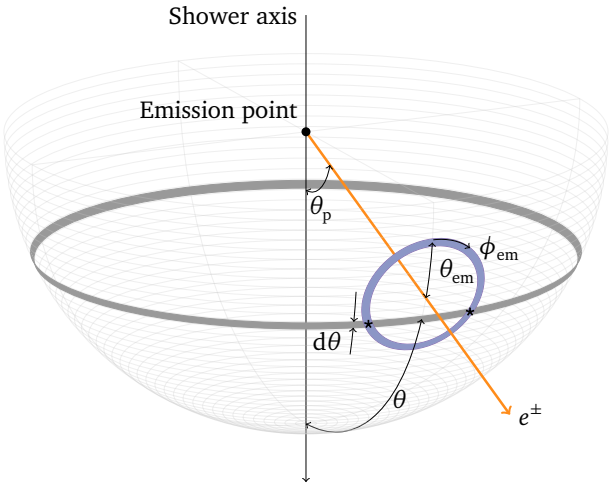

FIG. 2. Depiction of the intersecting region between the Cherenkov cone (blue ring) and the ring of width $d\theta$ around the angle θ (grey ring) in the unit sphere. There are two intersection points whenever $|\theta - \theta_p| < \theta_{em}$ and none otherwise.

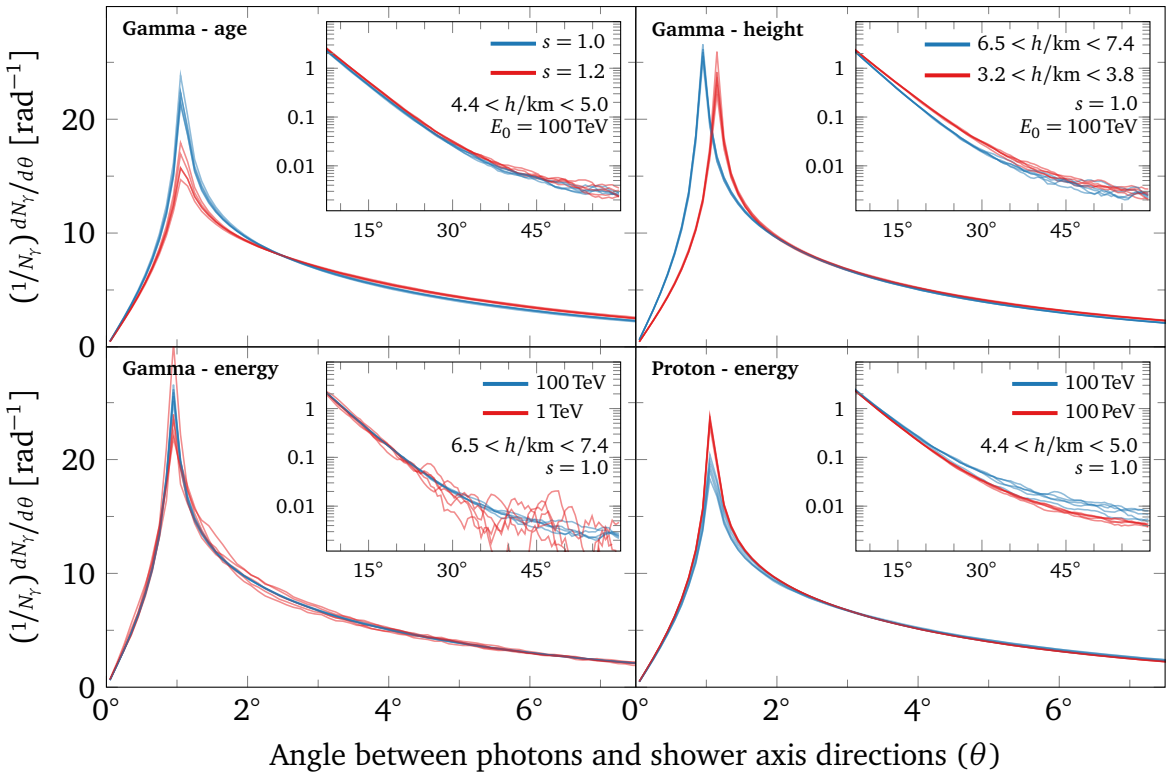

FIG. 3. Examples of simulated angular distributions of Cherenkov photons highlighting its dependency with respect to the shower age (top left), emission height (top right), primary energy in gamma-ray showers (bottom left), and primary energy in proton showers (bottom left).

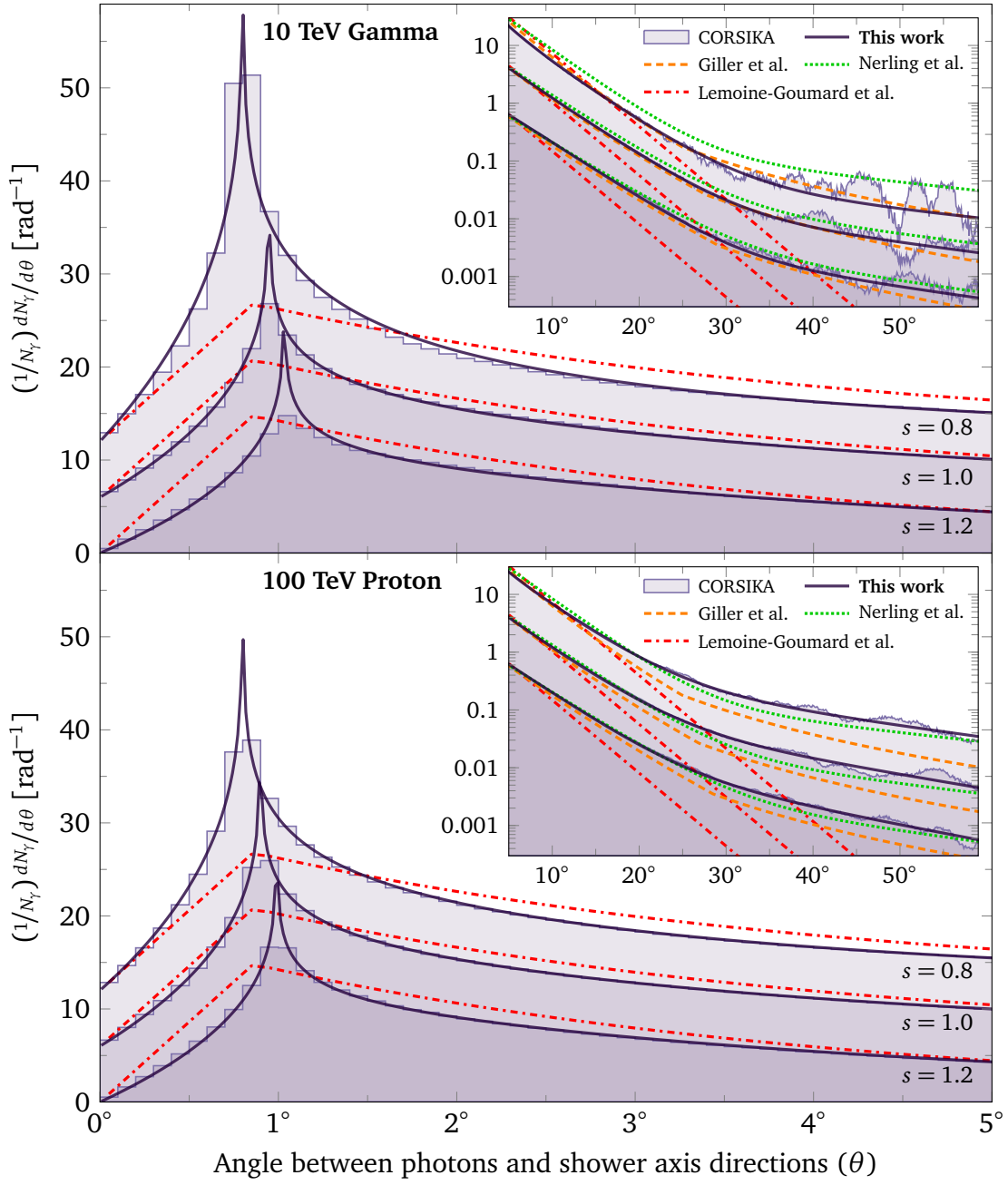

FIG. 4. Angular distribution of Cherenkov photons from a single gamma-ray (top) and proton (bottom) shower. CORSIKA simulations (filled histograms) are compared to the parametrized distributions (solid curves) at $s = 0.8$, 1.0, and 1.2 (indicated inside the plot). Predictions from Refs. [8, 24, 26] are shown for comparison (see legend). Curves of a common shower age are vertically displaced for better visualization.

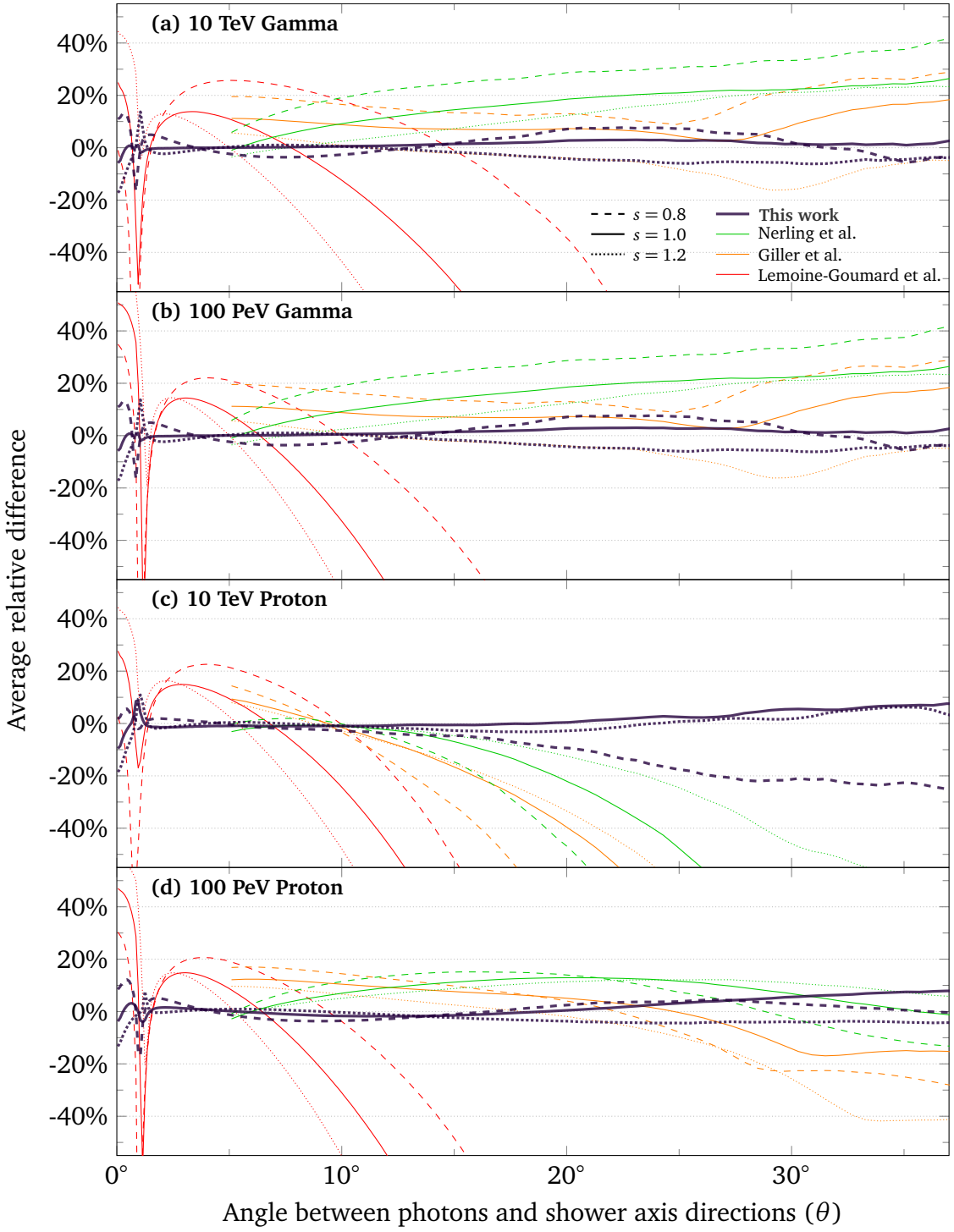

FIG. 5. Average relative deviation between parametrized and simulated angular distributions of Cherenkov photons at $s = 0.8$ (dashed curves), 1.0 (solid curves), and 1.2 (dotted curves). Each box depicts a single primary-energy combination, indicated in the top-left corner. Parametrization of this work is compared to predictions from Refs. [8, 24, 26] (see legend in the upper pannel).

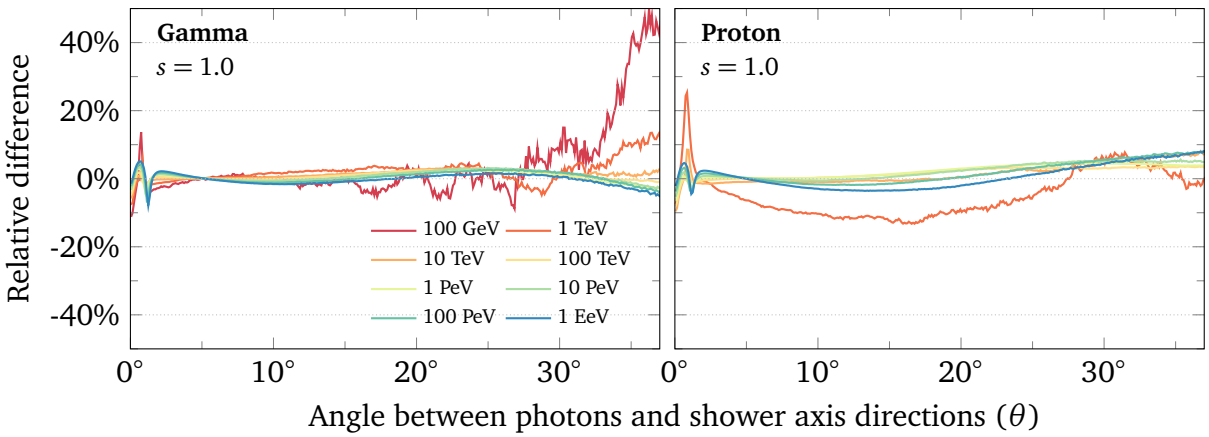

FIG. 6. Average relative deviation between parametrized and simulated angular distributions of Cherenkov photons at $s = 1.0$ for gamma-ray (left) and proton (right) showers at various primary energies.

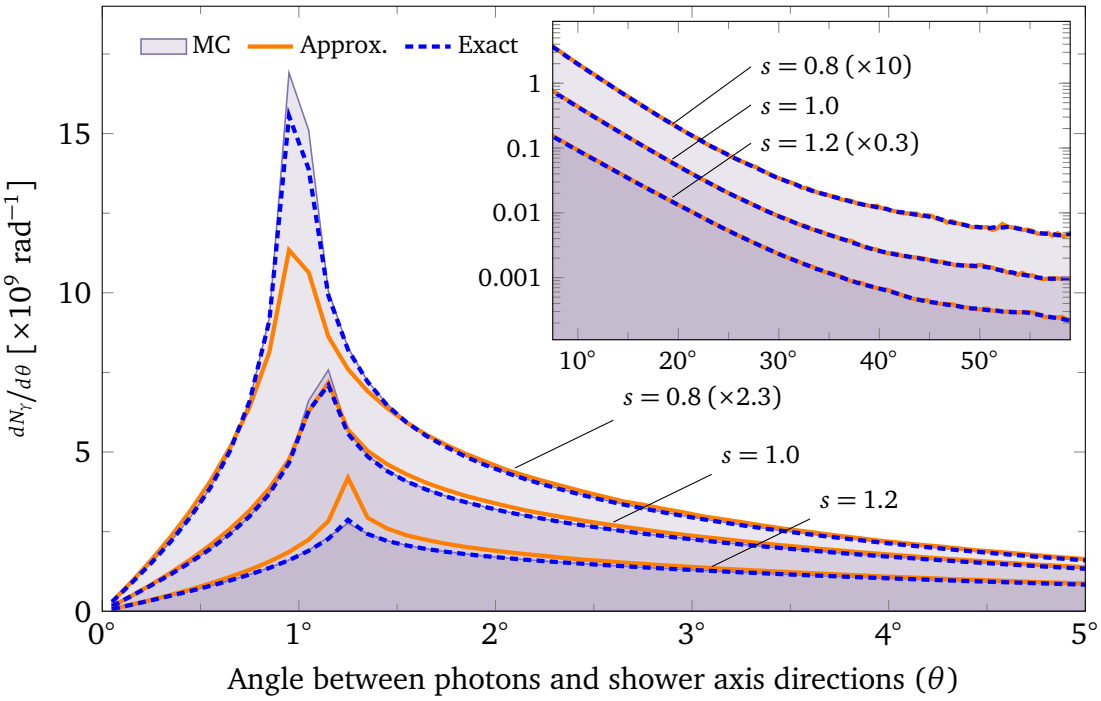

FIG. 7. Comparison of the exact (blue dashed) and the approximated (orange solid) models of Sections II and III to a simulated angular distribution of Cherenkov photons at three shower ages (see annotations inside the box). The inset plot shows the region $\theta > 5°$. To avoid superposition of the curves and therefore make the figure more clear, some curves were scaled by factors indicated together with the shower age.

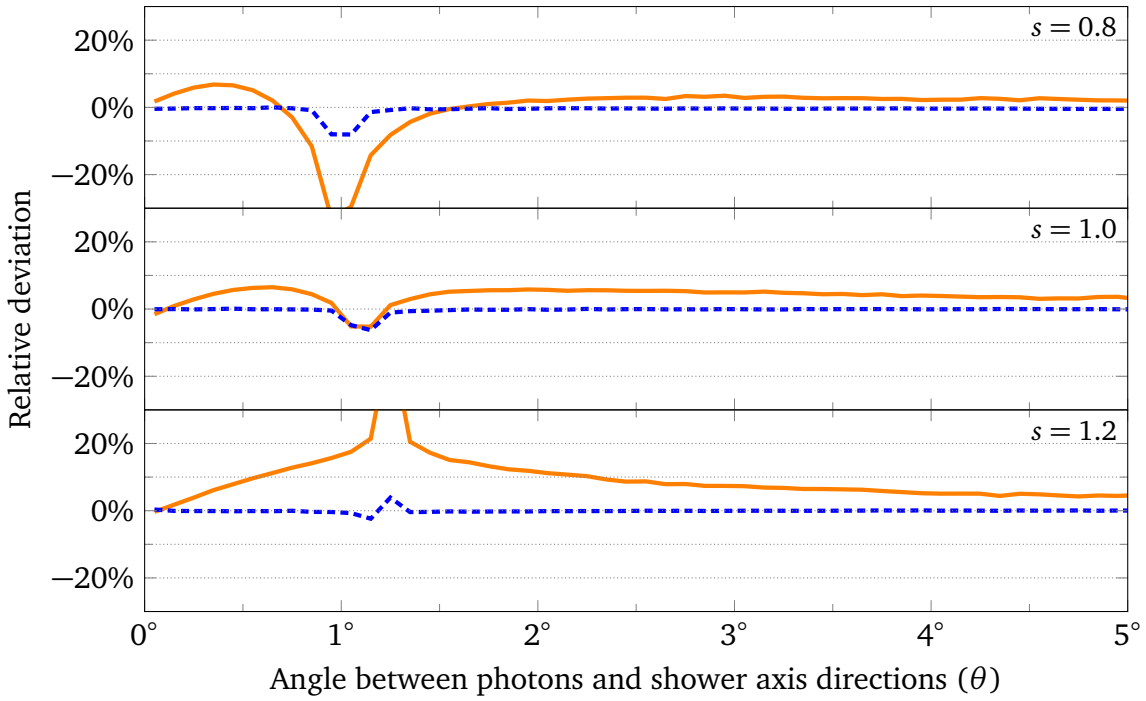

FIG. 8. Relative deviation between models of Sections II (blue dashed) and III (orange solid) and the simulated angular distribution of Cherenkov photons in the region of small angles. Curves are shown for three shower ages, indicated in the boxes.

7 A TECHNIQUE TO MEASURE $X_{\max}$ USING CHERENKOV LIGHT

In the paper listed as reference (77), A. Giler and collaborators propose a method to obtain the depth of shower maximum of extensive air showers from measurements performed by imaging atmospheric Cherenkov telescopes (IACT). This method introduces a new observable called $X_{\max}^{(\text{apparent})}$, which corresponds to the apparent depth of shower maximum derived from the longitudinal Cherenkov-light profiles seen by one or a group of telescopes. The value of $X_{\max}^{(\text{apparent})}$ is found to be linearly correlated to the real depth of maximum of the charged component of the shower $X_{\max}^{(\text{charged})}$. The main result of this study is to show that $X_{\max}^{(\text{charged})}$ can be reconstructed with reasonable accuracy through the measurement of $X_{\max}^{(\text{apparent})}$, under the conditions that the shower is not observed too close from its core and that the correlation between $X_{\max}^{(\text{charged})}$ and $X_{\max}^{(\text{apparent})}$ is given a priori.

The author of the present thesis has contributed to this study by providing the shower simulations from which the analysis is derived. This chapter aims to describe the simulations used in this study and to summarize the principal results. The discussion is structured as follows. In Section 7.1 the motivation to develop this technique is outlined in view of possible cosmic-ray studies. Section 7.2 describes the procedure used to simulate extensive air showers and to analyze the Cherenkov photons from each shower. Following, in Section 7.3 the analysis of the simulated Cherenkov-light profiles and the main results, which were obtained by A. Giler, are summarized. At last, some concluding remarks are presented in Section 7.4.

7.1 Motivation

Imaging telescopes constitute the major class of instruments used for ground-based gamma-ray astronomy. Such detectors are used to capture Cherenkov-light images of air showers from which the features of the primary particle can be extracted, including its type, its energy, and its arrival direction. In the current generation of IACT systems, H.E.S.S., MAGIC, and VERITAS, the potential of this type of detector to measure gamma-ray fluxes has been explored in arrays combining 2 to 5 telescopes, with analyses based on the stereoscopic view of extensive air showers. These IACT systems were designed to work as detectors of gamma rays having some tens of GeV up to some hundreds of TeV. In this energy regime, every observation of a gamma-ray source is accompanied by an overwhelming cosmic-ray background, whose flux is at least three orders of magnitude higher than the expected cosmic photon fluxes. The presence of this background has two notable implications: the first is that gamma-ray-based analyses have to efficiently reject events generated by cosmic-ray protons and nuclei based on the shower images; the sec-

ond is that IACTs have the potential to measure the cosmic-ray flux in an energy range slightly above the nominal range for detection of gamma rays.

The primal motivation for the current study lies in the possibility of performing cosmic-ray composition analyses using IACTs. It is foreseen that arrays such as VERITAS (140), for instance, with its 4 telescopes, can observe about 1000 proton events above 1 PeV per year. (77) This makes IACT systems especially suited to measure the cosmic-ray flux in the knee region, around which precise measurements of relative abundances of primary masses are scarce. Such measurements are of great importance for cosmic-ray physics, as knowledge of the fluxes of individual components around the knee region would represent a fundamental piece of information to better understand the transition from a galactic-dominant to an extragalactic-dominant flux of cosmic rays. (38) Therefore, developing a technique to disentangle the relative abundances of different primary masses using IACTs would result in an important scientific outcome. This is even more promising in view of the forthcoming Cherenkov Telescope Array (CTA) (167) that, with its larger effective area, may be able to observe the cosmic ray flux at the knee with even higher statistics and precision.

In this study, a new technique to measure the depth of shower maximum of the charged component of extensive air showers $X_{\max}^{(\text{charged})}$ is proposed. This observable is known to be correlated with the mass of the primary cosmic ray (see Section 4.1.3). Shower reconstruction algorithms from which the $X_{\max}^{(\text{charged})}$ of gamma-ray showers can be derived exist (177), with a resolution of $30\,\text{g/cm}^2$ and a small bias in the reconstructed value. The advantage of the technique presented here is that it is specifically targeted to reconstruct $X_{\max}^{(\text{charged})}$, which results in a resolution that improves with increasing energy in a method that is complementary to other analyses techniques.

7.2 Simulation procedure

All results from this study derive from simulations performed in the framework of CORSIKA 7.6300. (246) Specifically, CORSIKA is used to simulate the development of extensive air showers, including the detailed emission of Cherenkov photons and its propagation. Some important parameters used in all simulations are summarized in Table 2. Apart from these parameters, three types of primary particles are considered (gamma rays, proton, and iron nuclei) with four values of primary energy (10 TeV, 30 TeV, 100 TeV, and 300 TeV). For each of the 12 combinations of primary particle type and energy, a sample of 10^4 showers is generated. Along the simulation of each shower, the longitudinal evolution of the charged particle profile is sampled in steps of $5\,\text{g/cm}^2$ and a fit to a Gaisser-Hillas function (Equation 2.9) is used to extract $X_{\max}^{(\text{charged})}$.

During the simulation, the emission of Cherenkov photons is performed as usual in CORSIKA by producing bunches containing no more than 5 photons each. To simulate

Table 2 – CORSIKA steering parameters common to all simulations presented in Chapter 7

Parameter		Value
Particle energy cutoffs	Hadrons	300 MeV
	Muons	100 MeV
	Electrons	20 MeV
	Photons and π^0	20 MeV
Shower axis	Zenith angle	20°
	Azimuth angle	Random
Hadronic interaction models	Low energy ($E < 80$ GeV)	FLUKA (253)
	High energy ($E > 80$ GeV)	EPOS-LHC (258)
Observation altitude		2150 m

Source: By the author

what would be the detection of these photons in an ideal detector, a fictitious array of telescopes is simulated as represented in Figure 37. This array comprises 30 juxtaposed spherical photon-collection surfaces of 5 m radius in a linear arrangement. Each of these telescopes represents an ideal instrument in which all photons are efficiently collected and their arrival direction and impact position are exactly determined. The linear configuration of the simulated array allows for the study of the impact-parameter dependence of the observed Cherenkov-photon profiles.

Along with the simulation, information of every photon bunch hitting a detector is piped to an external program responsible to reconstruct the longitudinal and lateral profiles of Cherenkov photons at emission. This procedure relies on the definition of a shower-face plane (SFP), illustrated in Figure 37. Formally, the SFP is defined as the set of points $\vec{p}$ such that $(\vec{p}-\vec{p}_0)\cdot\hat{n} = 0$, where $\vec{p}_0$ is the shower impact point and $\hat{n}$ is a vector normal to the SFP. The normal vector $\hat{n}$, in its turn, is defined in terms of the shower axis direction $\hat{v}_\mathrm{s}$ and the position of the telescope $\vec{r}$ with respect to the impact position as $\hat{n} = \hat{v}_\mathrm{s} \times (\hat{r} \times \hat{v}_\mathrm{s})$. Therefore, for each telescope a different SFP is defined depending on the arrival direction of the primary particle. To account for the effect of the limited field of view (FOV) of a real detector, a cut is applied on photon arrival directions to select only photons that would be observed within a limited FOV. Typically, a cut of 10° is applied in this study, unless otherwise noted. All photon bunches surviving this cut are, then, projected back into the SFP, with the intersection point characterized by the slant atmospheric depth, measured along the shower axis direction, and the lateral position in meters, measured in the direction transversal to the shower axis. Examples of histograms obtained from projecting photons back into the SFP are shown in Figure 38 for 100 TeV showers observed at two different impact parameters.

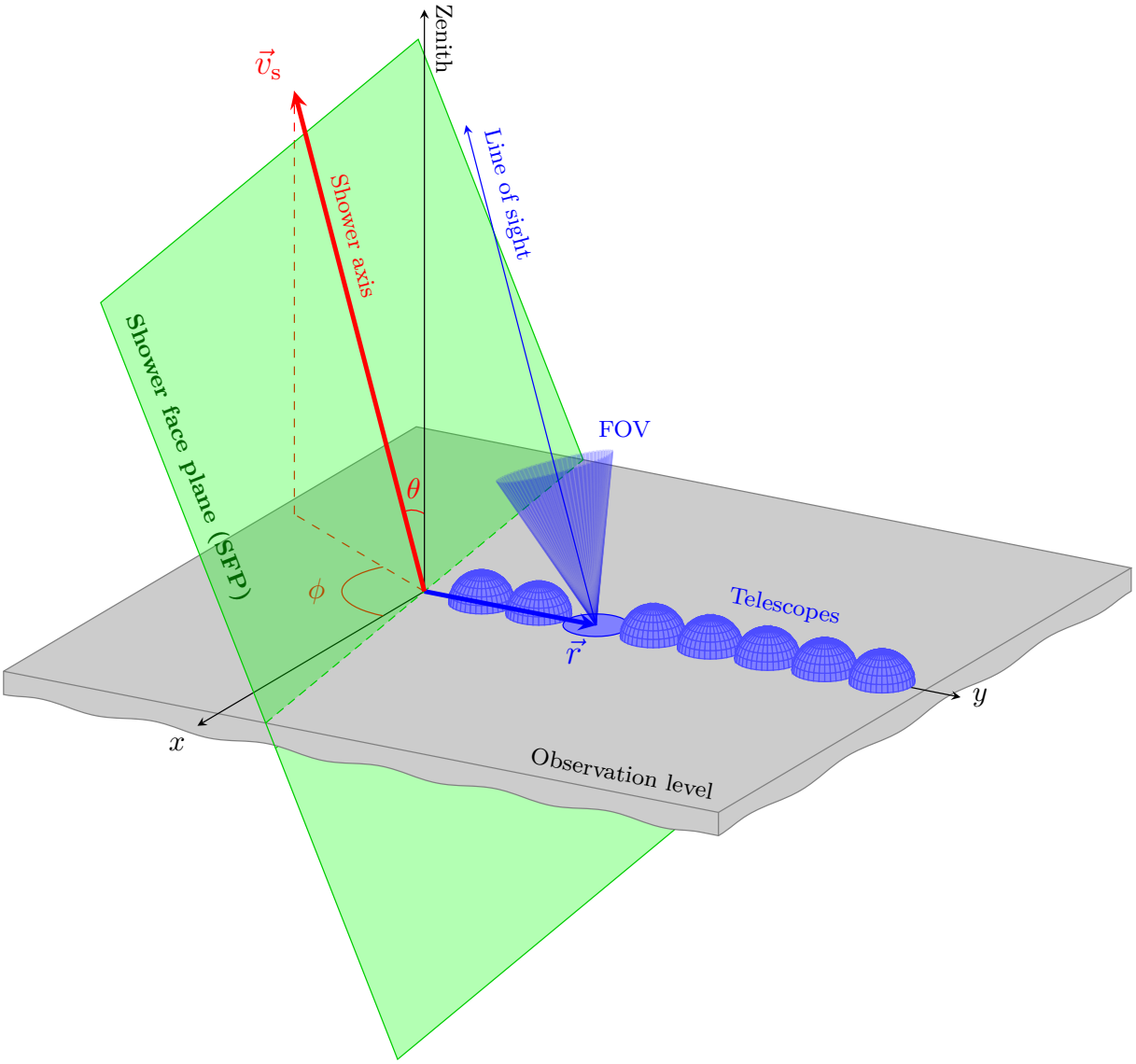

Figure 37 – Depiction of the shower-face plane and the array of ideal telescopes.

Source: By the author

The final products of the simulations, therefore, are the two-dimensional histograms with photons projected back into the SFP for various impact parameter values. In these distributions, the vertical direction is associated to the longitudinal evolution of the Cherenkov-light emission profiles along the shower axis. Simple comparison between the left and right plots of Figure 38 reveals that, when observed through Cherenkov light, each telescope will perceive a different depth of shower maximum $X_{\max}^{(\text{Cherenkov})}$, not necessarily coinciding with the real depth of shower maximum $X_{\max}^{(\text{charged})}$. This apparent depth of shower maximum, however, is a measurable quantity and its ability to be used to estimate $X_{\max}^{(\text{charged})}$ is explored in this study.

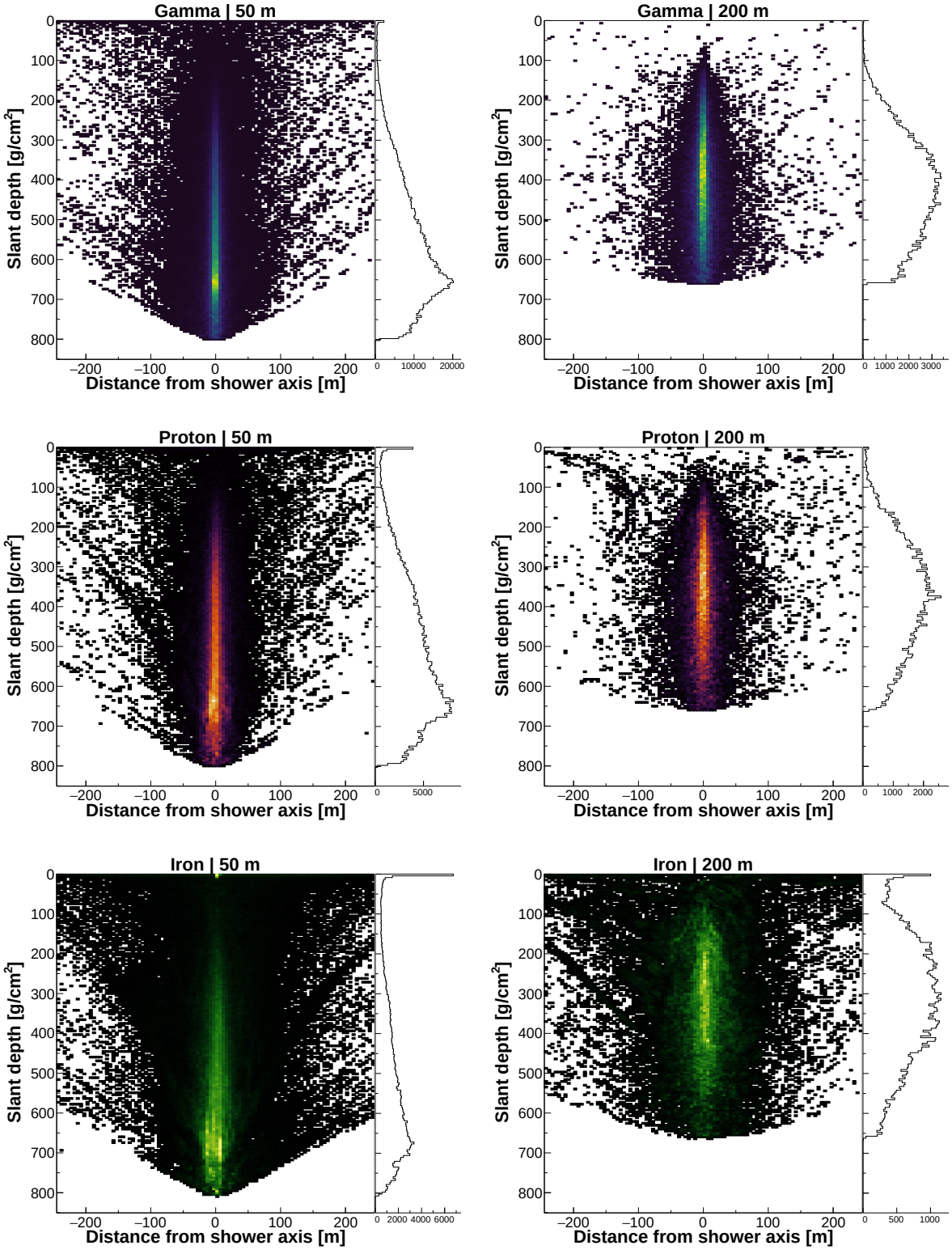

Figure 38 – Patterns generated by the projection of Cherenkov photons back into the shower-face plane for different primary types (left to right) and impact parameters (top to bottom).

Source: By the author

7.3 Results

From this point on, the study was carried by A. Giler with only minor contributions from the present author. This section aims to briefly describe the central ideas present in the analysis of the simulated showers and to summarize the results obtained.

A central concept in this study is that the observable $X_{\max}^{(\text{Cherenkov})}$, if measured outside the Cherenkov-light pool, correlates with $X_{\max}^{(\text{charged})}$ and allows for its reconstruction. Indeed, it is seen that $X_{\max}^{(\text{Cherenkov})}$ is approximately constant with respect to the impact parameter r in the region $150\,\text{m} \leq r \leq 200\,\text{m}$. Therefore, a third quantity, denoted $X_{\max}^{(\text{apparent})}$, is defined as the value of $X_{\max}^{(\text{Cherenkov})}$ averaged over a group of telescopes lying within this impact parameter region. An analysis of the joint distribution of $X_{\max}^{(\text{apparent})}$ and $X_{\max}^{(\text{charged})}$ from the simulated showers reveals that, in general, a linear form $X_{\max}^{(\text{charged})} = \alpha + \beta X_{\max}^{(\text{apparent})}$ provides a reasonable description of the correlation between these two variables. By extracting the values of α and β from the simulations, therefore, it is possible to estimate $X_{\max}^{(\text{charged})}$ from measurements of $X_{\max}^{(\text{apparent})}$.

The parameters α and β are determined using distinct configurations and the resolution of the technique in determining $X_{\max}^{(\text{charged})}$ is computed as the standard deviation of the distribution of the residuals between the reconstructed depth of shower maximum and the real value $X_{\max}^{(\text{charged})}$. Namely, the resolution is studied in three scenarios: i) varying the number and position of the telescopes used to compute $X_{\max}^{(\text{apparent})}$; ii) deriving α and β separately from gamma-ray and hadronic showers; iii) varying the FOV of the telescopes. The resulting resolution in each case is shown in Figure 39. The three plots in this figure exhibit the quality of the proposed technique by showing that the resolution improves with energy and is almost independent of the FOV for values $> 5°$.

7.4 Conclusion

In this chapter, a new technique to reconstruct $X_{\max}^{(\text{charged})}$ using Cherenkov light has been presented. This technique is the result from a collaboration with A. Giler and the contribution from the present author on the provision of shower simulations has been discussed in detail. The performance of the technique has been summarized in terms of the resolution in reconstructing $X_{\max}^{(\text{charged})}$ that, for energies $\geq 100\,\text{TeV}$ is of about $\sim 25\,\text{g/cm}^2$. Remarkably, the resolution obtained is comparable to that of fluorescence detectors. This result shows that IACTs have, indeed, a great potential to measure the depth of shower maximum of cosmic-ray showers in a region of the spectrum where mass-composition measurements need to be improved. Moreover, this technique introduces a new air shower observable, the $X_{\max}^{(\text{apparent})}$, that is derived independently of any other reconstruction technique and can be introduced in algorithms for the reconstruction of gamma-ray fluxes.

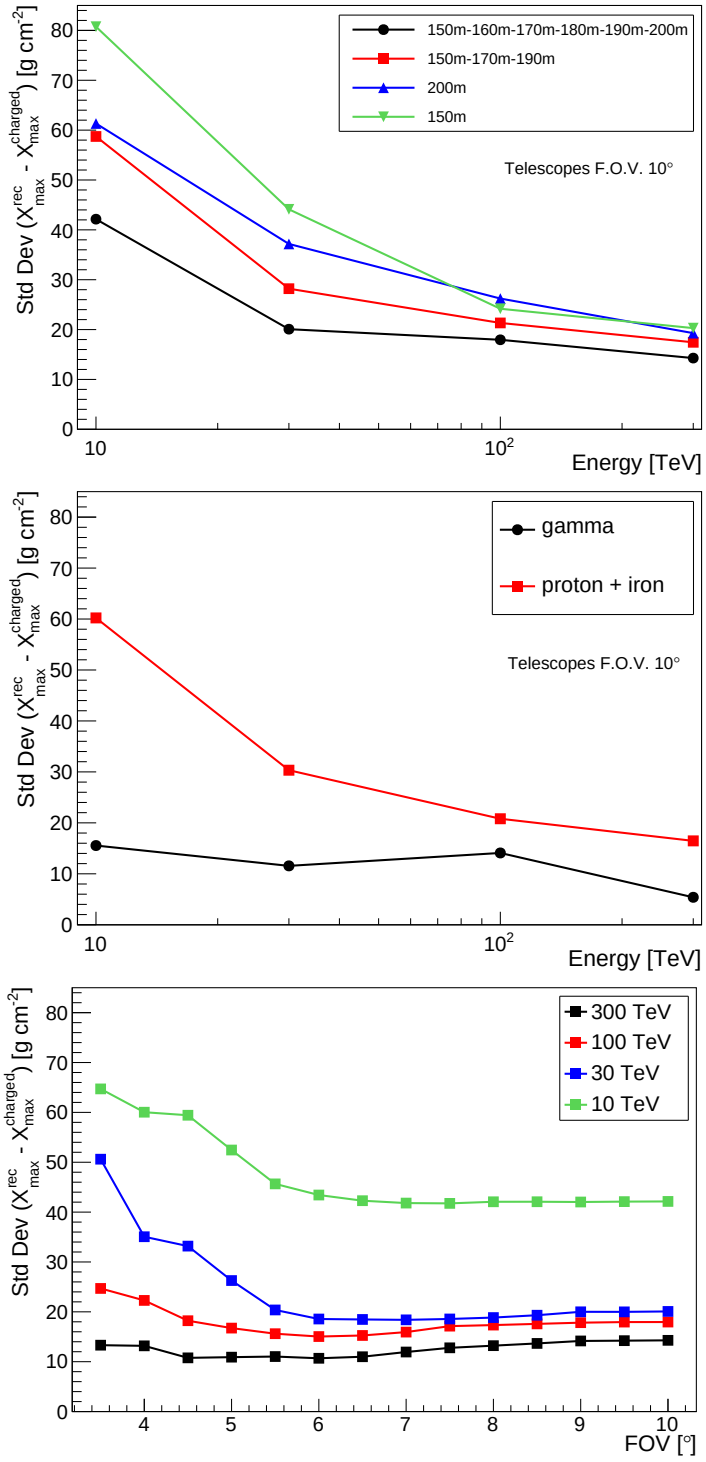

Figure 39 – Resolution on the reconstruction of $X_{\max}^{(\text{charged})}$. Top: as a function of energy for different telescope configurations. Middle: as a function of energy for gamma-ray and hadronic showers separately. Bottom: as a function of the telescope FOV for different primary energies.

Source: GILER *et al.* (77)

8 ON HADRONIC INTERACTION MODELS AND CHERENKOV TELESCOPES

In this chapter, the association of hadronic interaction models with uncertainties in the detection of extensive air showers through IACTs is investigated. This investigation is divided into two parts. In a first analysis, the basic Hillas parameters predicted from different hadronic interaction models are compared. The goal of this first study is to understand to which extent the uncertainties in the hadronic models affect the prescription of the Hillas parameters in simulations of IACTs. The results from this first study have been presented in a meeting of the Analysis and Simulation Working Group (ASWG) of the CTA after which a collaboration has been formed to develop a deeper analysis for the CTA, which forms the second part of the present investigation. This collaboration, lead by Michiko Ohishi, has the goal to determine the impact of uncertainties in hadronic interaction models on the estimated sensitivity of the CTA instrument.

Results of the analysis of basic image parameters and a summary of the results derived by M. Ohishi will be presented in this chapter, which is structured as follows. Section 8.1 exposes the fundamental motivation for associating IACT measurements with hadronic interaction models. Section 8.2 describes the simulation chain used to obtain the results of Section 8.3, in which the distributions of Hillas parameters are investigated. Section 8.4 summarizes results on the estimated CTA sensitivity. Section 8.5, the last of this chapter, comments on the results presented below and gives some concluding remarks.

8.1 Motivation

Understanding the uncertainties associated with the theoretical description of extensive air showers is vital for collaborations running cosmic-ray observatories as they reflect into uncertainties on the reconstructed primary fluxes. This is because the observables used to discriminate the primary particle and infer its properties are interpreted in light of computational frameworks relying on a complete theoretical modeling of the particle cascades. (82,161,171,265) Similarly, for experiments in the design or construction phase, simulations of extensive air showers are used both to improve the final design (169) and to estimate the instrumental performance. (266–267) Among all known sources of uncertainties in the description of extensive air showers, the modeling of hadronic interactions is critical. (34, 254–255)

Hadronic processes play a central role in the development of proton- and nuclei-induced showers as they drive the energy flow in the early stages of a cascade, thus determining the growth of the electromagnetic component, and also dictate the spectrum of muons that reach the ground. (226, 262) In the case of gamma-ray showers, photoproduc-

tion processes can give rise to a hadronic component whose relevance for gamma-ray observations is expected to be small (34), but still is not completely understood. (268) In what concerns the modeling of hadronic interactions, uncertainties are abundant. Hadronic particles are dynamic systems composed by quarks and gluons or, generically, by partons, which are subject to the strong interaction. The evolution of the partonic structure of hadrons and the interaction cross sections at the partonic level can not be completely described from first principles in Quantum Chromodynamics (QCD). (269) For this reason, phenomenological models have been proposed (257–259, 270) to describe the bulk of final states arising in hadronic processes. Being of phenomenological character, these models depend on several approximations and carry free parameters that have to be adjusted to fit collider data. (271) Then, they are extrapolated to unmeasured kinematic phase-space regions when used for air-shower physics. (272) These extrapolations give rise to uncertainties in the prescription of air-shower observables that are difficult to quantify.

Traditionally, hadronic interactions are modelled in the simulation of extensive air showers in two separate regimes: of low- and high-energy interactions, with a typical transition energy of 80 GeV (measured in the laboratory frame). Current IACT systems (147–149) already operate in an energy range which crosses this transition energy and, therefore, observations in this type of experiment are affected by the modeling of hadronic interactions in both regimes. In particular, it has been shown that the simulated lateral distribution of Cherenkov light at energies relevant for IACTs depends on the characteristics of hadronic interaction models (255) and that the value chosen for the transition energy is a source of uncertainty as well. (254) However, there is no dedicated study quantifying the effect of uncertainties in hadronic interaction models on the detector response of IACT systems. Such study, besides being naturally important for the experimental community, would provide an important feedback for the hadronic-model-builder community.

In the context of the forthcoming CTA, prospects for physical analyses with this experiment depend on the estimated instrument response to gamma-ray fluxes. In particular, the sensitivity of the instrument constrains the lowest value of gamma-ray signals that will be observed by the CTA and is therefore of great importance to plan future observations and derive the prospects for specific studies. The sensitivity of the CTA has been evaluated through a complete simulation chain including the description of extensive air showers and the full detector response. (208, 266) This computation has been carried out by the CTA collaboration with a single hadronic interaction model for the simulation of the hadronic background. The question as to determine if the estimated sensitivity carries uncertainties relative to the modeling of hadronic interactions, accordingly, remains open.

Following this reasoning, the purpose of this study is twofold. The first goal is to

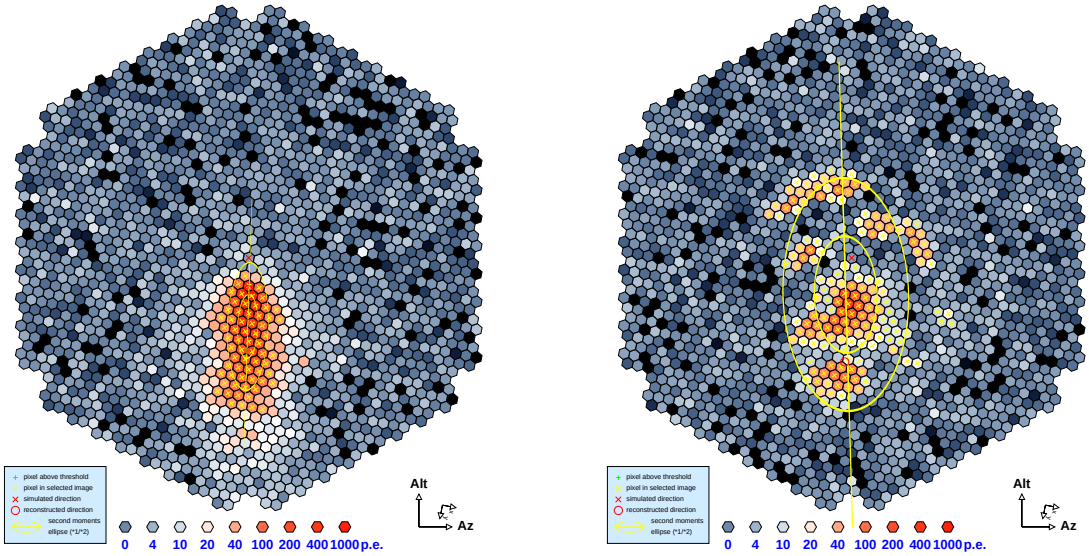

Figure 40 – Examples of simulated images of a gamma-ray (left) and proton (right) shower, both at 1 TeV and detected at a distance of 50 m from the shower core.

Source: By the author

investigate how sensible are the simulated distributions of Hillas parameters to differences in hadronic interaction models. In particular, the telescopes that will be deployed at the CTA observatory are considered in the simulations below. In the following, the impact of uncertainties in hadronic interaction models on the estimated sensitivity of the CTA is analyzed through its computation using different hadronic interaction models.

8.2 Simulation of IACTs

The simulations used to derive the distributions of Hillas parameters in this study were performed in tandem with those detailed in Section 7.2. Parameters used to steer CORSIKA simulations are the same used in that section (see Table 2), with the exception that the results presented here are for gamma-ray and proton showers only and include energy values down to 100 GeV, so to explore the energy regions covered by the three CTA telescope types. The spatial arrangement of the simulated telescopes also follows the approach of the previous chapter, which is illustrated in Figure 37.

To couple the response of the telescopes in the simulation chain, the `sim_telarray` package (273) is employed. During shower simulation, each Cherenkov-photon bunch generated by CORSIKA is piped to `sim_telarray`, which is responsible to account for the absorption of light in the atmosphere, to trace the photon trajectories in the optical systems of the telescopes, and to produce the electronic response on the telescope camera. The `sim_telarray` package provides a complete description of a telescope, including the mirror and camera configuration, the mirror reflectivity, and the efficiency in the con-

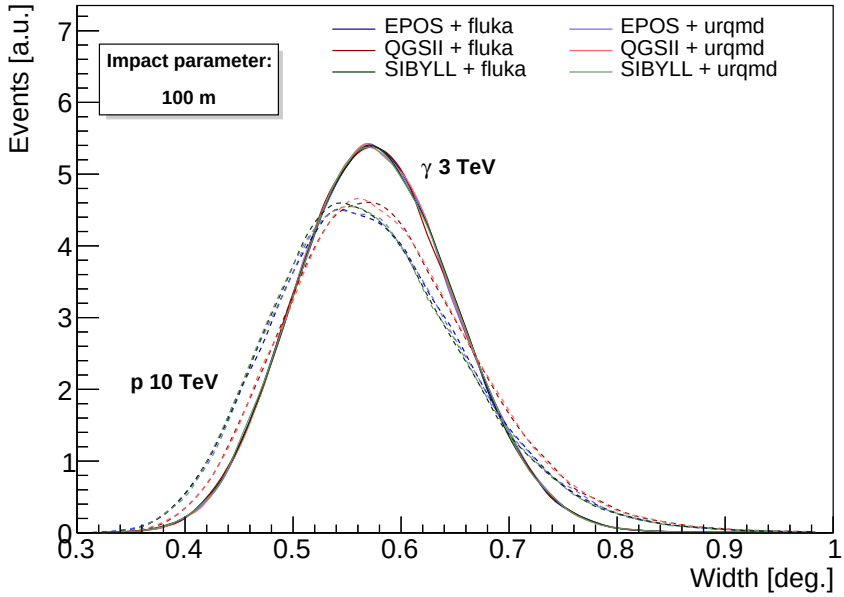

Figure 41 – Distribution of the image width as predicted by six different combination of hadronic interaction models for 3 TeV gamma ray and 10 TeV proton showers. The simulated telescope is an MST at a distance of 100 m from the shower core.

Source: By the author

version of photons in electronic signal. The parameters describing these configurations match those used in Prod3b simulations (164) by the CTA collaboration. In each simulated event, the center of the field of view of each telescope is aligned with the direction of the primary particle. No trigger at the array-level is defined in the simulation, meaning that an event is registered whenever at least one telescope is triggered.

Following the simulation of the detector response, which results in a raw image of the simulated shower, `sim_telarray` performs the image analysis procedure. This process starts with the imaging cleaning by employing a tail-cut algorithm, which requires a pixel to have an amplitude exceeding a certain threshold t_{low} and at least one neighbor pixel with a threshold t_{high} and vice versa. (171) From the cleaned image, the Hillas parameters are computed following the standard definitions. (172) An illustration of the images produced in the simulation can be found in Figure 40.

For this analysis, three parameters of shower images are considered, namely:

- Size: zeroth-order moment of the image, which is equivalent to the sum of the amplitudes of all pixels surviving the image cleaning procedure;
- Image length: standard deviation of the image along the direction of its major axis;
- Image width: standard deviation of the image along the direction of its minor axis.

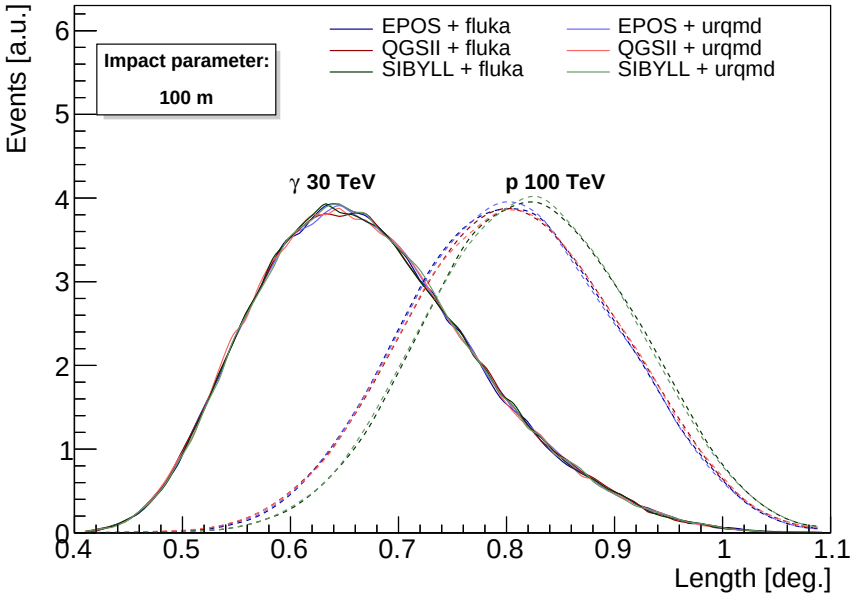

Figure 42 – Distribution of the image length as predicted by six different combination of hadronic interaction models for 30 TeV gamma ray and 100 TeV proton showers. The simulated telescope is an SST at a distance of 100 m from the shower core.

Source: By the author

The output of the simulation procedure comprises the values of image parameters for every triggered telescope in one event. This information is used to build the distributions of image parameters for each combination of primary type, energy, and distance between telescope and shower arrival point (impact parameter). Examples of these simulated parameter distributions can be found in Figures 41 and 42.

8.3 Basic image parameters

In this section, the overall impact of hadronic interaction models on the estimated values of Hillas parameters is investigated. For that, the average values of the parameters are computed and expressed as a function of the impact parameter, as illustrated in Figure 43. This figure shows the evolution of the average values of the image size (logarithm), the image width, and the image length as a function of the impact parameter.

To get a quantitative insight on the difference between the average parameters prescribed by different hadronic interaction models, a global average is defined as the parameter value at each point averaged over all hadronic interaction models. Below, a comparison between prescriptions from different hadronic interaction model combinations is performed in terms of the relative deviation to the global average of each parameter.

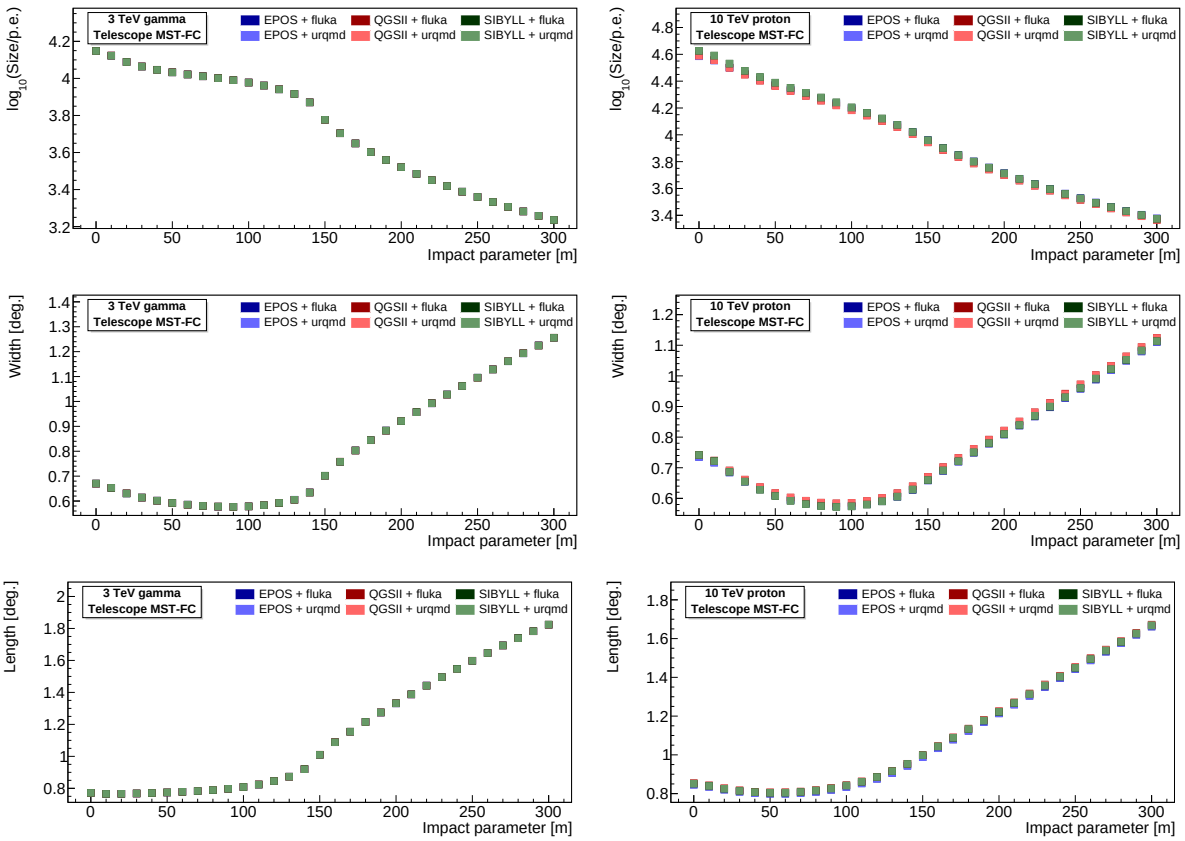

Figure 43 – Average value of the image parameters as a function of the distance between the telescope and the shower core. The logarithm of the total image amplitude (top), the image width (middle), and the image length (bottom) are shown for 3 TeV gamma ray showers (left) and 10 TeV proton showers (right) detected by the MST telescope.

Source: By the author

Image size

The image size (or amplitude) is analyzed in Figure 44. It is inferred from this figure that simulated gamma-ray showers (left panels) are, to a large extent, unaffected by the choice of a particular hadronic interaction model. Minor discrepancies (<0.5%), however, arise in the case of 30 TeV gamma-ray showers, as seen in the bottom-left plot.

Regarding proton showers (right panels in Figure 44), the image size varies from one hadronic interaction model to another. Even at low energies, considering showers at 300 GeV, the results for different models diverge to a factor up to 6% between each other. For showers measured too close from the core, discrepancies can be as large as 13% for 100 TeV showers, as seen in the right bottom plot.

Image width

The second parameter analyzed here is the image width, which corresponds to the

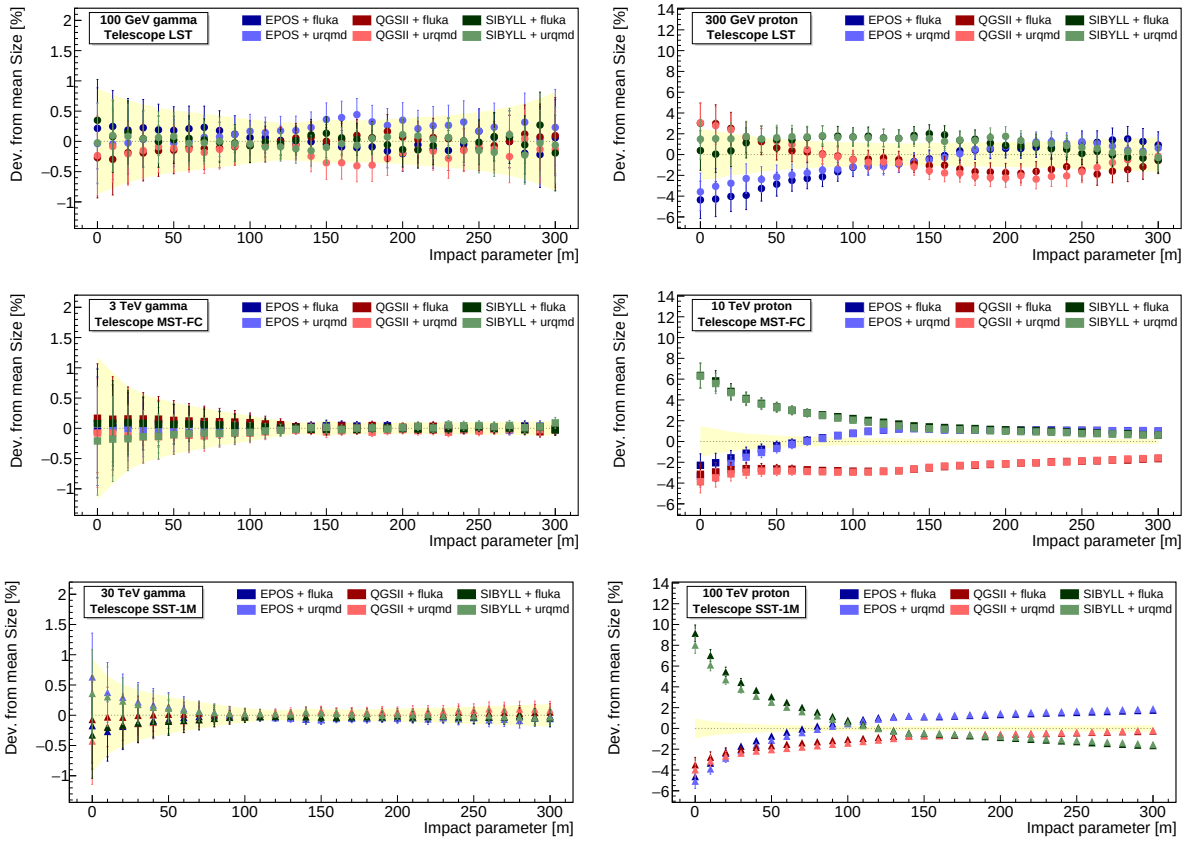

Figure 44 – Relative percentage deviation of the average image amplitude as computed by each hadronic interaction model with respect to a global mean, averaged over all models. Left (right) column is for gamma ray (proton) showers whose energies are indicated in the top left corner of each box.

Source: By the author

spread of a shower image in the direction perpendicular to its main axis. The impact of hadronic interaction models in the estimation of this variable can be assessed in Figure 45. This figure reiterates the idea that the simulation of gamma ray showers does not suffer from uncertainties on hadronic interaction models. As for proton showers, deviations of the order of 2% are seen in the right panels of Figure 45.

Image length

The image length, the last parameter analyzed here, provides a measurement of the image size along its major axis. Figure 46 shows the average deviation of this parameter as computed from different models. Again, as expected, no discrepancy between models is seen for gamma-ray showers. On the other hand, discrepancies in the case of proton showers increase with the primary energy. Differences on the average length between models, however, are smaller than 3% in proton showers.

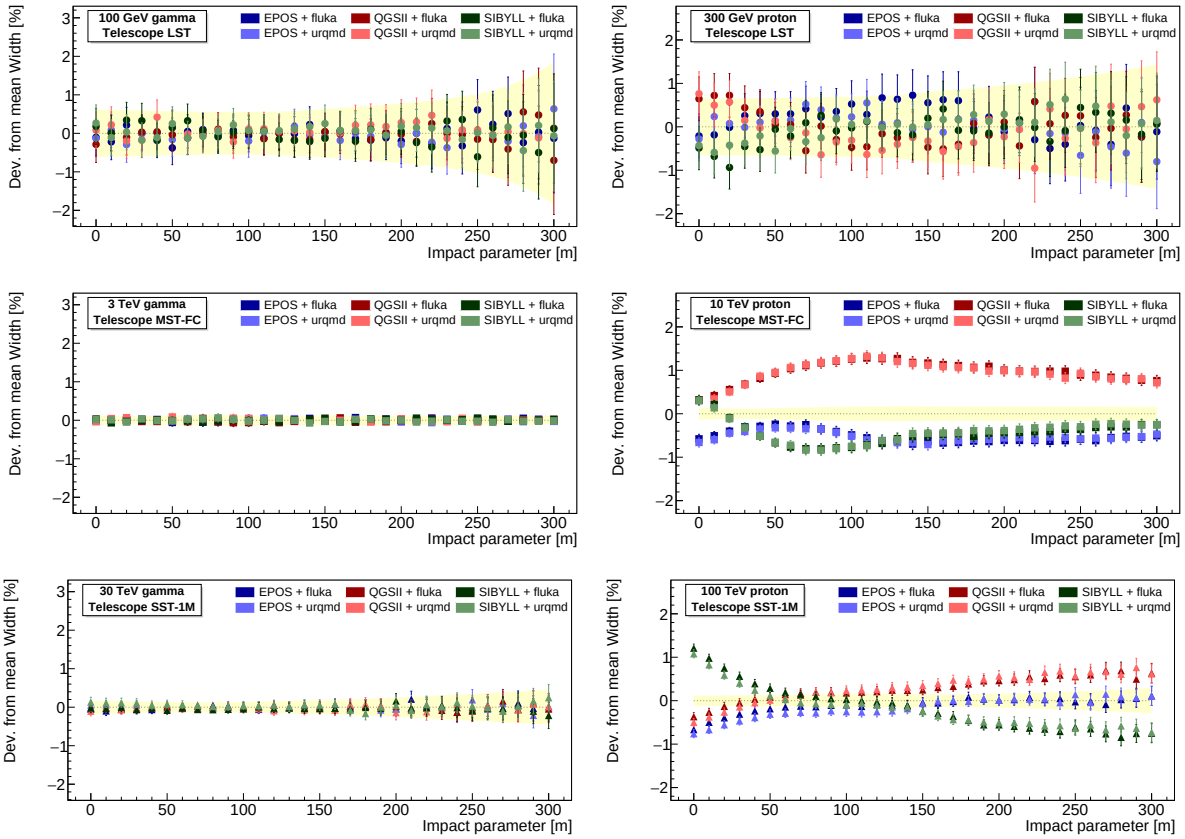

Figure 45 – Relative percentage deviation of the average image width as computed by each hadronic interaction model with respect to a global mean, averaged over all models. Left (right) column is for gamma ray (proton) showers whose energies are indicated in the top left corner of each box.

Source: By the author

8.4 Sensitivity of the Cherenkov Telescope Array

The results presented in the previous section are of preliminary character and were idealized as part of a major study towards the investigation of the relevance of hadronic interactions in IACT measurements. However, by getting in touch with M. Ohishi, who was already carrying out similar work in a more advanced stage, the present author and collaborators joined efforts with her towards a publication on the effect of the uncertainties of hadronic interaction models on the estimated CTA sensitivity. This collaboration includes other members from the ASWG and was established by 2018.

M. Ohishi has performed the computation of a set of sensitivity curves for the CTA using a set of different hadronic interaction models. From the comparison of the different curves computed using distinct models, an insight on uncertainties that accompany an estimated sensitivity curve can be obtained. A preliminary result of this work has been presented by M. Ohishi in the 16th International Conference on Topics in As-

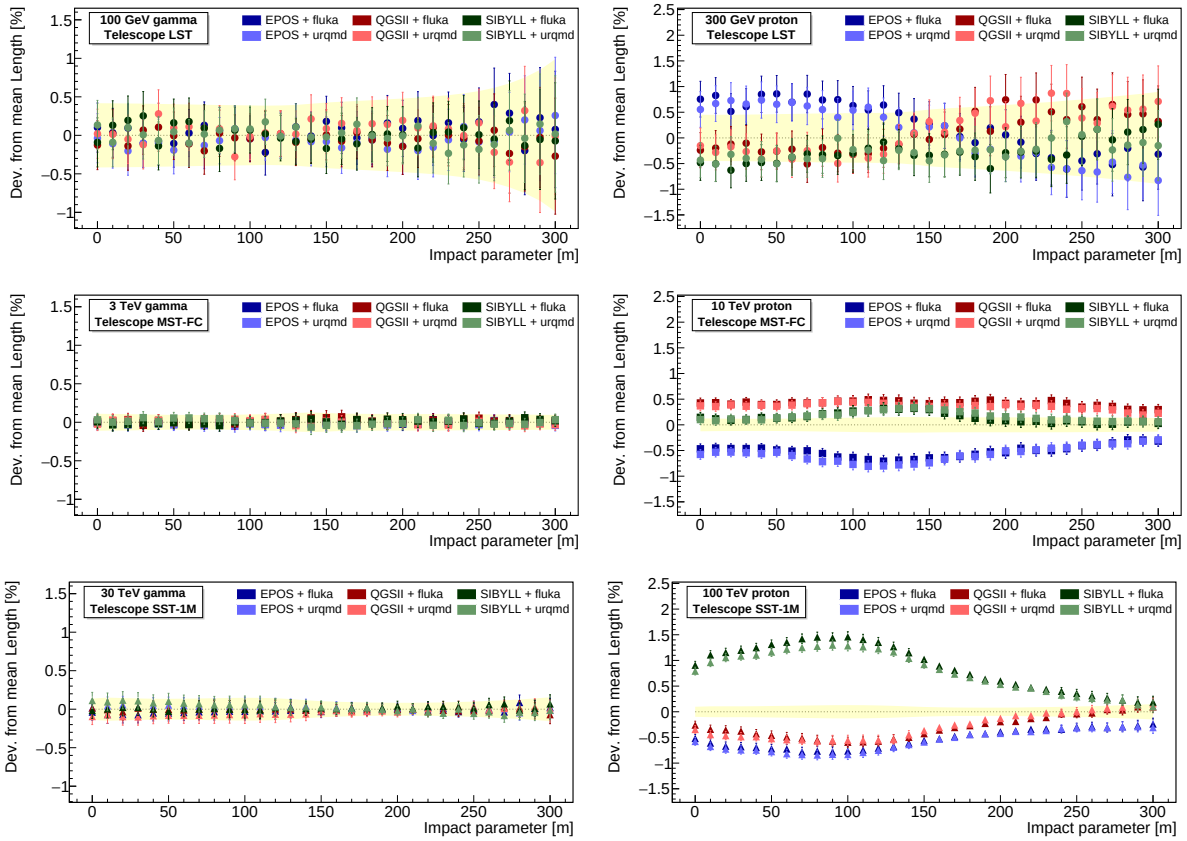

Figure 46 – Relative percentage deviation of the average image length as computed by each hadronic interaction model with respect to a global mean, averaged over all models. Left (right) column is for gamma ray (proton) showers whose energies are indicated in the top left corner of each box.

Source: By the author

troparticle and Underground Physics (TAUP 2019) and is available in the conference proceedings. (274) The sensitivity curves presented at this conference are reproduced in Figure 47. The curves shown in this figure carry the important message that there is a non-negligible uncertainty on the estimation of the CTA sensitivity that is due to modeling hadronic interactions. Indeed, discrepancies are most evident in the region from 1 TeV to 30 TeV, in which the average difference reach 32% when comparing EPOS-LHC and QGSJetII-04.

The present author has contributed to early discussions of this work and, more recently, on the writing of the manuscript of a paper with the computations by M. Ohishi. This manuscript is under internal revision in the CTA collaboration and will be submitted for publication soon.

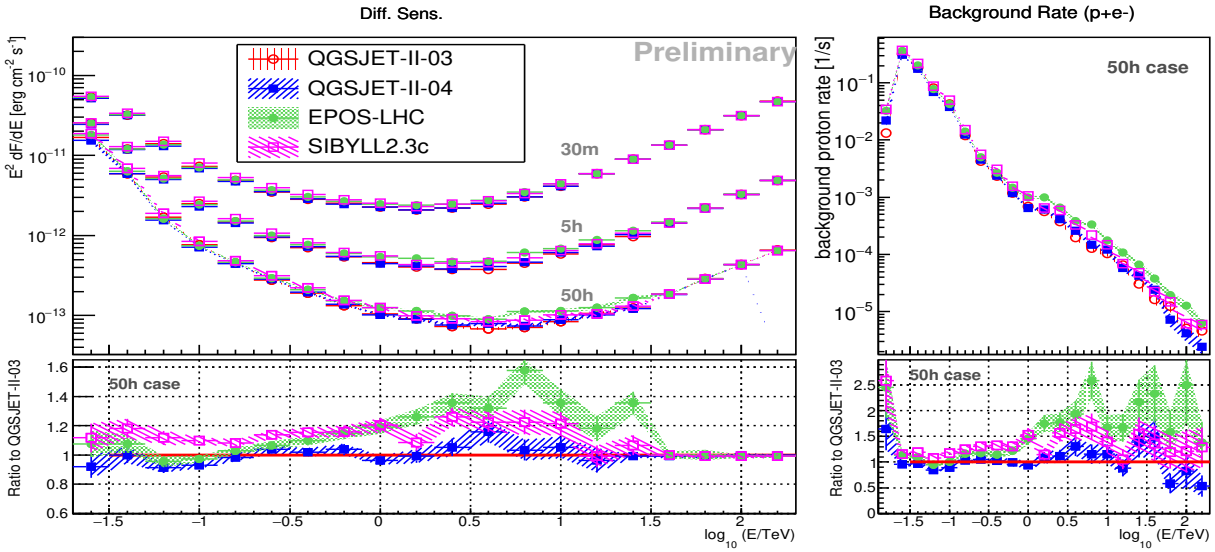

Figure 47 – Left: differential gamma-ray sensitivity curves computed for the CTA south array using different hadronic interaction models. The small plot at the bottom shows the ratios to the curve derived with QGSJetII-03. Right: residual background rate (after selection cuts) as prescribed from different hadronic interaction models and, at the bottom, ratios to QGSJetII-03.

Source: OHISHI *et al.* (274)

8.5 Conclusion

This chapter has been elaborated to discuss the role of hadronic interaction models in the context of IACT systems and, in particular, of the CTA. The original results from the present author are summarized in Section 8.2, in which the impact of hadronic interaction models on the Hillas parameters is investigated. From these results, it is clear that investigations on the importance of hadronic interaction models on IACT systems are necessary. It has been shown that the comparison of models, even when looking at the simple averages of the basic image parameters, reveals non-negligible discrepancies. In Section 8.4 the CTA sensitivity curves estimated with different hadronic interaction models were compared and it has been seen that a significant influence from hadronic interaction model exists. This work, lead by M. Ohishi, highlights the importance of studying hadronic interactions in the context of the CTA. Importantly, it shows that as observables at the CTA will be sensible to hadronic interactions, this experiment will have the potential to constrain hadronic interaction models from measurements of extensive air showers.

9 FINAL REMARKS

This thesis was dedicated to the study of extensive air showers from simulations in view of its detection by different ground-based detectors. As a summary, an outlook of the results from Chapters 5, 6, 7, and 8 is presented.

First, Chapter 5 was dedicated to study and parametrize the fluctuations of the depth at which a shower reaches its maximum, $X_{\max}$. Specifically, a study was performed to find the best functional form to describe the distributions of $X_{\max}$ in the ultra-high-energy range ($E \geq 10^{17}$ eV) and covering four groups of primary masses ($A = 1, 12, 28, 56$). An extensive library of extensive air showers was built, from which $X_{\max}$ distributions were extracted and fitted to three different functions. It was found that, in the overall case, the Generalized Gumbel distribution provides the best description of the simulated $X_{\max}$ distributions. All three functions studied, each with three parameters, were parametrized as a function of the primary energy and mass.

This study on the $X_{\max}$ distributions is of importance for the cosmic-ray physics community, as there was no available systematic comparison between the functions commonly used to describe these distributions prior to the current work. Beside that, previous parametrizations were not derived from the most up to date hadronic interaction models, as done in this study. In a more wide context, this work ultimately contributes to the understanding of the primary mass composition of ultra-high-energy cosmic rays and, therefore, to unveil their origin. Indeed, these results provide a practical tool to evaluate $X_{\max}$ distributions without having to simulate them and has already been used to constrain cosmic-ray-source models (275) and to study the acceptance of future observatories. (267)

The second study, presented in Chapter 6 of this thesis, consisted of a parametrization of the angular distribution of Cherenkov-light emission in extensive air showers. This study comprised, in a first step, a survey to understand what shower variables are necessary to describe the emission of Cherenkov light from air showers. After that, simplifications to an analytic, exact model were made to find a practical functional form that could be parametrized. A four-parameter function, then, was proposed. This function was parametrized in an energy range covering both typical IACT energies and Auger energies with the aim to provide a single, universal parametrization. Besides that, the studied angular interval comprises both detection regions relevant for IACTs and detection of ultra-high-energy cosmic rays. It was seen that the obtained parametrization largely improves the precision of previous works, mainly in the region $\theta < 5°$.

The third study was presented in Chapter 7. In this work, a method was developed

to reconstruct X_{max} using IACTs. The primary motivation for this study was the ability of IACTs to observe cosmic rays in the knee region and the possibility of understanding the mass composition on X_{max}-based analyses. The realization of the method relies on projecting the Cherenkov light reaching a detector back to a shower-face plane from which a longitudinal profile of Cherenkov-light emission can be derived and the corresponding depth of shower maximum computed. It was found that X_{max} can be effectively reconstructed with this method. A reasonable resolution ($\sigma \approx 20\,\mathrm{g/cm^2}$ at 100 TeV) that improves with increasing primary energy was found. By using a fictitious array of ideal telescopes on the simulation, this study serves as a proof of concept that X_{max} can be derived from the Cherenkov-light profiles seen by IACTs. Moreover, the study was based on the computation of a new observable that can be used to improve gamma-hadron separation in gamma-ray-based studies.

Finally, the fourth study was described in Chaper 8. This chapter dealt with an important aspect of the simulation of extensive air showers: hadronic interaction models. It was shown that different hadronic interaction models used in the simulation of IACT systems produce different outcomes in the simulation of detectors. In particular, the Hillas parameters width, length, and size were investigated and shown to be sensible to hadronic interactions for hadronic showers. In the following, the effect of the uncertainty in hadronic interaction models on the estimated sensitivity curve of the CTA was quantified. It was found that there is non-negligible influence of hadronic models on the estimation of the CTA sensitivity.

REFERENCES

1 HESS, V. F. Über Beobachtungen der durchdringenden Strahlung bei sieben Freiballonfahrten. **Physikalische Zeitschrift**, v. 13, n. 1084-1091, p. 24, 1912. Available at: https://www.mpi-hd.mpg.de/hfm/HESS/public/HessArticle.pdf. Access at: Dec. 2, 2020.

2 HILLAS, A. M. **Cosmic rays**. Oxford: Pergamon, 1972. (The Commonwealth and International Library: Selected Readings in Physics). DOI: 10.1016/C2013-0-02469-3. ISBN 978-0-08-016724-4.

3 KAMPERT, K.-H.; WATSON, A. A. Extensive air showers and ultra high-energy cosmic rays: a historical review. **The European Physical Journal H**, Springer Science and Business Media LLC, v. 37, n. 3, p. 359–412, July 2012. DOI: 10.1140/epjh/e2012-30013-x.

4 MILLIKAN, R. A.; OTIS, R. M. High frequency rays of cosmic origin II: mountain peak and airplane observations. **Physical Review**, American Physical Society, v. 27, n. 6, p. 645–658, June 1926. DOI: 10.1103/physrev.27.645.

5 MILLIKAN, R. A.; CAMERON, G. H. High frequency rays of cosmic origin III: measurements in snow-fed lakes at high altitudes. **Physical Review**, American Physical Society, v. 28, n. 5, p. 851–868, Nov. 1926. DOI: 10.1103/physrev.28.851.

6 BOTHE, W.; KOLHÖRSTER, W. Das Wesen der Höhenstrahlung. **Zeitschrift für Physik**, Springer Science and Business Media LLC, v. 56, n. 11-12, p. 751–777, Nov. 1929. DOI: 10.1007/bf01340137.

7 ANDERSON, C. D. The positive electron. **Physical Review**, American Physical Society, v. 43, n. 6, p. 491–494, Mar. 1933. DOI: 10.1103/physrev.43.491.

8 BLACKETT, P. M. S.; OCCHIALINI, G. P. S. Some photographs of the tracks of penetrating radiation. **Proceedings of the Royal Society A**, The Royal Society, v. 139, n. 839, p. 699–726, Mar. 1933. DOI: 10.1098/rspa.1933.0048.

9 MAZE, R. Étude d'un appareil à grand pouvoir de résolution pour rayons cosmiques. **Journal de Physique et le Radium**, EDP Sciences, v. 9, n. 4, p. 162–168, 1938. DOI: 10.1051/jphysrad:0193800904016200.

10 AUGER, P. *et al.* Extensive cosmic-ray showers. **Reviews of Modern Physics**, American Physical Society, v. 11, n. 3-4, p. 288–291, July 1939. DOI: 10.1103/revmodphys.11.288.

11 LINSLEY, J.; SCARSI, L.; ROSSI, B. Extremely energetic cosmic-ray event. **Physical Review Letters**, American Physical Society, v. 6, n. 9, p. 485–487, May 1961. DOI: 10.1103/physrevlett.6.485.

12 LINSLEY, J. Primary cosmic rays of energy 10^{17} to 10^{20} eV: the energy spectrum and arrival directions. *In*: INTERNATIONAL COSMIC RAY CONFERENCE, 8., 1963, Jaipur. **Proceedings** [**...**]. Bombay, India: Commercial Printing Press Ltd., 1963. v. 4,

p. 77–99. Available at: https://ui.adsabs.harvard.edu/abs/1963ICRC....4...77L. Access at: Dec. 3, 2020.

13 TENNENT, R. M. The Haverah Park extensive air shower array. **Proceedings of the Physical Society**, IOP Publishing, v. 92, n. 3, p. 622–631, Nov. 1967. DOI: 10.1088/0370-1328/92/3/315.

14 WINN, M. M. *et al.* The cosmic-ray energy spectrum above 10^{17} eV. **Journal of Physics G**: nuclear and particle physics, IOP Publishing, v. 12, n. 7, p. 653–674, July 1986. DOI: 10.1088/0305-4616/12/7/015.

15 CHIBA, N. *et al.* Akeno giant air shower array (AGASA) covering 100 km^2 area. **Nuclear Instruments and Methods in Physics Research Section A**: accelerators, spectrometers, detectors and associated equipment, Elsevier BV, v. 311, n. 1-2, p. 338–349, Jan. 1992. DOI: 10.1016/0168-9002(92)90882-5.

16 ANATOLY, I. The Yakutsk array experiment: main results and future directions. **EPJ Web of Conferences**, EDP Sciences, v. 53, p. 04003, 2013. DOI: 10.1051/epjconf/20135304003.

17 GREISEN, K. End to the cosmic-ray spectrum? **Physical Review Letters**, American Physical Society, v. 16, n. 17, p. 748–750, Apr. 1966. DOI: 10.1103/physrevlett.16.748.

18 ZATSEPIN, G.; KUZMIN, V. Upper limit of the spectrum of cosmic rays. **JETP Letters**, v. 4, p. 78–80, 1966.

19 ABBASI, R. U. *et al.* First observation of the Greisen-Zatsepin-Kuzmin suppression. **Physical Review Letters**, American Physical Society, v. 100, n. 10, p. 101101, Mar. 2008. DOI: 10.1103/physrevlett.100.101101.

20 ABRAHAM, J. *et al.* Observation of the suppression of the flux of cosmic rays above 4×10^{19} eV. **Physical Review Letters**, American Physical Society, v. 101, n. 6, p. 061101, Aug. 2008. DOI: 10.1103/physrevlett.101.061101.

21 TAKEDA, M. *et al.* Extension of the cosmic-ray energy spectrum beyond the predicted Greisen-Zatsepin-Kuz'min cutoff. **Physical Review Letters**, American Physical Society, v. 81, n. 6, p. 1163–1166, Aug. 1998. DOI: 10.1103/physrevlett.81.1163.

22 BALTRUSAITIS, R. M. *et al.* Evidence for a high-energy cosmic-ray spectrum cutoff. **Physical Review Letters**, American Physical Society, v. 54, n. 16, p. 1875–1877, Apr. 1985. DOI: 10.1103/physrevlett.54.1875.

23 WATSON, A. A. High-energy cosmic rays and the Greisen-Zatsepin-Kuz'min effect. **Reports on Progress in Physics**, IOP Publishing, v. 77, n. 3, p. 036901, Feb. 2014. DOI: 10.1088/0034-4885/77/3/036901.

24 AAB, A. *et al.* The Pierre Auger Cosmic Ray Observatory. **Nuclear Instruments and Methods in Physics Research Section A**: accelerators, spectrometers, detectors and associated equipment, Elsevier BV, v. 798, p. 172–213, Oct. 2015. DOI: 10.1016/j.nima.2015.06.058.

25 KAWAI, H. *et al.* Telescope Array Experiment. **Nuclear Physics B**: proceedings supplements, Elsevier BV, v. 175-176, p. 221–226, Jan. 2008. DOI: 10.1016/j.nuclphysbps.2007.11.002.

26 AAB, A. *et al.* Measurement of the cosmic-ray energy spectrum above 2.5×10^{18} eV using the Pierre Auger Observatory. **Physical Review D**, American Physical Society, v. 102, n. 6, p. 062005, Sept. 2020. DOI: 10.1103/physrevd.102.062005.

27 ABRAHAM, J. *et al.* Measurement of the depth of maximum of extensive air showers above 10^{18} eV. **Physical Review Letters**, American Physical Society, v. 104, n. 9, p. 091101, Mar. 2010. DOI: 10.1103/physrevlett.104.091101.

28 ABREU, P. *et al.* Interpretation of the depths of maximum of extensive air showers measured by the Pierre Auger Observatory. **Journal of Cosmology and Astroparticle Physics**, IOP Publishing, v. 2013, n. 02, p. 026–026, Feb. 2013. DOI: 10.1088/1475-7516/2013/02/026.

29 AAB, A. *et al.* Depth of maximum of air-shower profiles at the Pierre Auger Observatory: composition implications. **Physical Review D**, American Physical Society, v. 90, n. 12, p. 122006, Dec. 2014. DOI: 10.1103/physrevd.90.122006.

30 AAB, A. *et al.* Evidence for a mixed mass composition at the 'ankle' in the cosmic-ray spectrum. **Physics Letters B**, Elsevier BV, v. 762, p. 288–295, Nov. 2016. DOI: 10.1016/j.physletb.2016.09.039.

31 BELLIDO, J. Depth of maximum of air-shower profiles at the Pierre Auger Observatory: measurements above $10^{17.2}$ eV and composition implications. **Proceedings of Science**, v. 301, p. 506, 2017. DOI: 10.22323/1.301.0506.

32 AAB, A. *et al.* Inferences on mass composition and tests of hadronic interactions from 0.3 to 100 EeV using the water-Cherenkov detectors of the Pierre Auger Observatory. **Physical Review D**, American Physical Society, v. 96, n. 12, p. 122003, Dec. 2017. DOI: 10.1103/physrevd.96.122003.

33 YUSHKOV, A. Mass composition of cosmic rays with energies above $10^{17.2}$ eV from the hybrid data of the Pierre Auger Observatory. **Proceedings of Science**, v. 358, p. 482, 2019. DOI: 10.22323/1.358.0482.

34 ENGEL, R.; HECK, D.; PIEROG, T. Extensive air showers and hadronic interactions at high energy. **Annual Review of Nuclear and Particle Science**, Annual Reviews, v. 61, n. 1, p. 467–489, Nov. 2011. DOI: 10.1146/annurev.nucl.012809.104544.

35 PTUSKIN, V. Propagation of galactic cosmic rays. **Astroparticle Physics**, Elsevier BV, v. 39-40, p. 44–51, Dec. 2012. DOI: 10.1016/j.astropartphys.2011.11.004.

36 BLASI, P. The origin of galactic cosmic rays. **The Astronomy and Astrophysics Review**, Springer Science and Business Media LLC, v. 21, n. 1, p. 70, Nov. 2013. DOI: 10.1007/s00159-013-0070-7.

37 LIPARI, P.; VERNETTO, S. The shape of the cosmic ray proton spectrum. **Astroparticle Physics**, Elsevier BV, v. 120, p. 102441, July 2020. DOI: 10.1016/j.astropartphys.2020.102441.

38 ALOISIO, R. *et al.* Selected topics in cosmic ray physics. *In*: ALOISIO, R.; COCCIA, E.; VISSANI, F. (ed.). **Multiple messengers and challenges in astroparticle physics**. Cham: Springer International Publishing, 2018. cap. 1, p. 1–95. DOI: 10.1007/978-3-319-65425-6_1.

39 BLÜMER, J.; ENGEL, R.; HÖRANDEL, J. R. Cosmic rays from the knee to the highest energies. **Progress in Particle and Nuclear Physics**, Elsevier BV, v. 63, n. 2, p. 293–338, Oct. 2009. DOI: 10.1016/j.ppnp.2009.05.002.

40 BERTAINA, M. *et al.* The cosmic ray spectrum and composition measured by KASCADE-Grande between 10^{16} eV and 10^{18} eV. **Nuclear Physics B**: proceedings supplements, Elsevier BV, v. 256-257, p. 149–160, Nov. 2014. DOI: 10.1016/j.nuclphysbps.2014.10.018.

41 APEL, W. D. *et al.* Kneelike structure in the spectrum of the heavy component of cosmic rays observed with KASCADE-Grande. **Physical Review Letters**, American Physical Society, v. 107, n. 17, p. 171104, Oct. 2011. DOI: 10.1103/physrevlett.107.171104.

42 BUDNEV, N. *et al.* Tunka-25 air shower Cherenkov array: the main results. **Astroparticle Physics**, Elsevier BV, v. 50-52, p. 18–25, Dec. 2013. DOI: 10.1016/j.astropartphys.2013.09.006.

43 PROSIN, V. *et al.* Tunka-133: results of 3 year operation. **Nuclear Instruments and Methods in Physics Research Section A**: accelerators, spectrometers, detectors and associated equipment, Elsevier BV, v. 756, p. 94–101, Aug. 2014. DOI: 10.1016/j.nima.2013.09.018.

44 AARTSEN, M. G. *et al.* Measurement of the cosmic ray energy spectrum with IceTop-73. **Physical Review D**, American Physical Society, v. 88, n. 4, p. 042004, Aug. 2013. DOI: 10.1103/physrevd.88.042004.

45 SARAZIN, F. *et al.* What is the nature and origin of the highest-energy particles in the universe? **Bulletin of the American Astronomical Society**, v. 51, n. 3, p. 93, May 2019. Available at: https://baas.aas.org/pub/2020n3i093/release/1. Access at: Aug. 19, 2020.

46 DELIGNY, O. Cosmic rays around 10^{18} eV: implications of contemporary measurements on the origin of the ankle feature. **Comptes Rendus Physique**, Elsevier BV, v. 15, n. 4, p. 367–375, Apr. 2014. DOI: 10.1016/j.crhy.2014.02.009.

47 AAB, A. *et al.* Observation of a large-scale anisotropy in the arrival directions of cosmic rays above 8×10^{18} eV. **Science**, American Association for the Advancement of Scienc, v. 357, n. 6357, p. 1266–1270, Sept. 2017. DOI: 10.1126/science.aan4338.

48 AAB, A. *et al.* Large-scale cosmic-ray anisotropies above 4 EeV measured by the Pierre Auger Observatory. **The Astrophysical Journal**, American Astronomical Society, v. 868, n. 1, p. 4, Nov. 2018. DOI: 10.3847/1538-4357/aae689.

49 DELIGNY, O. The energy spectrum of ultra-high energy cosmic rays measured at the Pierre Auger Observatory and at the Telescope Array. **Proceedings of Science**, v. 358, p. 234, 2019. DOI: 10.22323/1.358.0234.

50 IVANOV, D. Energy spectrum measured by the Telescope Array. **Proceedings of Science**, v. 358, p. 298, 2019. DOI: 10.22323/1.358.0298.

51 AAB, A. *et al.* Features of the energy spectrum of cosmic rays above 2.5×10^{18} eV using the Pierre Auger Observatory. **Physical Review Letters**, American Physical Society, v. 125, n. 12, p. 121106, Sept. 2020. DOI: 10.1103/physrevlett.125.121106.

52 BEREZINSKY, V.; GAZIZOV, A.; GRIGORIEVA, S. On astrophysical solution to ultrahigh energy cosmic rays. **Physical Review D**, American Physical Society, v. 74, n. 4, p. 043005, Aug. 2006. DOI: 10.1103/physrevd.74.043005.

53 ALOISIO, R. *et al.* A dip in the UHECR spectrum and the transition from galactic to extragalactic cosmic rays. **Astroparticle Physics**, Elsevier BV, v. 27, n. 1, p. 76–91, Feb. 2007. DOI: 10.1016/j.astropartphys.2006.09.004.

54 ABU-ZAYYAD, T. *et al.* Evidence for changing of cosmic ray composition between 10^{17} and 10^{18} eV from multicomponent measurements. **Physical Review Letters**, American Physical Society, v. 84, n. 19, p. 4276–4279, May 2000. DOI: 10.1103/physrevlett.84.4276.

55 ABBASI, R. U. *et al.* A study of the composition of ultra-high-energy cosmic rays using the High-Resolution Fly's Eye. **The Astrophysical Journal**, American Astronomical Society, v. 622, n. 2, p. 910–926, Apr. 2005. DOI: 10.1086/427931.

56 GLUSHKOV, A. V. *et al.* Muons in extensive air showers of energies $e_0 = 10^{16.6}$–$10^{19.8}$ eV. **Journal of Experimental and Theoretical Physics Letters**, Pleiades Publishing Ltd, v. 71, n. 3, p. 97–101, Feb. 2000. DOI: 10.1134/1.568289.

57 ALOISIO, R.; BEREZINSKY, V.; BLASI, P. Ultra high energy cosmic rays: implications of Auger data for source spectra and chemical composition. **Journal of Cosmology and Astroparticle Physics**, IOP Publishing, v. 2014, n. 10, p. 020–020, Oct. 2014. DOI: 10.1088/1475-7516/2014/10/020.

58 ALOISIO, R.; BEREZINSKY, V.; GAZIZOV, A. Ultra high energy cosmic rays: the disappointing model. **Astroparticle Physics**, Elsevier BV, v. 34, n. 8, p. 620–626, Mar. 2011. DOI: 10.1016/j.astropartphys.2010.12.008.

59 TAYLOR, A. M. UHECR composition models. **Astroparticle Physics**, Elsevier BV, v. 54, p. 48–53, Feb. 2014. DOI: 10.1016/j.astropartphys.2013.11.006.

60 TAYLOR, A. M.; AHLERS, M.; HOOPER, D. Indications of negative evolution for the sources of the highest energy cosmic rays. **Physical Review D**, American Physical Society, v. 92, n. 6, p. 063011, Sept. 2015. DOI: 10.1103/physrevd.92.063011.

61 AAB, A. *et al.* Combined fit of spectrum and composition data as measured by the Pierre Auger Observatory. **Journal of Cosmology and Astroparticle Physics**, IOP Publishing, v. 2017, n. 04, p. 038–038, Apr. 2017. DOI: 10.1088/1475-7516/2017/04/038.

62 AAB, A. *et al.* The Pierre Auger Observatory and its upgrade. **Science Reviews - from the end of the world**, Centro de Estudios sobre Ciencia, Desarrollo y Educación Superior, v. 1, n. 4, p. 8–33, Sept. 2020.

63 ALLEKOTTE, I. *et al.* The surface detector system of the Pierre Auger Observatory. **Nuclear Instruments and Methods in Physics Research Section A**: accelerators, spectrometers, detectors and associated equipment, Elsevier BV, v. 586, n. 3, p. 409–420, Mar. 2008. DOI: 10.1016/j.nima.2007.12.016.

64 ABRAHAM, J. *et al.* Trigger and aperture of the surface detector array of the Pierre Auger Observatory. **Nuclear Instruments and Methods in Physics Research Section A**: accelerators, spectrometers, detectors and associated equipment, Elsevier BV, v. 613, n. 1, p. 29–39, Jan. 2010. DOI: 10.1016/j.nima.2009.11.018.

65 AAB, A. *et al.* Reconstruction of events recorded with the surface detector of the Pierre Auger Observatory. **Journal of Instrumentation**, IOP Publishing, v. 15, n. 10, p. P10021–P10021, Oct. 2020. DOI: 10.1088/1748-0221/15/10/p10021.

66 AAB, A. *et al.* Measurement of the cosmic ray spectrum above 4×10^{18} eV using inclined events detected with the Pierre Auger Observatory. **Journal of Cosmology and Astroparticle Physics**, IOP Publishing, v. 2015, n. 08, p. 049, Aug. 2015. DOI: 10.1088/1475-7516/2015/08/049.

67 ABRAHAM, J. *et al.* The fluorescence detector of the Pierre Auger Observatory. **Nuclear Instruments and Methods in Physics Research Section A**: accelerators, spectrometers, detectors and associated equipment, Elsevier BV, v. 620, n. 2-3, p. 227–251, Aug. 2010. DOI: 10.1016/j.nima.2010.04.023.

68 AVE, M. *et al.* Measurement of the pressure dependence of air fluorescence emission induced by electrons. **Astroparticle Physics**, Elsevier BV, v. 28, n. 1, p. 41–57, Sept. 2007. DOI: 10.1016/j.astropartphys.2007.04.006.

69 KUEMPEL, D.; KAMPERT, K.; RISSE, M. Geometry reconstruction of fluorescence detectors revisited. **Astroparticle Physics**, Elsevier BV, v. 30, n. 4, p. 167–174, Nov. 2008. DOI: 10.1016/j.astropartphys.2008.08.003.

70 BONIFAZI, C. The angular resolution of the Pierre Auger Observatory. **Nuclear Physics B**: proceedings supplements, Elsevier BV, v. 190, p. 20–25, May 2009. DOI: 10.1016/j.nuclphysbps.2009.03.063.

71 UNGER, M. *et al.* Reconstruction of longitudinal profiles of ultra-high energy cosmic ray showers from fluorescence and Cherenkov light measurements. **Nuclear Instruments and Methods in Physics Research Section A**: accelerators, spectrometers, detectors and associated equipment, Elsevier BV, v. 588, n. 3, p. 433–441, Apr. 2008. DOI: 10.1016/j.nima.2008.01.100.

72 GAISSER, T. K.; HILLAS, A. M. Reliability of the method of constant intensity cuts for reconstructing the average development of vertical showers. *In*: INTERNATIONAL COSMIC RAY CONFERENCE, 15., 1977, Plovdiv. **Proceedings [...]**. Bulgaria: Bulgarian Academy of Sciences, 1977. v. 8, p. 353–357. Available at: https://ui.adsabs.harvard.edu/abs/1977ICRC....8..353G. Access at: Dec. 30, 2020.

73 AAB, A. *et al.* Data-driven estimation of the invisible energy of cosmic ray showers with the Pierre Auger Observatory. **Physical Review D**, American Physical Society, v. 100, n. 8, p. 082003, Oct. 2019. DOI: 10.1103/physrevd.100.082003.

74 ABBASI, R. U. *et al.* The cosmic ray energy spectrum between 2 PeV and 2 EeV observed with the TALE detector in monocular mode. **The Astrophysical Journal**, American Astronomical Society, v. 865, n. 1, p. 74, Sept. 2018. DOI: 10.3847/1538-4357/aada05.

75 NOVOTNY, V. Measurement of the spectrum of cosmic rays above $10^{16.5}$ eV with Cherenkov-dominated events at the Pierre Auger Observatory. **Proceedings of Science**, v. 358, p. 374, 2019. DOI: 10.22323/1.358.0374.

76 NOVOTNÝ, V. **Measurement of the energy spectrum of cosmic rays using Cherenkov-dominated data at the Pierre Auger Observatory**. 2020. Ph. D. Thesis (Physics) — Charles University, Prague, Czech Republic, 2020. Available at: https://is.cuni.cz/webapps/zzp/detail/135800/. Access at: Dec. 7, 2020.

77 GILER, A. G. D. *et al.* Measuring the depth of shower maximum of extensive air showers using Cherenkov light. **Astroparticle Physics**, Elsevier BV, v. 124, p. 102508, Jan. 2021. DOI: 10.1016/j.astropartphys.2020.102508.

78 VERZI, V. Measurement of the energy spectrum of ultra-high energy cosmic rays using the Pierre Auger Observatory. **Proceedings of Science**, v. 358, p. 450, 2019. DOI: 10.22323/1.358.0450.

79 ABRAHAM, J. *et al.* Measurement of the energy spectrum of cosmic rays above 10^{18} eV using the Pierre Auger Observatory. **Physics Letters B**, Elsevier BV, v. 685, n. 4-5, p. 239–246, Mar. 2010. DOI: 10.1016/j.physletb.2010.02.013.

80 SETTIMO, M. Measurement of the cosmic ray energy spectrum using hybrid events of the Pierre Auger Observatory. **The European Physical Journal Plus**, Springer Science and Business Media LLC, v. 127, n. 8, p. 87, Aug. 2012. DOI: 10.1140/epjp/i2012-12087-9.

81 COLEMAN, A. Measurement of the cosmic ray flux near the second knee with the Pierre Auger Observatory. **Proceedings of Science**, v. 358, p. 225, 2019. DOI: 10.22323/1.358.0225.

82 KAMPERT, K.-H.; UNGER, M. Measurements of the cosmic ray composition with air shower experiments. **Astroparticle Physics**, Elsevier BV, v. 35, n. 10, p. 660–678, May 2012. DOI: 10.1016/j.astropartphys.2012.02.004.

83 UNGER, M. Composition studies with the Pierre Auger Observatory. **Nuclear Physics B**: proceedings supplements, Elsevier BV, v. 190, p. 240–246, May 2009. DOI: 10.1016/j.nuclphysbps.2009.03.094.

84 AAB, A. *et al.* Depth of maximum of air-shower profiles at the Pierre Auger Observatory. I. Measurements at energies above $10^{17.8}$ eV. **Physical Review D**, American Physical Society, v. 90, n. 12, p. 122005, Dec. 2014. DOI: 10.1103/physrevd.90.122005.

85 PEIXOTO, C. J. T. Estimating the depth of shower maximum using the surface detectors of the Pierre Auger Observatory. **Proceedings of Science**, v. 358, p. 440, 2019. DOI: 10.22323/1.358.0440.

86 HOLDER, J. TeV gamma-ray astronomy: a summary. **Astroparticle Physics**, Elsevier BV, v. 39-40, p. 61–75, Dec. 2012. DOI: 10.1016/j.astropartphys.2012.02.014.

87 HILLAS, A. Evolution of ground-based gamma-ray astronomy from the early days to the Cherenkov Telescope Arrays. **Astroparticle Physics**, Elsevier BV, v. 43, p. 19–43, Mar. 2013. DOI: 10.1016/j.astropartphys.2012.06.002.

88 MIRZOYAN, R. Brief history of ground-based very high energy gamma-ray astrophysics with atmospheric air Cherenkov telescopes. **Astroparticle Physics**, Elsevier BV, v. 53, p. 91–99, Jan. 2014. DOI: 10.1016/j.astropartphys.2013.11.004.

89 ALFVÉN, H.; HERLOFSON, N. Cosmic radiation and radio stars. **Physical Review**, American Physical Society, v. 78, n. 5, p. 616–616, June 1950. DOI: 10.1103/physrev.78.616.

90 BAADE, W.; ZWICKY, F. Remarks on super-novae and cosmic rays. **Physical Review**, American Physical Society, v. 46, n. 1, p. 76–77, July 1934. DOI: 10.1103/physrev.46.76.2.

91 MORRISON, P. On gamma-ray astronomy. **Il Nuovo Cimento**, Springer Science and Business Media LLC, v. 7, n. 6, p. 858–865, Mar. 1958. DOI: 10.1007/bf02745590.

92 COCCONI, G. An air shower telescope and the detection of 10^{12} eV photon sources. *In*: INTERNATIONAL COSMIC RAY CONFERENCE, 6., 1959, Moscow. **Proceedings** [**...**]. 1960. v. 2, p. 309–311. Available at: https://ui.adsabs.harvard.edu/abs/1960ICRC....2..309C. Access at: Jan. 23, 2021.

93 JELLEY, J. V. In days of yore. *In*: TURVER, K. E. (ed.). **Very high energy gamma ray astronomy**. Dordrecht: Springer Netherlands, 1987. p. 27–37. DOI: 10.1007/978-94-009-3831-1_4.

94 GALBRAITH, W.; JELLEY, J. V. Light pulses from the night sky associated with cosmic rays. **Nature**, Springer Science and Business Media LLC, v. 171, n. 4347, p. 349–350, Feb. 1953. DOI: 10.1038/171349a0.

95 WEEKES, T. C. Very high energy gamma-ray astronomy. **Physics Reports**, Elsevier BV, v. 160, n. 1-2, p. 1–121, Mar. 1988. DOI: 10.1016/0370-1573(88)90177-9.

96 KRAUSHAAR, W. L. *et al.* High-energy cosmic gamma-ray observations from the OSO-3 satellite. **The Astrophysical Journal**, American Astronomical Society, v. 177, p. 341, Nov. 1972. DOI: 10.1086/151713.

97 FICHTEL, C. E. *et al.* High-energy gamma-ray results from the second small astronomy satellite. **The Astrophysical Journal**, American Astronomical Society, v. 198, p. 163, May 1975. DOI: 10.1086/153590.

98 BIGNAMI, G. F. *et al.* Galaxies and gamma-ray astronomy. **The Astrophysical Journal**, American Astronomical Society, v. 232, p. 649, Sept. 1979. DOI: 10.1086/157323.

99 SWANENBURG, B. N. *et al.* Second COS-B catalog of high-energy gamma-ray sources. **The Astrophysical Journal**, American Astronomical Society, v. 243, p. L69, Jan. 1981. DOI: 10.1086/183445.

100 GEHRELS, N.; CHIPMAN, E.; KNIFFEN, D. The Compton Gamma Ray Observatory. **The Astrophysical Journal Supplement Series**, American Astronomical Society, v. 92, p. 351, June 1994. DOI: 10.1086/191978.

101 THOMPSON, D. J. *et al.* Calibration of the Energetic Gamma-Ray Experiment Telescope (EGRET) for the Compton Gamma-Ray Observatory. **The Astrophysical Journal Supplement Series**, American Astronomical Society, v. 86, p. 629, June 1993. DOI: 10.1086/191793.

102 THOMPSON, D. J. Gamma ray astrophysics: the EGRET results. **Reports on Progress in Physics**, IOP Publishing, v. 71, n. 11, p. 116901, Nov. 2008. DOI: 10.1088/0034-4885/71/11/116901.

103 HARTMAN, R. C. *et al.* The third EGRET catalog of high-energy gamma-ray sources. **The Astrophysical Journal Supplement Series**, American Astronomical Society, v. 123, n. 1, p. 79–202, July 1999. DOI: 10.1086/313231.

104 TAVANI, M. *et al.* The AGILE mission. **Astronomy & Astrophysics**, EDP Sciences, v. 502, n. 3, p. 995–1013, Jan. 2009. DOI: 10.1051/0004-6361/200810527.

105 ATWOOD, W. B. *et al.* The large area telescope on the Fermi gamma-ray space telescope mission. **The Astrophysical Journal**, American Astronomical Society, v. 697, n. 2, p. 1071–1102, May 2009. DOI: 10.1088/0004-637x/697/2/1071.

106 TAVANI, M. Space-based gamma-ray astrophysics. *In*: ALOISIO, R.; COCCIA, E.; VISSANI, F. (ed.). **Multiple messengers and challenges in astroparticle physics**. Cham: Springer International Publishing, 2018. cap. 3, p. 145–193. DOI: 10.1007/978-3-319-65425-6_3.

107 FAZIO, G. G. *et al.* An experiment to search for discrete sources of cosmic gamma rays in the 10^{11} to 10^{12} eV region. **Canadian Journal of Physics**, Canadian Science Publishing, v. 46, n. 10, p. S451–S455, May 1968. DOI: 10.1139/p68-268.

108 WEEKES, T. C. *et al.* A search for discrete sources of cosmic gamma rays of energy 10^{11}–10^{12} eV. **The Astrophysical Journal**, American Astronomical Society, v. 174, p. 165, May 1972. DOI: 10.1086/151479.

109 BERGE, D.; FUNK, S.; HINTON, J. Background modelling in very-high-energy γ-ray astronomy. **Astronomy & Astrophysics**, EDP Sciences, v. 466, n. 3, p. 1219–1229, Apr. 2007. DOI: 10.1051/0004-6361:20066674.

110 FAZIO, G. G. *et al.* Detection of high-energy gamma rays from the Crab nebula. **The Astrophysical Journal**, American Astronomical Society, v. 175, p. L117, Aug. 1972. DOI: 10.1086/180998.

111 TURVER, K. E.; WEEKES, T. C. Gamma-ray astronomy from 10 to 100 GeV. **Il Nuovo Cimento B**, Springer Science and Business Media LLC, v. 45, n. 1, p. 99–108, May 1978. DOI: 10.1007/bf02904077.

112 TURVER, K. E.; WEEKES, T. C. Gamma-rays above 100 GeV. **Philosophical Transactions of the Royal Society of London, Series A**, The Royal Society, v. 301, n. 1462, p. 615–628, June 1981. DOI: 10.1098/rsta.1981.0140.

113 WEEKES, T. C. *et al.* Observation of TeV gamma rays from the Crab Nebula using the atmospheric Cerenkov imaging technique. **The Astrophysical Journal**, American Astronomical Society, v. 342, p. 379, July 1989. DOI: 10.1086/167599.

114 CAWLEY, M. F. *et al.* Observations of the Crab Nebula at energies $> 4 \cdot 10^{11}$ eV. *In*: INTERNATIONAL COSMIC RAY CONFERENCE, 19., 1985, La Jolla. **Proceedings** [**...**]. Washington D.C., USA: National Aeronautics and Space Administration, 1985. v. 1, p. 131–134. Available at: https://ui.adsabs.harvard.edu/abs/1985ICRC....1..131C. Access at: Jan. 22, 2021.

115 HILLAS, A. M. Cerenkov light images of EAS produced by primary gamma rays and by nuclei. *In*: INTERNATIONAL COSMIC RAY CONFERENCE, 19., 1985, La Jolla. **Proceedings** [**...**]. Washington D.C., USA: National Aeronautics and Space Administration, 1985. v. 3, p. 445–448. Available at: https://ui.adsabs.harvard.edu/abs/1985ICRC....3..445H. Access at: Jan. 18, 2021.

116 VACANTI, G. *et al.* Gamma-ray observations of the Crab Nebula at TeV energies. **The Astrophysical Journal**, American Astronomical Society, v. 377, p. 467–479, Aug. 1991. DOI: 10.1086/170376.

117 PUNCH, M. *et al.* Supercuts: an improved method of selecting gamma-rays. *In*: INTERNATIONAL COSMIC RAY CONFERENCE, 22., 1991, Dublin. **Proceedings** [**...**]. Dublin, Ireland: The Dublin Institute for Advanced Studies, 1991. v. 1, p. 464–467. Available at: http://adsabs.harvard.edu/abs/1991ICRC....1..464P. Access at: Jan. 22, 2021.

118 LANG, M. J. *et al.* TeV observations of the Crab Nebula and other plerions in the epoch 1988-91. *In*: INTERNATIONAL COSMIC RAY CONFERENCE, 22., 1991, Dublin. **Proceedings** [**...**]. Dublin, Ireland: The Dublin Institute for Advanced Studies, 1991. v. 1, p. 204–207. Available at: http://adsabs.harvard.edu/abs/1991ICRC....1..204L. Access at: Jan. 22, 2021.

119 CATANESE, M. *et al.* Discovery of gamma-ray emission above 350 GeV from the BL Lacertae object 1Es 2344+514. **The Astrophysical Journal**, American Astronomical Society, v. 501, n. 2, p. 616–623, July 1998. DOI: 10.1086/305857.

120 HORAN, D. *et al.* Detection of the BL Lacertae object H1426+428 at TeV gamma-ray energies. **The Astrophysical Journal**, American Astronomical Society, v. 571, n. 2, p. 753–762, June 2002. DOI: 10.1086/340019.

121 PUNCH, M. *et al.* Detection of TeV photons from the active galaxy Markarian 421. **Nature**, Springer Science and Business Media LLC, v. 358, n. 6386, p. 477–478, Aug. 1992. DOI: 10.1038/358477a0.

122 QUINN, J. *et al.* Detection of gamma rays with $E > 300$ GeV from Markarian 501. **The Astrophysical Journal**, American Astronomical Society, v. 456, n. 2, p. L83–L86, Jan. 1996. DOI: 10.1086/309878.

123 AHARONIAN, F. *et al.* The time averaged TeV energy spectrum of MKN 501 of the extraordinary 1997 outburst as measured with the stereoscopic Cherenkov telescope system of HEGRA. **Astronomy and Astrophysics**, v. 349, p. 11–28, Sept. 1999. Available at: https://arxiv.org/abs/astro-ph/9903386. Access at: Jan. 20, 2021.

124 KONOPELKO, A. Performance of the stereoscopic system of the HEGRA imaging air Cerenkov telescopes: Monte Carlo simulations and observations. **Astroparticle Physics**, Elsevier BV, v. 10, n. 4, p. 275–289, May 1999. DOI: 10.1016/s0927-6505(98)00062-0.

125 CHUDAKOV, A. E. *et al.* On the high energy photons from local sources. *In*: INTERNATIONAL COSMIC RAY CONFERENCE, 8., 1963, Jaipur. **Proceedings** [**...**]. Bombay, India: Commercial Printing Press Ltd., 1963. v. 4, p. 199–204. Available at: http://adsabs.harvard.edu/abs/1963ICRC....4..199C. Access at: Jan. 23, 2021.

126 GRINDLAY, J. E. *et al.* Results of a southern-hemisphere search for gamma-ray sources at energies of at least 300 GeV. **The Astrophysical Journal**, American Astronomical Society, v. 201, p. 82, Oct. 1975. DOI: 10.1086/153861.

127 SHUBNELL, M. *et al.* GRANITE: a steroscopic imaging cherenkov telescope system. **AIP Conference Proceedings**, AIP, v. 280, n. 1, p. 1171–1175, 1993. DOI: 10.1063/1.44150.

128 NESHPOR, Y. I. *et al.* BL Lac: A new ultrahigh-energy gamma-ray source. **Astronomy Reports**, Pleiades Publishing Ltd, v. 45, n. 4, p. 249–254, Apr. 2001. DOI: 10.1134/1.1361316.

129 LORENZ, E.; WAGNER, R. Very-high energy gamma-ray astronomy. **The European Physical Journal H**, Springer Science and Business Media LLC, v. 37, n. 3, p. 459–513, July 2012. DOI: 10.1140/epjh/e2012-30016-x.

130 NAUROIS, M. de; MAZIN, D. Ground-based detectors in very-high-energy gamma-ray astronomy. **Comptes Rendus Physique**, Elsevier BV, v. 16, n. 6-7, p. 610–627, Aug. 2015. DOI: 10.1016/j.crhy.2015.08.011.

131 PÜHLHOFER, G. *et al.* The technical performance of the HEGRA system of imaging air Cherenkov telescopes. **Astroparticle Physics**, Elsevier BV, v. 20, n. 3, p. 267–291, Dec. 2003. DOI: 10.1016/j.astropartphys.2003.06.001.

132 AHARONIAN, F. *et al.* Evidence for TeV gamma ray emission from Cassiopeia A. **Astronomy & Astrophysics**, EDP Sciences, v. 370, n. 1, p. 112–120, Apr. 2001. DOI: 10.1051/0004-6361:20010243.

133 AHARONIAN, F. *et al.* Is the giant radio galaxy M87 a TeV gamma-ray emitter? **Astronomy & Astrophysics**, EDP Sciences, v. 403, n. 1, p. L1–L5, Apr. 2003. DOI: 10.1051/0004-6361:20030372.

134 AHARONIAN, F. *et al.* An unidentified TeV source in the vicinity of Cygnus OB2. **Astronomy & Astrophysics**, EDP Sciences, v. 393, n. 2, p. L37–L40, Sept. 2002. DOI: 10.1051/0004-6361:20021171.

135 BERNLÖHR, K. *et al.* The optical system of the H.E.S.S. imaging atmospheric cherenkov telescopes. part I: layout and components of the system. **Astroparticle Physics**, Elsevier BV, v. 20, n. 2, p. 111–128, Nov. 2003. DOI: 10.1016/s0927-6505(03)00171-3.

136 CORNILS, R. *et al.* The optical system of the H.E.S.S. imaging atmospheric Cherenkov telescopes. part II: mirror alignment and point spread function. **Astroparticle Physics**, Elsevier BV, v. 20, n. 2, p. 129–143, Nov. 2003. DOI: 10.1016/s0927-6505(03)00172-5.

137 BOLMONT, J. *et al.* The camera of the fifth H.E.S.S. telescope. Part I: system description. **Nuclear Instruments and Methods in Physics Research Section A**: accelerators, spectrometers, detectors and associated equipment, Elsevier BV, v. 761, p. 46–57, Oct. 2014. DOI: 10.1016/j.nima.2014.05.093.

138 BAIXERAS, C. *et al.* Commissioning and first tests of the MAGIC telescope. **Nuclear Instruments and Methods in Physics Research Section A**: accelerators, spectrometers, detectors and associated equipment, Elsevier BV, v. 518, n. 1-2, p. 188–192, Feb. 2004. DOI: 10.1016/j.nima.2003.10.057.

139 ALEKSIĆ, J. *et al.* Performance of the MAGIC stereo system obtained with Crab Nebula data. **Astroparticle Physics**, Elsevier BV, v. 35, n. 7, p. 435–448, Feb. 2012. DOI: 10.1016/j.astropartphys.2011.11.007.

140 HOLDER, J. *et al.* The first VERITAS telescope. **Astroparticle Physics**, Elsevier BV, v. 25, n. 6, p. 391–401, July 2006. DOI: 10.1016/j.astropartphys.2006.04.002.

141 HOLDER, J. Veritas: status and highlights. *In*: INTERNATIONAL COSMIC RAY CONFERENCE, 32., 2011, Beijing. **Proceedings** [**...**]. Beijing, China, 2011. v. 12, p. 137–145. DOI: 10.7529/ICRC2011/V12/H11.

142 ABEYSEKARA, A. U. *et al.* Observation of the Crab Nebula with the HAWC gamma-ray observatory. **The Astrophysical Journal**, American Astronomical Society, v. 843, n. 1, p. 39, June 2017. DOI: 10.3847/1538-4357/aa7555.

143 ABEYSEKARA, A. *et al.* Sensitivity of the high altitude water Cherenkov detector to sources of multi-TeV gamma rays. **Astroparticle Physics**, Elsevier BV, v. 50-52, p. 26–32, Dec. 2013. DOI: 10.1016/j.astropartphys.2013.08.002.

144 ALBERT, A. *et al.* 3HWC: The third HAWC catalog of very-high-energy gamma-ray sources. **The Astrophysical Journal**, American Astronomical Society, v. 905, n. 1, p. 76, Dec. 2020. DOI: 10.3847/1538-4357/abc2d8.

145 OAKES, L. *et al.* Combined dark matter searches towards dwarf spheroidal galaxies with Fermi-LAT, HAWC, HESS, MAGIC and VERITAS. **Proceedings of Science**, v. 358, p. 012, 2019. DOI: 10.22323/1.358.0012.

146 JARDIN-BLICQ, A.; MARANDON, V.; BRUN, F. A complementary view of the galactic plane in TeV gamma rays by HAWC and H.E.S.S. **Proceedings of Science**, v. 358, p. 706, 2019. DOI: 10.22323/1.358.0706.

147 THE MAGIC TELESCOPES. Available at: https://magic.mpp.mpg.de/. Access at: Jan. 24, 2021.

148 VERITAS: Very Energetic Radiation Imaging Telescope Array System. Available at: https://veritas.sao.arizona.edu/. Access at: Jan. 24, 2021.

149 THE HIGH ENERGY STEREOSCOPIC SYSTEM. Available at: https://www.mpi-hd.mpg.de/hfm/HESS/. Access at: Jan. 24, 2021.

150 FEGAN, S. **Kifune plot**. GitHub: sfegan. Available at: https://github.com/sfegan/kifune-plot. Access at: Jan. 24, 2021.

151 WAKELY, S. P.; HORAN, D. TeVCat: an online catalog for very high energy gamma-ray astronomy. *In*: INTERNATIONAL COSMIC RAY CONFERENCE, 30., 2007, Mérida. **Proceedings** [...]. Mexico City, Mexico: Universidad Nacional Autónoma de México, 2008. v. 3, p. 1341–1344. Available at: https://indico.nucleares.unam.mx/event/4/contribution/378. Access at: Jan. 24, 2021.

152 KIFUNE, T. Ground-based gamma-ray astronomy: general remarks. **Il Nuovo Cimento C**, Springer Science and Business Media LLC, v. 19, n. 6, p. 953–957, Nov. 1996. DOI: 10.1007/bf02508136.

153 RIEGER, F. M.; OÑA-WILHELMI, E. de; AHARONIAN, F. A. TeV astronomy. **Frontiers of Physics**, Springer Science and Business Media LLC, v. 8, n. 6, p. 714–747, June 2013. DOI: 10.1007/s11467-013-0344-6.

154 FUNK, S. Ground- and space-based gamma-ray astronomy. **Annual Review of Nuclear and Particle Science**, Annual Reviews, v. 65, n. 1, p. 245–277, Oct. 2015. DOI: 10.1146/annurev-nucl-102014-022036.

155 HALZEN, F. Pionic photons and neutrinos from cosmic ray accelerators. **Astroparticle Physics**, Elsevier BV, v. 43, p. 155–162, Mar. 2013. DOI: 10.1016/j.astropartphys.2011.10.003.

156 ACERO, F. *et al.* Gamma-ray signatures of cosmic ray acceleration, propagation, and confinement in the era of CTA. **Astroparticle Physics**, Elsevier BV, v. 43, p. 276–286, Mar. 2013. DOI: 10.1016/j.astropartphys.2012.05.024.

157 ABDALLA, H. *et al.* **Sensitivity of the Cherenkov Telescope Array for probing cosmology and fundamental physics with gamma-ray propagation**. 2020. Preprint arXiv:2010.01349. Available at: https://arxiv.org/abs/2010.01349. Access at: Jan. 24, 2021.

158 ACHARYYA, A. *et al.* Sensitivity of the cherenkov telescope array to a dark matter signal from the galactic centre. **Journal of Cosmology and Astroparticle Physics**, IOP Publishing, v. 2021, n. 01, p. 057, Jan. 2021. DOI: 10.1088/1475-7516/2021/01/057.

159 ABRAMOWSKI, A. *et al.* Measurement of the extragalactic background light imprint on the spectra of the brightest blazars observed with H.E.S.S. **Astronomy & Astrophysics**, EDP Sciences, v. 550, p. A4, Jan. 2013. DOI: 10.1051/0004-6361/201220355.

160 BYKOV, A. *et al.* Particle acceleration in relativistic outflows. **Space Science Reviews**, Springer Science and Business Media LLC, v. 173, n. 1-4, p. 309–339, June 2012. DOI: 10.1007/s11214-012-9896-y.

161 AHARONIAN, F. *et al.* First ground-based measurement of atmospheric Cherenkov light from cosmic rays. **Physical Review D**, American Physical Society, v. 75, n. 4, p. 042004, Feb. 2007. DOI: 10.1103/physrevd.75.042004.

162 ARCHER, A. *et al.* Measurement of the iron spectrum in cosmic rays by VERITAS. **Physical Review D**, American Physical Society, v. 98, n. 2, p. 022009, July 2018. DOI: 10.1103/physrevd.98.022009.

163 SCIASCIO, G. D. The LHAASO experiment: From gamma-ray astronomy to cosmic rays. **Nuclear and Particle Physics Proceedings**, Elsevier BV, v. 279-281, p. 166–173, Oct. 2016. DOI: 10.1016/j.nuclphysbps.2016.10.024.

164 ACHARYYA, A. *et al.* Monte Carlo studies for the optimisation of the Cherenkov Telescope Array layout. **Astroparticle Physics**, Elsevier BV, v. 111, p. 35–53, Sept. 2019. DOI: 10.1016/j.astropartphys.2019.04.001.

165 AHARONIAN, F. *et al.* High energy astrophysics with ground-based gamma ray detectors. **Reports on Progress in Physics**, IOP Publishing, v. 71, n. 9, p. 096901, Aug. 2008. DOI: 10.1088/0034-4885/71/9/096901.

166 VÖLK, H. J.; BERNLÖHR, K. Imaging very high energy gamma-ray telescopes. **Experimental Astronomy**, Springer Science and Business Media LLC, v. 25, n. 1-3, p. 173–191, Mar. 2009. DOI: 10.1007/s10686-009-9151-z.

167 ACHARYA, B. *et al.* Introducing the CTA concept. **Astroparticle Physics**, Elsevier BV, v. 43, p. 3–18, Mar. 2013. DOI: 10.1016/j.astropartphys.2013.01.007.

168 ADAMS, C. B. *et al.* **Detection of the Crab Nebula with the 9.7 m prototype Schwarzschild-Couder telescope**. 2020. Preprint arXiv:2012.08448. Available at: https://arxiv.org/abs/2012.08448. Access at: Jan. 25, 2021.

169 BERNLÖHR, K. *et al.* Monte Carlo design studies for the cherenkov telescope array. **Astroparticle Physics**, Elsevier BV, v. 43, p. 171–188, Mar. 2013. DOI: 10.1016/j.astropartphys.2012.10.002.

170 FIASSON, A. *et al.* Optimization of multivariate analysis for IACT stereoscopic systems. **Astroparticle Physics**, Elsevier BV, v. 34, n. 1, p. 25–32, Aug. 2010. DOI: 10.1016/j.astropartphys.2010.04.006.

171 AHARONIAN, F. *et al.* Observations of the Crab nebula with HESS. **Astronomy & Astrophysics**, EDP Sciences, v. 457, n. 3, p. 899–915, Sept. 2006. DOI: 10.1051/0004-6361:20065351.

172 FEGAN, D. J. γ/hadron separation at TeV energies. **Journal of Physics G**: nuclear and particle physics, IOP Publishing, v. 23, n. 9, p. 1013–1060, Sept. 1997. DOI: 10.1088/0954-3899/23/9/004.

173 ALBERT, J. *et al.* Implementation of the random forest method for the imaging atmospheric Cherenkov telescope MAGIC. **Nuclear Instruments and Methods in Physics Research Section A**: accelerators, spectrometers, detectors and associated equipment, Elsevier BV, v. 588, n. 3, p. 424–432, Apr. 2008. DOI: 10.1016/j.nima.2007.11.068.

174 ARCHER, A. *et al.* Measurement of cosmic-ray electrons at TeV energies by VERITAS. **Physical Review D**, American Physical Society, v. 98, n. 6, p. 062004, Sept. 2018. DOI: 10.1103/physrevd.98.062004.

175 BOHEC, S. L. *et al.* A new analysis method for very high definition Imaging Atmospheric Cherenkov Telescopes as applied to the CAT telescope. **Nuclear Instruments and Methods in Physics Research Section A**: accelerators, spectrometers, detectors and associated equipment, Elsevier BV, v. 416, n. 2-3, p. 425–437, Nov. 1998. DOI: 10.1016/s0168-9002(98)00750-5.

176 NAUROIS, M. de; ROLLAND, L. A high performance likelihood reconstruction of γ-rays for imaging atmospheric Cherenkov telescopes. **Astroparticle Physics**, Elsevier BV, v. 32, n. 5, p. 231–252, Dec. 2009. DOI: 10.1016/j.astropartphys.2009.09.001.

177 PARSONS, R.; HINTON, J. A monte carlo template based analysis for air-Cherenkov arrays. **Astroparticle Physics**, Elsevier BV, v. 56, p. 26–34, Apr. 2014. DOI: 10.1016/j.astropartphys.2014.03.002.

178 LEMOINE-GOUMARD, M.; DEGRANGE, B.; TLUCZYKONT, M. Selection and 3D-reconstruction of gamma-ray-induced air showers with a stereoscopic system of atmospheric Cherenkov telescopes. **Astroparticle Physics**, Elsevier BV, v. 25, n. 3, p. 195–211, Apr. 2006. DOI: 10.1016/j.astropartphys.2006.01.005.

179 NAUMANN-GODÓ, M.; LEMOINE-GOUMARD, M.; DEGRANGE, B. Upgrading and testing the 3D reconstruction of gamma-ray air showers as observed with an array of imaging atmospheric Cherenkov telescopes. **Astroparticle Physics**, Elsevier BV, v. 31, n. 6, p. 421–430, July 2009. DOI: 10.1016/j.astropartphys.2009.04.006.

180 SHILON, I. *et al.* Application of deep learning methods to analysis of imaging atmospheric cherenkov telescopes data. **Astroparticle Physics**, Elsevier BV, v. 105, p. 44–53, Feb. 2019. DOI: 10.1016/j.astropartphys.2018.10.003.

181 JACQUEMONT, M. *et al.* GammaLearn: a deep learning framework for IACT data. **Proceedings of Science**, v. 358, p. 705, 2019. DOI: 10.22323/1.358.0705.

182 CASTAÑO, D. N. *et al.* CTLearn: deep learning for gamma-ray astronomy. **Proceedings of Science**, v. 358, p. 752, 2019. DOI: 10.22323/1.358.0752.

183 DRURY, L. O. An introduction to the theory of diffusive shock acceleration of energetic particles in tenuous plasmas. **Reports on Progress in Physics**, IOP Publishing, v. 46, n. 8, p. 973–1027, Aug. 1983. DOI: 10.1088/0034-4885/46/8/002.

184 BLANDFORD, R.; EICHLER, D. Particle acceleration at astrophysical shocks: a theory of cosmic ray origin. **Physics Reports**, Elsevier BV, v. 154, n. 1, p. 1–75, Oct. 1987. DOI: 10.1016/0370-1573(87)90134-7.

185 SPURIO, M. **Probes of multimessenger astrophysics**: charged cosmic rays, neutrinos, γ-rays and gravitational waves. 2nd. ed. Cham: Springer, 2018. (Astronomy and Astrophysics Library). DOI: 10.1007/978-3-319-96854-4. ISBN 978-3-319-96854-4.

186 ALIU, E. *et al.* Observation of pulsed γ-rays above 25 GeV from the Crab pulsar with MAGIC. **Science**, American Association for the Advancement of Science, v. 322, n. 5905, p. 1221–1224, Nov. 2008. DOI: 10.1126/science.1164718.

187 ANSOLDI, S. *et al.* Teraelectronvolt pulsed emission from the Crab Pulsar detected by MAGIC. **Astronomy & Astrophysics**, EDP Sciences, v. 585, p. A133, Jan. 2016. DOI: 10.1051/0004-6361/201526853.

188 ABDALLA, H. *et al.* First ground-based measurement of sub-20 GeV to 100 GeV γ-rays from the Vela pulsar with H.E.S.S. II. **Astronomy & Astrophysics**, EDP Sciences, v. 620, p. A66, Dec. 2018. DOI: 10.1051/0004-6361/201732153.

189 ACCIARI, V. A. *et al.* Detection of the Geminga pulsar with MAGIC hints at a power-law tail emission beyond 15 GeV. **Astronomy & Astrophysics**, EDP Sciences, v. 643, p. L14, Nov. 2020. DOI: 10.1051/0004-6361/202039131.

190 SPIR-JACOB, M. *et al.* Detection of sub-100 GeV γ-ray pulsations from PSR B1706-44 with H.E.S.S. **Proceedings of Science**, v. 358, p. 799, 2019. DOI: 10.22323/1.358.0799.

191 ABDALLA, H. *et al.* The H.E.S.S. Galactic plane survey. **Astronomy & Astrophysics**, EDP Sciences, v. 612, p. A1, Apr. 2018. DOI: 10.1051/0004-6361/201732098.

192 ABDALLA, H. *et al.* The population of TeV pulsar wind nebulae in the H.E.S.S. galactic plane survey. **Astronomy & Astrophysics**, EDP Sciences, v. 612, p. A2, Apr. 2018. DOI: 10.1051/0004-6361/201629377.

193 ABDALLA, H. *et al.* Detection of very-high-energy γ-ray emission from the colliding wind binary η Car with H.E.S.S. **Astronomy & Astrophysics**, EDP Sciences, v. 635, p. A167, Mar. 2020. DOI: 10.1051/0004-6361/201936761.

194 ABEYSEKARA, A. U. *et al.* Periastron observations of TeV gamma-ray emission from a binary system with a 50-year period. **The Astrophysical Journal**, American Astronomical Society, v. 867, n. 1, p. L19, Oct. 2018. DOI: 10.3847/2041-8213/aae70e.

195 AHARONIAN, F. *et al.* Discovery of very-high-energy γ-rays from the galactic centre ridge. **Nature**, Springer Science and Business Media LLC, v. 439, n. 7077, p. 695–698, Feb. 2006. DOI: 10.1038/nature04467.

196 ABRAMOWSKI, A. *et al.* Acceleration of petaelectronvolt protons in the Galactic Centre. **Nature**, Springer Science and Business Media LLC, v. 531, n. 7595, p. 476–479, Mar. 2016. DOI: 10.1038/nature17147.

197 ABDALLA, H. *et al.* Characterising the VHE diffuse emission in the central 200 parsecs of our galaxy with H.E.S.S. **Astronomy & Astrophysics**, EDP Sciences, v. 612, p. A9, Apr. 2018. DOI: 10.1051/0004-6361/201730824.

198 ACCIARI, V. *et al.* Observation of Markarian 421 in TeV gamma rays over a 14-year time span. **Astroparticle Physics**, Elsevier BV, v. 54, p. 1–10, Feb. 2014. DOI: 10.1016/j.astropartphys.2013.10.004.

199 ALEKSIĆ, J. *et al.* The 2009 multiwavelength campaign on Mrk 421: variability and correlation studies. **Astronomy & Astrophysics**, EDP Sciences, v. 576, p. A126, Apr. 2015. DOI: 10.1051/0004-6361/201424216.

200 ACCIARI, V. A. *et al.* A connection between star formation activity and cosmic rays in the starburst galaxy M82. **Nature**, Springer Science and Business Media LLC, v. 462, n. 7274, p. 770–772, Nov. 2009. DOI: 10.1038/nature08557.

201 ACERO, F. *et al.* Detection of gamma rays from a starburst galaxy. **Science**, American Association for the Advancement of Science, v. 326, n. 5956, p. 1080–1082, Sept. 2009. DOI: 10.1126/science.1178826.

202 ACKERMANN, M. *et al.* The first Fermi-LAT gamma-ray burst catalog. **The Astrophysical Journal Supplement Series**, American Astronomical Society, v. 209, n. 1, p. 11, Oct. 2013. DOI: 10.1088/0067-0049/209/1/11.

203 PETRY, D. The MAGIC telescope: prospects for GRB research. **Astronomy and Astrophysics Supplement Series**, EDP Sciences, v. 138, n. 3, p. 601–602, Sept. 1999. DOI: 10.1051/aas:1999369.

204 AHARONIAN, F. *et al.* HESS observations of γ-ray bursts in 2003-2007. **Astronomy & Astrophysics**, EDP Sciences, v. 495, n. 2, p. 505–512, Jan. 2009. DOI: 10.1051/0004-6361:200811072.

205 ACCIARI, V. A. *et al.* VERITAS observations of gamma-ray bursts detected by SWIFT. **The Astrophysical Journal**, American Astronomical Society, v. 743, n. 1, p. 62, Nov. 2011. DOI: 10.1088/0004-637x/743/1/62.

206 ACHARYA, B. S. *et al.* **Science with the Cherenkov Telescope Array**. New Jersey: World Scientific Publishing Company, 2018. DOI: 10.1142/10986. ISBN 9789813270084.

207 CARAVEO, P. A. The golden age of high-energy gamma-ray astronomy: the Cherenkov Telescope Array in the multimessenger era. **La Rivista del Nuovo Cimento**, Springer Science and Business Media LLC, v. 43, n. 6, p. 281–318, Apr. 2020. DOI: 10.1007/s40766-020-00006-3.

208 CHERENKOV TELESCOPE ARRAY OBSERVATORY. Available at: https://www.cta-observatory.org/. Access at: Jan. 24, 2021.

209 DUBUS, G. *et al.* Surveys with the Cherenkov Telescope Array. **Astroparticle Physics**, Elsevier BV, v. 43, p. 317–330, Mar. 2013. DOI: 10.1016/j.astropartphys.2012.05.020.

210 CORTINA, J. Status of the large size telescopes of the Cherenkov Telescope Array. **Proceedings of Science**, v. 358, p. 653, 2019. DOI: 10.22323/1.358.0653.

211 GLICENSTEIN, J.-F. Status of the Davies Cotton and Schwarzschild-Couder medium sized telescopes for the Cherenkov Telescope Array. **Proceedings of Science**, v. 358, p. 269, 2019. DOI: 10.22323/1.358.0269.

212 HELLER, M. *et al.* The SST-1M project for the Cherenkov Telescope Array. **Proceedings of Science**, v. 358, p. 694, 2019. DOI: 10.22323/1.358.0694.

213 MINEO, T. *et al.* Muon calibration of the ASTRI-Horn telescope: preliminary results. **Proceedings of Science**, v. 358, p. 744, 2019. DOI: 10.22323/1.358.0744.

214 DMYTRIIEV, A. *et al.* Assessment of the GCT prototype's optical system implementation and other key performances for the Cherenkov Telescope Array. **Proceedings of Science**, v. 358, p. 663, 2019. DOI: 10.22323/1.358.0663.

215 PERESANO, M.; KOSACK, K. CTAPIPE: a low-level data processing framework for the Cherenkov Telescope Array. **Proceedings of Science**, v. 358, p. 717, 2019. DOI: 10.22323/1.358.0717.

216 CARLSON, J. F.; OPPENHEIMER, J. R. On multiplicative showers. **Physical Review**, American Physical Society, v. 51, n. 4, p. 220–231, Feb. 1937. DOI: 10.1103/physrev.51.220.

217 HEITLER, W. **The quantum theory of radiation**. 3rd. ed. Oxford: Oxford University Press, 1954. (International Series of Monographs on Physics).

218 GAISSER, T.; ENGEL, R.; RESCONI, E. **Cosmic rays and particle physics**. 2nd. ed. Cambridge: Cambridge University Press, 2016. DOI: 10.1017/CBO9781139192194. ISBN 978-0-521-01646-9.

219 ROSSI, B.; GREISEN, K. Cosmic-ray theory. **Reviews of Modern Physics**, American Physical Society, v. 13, n. 4, p. 240–309, Oct. 1941. DOI: 10.1103/revmodphys.13.240.

220 GREISEN, K. The extensive air showers. *In*: WILSON, J. G. (ed.). **Progress in cosmic ray physics**. Amsterdam: North-Holland Publishing Company, 1956. v. 3, cap. 1, p. 1–142.

221 MIGDAL, A. B. Bremsstrahlung and pair production in condensed media at high energies. **Physical Review**, American Physical Society, v. 103, n. 6, p. 1811–1820, Sept. 1956. DOI: 10.1103/physrev.103.1811.

222 CILLIS, A. N. *et al.* Influence of the LPM effect and dielectric suppression on particle air showers. **Physical Review D**, American Physical Society, v. 59, n. 11, p. 113012, May 1999. DOI: 10.1103/physrevd.59.113012.

223 ERBER, T. High-energy electromagnetic conversion processes in intense magnetic fields. **Reviews of Modern Physics**, American Physical Society, v. 38, n. 4, p. 626–659, Oct. 1966. DOI: 10.1103/revmodphys.38.626.

224 STANEV, T.; VANKOV, H. P. Nature of the highest energy cosmic rays. **Physical Review D**, American Physical Society, v. 55, n. 3, p. 1365–1371, Feb. 1997. DOI: 10.1103/physrevd.55.1365.

225 VANKOV, H. P.; INOUE, N.; SHINOZAKI, K. Ultrahigh energy gamma rays in the geomagnetic field and atmosphere. **Physical Review D**, American Physical Society, v. 67, n. 4, p. 043002, Feb. 2003. DOI: 10.1103/physrevd.67.043002.

226 ARBELETCHE, L. B.; GONÇALVES, V. P.; MÜLLER, M. A. Investigating the influence of diffractive interactions on ultrahigh-energy extensive air showers. **International Journal of Modern Physics A**, World Scientific, v. 33, n. 26, p. 1850153, Sept. 2018. DOI: 10.1142/s0217751x18501531.

227 CALCAGNI, L. *et al.* LHC updated hadronic interaction packages analyzed up to cosmic-ray energies. **Physical Review D**, American Physical Society, v. 98, n. 8, p. 083003, Oct. 2018. DOI: 10.1103/physrevd.98.083003.

228 ANCHORDOQUI, L. A. Ultra-high-energy cosmic rays. **Physics Reports**, Elsevier BV, v. 801, p. 1–93, Apr. 2019. DOI: 10.1016/j.physrep.2019.01.002.

229 MATTHEWS, J. A Heitler model of extensive air showers. **Astroparticle Physics**, Elsevier BV, v. 22, n. 5-6, p. 387–397, Jan. 2005. DOI: 10.1016/j.astropartphys.2004.09.003.

230 HÖRANDEL, J. R. Cosmic rays from the knee to the second knee: 10^{14} to 10^{18} eV. **Modern Physics Letters A**, World Scientific Pub Co Pte Lt, v. 22, n. 21, p. 1533–1551, July 2007. DOI: 10.1142/s0217732307024139.

231 MONTANUS, J. An extended Heitler-Matthews model for the full hadronic cascade in cosmic air showers. **Astroparticle Physics**, Elsevier BV, v. 59, p. 4–11, July 2014. DOI: 10.1016/j.astropartphys.2014.03.010.

232 LINSLEY, J. Structure of large air showers at depth 834 g/cm^2: applications. *In*: INTERNATIONAL COSMIC RAY CONFERENCE, 15., 1977, Plovdiv. **Proceedings** [**...**]. Bulgaria: Bulgarian Academy of Sciences, 1977. v. 12, p. 89–96. Available at: http://adsabs.harvard.edu/abs/1977ICRC...12...89L. Access at: Jan. 2, 2021.

233 LINSLEY, J.; WATSON, A. A. Validity of scaling to 10^{20} eV and high-energy cosmic-ray composition. **Physical Review Letters**, American Physical Society, v. 46, n. 7, p. 459–463, Feb. 1981. DOI: 10.1103/physrevlett.46.459.

234 MATTHEWS, J. Energy flow in air showers. *In*: INTERNATIONAL COSMIC RAY CONFERENCE, 27., 2001, Hamburg. **Proceedings** [**...**]. Katlenburg-Lindau, Germany: Copernicus Gesellschaft, 2001. v. 1, p. 261–264. Available at: http://icrc2001.uni-wuppertal.de/ICRC2001/papers/ici6261_p.pdf. Access at: Jan. 2, 2021.

235 ENGEL, J. *et al.* Nucleus-nucleus collisions and interpretation of cosmic-ray cascades. **Physical Review D**, American Physical Society, v. 46, n. 11, p. 5013–5025, Dec. 1992. DOI: 10.1103/physrevd.46.5013.

236 AAB, A. *et al.* Muons in air showers at the Pierre Auger Observatory: mean number in highly inclined events. **Physical Review D**, American Physical Society, v. 91, n. 3, p. 032003, Feb. 2015. DOI: 10.1103/physrevd.91.032003.

237 BLAESS, S.; BELLIDO, J.; DAWSON, B. Reducing the model dependence in the cosmic ray composition interpretation of $X_{\max}$ distributions. **Proceedings of Science**, v. 301, p. 490, 2017. DOI: 10.22323/1.301.0490.

238 ARSENE, N.; SIMA, O. UHECRs mass composition from $X_{\max}$ distributions. **The European Physical Journal C**, Springer Science and Business Media LLC, v. 80, n. 1, p. 48, Jan. 2020. DOI: 10.1140/epjc/s10052-020-7634-2.

239 LIPARI, P. Concepts of "age" and "universality" in cosmic ray showers. **Physical Review D**, American Physical Society, v. 79, n. 6, p. 063001, Mar. 2009. DOI: 10.1103/physrevd.79.063001.

240 NERLING, F. *et al.* Universality of electron distributions in high-energy air showers – description of Cherenkov light production. **Astroparticle Physics**, Elsevier BV, v. 24, n. 6, p. 421–437, Jan. 2006. DOI: 10.1016/j.astropartphys.2005.09.002.

241 GILLER, M. *et al.* Similarity of extensive air showers with respect to the shower age. **Journal of Physics G**: nuclear and particle physics, IOP Publishing, v. 31, n. 8, p. 947–958, June 2005. DOI: 10.1088/0954-3899/31/8/023.

242 LAFEBRE, S. *et al.* Universality of electron-positron distributions in extensive air showers. **Astroparticle Physics**, Elsevier BV, v. 31, n. 3, p. 243–254, Apr. 2009. DOI: 10.1016/j.astropartphys.2009.02.002.

243 GILLER, M.; ŚMIAŁKOWSKI, A.; WIECZOREK, G. An extended universality of electron distributions in cosmic ray showers of high energies and its application. **Astroparticle Physics**, Elsevier BV, v. 60, p. 92–104, Jan. 2015. DOI: 10.1016/j.astropartphys.2014.04.003.

244 ŚMIAŁKOWSKI, A.; GILLER, M. Universality of electron distributions in extensive air showers. **The Astrophysical Journal**, American Astronomical Society, v. 854, n. 1, p. 48, Feb. 2018. DOI: 10.3847/1538-4357/aaa488.

245 HILLAS, A. M. Angular and energy distributions of charged particles in electron-photon cascades in air. **Journal of Physics G**: nuclear and particle physics, IOP Publishing, v. 8, n. 10, p. 1461–1473, Oct. 1982. DOI: 10.1088/0305-4616/8/10/016.

246 HECK, D. *et al.* **CORSIKA**: a monte carlo code to simulate extensive air showers. Karlsruhe, 1998. Available at: https://www.iap.kit.edu/corsika/70.php. Access at: Sept. 3, 2019.

247 BERGMANN, T. *et al.* One-dimensional hybrid approach to extensive air shower simulation. **Astroparticle Physics**, Elsevier BV, v. 26, n. 6, p. 420–432, Jan. 2007. DOI: 10.1016/j.astropartphys.2006.08.005.

248 PIEROG, T. *et al.* First results of fast one-dimensional hybrid simulation of EAS using CONEX. **Nuclear Physics B**: proceedings supplements, Elsevier BV, v. 151, n. 1, p. 159–162, Jan. 2006. DOI: 10.1016/j.nuclphysbps.2005.07.029.

249 BOSSARD, G. *et al.* Cosmic ray air shower characteristics in the framework of the parton-based Gribov-Regge model NEXUS. **Physical Review D**, American Physical Society, v. 63, n. 5, p. 054030, Feb. 2001. DOI: 10.1103/physrevd.63.054030.

250 BAACK, D. **Data reduction for CORSIKA**. Dortmund, 2016. DOI: 10.17877/DE290R-19158.

251 NELSON, W. R.; HIRAYAMA, H.; ROGERS, D. W. **The EGS4 code system**. Stanford, 1985. Available at: https://www-public.slac.stanford.edu/scidoc/docMeta.aspx?slacPubNumber=slac-R-265. Access at: Jan. 14, 2021.

252 BLEICHER, M. *et al.* Relativistic hadron-hadron collisions in the ultra-relativistic quantum molecular dynamics model. **Journal of Physics G**: nuclear and particle physics, IOP Publishing, v. 25, n. 9, p. 1859–1896, Sept. 1999. DOI: 10.1088/0954-3899/25/9/308.

253 BATTISTONI, G. *et al.* Overview of the FLUKA code. **Annals of Nuclear Energy**, Elsevier BV, v. 82, p. 10–18, Aug. 2015. DOI: 10.1016/j.anucene.2014.11.007.

254 PARSONS, R.; SCHOORLEMMER, H. Systematic differences due to high energy hadronic interaction models in air shower simulations in the 100 GeV–100 TeV range. **Physical Review D**, American Physical Society, v. 100, n. 2, p. 023010, July 2019. DOI: 10.1103/physrevd.100.023010.

255 PARSONS, R. *et al.* Systematic uncertainties in air shower measurements from high-energy hadronic interaction models. **Astroparticle Physics**, Elsevier BV, v. 34, n. 11, p. 832–839, June 2011. DOI: 10.1016/j.astropartphys.2011.02.007.

256 AAB, A. *et al.* Testing hadronic interactions at ultrahigh energies with air showers measured by the Pierre Auger Observatory. **Physical Review Letters**, American Physical Society, v. 117, n. 19, p. 192001, Oct. 2016. DOI: 10.1103/physrevlett.117.192001.

257 OSTAPCHENKO, S. Monte Carlo treatment of hadronic interactions in enhanced pomeron scheme: QGSJET-II model. **Physical Review D**, American Physical Society, v. 83, n. 1, p. 014018, Jan. 2011. DOI: 10.1103/physrevd.83.014018.

258 PIEROG, T. *et al.* EPOS LHC: Test of collective hadronization with data measured at the CERN Large Hadron Collider. **Physical Review C**, American Physical Society, v. 92, n. 3, p. 034906, Sept. 2015. DOI: 10.1103/physrevc.92.034906.

259 FEDYNITCH, A. *et al.* Hadronic interaction model Sibyll 2.3c and inclusive lepton fluxes. **Physical Review D**, American Physical Society, v. 100, n. 10, p. 103018, Nov. 2019. DOI: 10.1103/physrevd.100.103018.

260 ARRABITO, L. *et al.* Optimizing Cherenkov photons generation and propagation in CORSIKA for CTA Monte-Carlo simulations. **Computing and Software for Big Science**, Springer Science and Business Media LLC, v. 4, n. 1, p. 9, July 2020. DOI: 10.1007/s41781-020-00042-y.

261 PEIXOTO, C. J. T.; SOUZA, V. de; BELLIDO, J. A. Comparison of the moments of the distribution predicted by different cosmic ray shower simulation models. **Astroparticle Physics**, Elsevier BV, v. 47, p. 18–30, July 2013. DOI: 10.1016/j.astropartphys.2013.05.011.

262 GRIEDER, P. K. F. **Extensive air showers**: high energy phenomena and astrophysical aspects. Heidelberg: Springer, 2010. DOI: 10.1007/978-3-540-76941-5. ISBN 978-3-540-76941-5.

263 JELLEY, J. V.; PORTER, N. A. Cerenkov radiation from the night sky, and its application to γ-ray astronomy. **Quarterly Journal of the Royal Astronomical Society**, v. 4, p. 275, Sept. 1963.

264 JARDIN-BLICQ, A. **The TeV γ-ray emission of the Galactic Plane**: HAWC and H.E.S.S. observations of the Galactic Plane and detailed study of the region surrounding 2HWC J1928+177. 2019. Ph. D. Thesis (Natural Sciences) — University of Heidelberg, Heidelberg, Germany, 2019. DOI: 10.11588/HEIDOK.00026779.

265 AHARONIAN, F. *et al.* Energy spectrum of cosmic-ray electrons at TeV energies. **Physical Review Letters**, American Physical Society, v. 101, n. 26, Dec. 2008. DOI: 10.1103/physrevlett.101.261104.

266 MAIER, G. *et al.* Performance of the Cherenkov Telescope Array. **Proceedings of Science**, v. 358, p. 733, 2019. DOI: 10.22323/1.358.0733.

267 ANCHORDOQUI, L. A. *et al.* Performance and science reach of the Probe of Extreme Multimessenger Astrophysics for ultrahigh-energy particles. **Physical Review D**, American Physical Society, v. 101, n. 2, p. 023012, Jan. 2020. DOI: 10.1103/physrevd.101.023012.

268 CORNET, F. *et al.* Photoproduction models for total cross section and shower development. **EPJ Web of Conferences**, EDP Sciences, v. 99, p. 10005, 2015. DOI: https://doi.org/10.1051/epjconf/2015991000510.1051/epjconf/20159910005.

269 BARONE, V.; PREDAZZI, E. **High-energy particle diffraction**. Berlin: Springer Berlin Heidelberg, 2002. (Texts and Monographs in Physics). DOI: 10.1007/978-3-662-04724-8. ISBN 978-3-662-04724-8.

270 OSTAPCHENKO, S. Cosmic ray interaction models: an overview. **EPJ Web of Conferences**, EDP Sciences, v. 120, p. 04003, 2016. DOI: 10.1051/epjconf/201612004003.

271 D'ENTERRIA, D. *et al.* Constraints from the first LHC data on hadronic event generators for ultra-high energy cosmic-ray physics. **Astroparticle Physics**, Elsevier BV, v. 35, n. 2, p. 98–113, Sept. 2011. DOI: 10.1016/j.astropartphys.2011.05.002.

272 ULRICH, R.; ENGEL, R.; UNGER, M. Hadronic multiparticle production at ultrahigh energies and extensive air showers. **Physical Review D**, American Physical Society, v. 83, n. 5, Mar. 2011. DOI: 10.1103/physrevd.83.054026.

273 BERNLöHR, K. Simulation of imaging atmospheric Cherenkov telescopes with CORSIKA and sim_telarray. **Astroparticle Physics**, Elsevier BV, v. 30, n. 3, p. 149–158, Oct. 2008. DOI: 10.1016/j.astropartphys.2008.07.009.

274 OHISHI, M. *et al.* Influence of uncertainty in hadronic interaction models on the sensitivity estimation of Cherenkov Telescope Array. **Journal of Physics**: conference series, IOP Publishing, v. 1468, p. 012073, Feb. 2020. DOI: 10.1088/1742-6596/1468/1/012073.

275 MUZIO, M. S.; UNGER, M.; FARRAR, G. R. Progress towards characterizing ultrahigh energy cosmic ray sources. **Physical Review D**, American Physical Society, v. 100, n. 10, p. 103008, Nov. 2019. DOI: 10.1103/physrevd.100.103008.